Characterize planetary systems of nearby active red dwarfs with SPIRou

Baptiste Klein

Université Fédérale
Toulouse Midi-Pyrénées

THÈSE

En vue de l'obtention du

DOCTORAT DE L'UNIVERSITÉ DE TOULOUSE

Délivré par :

Université Toulouse 3 Paul Sabatier (UT3 Paul Sabatier)

Présentée et soutenue par :
Baptiste KLEIN
le 16/12/2020

Titre :
Caractériser les systèmes planétaires de naines rouges actives proches avec SPIRou

---

École doctorale et discipline ou spécialité :
ED SDU2E : Astrophysique, Sciences de l'Espace, Planétologie

Unité de recherche :
Institut de Recherche en Astrophysique et Planétologie (IRAP, UMR 5277)

Directeur/trice(s) de Thèse :
Jean-François DONATI

Jury :
Michel RIEUTORD, Professeur , Président du jury
Andrew COLLIER CAMERON, Professeur , Rapporteur
François BOUCHY, Professeur associé, Rapporteur
Magali DELEUIL, Professeur, Examinatrice
Bruno BÉZARD, Astronome, Examinateur
Jean-François DONATI, Directeur de Recherche; Directeur de thèse

Abstract

In the past two decades, about 4300 exoplanets embedded in more than 3000 planetary systems have been discovered. Among these planets, only a handful of Earth-like planets orbiting in the habitable zone (HZ) of their host star were found, most of them being too far away to probe their atmosphere with forthcoming missions like the JWST and the ELTs, and search for potential biosignatures therein. Detecting new nearby HZ terrestrial planets is therefore an essential step in the quest for extraterrestrial life. M dwarfs are key targets in this venture. They largely dominate the stellar population in the solar neighborhood, they are known to frequently host multiple low-mass planets, and they feature smaller radii and closer-in HZ than Sun-like stars, making it easier to detect Earth-twins around them. Moreover, studying the formation and evolution of HZ planets is key for understanding the hypothetical emergence of life. Detecting and characterizing planetary systems around young pre-main-sequence (PMS) stars is thus an unavoidable step in the search for potentially habitable exoplanets. However, monitoring the radial velocity (RV) of M dwarfs and PMS stars with high-precision spectrometers like HARPS is an arduous task given the intrinsic faintness of these stars at visible wavelengths. Moreover, both types of stars are also known to exhibit intense magnetic activity inducing RV signals that overshadow the planet signatures, making them extremely difficult to detect.

The favored spectral range to detect planets around M dwarfs and low-mass PMS stars is the near-infrared (nIR), where both types of stars emit most of their light. Stellar activity RV signals are expected to be weaker in this domain than at visible wavelengths, making it easier to separate the planet RV signatures from stellar jitters. Moreover, the enhanced Zeeman signatures in the nIR boost the spectropolarimetric sensitivity to both large- and small-scale magnetic fields at the stellar surface, giving the opportunity to constrain the processes driving stellar activity in M dwarfs and low-mass PMS, and model the associated RV signals. Thanks to its high-precision velocimetric and spectropolarimetric capabilities in the nIR, SPIRou, at the Canada-France-Hawaii telescope, has the potential to revolutionize our knowledge of the planetary systems around nearby M dwarfs and low-mass PMS stars.

In this thesis, we investigate how the capabilities of SPIRou can be used to characterize close-in planetary systems around M dwarfs and PMS stars, as well as investigate their surface magnetic fields and activity. Through realistic simulations of RV follow-ups of the ultracool dwarf TRAPPIST-1 and the PMS star K2-33, we assess the ability of SPIRou to recover the masses of transiting planets under different observational schemes and noise levels. This preliminary work was followed by actual spectropolarimetric observations of the PMS star AU Microscopii (AU Mic) with SPIRou. These observations enabled us to successfully measure the mass of the close-in transiting Neptune-sized planet AU Mic b, and to reconstruct the distributions of brightness and magnetic field at the surface of the star using Zeeman-Doppler imaging. This technique was also applied to ESPaDOnS/HARPS-Pol spectropolarimetric observations of a set of low-mass stars with various properties : V471 Tau (K2 dwarf), EPIC 211889233 (M0 dwarf) and Proxima Centauri (M5.5 dwarf), allowing us to explore the exotic dynamo processes underlying their activity phenomena. Finally, we developed a framework to probe the composition of the atmospheres of transiting planets using SPIRou spectroscopic capabilities. Applying this framework to spectroscopic observations of the transit of the well-known hot Jupiter HD 189733 b resulted in a fair detection of water in the planet atmosphere, confirming the ability of SPIRou to carry out transmission spectroscopy of hot transiting giants.

Resumé

Les deux dernières décennies ont été marquées par la découverte d'environ 4300 exoplanètes réparties dans plus de 3000 systèmes planétaires. Cependant seule une poignée de planètes semblables à la Terre, en orbite dans la zone habitable (ZH) de leur étoile hôte, ont été détectées à ce jour, bon nombre d'entre elles étant trop éloigné pour la recherche de biomarqueurs dans leur atmosphère avec le JWST et les ELTs. Les naines M sont des cibles de choix dans la quête de vie extra-terrestre. Outre le fait qu'elles constituent la vaste majorité des étoiles du voisinage solaire, les naines M présentent à la fois des rayons plus petits et des ZH plus compactes que leurs homologues solaires, facilitant ainsi la recherche de jumelles terrestres dans leur voisinage. En parallèle, l'étude de la formation et de l'évolution des systèmes planétaires est essentielle pour comprendre comment la vie peut émerger dans un système semblable à la Terre. La détection de planètes autour des étoiles « pré-séquence principale » (PSP) constitue par conséquent un objectif indissociable de celui de la recherche des exoplanètes dans la ZH. Toutefois la mesure précise de la vitesse radiale (VR) des naines M et des étoiles PSP est ardue en raison de la faible luminosité de ces étoiles dans le domaine visible. De plus, ces deux types d'étoiles sont connus pour leur intense activité magnétique induisant des signaux en VR qui éclipsent les signatures des planètes, les rendant ainsi extrêmement difficiles à détecter.

L'observation des naines M et des étoiles PSP de faible masse dans le proche infrarouge (nIR), où les deux types d'étoiles émettent la majeure partie de leur lumière, est essentielle pour détecter des systèmes planétaires en orbite autour d'elles. L'amplitude des signaux VR induits par l'activité stellaire est plus faible dans le nIR que dans le domaine visible, ce qui devrait faciliter la séparation des signatures VR planétaires de celles d'origine stellaire. De plus, l'intensification des signatures de Zeeman dans le proche infrarouge augmente la sensibilité spectropolarimétrique aux champs magnétiques de petite et grande échelle à la surface stellaire, permettant ainsi d'investiguer les processus régissant l'activité stellaire dans les naines M et les étoiles PSP de faibles masses, et de modéliser les signaux RV associés. Fort de ses capacités vélocimétriques et spectropolarimétriques dans le nIR, SPIRou a le potentiel de révolutionner notre connaissance des systèmes planétaires autour de ces deux types d'étoiles situées dans le voisinage solaire.

Dans cette thèse, nous étudions comment les capacités de SPIRou peuvent être mises à profit pour caractériser les systèmes planétaires autour des naines M et des étoiles PSP, ainsi que pour étudier leurs champs magnétiques de surface et l'activité qu'ils induisent. Au moyen de simulations réalistes d'observations en VR, nous avons d'abord évalué la capacité de SPIRou à mesurer des masses planétaires en fonction de la stratégie d'observation et du niveau de bruit de mesure. Ce travail préliminaire nous a permis d'obtenir des observations spectropolarimétriques de l'étoile PSP AU Microscopii avec SPIRou, desquelles nous avons pu détecter la signature VR de la planète AU Mic b et reconstruire les distributions de brillance et de champ magnétique à la surface de l'étoile au moyen de l'imagerie Zeeman-Doppler. Cette technique a également été appliquée à des observations spectropolarimétriques d'un ensemble d'étoiles de faible masse aux propriétés diverses (V471 Tau, EPIC 211889233 et Proxima Centauri), permettant ainsi d'explorer les processus de dynamo sous-jacents à leurs phénomènes d'activité. Enfin, l'analyse d'observations spectroscopiques du transit du Jupiter chaud HD 189733 b avec SPIRou nous a permis d'obtenir une détection d'eau dans l'atmosphère de la planète, démontrant ainsi la capacité de l'instrument à effectuer de la spectroscopie de transmission de planètes géantes.

Contents

Remerciements

Le présent document détaille l'ensemble des travaux de recherche auxquels j'ai contribué au cours de ma thèse de doctorat à l'Institut de Recherche en Astrophysique et Planétologie. Jamais je n'aurais pu imaginer, il y a trois ans de cela, vivre une expérience aussi enrichissante, tant sur le plan scientifique où j'ai eu l'opportunité acquérir un savoir-faire dans des domaines aussi diverses qu'excitants, que sur le plan personnel. Tout cela n'aurait cependant pas été possible sans toutes les personnes que j'ai eu la chance de cotoyer durant ces trois dernières années et que je souhaite chaleureusement remercier avant d'entrer dans le vif du sujet.

Les travaux effectués pendant ma thèse et présentés dans ce manuscrit ont été financés par le programme de recherche et innovation H2020 du conseil de recherche européen (ERC, #740651 NewWorlds) que je remercie bien cordialement.

Je souhaiterais exprimer ma reconnaissance aux rapporteurs de mon manuscrit de thèse, Andrew Collier Cameron et François Bouchy, pour leur relecture méticuleuse et leurs commentaires perspicaces. Ma reconnaissance s'étend également aux examinateurs de ma soutenance de thèse, Magali Deleuil, Bruno Bézard et Michel Rieutord.

Je souhaite ensuite addresser des remerciements particulièrement chaleureux à mon directeur de thèse, Jean-François Donati, pour m'avoir fait confiance et soutenu tout au long de ce passionnant projet de thèse et pour m'avoir initié avec pédagogie à des domaines aussi complexes que l'imagerie Zeeman-Doppler, la spectropolarimétrie et vélocimétrie à haute précision, et la modélisation de séries temporelles en photométrie et vitesse radiale. Mes remerciements s'étendent naturellement aux membres de l'équipe de l'*ERC NewWorlds*, en particulier à Claire Moutou, Florian Debras et Clément Baruteau, toujours disponibles et ayant fait preuve d'un enthousiasme inébranlable lors de nos discussions scientifiques qui, j'espère, pourront mener à de futures collaborations fructueuses. Je tiens également à remercier toute l'équipe SPIRou, en particulier Xavier Delfosse, Andrès Carmona, Julien Rameau, Thierry Forveille, Julien Morin, Guillaume Hébrard, Étienne Artigau, René Doyon. Enfin, je suis reconnaissant envers les membres du groupe scientifique PS2E, toujours ouverts aux discussions et dont les traditionnels "workshops" annuels me laisseront un souvenir impérissable.

Au sein de l'Observatoire Midi-Pyrénées, je tiens à remercier les membres du GIS de l'équipe SPIP (en particulier Marielle, Sébastien, Driss, Yohan, Zalpha, Michel, Bruno), que je prenais plaisir à retrouver régulièrement pour le café du matin, ainsi que les membres de l'équipe Neo-Narval (Torsten, Jean-Baptiste à Toulouse et René, Rémi, Francis, Prazeres, Philippe, Frank, Laurent, Guillaume à Tarbes) qui m'ont superbement accueilli lors de mon stage de césure et qui ont grandement contribué à faire de l'astrophysique ma vocation. Je tiens également à exprimer ma reconnaissance à l'équipe SISU, et en particulier à Hervé, Mégane, Simon, Mehdi et Andréa qui ont su m'épauler dans les moments les plus sombres de mes estimateurs Bayésiens. Enfin, je tiens à remercier toutes le personnel de l'IRAP/OMP avec lequel j'ai eu la chance d'interagir, notamment en tant que représentant des doctorants au conseil du laboratoire de l'IRAP (en particulier Christine, Julie, Audrey, Williams, Gabi, Camille, Didier, Josette, Sylvie, Émilie, Loïc, Carole, Sébastien).

Venons-en maintenant à des remerciements plus personnels à tous ceux que j'ai eu le plaisir de cotoyer durant ces années de thèse. Viennent tout d'abord mes grands "frères/sœurs" de thèse:

Pascal, Julien, Élodie, Logithan, et, en particulier, Louise, toujours présents pour m'aider à décompresser et dont l'expérience m'a grandement profité durant ces trois années de thèse. Petits "frères/sœurs" scientifiques, Bonnie, Paul et Benjamin, sachez que serai toujours disponible pour vous. Je remercie également l'équipe des doctorants/stagiaires, dont je citerai Anthony, Grégoire, Bonnie, Mélina, Jean-Sébastien, Tianqi et Stefano, pour ces parties de tarot endiablées (tâchez de faire perdurer la tradition). J'ai évidemment une pensée toute particulière à mes collègues et surtout amis du bureau B137, Louise et Geoffroy, que j'ai été plus qu'heureux de retrouver tous les jours pendant deux ans, puis Benjamin et Merwan, à qui je souhaite le meilleur pour la thèse en cours. J'élargis ces remerciements à l'équipe des "bras-cassés", Édoardo, Adrien, Louise, Geoffroy, Pauline, Mathilde, pour tous les beaux moments que nous avons passés ensemble. Damien, Gaylor, c'est avec grand plaisir que je vous attends pour un "blind test" intense dans les bars à jeu "underground" d'Oxford. Je souhaiterais également remercier mes compagnons de vélo, Julien (prépare-toi pour la Norvège), Edoardo et Geoffroy (je vous attends pour les montagnes d'Oxford). Finalement, comment ne pas terminer en beauté par mes magnifiques compagnons de basketball, Florian et Jean-Sébastien, du groupe de travail FARINE habilement recyclé en un groupe de café et de dégustation de viennoiseries.

Mes années de thèse auraient été bien plus tristes sans la médiation scientifique, en particulier au sein de l'association UniverSCiel[1], qui méritait un paragraphe à part dans ce chapitre. Un merci particulier à Marina, Wilhem, Anne, Edoardo, Adrian, Geoffroy, Mélissa, Louise, Inès, Vincent, Pierre-Marie, Amaury, Clara, Mickaël, Gabriel, Sacha, Philippe, Simon, Anthony, Tristan, Claire, Gabi, Abraham, Emmy pour ces moments inoubliables que nous avons vécus ensembles, que ce soit au travers des différents festivals d'AstroJeunes et de Scientilivre, où lors d'interventions ponctuelles dans des écoles. Un merci tout particulier aux membres du bureau 2019 de l'association (Sacha, Mickaël, Simon, Adrien et Edoardo), ainsi qu'aux responsables du pôle communication (Inés, Gabriel, Wilhem) et Edoardo, qui ont su m'enseigner l'art délicat de la communication sur les réseaux sociaux! Enfin, merci à Isabelle de m'avoir permis d'intervenir à deux reprises dans sa classe de Terminale européenne.

Merci à tous mes amis de l'ISAE-SUPAERO, en particulier, le groupe avec mon ancien colocataire Baptiste, Robin (222), Paul, Quentin(s), Jean et Kath, Benjamin, mais également mon binôme, Nicolas et mes camarades du master ASEP (Clara, Marion, Mickaël, Gauthier, Sacha, Alexis, Clément, Ghislain, Arnaud) que je prendrai plaisir à revoir. Je tiens également à adresser une pensée des plus chaleureuses à mes amis de classes préparatoires aux grandes écoles avec lesquels je suis resté soudé durant toutes ces années, notamment Carole, Chloé, Guillaume, Antonin, Marine, Sophie ainsi qu'aux professeurs qui ont toujours cru en moi (notamment M. Bougnol et M. Fleck). Enfin, viennent mes amis d'enfance que je prends un immense plaisir à retrouver dès que l'occasion se présente, Vincent, Raphaël (et la famille Schimchowitsch), Julien, Lucie, Albane, Greg, Adèle, Léa. J'ajouterai une pensée à M., D., A., S., G., A., G., et V., qui se reconnaîtront en lisant ces quelques lignes.

Comment ne pas conclure ce chapitre par remercier les membres de ma famille qui ont toujours montré un intérêt sans faille pour mes travaux assorti d'un soutien inébranlable. Tout d'abord, un grand merci à Richard et sa famille dont les conseils avisés m'ont permis de prendre les bonnes décisions et d'arriver là où j'en suis actuellement. Mes oncles/tantes et cousins/cousines que je prends un immense plaisir à revoir dès que l'occasion se présente, ont une place particulière dans ce paragraphe. Tous mes grands-parents et Jean-Marie et Édith, vous avez toujours été des exemples de bienveillance et d'affection que votre soutien indéfectible pendant ma thèse n'a cessé de confirmer. Maman, Papa, vous avez toujours été incroyables, tant dans les décisions que vous avez prises tout au long de ma vie, que par l'amour et l'attention que vous m'avez et que vous continuez à me donner tous les jours et que je vous rends, à ma manière, mais qui est tout aussi fort. Le présent

[1] http://universciel.info/

manuscrit vous est dédié.

Foreword

Since the detection of the first exoplanet orbiting a solar-like star by Mayor & Queloz (1995), cutting-edge developments in instrumentation and data analysis have made it possible to detect several thousands of exoplanets embedded in a great variety of planetary systems[2]. Most of these exoplanets have been indirectly detected either by monitoring the radial velocity (RV) wobbles that they produce on their host star with high-precision velocimeters, or by measuring the light dimming induced when the planet crosses the stellar disk with photometers. However, detecting Earth-like planets orbiting in the habitable zone (HZ; Kasting et al., 1993; Kopparapu et al., 2013) of their host star remains challenging even for state-of-the-art high-precision ground-based velocimeters and space-based photometers, given the weak RV signatures and shallow transit depths induced by these planets (of about respectively $0.1\,\mathrm{m\,s^{-1}}$ and 0.1 mmag for the Earth around the Sun). As a consequence, only a dozen of HZ Earth-like planets have been unveiled so far (e.g., Jenkins et al., 2015; Anglada-Escudé et al., 2016; Gillon et al., 2017; Dittmann et al., 2017; Zechmeister et al., 2019), only half of them being close enough for a potential atmospheric characterization with new-generation space-based missions like the JWST (Gardner et al., 2006) or ground-based giant telescopes like the ESO ELTs[3]. Detecting new nearby HZ planets amenable to an atmospheric characterization is therefore an essential step in the quest extra-terrestrial life.

M dwarfs are the most promising targets to unveil Earth-like exoplanets with precise masses and radii. Beyond the fact that they largely outnumber stars with earlier spectral type in the solar neighborhood (Henry et al., 2006), they feature smaller sizes and masses, and more compact HZs, making nearby Earth analogs easier to detect. M dwarfs are known to frequently host multiple terrestrial planetary systems (Dressing & Charbonneau, 2015; Gaidos et al., 2016) especially at late spectral types (Gillon et al., 2017). As the majority of nearby very-low-mass M dwarfs remains poorly-explored with Doppler spectroscopy or transit photometry, this suggests that many thrilling nearby terrestrial planetary systems are still undiscovered. In parallel to the search for temperate Earth-like planets, investigating the processes driving planetary formation and evolution is a primary goal to understand how life could emerge and be maintained at the surface of Earth analogs (Raymond et al., 2014; Bolmont et al., 2017; Bolmont, 2018). Hence the need to detect and characterize exoplanets during their formation and the early stages of their evolution. Pre-main-sequence (PMS) stars, either surrounded by a planet-forming accretion disk (in the so-called classical T Tauri stage during 1-10 Myr after the star formation; Richert et al., 2018), or shortly after the disk dissipation (in the so-called weak-line T Tauri and post-T Tauri phases) are therefore primary targets to understand how Earth-like worlds are born.

However, both M dwarfs and PMS stars exhibit intense dynamo-powered magnetic activity whose manifestations, such as dark and bright inhomogeneities at the stellar surface, induce photometric and RV signals that overshadow or even mimic planet signatures (e.g., Saar & Donahue, 1997; Queloz et al., 2001; Desort et al., 2007), making them extremely difficult to detect. On the

[2] See the statistics of exoplanet detections in https://exoplanetarchive.ipac.caltech.edu/docs/counts_detail.html

[3] https://www.eso.org/public/france/teles-instr/elt/

other hand, magnetically-driven stellar winds as well as flares and coronal mass ejections strongly affect the atmosphere and surface habitability conditions of their close-in planets (e.g., Lammer et al., 2003, 2007; Vidotto et al., 2014a; Tilley et al., 2017). Spectropolarimetry is the best way to model the large-scale topologies of stellar magnetic fields, and thereby investigate the processes powering magnetic activity. Through the Zeeman effect, magnetic fields at the photospheric level induce distortions on the spectral lines and polarized signatures that can be inverted into a map of the large-scale magnetic field using Zeeman-Doppler imaging (ZDI; Donati & Landstreet, 2009). However, only a few PMS stars (e.g., Donati et al., 2010, 2012; Yu et al., 2019; Hill et al., 2019) and M dwarfs (e.g., Donati et al., 2008b; Morin et al., 2008b, 2010) have seen their magnetic topology constrained with ZDI and their underlying dynamo processes remain unclear.

Observing in the near-infrared (nIR), where both low-mass PMS stars and M dwarfs mostly emit their light, is an essential step to detect planets around them and constrain their activity. At nIR wavelengths, the amplitude of the RV signals induced by stellar surface inhomogeneities is weaker than at optical wavelengths (Mahmud et al., 2011; Crockett et al., 2012), making it easier to separate the stellar jitter from the planet signatures. Moreover, the enhanced Zeeman effect in the nIR strongly boosts the spectropolarimetric sensitivity to both large- and small-scale components of the stellar magnetic fields. The nIR high-resolution spectropolarimeter and high-precision velocimeter SPIRou (Donati et al., 2020a) at the Canada-France-Hawaii telescope (CFHT) is therefore well-suited to carry out a thorough search for planetary systems around nearby M dwarfs and PMS stars, and investigate the dynamo processes underlying the magnetic activity of these stars.

My thesis, funded by the ERC project NEwWorlds[4], takes place in conjunction with the first SPIRou observations collected in the end of the year 2018. This thesis aims at using SPIRou velocimetric, spectroscopic and spectropolarimetric capabilities to constrain planetary systems around M dwarfs and low-mass PMS stars and investigate their magnetic activity by modeling their surface magnetic fields and inhomogeneities using ZDI. After detailing the astrophysical context of the search for planetary systems around both types of stars in Chapter 1, I present simulations of nIR high-precision velocimetric follow-ups of magnetically active targets of the SPIRou large observing programme in order to assess the impact of the observational strategy, stellar activity, and measurement noise on the recovered planetary signals in Chapter 2. In Chapter 3, I investigate the magnetic activity exhibited by a set of low-mass stars with various properties using ZDI. Chapter 4 is dedicated to the detection and mass measurement of the close-in transiting Neptune-sized planet orbiting the PMS star AU Microscopii. Finally, Chapter 5 presents a preliminary analysis of the atmosphere of the hot Jupiter HD 189733 b from sequences of spectra collected with SPIRou during transits of the planet. We conclude and outline the perspectives of this work in Chapter 6.

[4] https://www.newworlds-erc.eu/science-goals/

Avant-propos

Depuis la détection de la première exoplanète en orbite autour d'une étoile de type solaire par Mayor & Queloz (1995), des développements de pointe en matière d'instrumentation et d'analyse des données ont permis de détecter plusieurs milliers d'exoplanètes réparties dans une grande variété de systèmes planétaires[5]. La plupart de ces planètes ont été détectées de façon indirecte, soit observant les oscillations de la vitesse radiale (VR) qu'elles induisent sur leur étoile hôte au moyen de vélocimètres à haute précision, soit en mesurant la diminution de lumière engendrée par le passage de la planète devant le disque stellaire à l'aide de photomètres. Cependant la détection de planètes telluriques en orbite dans la zone habitable (ZH ; Kasting et al., 1993; Kopparapu et al., 2013) de leur étoile hôte reste une tâche ardue et ce, même pour des vélocimètres/photomètres de pointe, en raison du minuscule impact de ces planètes sur la VR de l'étoile (de l'ordre de $0{,}1\,\mathrm{m\,s^{-1}}$ pour la Terre sur le Soleil), et de la faible profondeur de leur transit photométrique (de l'ordre de 0,1 mmag pour le transit de la Terre devant le Soleil). En conséquence, seule une dizaine de planètes telluriques en orbite dans la ZH de leur étoile hôte ont été dévoilées à ce jour (e.g., Jenkins et al., 2015; Anglada-Escudé et al., 2016; Gillon et al., 2017; Dittmann et al., 2017; Zechmeister et al., 2019), la moitié seulement étant suffisamment proche pour espérer une caractérisation de leur atmosphère par la nouvelle génération de télescopes comme le JWST (Gardner et al., 2006) ou les télescopes géants de l'ELT[6]. Détecter de nouvelles planètes potentiellement habitables susceptibles de faire l'objet d'une caractérisation atmosphérique est donc une étape clé dans la quête de la vie extra-terrestre.

Les naines M sont les cibles les plus prometteuses pour dévoiler des exoplanètes semblables à la Terre. Outre le fait qu'elles constituent la vaste majorité des étoiles du voisinage solaire (Henry et al., 2006), les naines M présentent à la fois des rayons plus petits et des ZHs plus compactes que leurs homologues solaires, facilitant ainsi la détection d'analogues terrestres autour d'elles. De plus, la plupart de ces étoiles hébergent des systèmes planétaires multiples (Dressing & Charbonneau, 2015; Gaidos et al., 2016; Gillon et al., 2017). Étant donné que la majorité des naines M de faibles masses demeure relativement peu explorée en vélocimétrie et photométrie, cela suggère que de nombreuses planétes telluriques restent à découvrir dans le voisinage solaire. En parallèle de la recherche de planètes habitables, l'étude des processus qui régissent la formation et l'évolution des systèmes planètaires est un objectif primordial pour comprendre comment la vie pourrait potentiellement émerger et se maintenir à la surface de jumelles de la Terre (Raymond et al., 2014; Bolmont et al., 2017; Bolmont, 2018). Cela nécessite de détecter et caractériser des exoplanètes au cours de leur formation et des premières étapes de leur évolution. Les étoiles pré-séquence principale (PSP), soit lorsqu'elles sont entourées d'un disque d'accrétion où a lieu la formation planétaire, (dans la phase dite de T Tauri classique qui a dure de 1 à 10 Myr après la formation de l'étoile ; Richert et al., 2018), ou peu après la dissipation du disque (dans les phases dites de T Tauri à raies faibles et de post-T Tauri), sont donc des cibles de choix pour comprendre comment naissent les mondes

[5] Les statistiques des détections d'exoplanètes peuvent être consultées sur la page suivante : https://exoplanetarchive.ipac.caltech.edu/docs/counts_detail.html.

[6] https://www.eso.org/public/france/teles-instr/elt/

semblables à la Terre.

Cependant, les naines M et les étoiles PSP présentent toutes deux une activité magnétique intense, alimentée par des processus dynamo au sein de leur intérieur convectif, dont les manifestations telles que l'apparition de taches à la surface de l'étoile, induisent des signaux photométriques et VR qui éclipsent voire imitent les signatures des planètes (e.g., Saar & Donahue, 1997; Queloz et al., 2001; Desort et al., 2007), les rendant extrêmement difficiles à détecter. D'autre part, les vents stellaires d'origine magnétique ainsi que les éruptions stellaires et les éjections de masse coronale affectent fortement l'atmosphère et les conditions d'habitabilité de surface de leurs planètes proches (e.g., Lammer et al., 2003, 2007; Vidotto et al., 2014a; Tilley et al., 2017). La spectropolarimétrie est le meilleur moyen de d'accéder aux topologies à grande échelle des champs magnétiques stellaires, et, par conséquent, d'étudier les processus qui alimentent l'activité magnétique. L'effet Zeeman induit par les champs magnétiques présents au niveau de la photosphère se traduit observationellement par des déformations de raies spectrales et des signatures polarisées qui peuvent être inversées en une distribution surfacique de champ magnétique à grande échelle au moyen de l'imagerie Zeeman-Doppler (ZDI ; Donati & Landstreet, 2009). Cependant, seules quelques étoiles PSP (e.g., Donati et al., 2010, 2012; Yu et al., 2019; Hill et al., 2019) et naines M (e.g., Donati et al., 2008b; Morin et al., 2008b, 2010) ont vu leur topologie magnétique reconstruite par ZDI. De ce fait, les processus de dynamos sous-jacents restent relativement méconnus à ce jour.

L'observation dans le proche infrarouge (nIR), où les étoiles PSP de faible masse et les naines M émettent principalement leur lumière, est essentielle pour détecter et caractériser leurs systèmes planétaires. Dans le nIR, l'amplitude des signaux de VR induits par les inhomogénéités à la surface stellaire est plus faible que dans le domaine optique (Mahmud et al., 2011; Crockett et al., 2012), facilitant ainsi la séparation des contributions stellaires et planétaires. De plus, l'intensification de l'effet Zeeman dans le proche infrarouge augmente fortement la sensibilité spectropolarimétrique aux composantes à petite et grande échelles du champs magnétique stellaire. Fort de son domaine spectral couvrant l'ensemble du domaine proche infrarouge, le spectropolarimètre et vélocimètre à haute précision SPIRou (Donati et al., 2020a), installé au télescope Canada-France-Hawaii au courant de l'année 2018, est donc bien adapté pour effectuer une recherche approfondie des systèmes planétaires autour des étoiles PSP et des naines M du voisinage solaire, tout en étudiant les processus de dynamo sous-jacents à l'activité magnétique de ces étoiles.

Ma thèse, financée par le projet ERC NEwWorlds[7], se déroule en conjonction avec les premières observations SPIRou recueillies à la fin de l'année 2018. Cette thèse vise à utiliser les capacités vélocimétriques, spectroscopiques et spectropolarimétriques de SPIRou pour caractériser les systèmes planétaires autour des étoiles M et PSP de faible masse, tout en étudiant leur activité magnétique via la modélisation des champs magnétiques et des inhomogénéités en brillance à leur surface à l'aide de ZDI.

Après avoir détaillé le contexte astrophysique de la recherche de systèmes planétaires autour des deux types d'étoiles au chapitre 1, je présente au chapitre 2 des simulations de suivi vélocimétrique à haute précision dans le proche infrarouge de cibles magnétiquement actives du large programme d'observation de SPIRou, destinées à évaluer l'impact de la stratégie d'observation, de l'activité stellaire et du bruit de mesure sur l'extraction des signaux planétaires. Dans le chapitre 3, j'étudie l'activité magnétique d'un ensemble d'étoiles de faible masse aux propriétés diverses à l'aide de la ZDI. Le chapitre 4 est consacré à la détection et à la mesure de la masse du Neptune chaud en orbite autour de l'étoile PMS AU Microscopii. Enfin, le chapitre 5 présente une analyse préliminaire de l'atmosphère du Jupiter chaud HD 189733 b réalisée à partir de séquences de spectres collectés avec SPIRou lors de transits de la planète. La conclusion et les perspectives viennent clôturer cet exposé dans le chapitre 6.

[7] https://www.newworlds-erc.eu/science-goals/

1 | Introduction: the search for exoplanets around low-mass stars

Contents

In this introductory chapter, we place the search for exoplanets around M dwarfs and low-mass PMS stars in its astrophysical context. After describing the current paradigm of the formation and evolution of star-planet systems in Section 1.1, we take stock of the search for exoplanets, focusing in particular on the results of Doppler spectroscopy and transit photometry, in Section 1.2. In Section 1.3, we outline the current status of the search for exoplanets in the specific cases of M dwarfs and low-mass PMS stars. Stellar activity, which is a major barrier to the search for planets around both types of stars, is described along with its filtering and modeling techniques in Section 1.4. Finally, we outline how nIR high-precision spectroscopy, and in particular the SPIRou spectropolarimeter, has the potential to achieve a breakthrough in the search for exoplanets around these stars in Section 1.5, before giving a brief overview of the manuscript in Section 1.6.

1.1 A brief introduction of star-planet formation and evolution

Stars and planets are intrinsically linked throughout their lives. As a consequence, understanding the physical processes driving the star formation is critical to study the birth of planetary systems and their evolution in the early stages of their lives. In this section, we briefly describe the paradigm of planet formation and early evolution around low-mass stars (i.e., of mass smaller than $\sim$1.5 $M_\odot$). After a short introduction about the zoology of evolved low-mass stars, we describe how stars form from giant clouds of gas and dust to the main-sequence. We then detail the current paradigm of planet formation from the accretion disk surrounding newly-formed low-mass stars, before outlining their orbital evolution during the few Myr following their birth. For more information about stellar formation and evolution, the reader is invited to consult the books of Maeder (2009), Bodenheimer (2011) and Beech (2019) from which Sections 1.1.1 and 1.1.2 inspire. For planet formation and evolution, I recommend the recent reviews of Baruteau et al. (2016) and Armitage (2018).

1.1.1 Zoology of low-mass stars through the HR diagram

Following their formation within giant collapsing clouds of gas and dust, stars start burning hydrogen through thermonuclear fusion in their cores. When nuclear fusion becomes the dominant mechanism of energy production (and thus compensates the energy released by gravitational contraction), stars enter the so-called main-sequence (MS) phase where they will spend most of their lives. Low-mass stars remain roughly stable in effective temperature $T_{\rm eff}$ and luminosity[1] throughout the MS and occupy a well-defined region of the Hertzsprung-Russel (HR) diagram (or temperature-luminosity diagram; see Figure 1.1). Depending on their effective temperature, MS stars exhibit different prominent spectral lines used as a basis of the so-called Harvard spectral classification, commonly used in the community. Seven spectral types (O, B, A, F, G, K and M, from the hottest to the coolest; see the different stellar spectral types on the X-axis on top of Figure 1.1) are used in the Harvard spectral classification, each spectral type being divided into 10 sub-types. Low-mass stars, on which we focus in this section, belong to spectral types G, K and M (i.e., $T_{\rm eff} \lesssim 6000$ K).

The typical inner structure of low-mass stars of mass larger than $\sim$0.35 $M_\odot$ is illustrated on the Sun in Figure 1.2. For these stars, the energy released by the thermonuclear fusion of hydrogen in

[1] In practice, the production of helium from the combustion of hydrogen in stellar cores increases the opacity of the stellar interior which, in turn, induces an increase in stellar luminosity (by a few tens of percents throughout the MS). As a result, the stellar radius slowly increases throughout the MS (by a few percents).

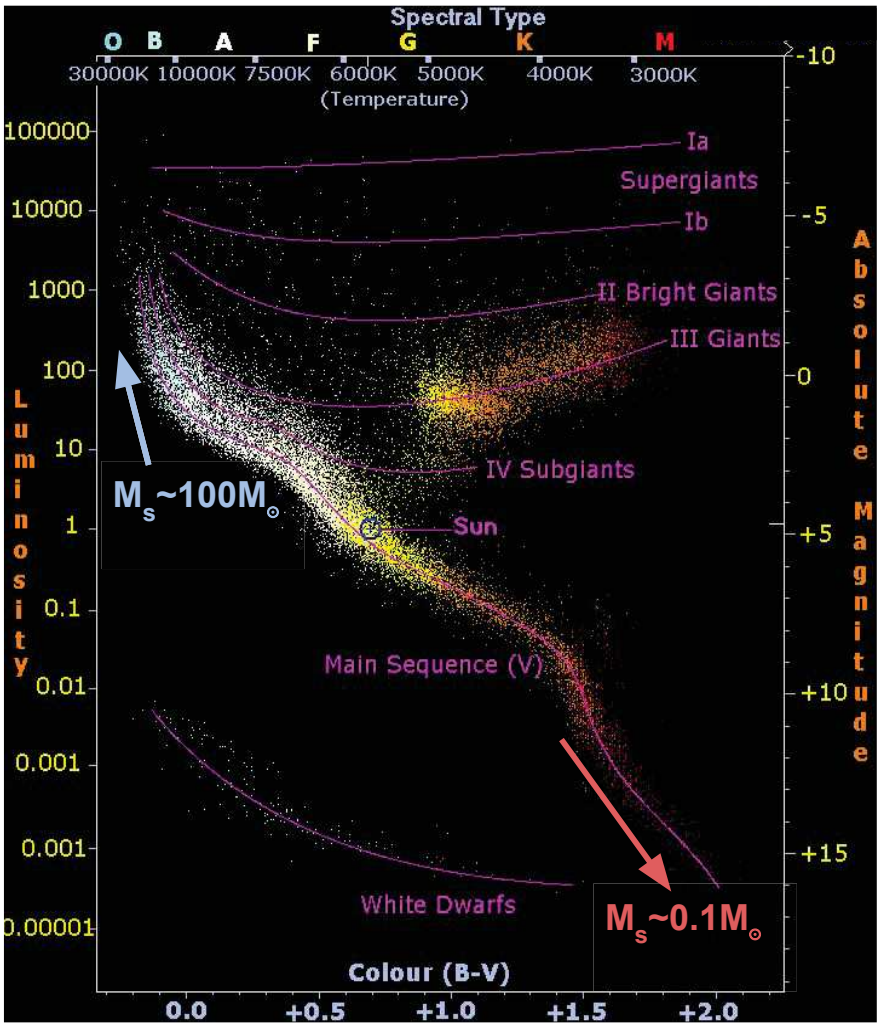

Figure 1.1 – Luminosity-effective temperature diagram (a.k.a. Hertzsprung-Russell or HR diagram). Source: adapted from R. Powell (http://www.atlasoftheuniverse.com/hr.html).

the radiative core is transported outward by radiation through the densest and hottest region of the star: the radiative zone. This region is surrounded by an envelope featuring a steep temperature gradient. In the Sun, for example, the temperature goes from $\sim 2\times10^6$ K on top of the radiative zone to $\sim$6000 K close to the surface. As a result, the Schwarzschild criterion is no longer fulfilled in the envelope and energy is primarily transported by convection. The radial extent of the convective envelope increases with decreasing mass. Whereas this zone extends no further than $\sim 0.29\,R_\odot$ for the Sun, stars of mass lower than $\sim 0.35\,M_\odot$ are entirely convective (Baraffe et al., 1998).

The stellar mass M_s drives the post-MS evolution. The most massive low-mass stars ($M_\mathrm{s} \gtrsim 0.5\,M_\odot$) spend typically a few Gyr on the MS[2], until their hydrogen supply is exhausted. At this stage, the temperature T_c within the dense helium stellar core is too low to initiate the thermonuclear fusion of helium ($\sim 10^8$ K). The star evolves on nuclear time scales (e.g., $\sim$1 Gyr for the Sun) into a red giant: its core contracts and the temperature and density increase therein. On the other hand, as a result of the thermonuclear combustion of hydrogen occuring in the layers surrounding the core, helium keeps accumulating in the stellar core which ends up being degenerated (i.e., the particles cannot get any closer without violating the Pauli exclusion principle). The ignition of the thermonuclear fusion of helium in the degenerated core is extremely intense and brief (a few

[2] The time spent on the MS phase varies as $\sim {M_\mathrm{s}}^{-2.5}$ for intermediate mass stars like the Sun (Maeder, 2009).

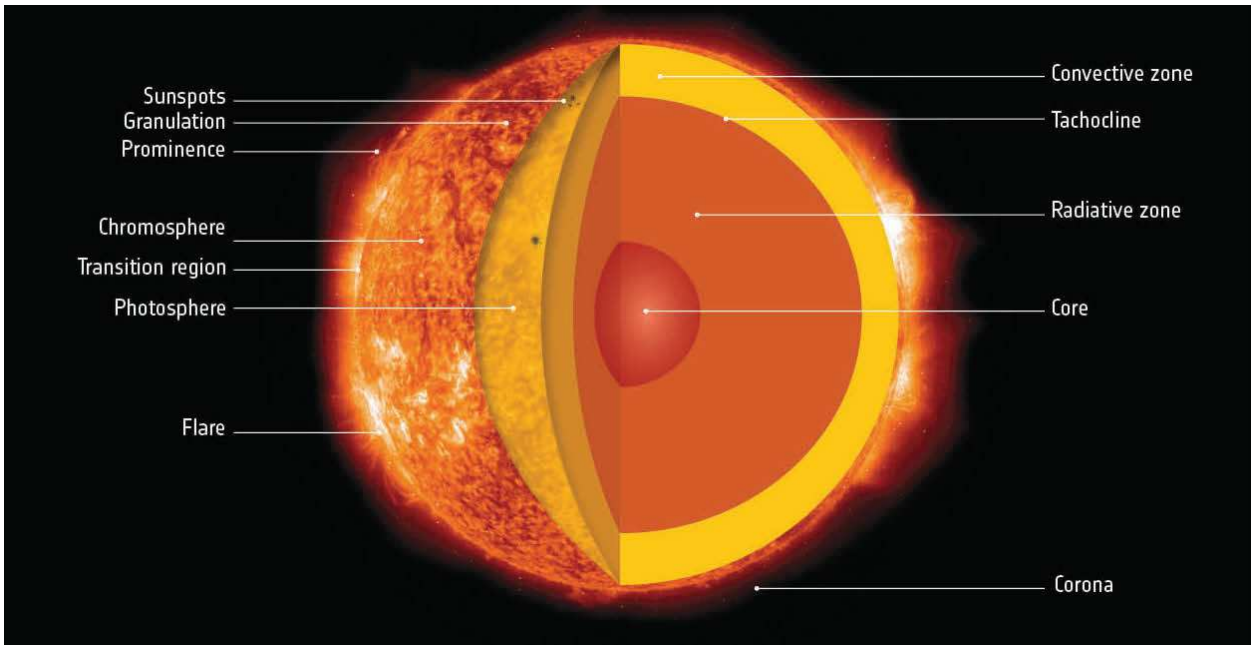

Figure 1.2 – Illustration of the internal and external structures of the Sun. Source: *ESA*.

thousands of seconds for the sun; e.g., Deupree, 1996; Mocák et al., 2010), and referred to as the *helium flash* in the literature. This runaway process rapidly increases the core temperature until the thermal pressure overcomes the degeneracy of the stellar core which then expands and cools down while keeping burning helium on nuclear time scales. After running out of nuclear fuel, the star is not massive enough to initiate the combustion of carbon in the so-called CNO cycle. As a result, the star expels its outer layers through superwinds and its core contracts and cools down into a white dwarf. Finally, very-low-mass stars, whose lifetime is larger than the age of the Universe, (i.e., $M_{\rm s} \lesssim 0.5\,M_{\odot}$) have not yet been observed after the MS.

1.1.2 The formation of low-mass stars

In the current paradigm of star formation, low-mass stars form from the gravitational collapse of denser regions of giant clouds of gas and dust in the interstellar medium. They then go through a protostellar phase where they accrete most of their mass from their surrounding environment, and through a pre-main-sequence (PMS) phase where they contract until reaching the main-sequence. Through the different stages of their formation, young stellar objects (YSOs; i.e., Protostars and PMS stars and their circumstellar environment) exhibit peculiar spectral energy distributions (SEDs) enclosing information on their structure and on the various processes driving their evolution. These SEDs are used to classify YSOs into four classes (0, I, II and III) reflecting their evolutionary stage between their formation and the MS.

YSOs are often observed in gravitationally-bound clusters or OB associations immersed in regions of dust and gas called star-forming regions (SFRs). The closest SFRs such as the ρ Ophiuchi cloud complex (located at $\sim$130 pc away from the Sun Wilking et al., 2008), the Taurus molecular cloud (at $\sim$140 pc; Torres et al., 2009), or the Orion nebula (at $\sim$400 pc; Kuhn et al., 2019), are excellent laboratories to provide observational constraints on the processes driving star (and planet) formation, e.g., by measuring the stellar initial mass function (see the review of Offner et al., 2014), or by probing the surrounding environment of their YSOs with high-contrast imagers and interferometers (e.g., O'Dell & Wong, 1996; ALMA Partnership et al., 2015). In this section, I briefly describe the main phases of the star formation from molecular clouds to the MS. An overview

of the evolutionary stages described in this section is given in the cartoon shown in Figure 1.3.

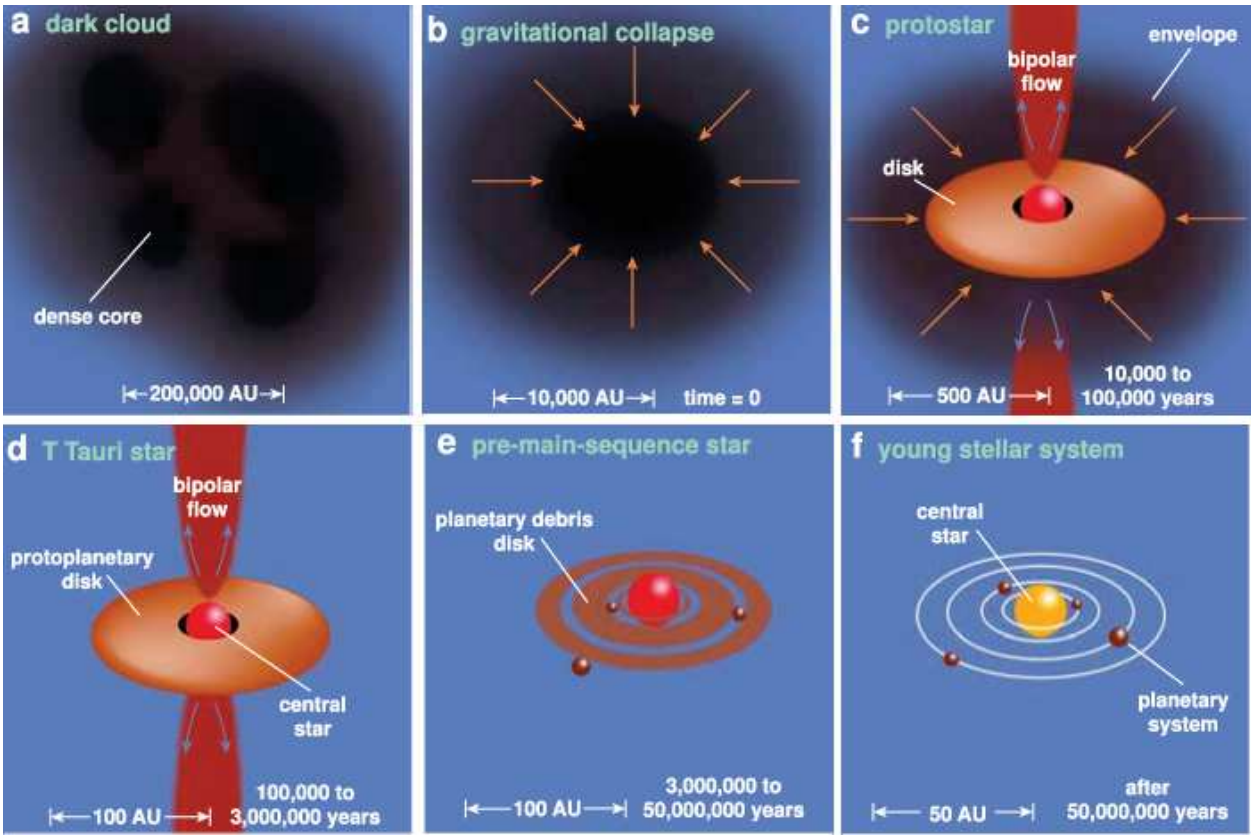

Figure 1.3 – Illustration of the main stages of the formation of solar-like stars (source: Greene, 2001).

1.1.2.1 Molecular clouds

Star formation arises within gravitationally bound molecular clouds of width $\sim$10 pc in the interstellar medium. These quiescent and cold ($T \sim 10$ K) regions are mostly composed of gaseous molecular Hydrogen, H_2, with traces of dust and heavier gases (e.g., CO and NH_3, used to probe the cloud structure; see the reviews of van Dishoeck et al., 1993; Langer et al., 2000). Giant molecular clouds are sculpted by filaments featuring column densities of remarkably constant inner widths of $\sim$0.1 pc (e.g., André et al., 2010; Arzoumanian et al., 2011, 2013; André et al., 2014; Arzoumanian et al., 2018) which accrete the surrounding material into $\sim$1-pc wide denser inner regions, called pre-stellar cores, where star formation arises (Larson, 1969).

Pre-stellar cores are balanced between gravitational energy, which favours their collapse, and thermal, turbulent, rotational, and magnetic energies, that tend to prevent collapse. Under the effects of ambipolar diffusion of the magnetic field (Nakamura & Li, 2005), turbulence-induced shocks within the clouds (Mac Low & Klessen, 2004; Crutcher, 2012), and/or external phenomena (e.g., exploding supernovae, cloud-cloud collision or galactic density waves; see Preibisch et al., 2002; Bodenheimer, 2011), pre-stellar cores initiate their gravitational collapse. The latter occurs in two successive phases (Larson, 1969; Masunaga et al., 1998; Masunaga & Inutsuka, 2000). During the so-called first collapse, the pre-stellar core contracts isothermally until the thermal pressure in the central region compensates the gravitational forces (corresponding to a core density of $\rho \sim 10^{-10}$ cm^{-3}; Maeder, 2009). As this stage, the temperature in the central region is large enough (i.e., $\gtrsim 2000$ K) to dissociate molecular hydrogen. This process releases enough energy for the pre-

stellar core to undergo a phase of adiabatic collapse, which continues until the center density reaches $\sim 10^{20}\,\mathrm{cm}^{-3}$, when the protostar is said to be born (Tomida et al., 2013). Since the second collapse only occurs in the central region of the first core, the protostar is surrounded by the remnants of the first core. If the pre-stellar core features a very low angular momentum, the surrounding envelope is rapidly accreted onto the protostar (Masunaga & Inutsuka, 2000). Otherwise, the first core remnants evolve into a rotationally-supported circumstellar disk after the protostar formation (Machida & Matsumoto, 2011; Machida & Basu, 2019). In what follows, we only consider rotating protostars hosting a circumstellar disk, where planet formation is thought to arise.

1.1.2.2 The protostellar phase

At the beginning of the protostellar phase, the system is composed of a rotating pre-stellar core surrounded by a circumstellar disk bathed in uncollapsed residuals of the primordial envelope. The protostar lies in the class-0 stage, characterized by a SED dominated by a cold black body emission (mostly in the far-infrared and submillimetric domains). The mass of the envelope remains significantly larger than that of the protostar, as most of the envelope material has enough angular momentum not to fall in the central core. The orbital energy of this material dissipates through collisons until the infalling material reaches a minimum-energy configuration while conserving angular momentum, forming a coplanar circumstellar disk which extends up to distances $\gtrsim 100\,\mathrm{au}$ on time-scales of $\sim 10^4\,\mathrm{yr}$ (e.g., Masunaga & Inutsuka, 2000; Machida & Matsumoto, 2011). The gradual increase in the disk density triggers episodic gravitational instabilities, leading to time-variable accretion of the disk material onto the protostar accompanied by high-velocity collimated bipolar jets (Machida & Basu, 2019). The protostar accretes mass from its circumstellar disk at a large rate of $\sim 10^{-6}\,\mathrm{M}_\odot/\mathrm{yr}$ until the envelope is depleted. When the protostar is more massive than the circumstellar envelope, it enters class I protostar (see panel c of Figure 1.3), characterized by weaker accretion rate ($\sim 10^{-7}\,\mathrm{M}_\odot/\mathrm{yr}$), and less powerful jets and outflows. In this stage, the SED features a nearly black body continuum at mid-infrared wavelengths from the protostar thermal emission, with a significant excess of continuum at far-infrared and submillimetric wavelengths. This phase lasts for roughly $10^5\,\mathrm{yr}$, until the protostar reaches a core temperature of $\sim 10^6\,\mathrm{K}$ and starts burning deuterium in its center (Larson, 2003; Evans et al., 2009). In this process, the released energy is high enough for the convection to overcome radiation in the proto-stellar interior (Stahler & Palla, 2005): a star is born.

1.1.2.3 Pre-main sequence phase

Low-mass PMS stars (see panels d and e in Figure 1.3) quickly consume their deuterium supply and the released nuclear energy is not sufficient to balance the gravitational energy. As a consequence, the stars contract and their luminosity decreases at roughly constant temperature in the so-called Hayashi tracks of the HR diagram (see Hayashi, 1961, and Figure 1.4). After having spent a few Myr on the Hayashi tracks, PMS stars of mass larger than $\sim 0.5\,M_\odot$ develop a radiative core and undergo a phase of temperature increase at roughly constant luminosity, along the so-called Henyey tracks of the HR diagram (Henyey et al., 1955). Less massive stars keep following the Hayashi track up to the main sequence and remain fully-convective. Due to stellar contraction, the central temperature of the star keeps increasing during both Hayashi and Henyey tracks until the hydrogen combustion threshold (i.e., $10^7\,\mathrm{K}$) is reached. As a result of their degenerated core preventing the central temperature from rising above this threshold, PMS stars less massive than $0.08\,M_\odot$ never initiate the thermonuclear fusion of hydrogen and are referred to as brown dwarfs.

When it enters the PMS phase (class II SED, panel d of Figure 1.3), the system is composed of a central star surrounded by a keplerian disk and the primary envelope is now mostly depleted. The SED of the system is composed of the continuum emission from the PMS star (resembling that

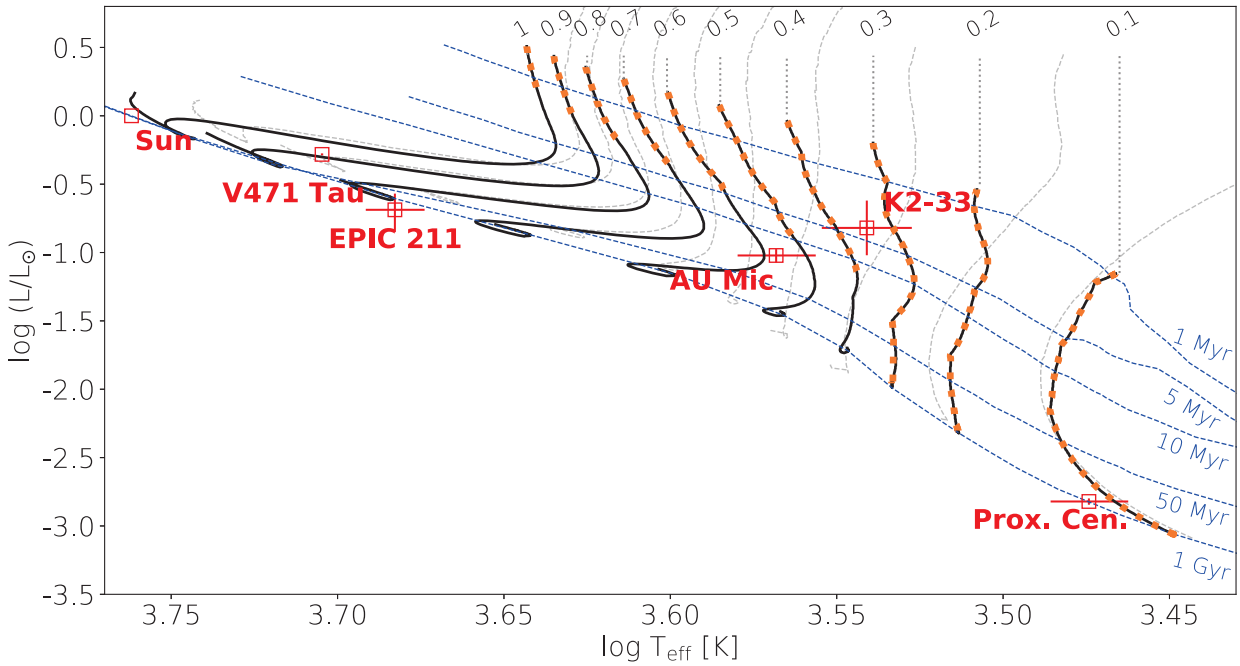

Figure 1.4 – Evolutionary tracks of low-mass PMS stars of different masses (indicated in solar masses on the top of the figure) on the HR diagram, computed from Baraffe et al. (2015) (black solid lines) and Siess et al. (2000) (gray dashed lines) models. The blue dashed lines indicate isochrones of the Baraffe et al. (2015) model at 1, 5, 10, 50 and 1000 Myr. The orange dotted portion of each track indicates when the star is predicted to be fully-convective by the model. The different stars studied in Chapter 3 are indicated by the red squares. For comparison, we also, indicate the position of the Sun.

of the future MS star) along with an infrared/submillimetric excess induced by the emission of the dust in the disk. The central star, called classical T Tauri star (cTTS), keeps accreting the disk material at rates of $\sim 10^{-8}\,M_\odot/yr$ (see Hartmann et al., 2016, for a review of accretion processes during the PMS phase). CTTSs feature intense and complex magnetic fields of several kilogauss (e.g., Johns-Krull et al., 1999a; Johns-Krull, 2007), whose surface topology has only recently started to be constrained (see Donati et al., 2010, 2012, and the results of the MAPP science program). These magnetic fields play a central role in the evolution of cTTSs. First, the magnetic field of the star creates a cavity (called magnetospheric gap) of typically 5-10 stellar radii, where gas elements, mostly ionized, are no longer dominated by thermal pressure and fall onto the star. Due to a magnetic coupling between the disk and the star at the edge of the magnetospheric cavity, the disk material is funneled along the field lines onto the star (Bouvier et al., 2007). Under the effect of hydrodynamic turbulence in the disk and/or magnetized winds ejecting the particles from the surface of the disk (see the reviews of Armitage, 2015; Hartmann et al., 2016, and the references therein), the disk material drifts towards its inner edge, where it is accreted onto the central star. Finally, the magnetic field plays a crucial role in the evolution of the stellar rotation rate. Classical TTSs appear to rotate much slower than one would expect from their contraction (Rebull et al., 2004). In the standard *disk-locking* paradigm, the star-disk magnetic coupling leads the star to co-rotate with the inner edge of the disk (Ghosh & Lamb, 1979). In practice, disk-locking is a complex adaptive process which depends on the magnetic field and on the various sources of angular momentum gain/loss (see Bouvier et al., 2014, for a review).

On time scales of about 1-10 Myr (Bell et al., 2013; Richert et al., 2018), the circumstellar disk material is progressively depleted by accretion onto the star, photoevaporation and planet formation (Armitage, 2011). Once the inner disk material is exhausted, the star becomes a weak-line T Tauri

star (wTTS, class III pre-stellar object). Its SED resembles that of the central star, except that a weak excess at far-infrared and submillimetric wavelengths can still betray the presence of a debris disk around the star (Hughes et al., 2018). Released from the disk-braking, wTTSs spin up under the effect of their contraction. The shrinking of low-mass stars lasts throughout both the weak-line T Tauri phase (10-15 Myr, Martin, 1997) and the post T Tauri phase[3], until the star reaches the main sequence. The more massive the PMS star, the shorter the contraction time scale. For example, the contraction phase lasts for ∼20 Myr for a solar-mass star, whereas it takes more than 100 Myr for a star with $M_s = 0.5\,M_\odot$. Around the zero-age main-sequence (ZAMS), the contraction progressively slows down and the star starts losing angular momentum through magnetized stellar winds (Weber & Davis, 1967; Kawaler, 1988; Réville et al., 2015; Gallet & Bouvier, 2015), which lasts throughout the MS phase.

1.1.3 Planet formation around low-mass stars

1.1.3.1 Structure and properties of protoplanetary disks

Planets form in the accretion disk (called protoplanetary disk) of gas and dust surrounding PMS stars, whose structure and main properties are illustrated in Fig. 1.5. At this stage, the star has almost reached its final mass, and the disk is typically 100 times less massive than the star, although measurements of the disk mass are often plagued with large errors (based on the disk's supposedly optically thin integrated intensity at radio wavelengths and assuming a gas-to-dust ratio of 0.01, a highly uncertain value based on interstellar medium studies; see Williams & Cieza, 2011; Williams & Best, 2014). In the radial direction, the disk surface density decreases roughly as r^{-1}, where r is the radial distance to the star, up to the outer edge of the disk, at $r \sim 100$ au (e.g., Andrews et al., 2010). Perpendicularly to the disc mid-plane, the pressure scale height evolves slightly faster than linearly with r, explaining the observed "bowl"-shape vertical structure of edge-on disks (e.g., see the high-resolution observations of the HH 30 disk with the Hubble Space Telescope in Cotera et al., 2001), and reaches a aspect ratio (i.e., the ratio between of the height of the disk to its radius) of 0.1 at the outer edge of the disk. The latter can be roughly described as an optically thick cold interior, whose temperature structure is mostly controlled by stellar irradiation ($T \propto r^{-1/2}$, Kenyon & Hartmann (1987)), sandwiched between an optically thin warmer molecular layer, heated by the stellar UV emission, and a hot atmosphere heated up by X-ray emission triggered by the accretion of disk material in the vicinity of the star (Armitage, 2015). Observationally, protoplanetary disks are mostly probed from the dust thermal emission (i.e., submillimetric and radio excesses) and narrow gas emission lines (mainly CO isotopologs, see Carmona, 2010).

1.1.3.2 The different steps of planet formation

There is currently no consensus on how planets form within protoplanetary disks. In this paragraph, we briefly describe the planet formation from the so-called core accretion scenario, which currently stands as a paradigm for planet formation, even though some crucial steps of the process remain poorly understood mainly due to very few direct observations of forming planets.

[3] Post T Tauri stars (pTTSs) are PMS stars featuring intermediate properties between T Tauri stars, associated to the molecular clouds where they formed, and MS stars (Mamajek et al., 2002). Similarly to T Tauri stars, pTTSs are located above the MS in the HR diagram and are thereby relatively well separated from their more evolved counterparts. Distinguishing between wTTSs and pTTSs is much harder (Herbig, 1978). Weak-line T Tauri stars of mass lower than the Sun exhibit a surface abundance of lithium which is carried down on time scales of a few Myr by convection to layers of high temperature where it is destroyed. As a consequence, pTTSs exhibit much weaker lithium absorption signatures than wTTSs (Martin, 1997). Note however that this criterion is questioned by the relatively high dispersion of the observed lithium abundances on both pTTSs and wTTSs, making it difficult to determine a threshold to unambiguously disentangle between the two types of stars (Jensen, 2001).

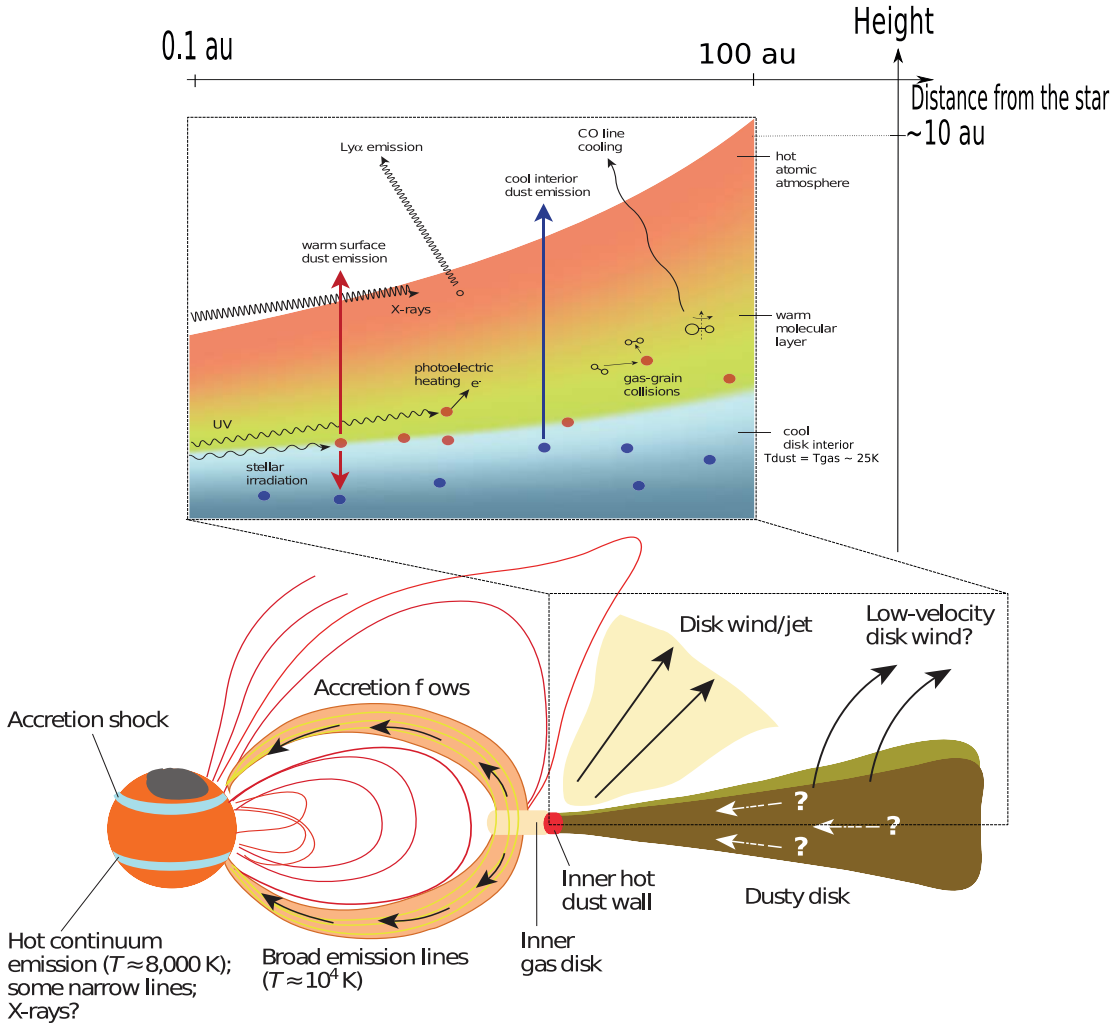

Figure 1.5 – Illustration of the structure of a protoplanetary disk viewed from the side. In the bottom panel, we show a cartoon of a cTTS star accreting its circumstellar disk material (source: Hartmann et al., 2016). The red solid lines indicate the magnetic field lines. In the top panel, we show an illustration of physical processes controlling the thermal and emission properties of protoplanetary disk (source: Armitage, 2015).

Under the effect of aerodynamic forces from the disk gas, μm-sized dust grains and progressively grow everywhere in the disk until they turn into pebbles of 1 to 10 mm. The growth of pebbles beyond the centimeter level remains unclear. Given their sizes, pebbles are highly sensitive to the aerodynamic drag exerted by the disk gas and tend to drift inwards at high velocity (up to $50\,\mathrm{m\,s^{-1}}$ for a m-sized body, resulting in a drift time scale as short as a few hundred years at a few au in a typical disk model). Moreover, their collision with other pebbles results either in the fragmentation of the system (at high relative velocity) or to a simple bouncing (see the results of laboratory collisions in Güttler et al., 2010; Weidling et al., 2012). To explain the growth of pebbles to km-sized planetesimals, we need to account for the drag induced by the dust on the gas (a.k.a. dust feedback) in the so-called streaming instability (Youdin & Goodman, 2005). The dust feedback allows to slow the radial drift of clumps of pebbles, resulting in increasingly long dust filaments that gravitationally collapse into planetesimals of 10-100 km when the filament density is larger than the Roche limit (Johansen et al., 2014). Note however that the growth of pebbles is

still actively debated in the current literature (see Section 2 of Baruteau et al., 2016).

At the planetesimal stage, gravity dominates over surface forces and the growth of planetesimals occurs through two-body collisions. From masses of $\sim 10^{-8}$ to $\sim 10^{-2}\,M_\oplus$, the size R of a planetary embryo increases like R^2: it is the runaway growth. After this stage, the remaining accretable planetesimals by the massive body (a.k.a. the oligarch), are sparser with more dispersed orbits and, consequently, the growth rate no longer depends on R: this is the oligarchic growth. Each oligarch accretes all the available mass along or close to its orbit and becomes a planet core. Note that this process is matter of debate. For example, the time scale to build up a sufficiently massive core to explain the formation of Jupiter or Saturn exceeds the typical lifetime of a protoplanetary disk ($\sim$3 Myr; Haisch et al., 2001). Inward migration induced by oligarch-disk interaction could overcome this challenge (Alibert et al., 2005; Ida & Lin, 2008). Another increasingly popular explanation is that planet cores do not arise by collisions of km-sized planetesimals, but rather by the accretion of cm-sized pebbles, which turns out to be a particularly efficient process to build planet cores of several Earth masses (e.g., Johansen & Lacerda, 2010; Lambrechts & Johansen, 2012; Bitsch et al., 2019). If the planet core is massive enough (mass typically larger than $\sim 10\,M_\oplus$), it accretes all the disk gas available nearby through a runaway process until no more supply of gas is left, and becomes a gas giant (Pollack et al., 1996).

1.1.4 Evolution of planetary systems

During and after their formation, planets undergo interactions with the remaining protoplanetary disk, the host star, and other planets in the system which affect their orbital parameters. The most striking demonstration of these mechanisms is the existence of hot Jupiters (i.e., Jupiter-mass planets orbiting at $\lesssim 0.1$ au from their host star such as 51 Pegasi b Mayor & Queloz, 1995). In situ formation of hot Jupiters (hJs) is unlikely because of the lack of gas supply in the vicinity of the star (e.g., Coleman et al., 2017). The current paradigm is that hJs form at a few au from their host star and are massive enough to open a gap along their orbit (see Crida et al., 2006). Under the effect of the outer disk gas exerting a stronger torque than its inner disk counterpart, the planet rapidly migrates inwards (in the co-called type II migration) until reaching the magnetospheric cavity at the inner edge of the disk on time scales of $\sim 10^4$-10^5 yr after the planet has reaches its final mass (see Baruteau et al., 2014, and the references therein). At this distance, hJs undergo strong tidal forces from the host star which tend to circularize their orbit and synchronize their rotation period with their orbital period. Planets of mass smaller than $\sim 10\,M_\oplus$ are not massive enough to open a gap in the disk and undergo a generally slower inward migration (called type-I migration) on time scales of $\sim$1 Myr, which is stopped by enhanced opacity regions of the disk (e.g., ice or silicate evaporation lines, Bitsch et al., 2014) or by its dissipation. Finally, intermediate mass planets (i.e., Saturn-mass planets) are massive enough to open a partial gap in the disk along their orbit and migrate, through a complex regime (type III migration), either inward or outward depending on the mass of the disk (Baruteau et al., 2014).

Disk migrations are thought to preserve zero obliquities and low eccentricities for the planet orbits. However, observations have shown that while hJs feature indeed relatively low eccentricities, about one third of them exhibit large sky-projected obliquities between the orbital plane and the stellar equatorial planet (Winn & Fabrycky, 2015). Gravitational interactions between disk-migrating planets and other massive planets in the system (planet-planet scattering; Rasio & Ford, 1996; Chatterjee et al., 2008; Jurić & Tremaine, 2008) and/or Kozai-Lidov cycles with a nearby inclined stellar companion (Wu & Murray, 2003; Fabrycky & Tremaine, 2007) are invoked to explain the distribution of hJs obliquities. These mechanisms are likely to significantly enhance the eccentricity and inclination of planet orbits. Planets on highly eccentric orbit undergo tidal forces induced by the star every time they pass through their periastron, which contributes to

their migration. Close to the star, the eccentricity of their orbit is rapidly damped through tidal interactions with the host star whereas the orbit alignment process takes significantly longer (Dawson & Johnson, 2018). High-eccentricity migration scenarios have been suggested to explain the formation of all hot Jupiters (Triaud et al., 2010; Albrecht et al., 2012). However, these scenarios, in which planet migration and orbit circularization occur over typically more than ∼100 Myr, fail at explaining the recently unveiled hJs around stars younger than 25 Myr (e.g., Donati et al., 2016; Yu et al., 2017).

1.2 Current status of the search for exoplanets from Doppler and transit surveys

Since the detection of the first exoplanet orbiting a solar-like star by Mayor & Queloz (1995), about 4300 exoplanets have been detected and several thousands of planet candidates still remain to be confirmed. These detections, carried out with various techniques yielding complementary planet parameters, have revealed a great variety of planetary systems which has turned the paradigm of planetary formation and evolution upside down. In this section, we take stock of the search for exoplanets around low-mass stars, focusing in particular on the detection methods based on Doppler spectroscopy and transit photometry that we use in this thesis. We redirect the interested reader towards the book of Perryman (2018) for a comprehensive view of the various techniques for planet detection and characterization.

1.2.1 A brief overview of exoplanet detection techniques

The various methods to unveil and characterize exoplanets can be divided in two main types: those that directly measure the light emitted by the planet, and indirect techniques, based on the effects induced by the planet on its host star.

High-contrast imaging allows to directly detect the light emitted by a substellar object[4] (planet or brown dwarf). This measurement is challenging due to the very low star-planet angular separations and the huge star-planet contrasts (e.g., a Sun-Jupiter system located at 10 pc features an angular separation of 0.5 arcsec and a star-to-planet contrast of $\sim 10^9$). State-of-the-art imagers, such as SPHERE at the VLT (Beuzit et al., 2008) or GPI at the Gemini-South telescope (Macintosh et al., 2014), are thus equipped with adaptive optics, to improve spatial resolution, and coronographic masks, to get rid of the stellar light (see Bowler, 2016, for a review). As things stand, direct imaging is mostly limited to the detection of nearby massive planets (i.e., of a few M_{jup}) orbiting at large distance from their host star (typically further than a few au) and presenting a favourable star-to-planet contrast ratio (e.g., young systems with hot contracting planets). Since the first direct detection of a planet by Chauvin et al. (2004), about fifty massive planets were unveiled with direct imaging (e.g., Kalas et al., 2008; Marois et al., 2010; Lagrange et al., 2010, for the most notorious detections). By coupling high-contrast imaging with high-resolution spectroscopy, one has the potential to directly probe the atmosphere of exoplanets. This gave rise to ambitious projects aimed at characterizing the atmosphere of nearby Earth-sized planets with next-generation giant telescopes like the ELTs (Snellen et al., 2013, 2015; Lovis et al., 2017).

On the other hand, indirect methods complement the landscape of directly imaged exoplanets. By measuring the radial velocity wobbles induced by a planet on its host star, Doppler spectroscopy (or velocimetry, see Section 1.2.2) enables to access the planet mass, orbital period, and eccentricity. In a complementary way, transit photometry, which measures the light dimming when the planet

[4] A substellar object (i.e., of mass lower than $\sim 0.08\,M_\odot \approx 80\,M_{jup}$) is referred to as a planet if its mass lies below $\sim 13\,M_{jup}$, and as a brown dwarf otherwise (Burrows et al., 1997).

passes between the star and the observer, yields the planet radius as well as its orbital period and inclination. Velocimetric and spectroscopic observations of planetary transits enable to (i) access the mutual inclination between the stellar rotation axis and the planet orbital plane (through the Rossiter-MacLaughlin effect; Fabrycky & Winn, 2009) and (ii) probe the structure and composition of the planet atmosphere (Madhusudhan, 2019). Other indirect exoplanet detection methods such as microgravitational lensing (Tsapras, 2018), astrometry (Perryman, 2018), interferometry (Gravity Collaboration et al., 2019) or chronometry (e.g., the detection of planets around pulsars; Wolszczan & Frail, 1992) contribute to the versatility of the current exoplanet landscape, but are not discussed in detail in this manuscript which focuses on Doppler spectroscopy and transit photometry.

1.2.2 Doppler spectroscopy

1.2.2.1 General principle

Doppler spectroscopy is an indirect method to unveil exoplanets from the wobbles that they induce on their host star's radial velocity (RV; i.e., the line-of-sight projection of the velocity vector of the star). Due to the reciprocal star-planet gravitational interaction, the star revolves around the barycenter of the star-planet system. If the orbital plane is not orthogonal to the line-of-sight, the variations of stellar RV along the orbit induce periodic Doppler shifts of the stellar lines that are in principle detectable from the Earth.

Using Newton's and Kepler's laws for planetary motion, one can express the RV signature V_p induced by a planet on its host star as a function of the time t and the system parameters such that (see the demonstration in Section 2.1 of Perryman, 2018):

$$V_\mathrm{p}(t) = K_\mathrm{s}[\cos(\omega + \nu(t)) + e\cos\omega], \tag{1.1}$$

where ω is the argument of the periapsis of the stellar orbit, e its eccentricity, ν its true anomaly (which also depends on the orbital period P_orb, phase and eccentricity of the planet), and K_s, the semi-amplitude of the planet-induced signal which depends on the masses of the star, M_s, and of the planet, M_p, such that

$$K_\mathrm{s} = \left(\frac{2\pi G}{P_{orb}}\right)^{1/3} \frac{M_\mathrm{p}\sin i_\mathrm{p}}{(M_\mathrm{s}+M_\mathrm{p})^{2/3}} \frac{1}{\sqrt{1-e^2}}, \tag{1.2}$$

i_p referring to the inclination of the orbital plane of the star-planet system. As a consequence, by monitoring the RV variations of a given star, one can access the orbital properties (especially P_orb and e) as well as the minimum mass $M_\mathrm{p}\sin i_\mathrm{p}$ of the planet, provided that its orbital cycle is well-covered by the observations. In practice, the measured RV is the combination of the RV signals induced by the planets in the system and by stellar activity (see Section 1.4), making the estimation of the planet parameters tricky.

The stellar RV, V_r, is measured using the Doppler-Fizeau effect from the shift between the wavelengths of the light emitted in the stellar rest frame, λ_0, and those measured in the Geocentric frame, λ_obs, such that

$$V_\mathrm{r} \approx c_0 \frac{\lambda_\mathrm{obs}-\lambda_0}{\lambda_0}, \tag{1.3}$$

where c_0 is the speed of light in the vacuum. As a result, a negative/positive RV respectively corresponds to a blueshift/redshift of the source. For example, Jupiter produces a RV signatures of $K_\mathrm{s} = 12\,\mathrm{m\,s^{-1}}$ on the Sun, which corresponds to a Doppler shift of about 2×10^{-5} nm at

$\lambda_0 = 550\,\mathrm{nm}$. In other words, to detect a Jupiter analog around a solar-like star, the wavelength of the stellar spectral lines must be measured with a relative precision of $\sim 10^{-8}$ on time scales of a few years. Dedicated spectrographs, called velocimeters, are thus needed to provide high-precision measurements of the temporal variation of the position of the stellar lines.

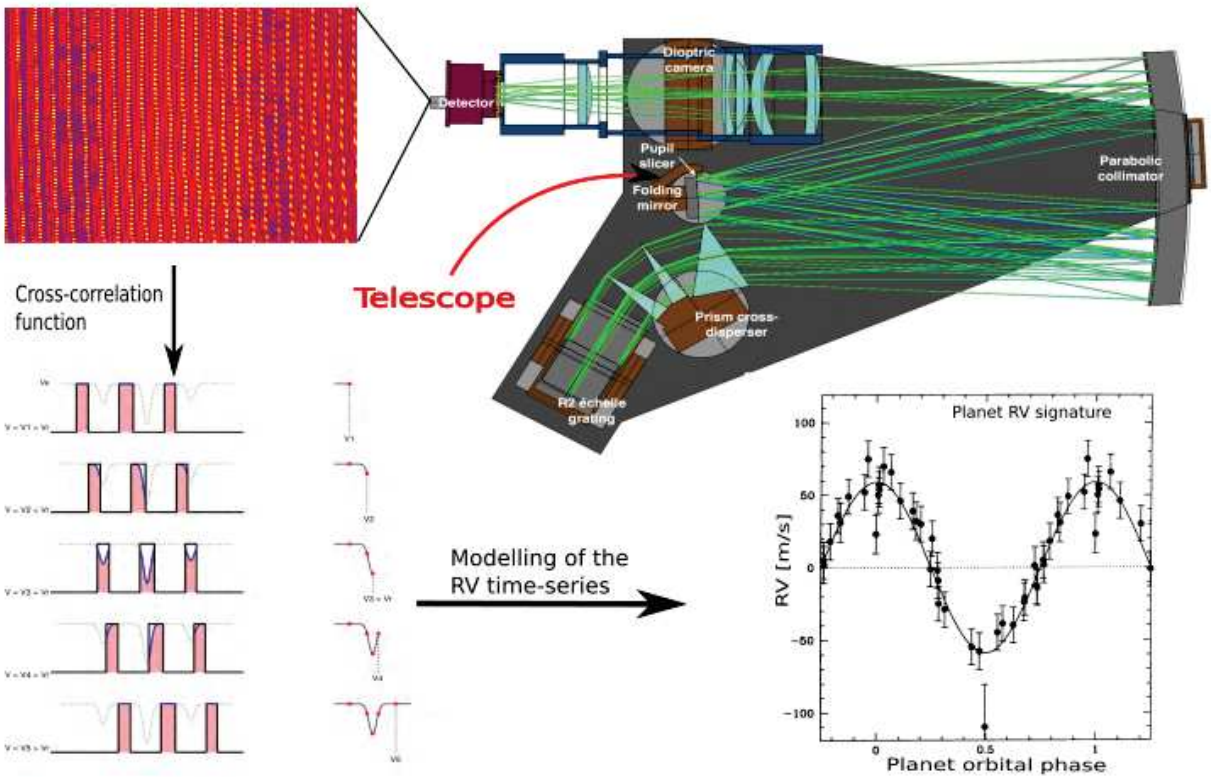

Figure 1.6 – Illustration of the RV measurement principle. *Top right:* optical view of the SPIRou spectrograph (Donati et al., 2018). The input light beam coming from the telescope is indicated by the red arrow. *Top left:* portion of a nIR echelle spectrum of the M dwarf AD Leo collected with SPIRou (first light, credit: SPIRou team). Each column of three vertical bars corresponds to one SPIRou order. In each column, the first two vertical bars contain the science spectrum (measured in two polarization states), whereas the last bar contains the Fabry-Perot calibration spectrum. *Bottom right:* illustration of the cross-correlation procedure to compute the average line profile from the observed spectra (credit: Melo 2001 Ph.D. Thesis). *Bottom right:* RV signature induced by 51 Pegasi b on its host star (source: Mayor & Queloz, 1995).

1.2.2.2 High-precision RV measurement

Precise velocimetric measurements are carried out using échelle spectrographs. The general principle is to spread the incoming light beam into a wide range of diffraction orders covering the spectral domain of the instrument using an échelle grating (e.g., 72 orders ranging from 380 to 690 nm for HARPS; Mayor et al., 2003). These orders are then dispersed again in the direction orthogonal to the direction of the échelle grating diffraction using a cross-dispersion system (typically a set of prisms or a grating; see the optical view of SPIRou in the upper right panel of Figure 1.6). All the cross-dispersed orders are then simultaneously recorded on a detector (generally a CCD or a H4RG for optical and nIR domains, respectively).

The thousands of stellar lines recorded by the detector are affected in a systematic way by the Doppler shifts induced by the planet on the star. Using a list of N stellar lines covering the entire spectral domain of the instrument, one can compute an average line profile, I, using the

cross-correlation method (Baranne et al., 1996) or, equivalently, Least-Squares Deconvolution (see Donati et al., 1997, and the description in Section 3.2.1). This process highly increases the signal-to-noise ratio (S/N) of the average line profile[5], and so does the precision on the RV measurement. The RV information lies essentially where the slopes of the average spectral line are steepest, or, equivalently, where $|\partial I/\partial\lambda|$ is large (Pepe & Lovis, 2008). Hence the need for the spectrograph to have a large resolving power $\mathscr{R} = \lambda/\Delta\lambda$, where $\Delta\lambda$ is the full-width at half maximum (FWHM) of the instrumental profile at wavelength λ, so that the stellar lines are resolved. This condition is typically fulfilled for $\mathscr{R} \gtrsim 50\,000$ - $100\,000$ for a slowly-rotating solar-type star observed in the optical domain (Bouchy et al., 2001).

Measuring stellar RV at the $\mathrm{m\,s^{-1}}$-precision level is a challenging process as any effect inducing even a slight shift in the position of the spectral lines will be interpreted as a stellar Doppler shift (e.g., a shift of 0.05 Å yields errors of $\sim$0.3 $\mathrm{m\,s^{-1}}$ in the optical domain; Pepe & Lovis, 2008). Hence the need to precisely assess the contribution of the various sources of errors that could plague the RV measurement process. The first limitation in RV precision comes from the photon noise σ_{ph} which gives a fundamental precision limit depending on the star, the S/N of the observations, and the spectral domain of the spectrograph (Bouchy et al., 2001). The broader spectral lines, the lower $|\partial I/\partial\lambda|$, and the larger σ_{ph}. Due to the rotation of the star, half of the stellar disk is moving towards the observer and the emitted light appears blueshifted, whereas the other half of the disk is moving outwards and the emitted light appears redshifted. As a consequence, the stellar lines are broadened by stellar rotation (this effect is referred to as Doppler broadening). The faster the star rotates with respect to the observer, the stronger the Doppler broadening and the larger σ_{ph}. For example, at a given S/N, the photon noise increases by $\sim$32 between two Sun-like stars of projected rotational velocities of 2 and 20 $\mathrm{km\,s^{-1}}$ (Lovis & Fischer, 2010).

Another major prerequisite to achieve high-precision velocimetry is to have a stable wavelength reference to which to compare the position of the spectral lines. Two different calibration procedures are used in high-precision velocimetry. In the so-called self-calibration technique (e.g., Campbell & Walker, 1979; Butler et al., 1996; Mahadevan & Ge, 2009), the incident stellar beam goes through a reference gas absorption cell (typically an iodine gas cell at visible wavelengths). This method allows to achieve RV precisions of 1-3 $\mathrm{m\,s^{-1}}$ on velocimeters like HIRES (Vogt et al., 1994) or CHIRON (Tokovinin et al., 2013), but is limited by the fact that (i) a significant part of the incident flux is absorbed by the gas cell (e.g., about half for a iodine cell) and (ii) the spectral domain where the gas cells can imprint the reference spectrum is relatively narrow (about 150 nm for the iodine cell, Butler et al., 1996), which restricts the number of available spectral lines. In contrast to the self-calibration technique which is relatively easy to implement on a given échelle spectrograph, the so-called *simultaneous reference* technique requires a specific design of the velocimeter to be implemented (Baranne et al., 1996). In this technique, the stellar light is simultaneously recorded with the light produced by a reference lamp (e.g., Thorium-Argon for HARPS), or by a high repetition rate system such as a stabilized Fabry-Pérot interferometer (coupled with a broadband light source; e.g., Schwab et al., 2015) or a laser-frequency comb (e.g., Phillips et al., 2012). As the stellar and reference light beams follow close optical paths, one can compute the stellar RV from the relative variation of the position of the stellar lines with respect to the reference spectral lines. This assumption presupposes that both calibration and science channels are affected in the same way by instrumental RV shifts, which is only fulfilled if the spectrograph environment is highly-stabilized in pressure and temperature. As a consequence, high-precision velocimeters using the simultaneous reference calibration technique are installed in vacuum vessels stabilized in temperature (typically within $\sim$0.01 K for HARPS; Mayor et al., 2003). These requirements,

[5] In the ideal case of N identical individual lines featuring the same S/N, the S/N of the average line profile increases by $\sim \sqrt{N}$. In practice, the S/N and shape of the line profile vary from one individual line to the other, making the multiplex gain much more complex to estimate analytically.

restrictive as they may be, have made it possible to achieve the highest RV precisions reached so far (e.g., $0.8\,\mathrm{m\,s^{-1}}$ for HARPS and $\sim 0.5\,\mathrm{m\,s^{-1}}$ for ESPRESSO Pepe et al., 2020), so much so that the simultaneous reference calibration technique emerges as the favoured solution for forthcoming projects of extreme precision radial velocity (Pasquini et al., 2008; Jurgenson et al., 2016; Thompson et al., 2016).

Other sources of RV measurement error arising, among others, from the light injection stability, the wavelength-dependent dispersion of the Earth atmosphere, the contamination by telluric lines, or problems inherent to the detector need to be corrected either instrumentally or as a post-processing step (see Pepe & Lovis, 2008, for a detailed list of potential errors on the RV measurement process). The RV measurement is carried out in the geocentric frame, and, thus, needs to be corrected from the barycentric Earth radial velocity (BERV), i.e., the RV of the instrument in the solar system frame, which varies by $\pm 30\,\mathrm{km\,s^{-1}}$ throughout the year. This process yields additional RV measurement errors that are generally small compared to other instrumental errors, but could become more problematic for extreme precision RV measurements. Finally, the RV measurement procedure itself is a source of errors. The cross-correlation process relies on a predefined line list that likely introduces errors on the RV measurement (e.g., mismatch between synthetic and stellar lines). Over the past few years, new RV measurement techniques based on empirically-built masks (Astudillo-Defru et al., 2015) or on template-free data-driven methods (Rajpaul et al., 2020) have shown promising results and will be probably exploited in the quest for extreme precision RV in the near future.

1.2.2.3 Brief history of the field and perspectives

The first exoplanet orbiting a solar-type star, 51 Pegasi b, was detected by Doppler spectroscopy using the high-precision velocimeter ELODIE, at the Haute-Provence observatory (Mayor & Queloz, 1995). This $\sim 0.5\,\mathrm{M_{jup}}$-mass planet induces a RV signature of semi-amplitude $120\,\mathrm{m\,s^{-1}}$ detectable by the velocimeters of the time (e.g., ELODIE allows to measure RVs with an accuracy of $\sim 13\mathrm{m\,s^{-1}}$; Baranne et al., 1996). Just a few years after, the flowering of $\mathrm{m\,s^{-1}}$-precision spectrographs like HARPS (Mayor et al., 2003) and its twin in the northern hemisphere, HARPS-N (Cosentino et al., 2012), SOPHIE (Perruchot et al., 2008) or HIRES (Vogt et al., 1994), resulted in the detection of planets of increasingly smaller masses (e.g., Santos et al., 2004; Marcy et al., 2005; Lovis et al., 2006; Anglada-Escudé et al., 2016). The last few years have seen the arrival of ambitious projects aimed at reaching a long-term RV precision of $10\,\mathrm{cm\,s^{-1}}$ in order to detect Earth twins around solar analogs (e.g., ESPRESSO, HARPS3, EXPRESS, CODEX, respectively presented in Pepe et al., 2010; Thompson et al., 2016; Jurgenson et al., 2016; Pasquini et al., 2008). In parallel, nIR high-precision velocimeters have recently started observing with a goal RV precision of $1\,\mathrm{m\,s^{-1}}$, which paves the way for detections of Earth-mass planets around red dwarfs (e.g., Quirrenbach et al., 2012; Tamura et al., 2012; Claudi et al., 2017; Wildi et al., 2017; Donati et al., 2018), as described further in Sec. 1.5.

1.2.3 Transiting planets

Transit photometry

A planetary transit is observed when a planet passes between its host star and the observer. As illustrated in Fig. 1.7, during the primary transit of a planet, the luminous flux received from the host star decreases by

$$\Delta F = \left(\frac{R_\mathrm{p}}{R_\mathrm{s}}\right)^2, \tag{1.4}$$

where R_p and R_s are respectively the radii of the planet and the star. Provided that the stellar properties are accurately known, primary transit curves yield the planet radius and orbit inclination (depending on the shape of the transit curve), whereas the recurrence time scale of the primary transit allows to constrain the planet orbital period. Measuring the ellipticity of the planet orbit is in principle possible from the asymmetries between the ingress and outgress parts of transit curves, but this measurement remains challenging since this effect could easily be mistaken with white noise or stellar induced signals (e.g., flares or surface inhomogeneities), especially for low-to-moderate ellipticities. Measuring the planet mass is not possible from the transit curve itself. However, dynamical planet-planet interactions in multi-planet systems slightly affect the planet orbits, inducing variations in the transit timings. By modeling the transit-timing variations (TTVs) using N-body simulations, one can estimate the planet masses and orbit ellipticities, as well as probe outer non-transiting planets in the system (Agol et al., 2005; Holman & Murray, 2005). As the planet pursues its orbit after its primary transit, it reflects an increasing amount of stellar light (see Figure 1.7) until being occulted by the star, during the so-called secondary eclipse. The decrease in the flux during the secondary eclipse yields the equilibrium temperature of the planet (see Section 5.1.2 and e.g., Charbonneau et al., 2005). Moreover, the evolution of the planet flux throughout its orbit can be inverted into a longitudinal distribution of temperature in the planet atmosphere (Knutson et al., 2007).

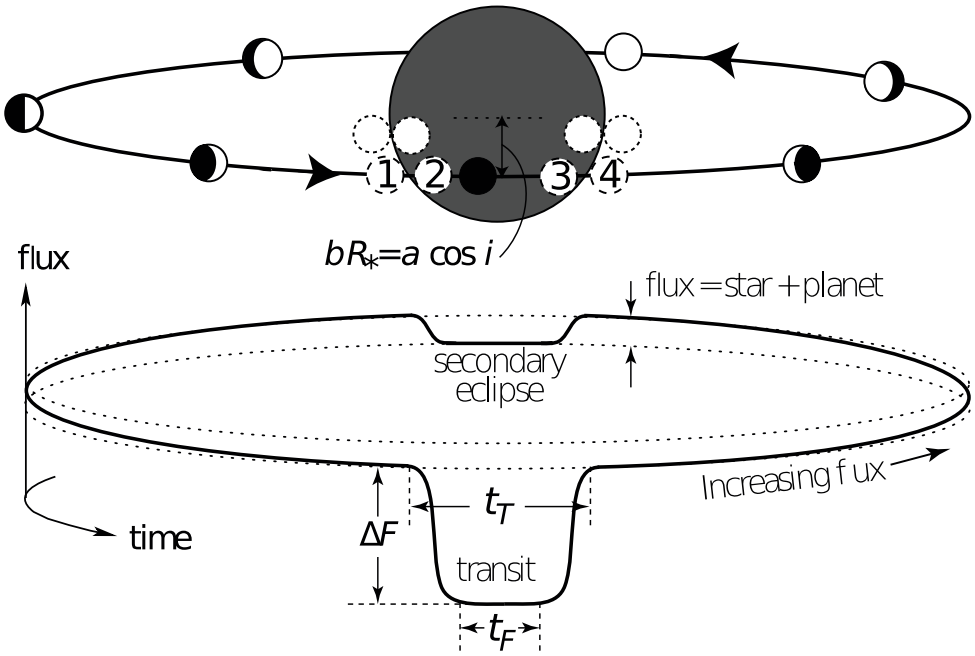

Figure 1.7 – Illustration of the orbit of a transiting planet (top) and the corresponding light curve (bottom) (source: Winn, 2009; Perryman, 2011).

The probability for a planet to transit its host star varies as R_s/a_p, where a_p is the semi-major axis of the planet orbit. For example, the probability for a Sun-like star to host a transiting Earth twin is as low as 0.4%. This explains why the first detections of planetary transits only involved hot Jupiters already known from Doppler spectroscopy (e.g., Charbonneau et al., 2000; Bouchy et al., 2005, for HD 209458 b and HD 189733 b, respectively). Ground-based surveys like HAT (Bakos et al., 2004), WASP (Pollacco et al., 2006), or KELT (Pepper et al., 2007) have made it possible to probe larger portions of the sky, allowing thereby to detect increasingly smaller planets, from warm Neptunes (e.g., Gillon et al., 2007; Bakos et al., 2010) to super Earths (Charbonneau et al., 2009).

Thanks to their ability to carry out precise long-term continuous monitorings of a large amount of stars, space-based missions like CoRoT (Auvergne et al., 2009), Kepler (Borucki et al., 2010), and its successor K2 (Howell et al., 2014) have detected thousands of planet candidates, setting a milestone in the quest for exoplanets. Together with high-precision ground based surveys like TRAPPIST/SUPECULOOS (Gillon et al., 2013) or MEarth (Nutzman & Charbonneau, 2008), they led to the discovery of the first transiting Earth-sized planets (e.g., Pepe et al., 2013; Berta-Thompson et al., 2015; Gillon et al., 2017). As of today, the TESS mission (Ricker et al., 2015) is constantly feeding us with new targets (80 confirmed planets and more than 2300 candidates as of October 2020[6] including exciting planetary systems; e.g., Gilbert et al., 2020; Plavchan et al., 2020b). Finally, in the near future, the PLATO 2.0 mission (Rauer et al., 2014) offers exciting prospects in the quest for Earth twins around solar analogs.

Velocimetric and spectroscopic observations of transiting planets

Transiting planets are primary targets for velocimetric observations. During the primary transit, the planet successively occults the blueshifted and redshifted parts of the rotating stellar disk, inducing thereby a distortion in the disk-integrated spectral line. This so-called Rossiter-Mc Laughlin effect (RM; Rossiter, 1924; McLaughlin, 1924) induces a characteristic RV signature whose shape and amplitude depend on the portion of the stellar disk crossed by the planet and, thus, on the sky-projected inclination of the planet orbital plane with respect to the stellar rotation axis (Queloz et al., 2010; Fabrycky & Winn, 2009; Collier Cameron et al., 2010; Winn & Fabrycky, 2015). Inversely, the distortions of the spectral lines along the transit chord enclose information on stellar properties (e.g., convection, differential rotation) that can be recovered through the so-called reloaded RM effect (Cegla et al., 2016). Transiting planets are also particularly suited for velocimetric follow-ups. The orbital period and phase unveiled from the transit light curve are valuable priors for RV analyses (see Chapter 2). Combining transit photometry and high-precision velocimetry enables to constrain the mean bulk density of the planets, and thereby obtain a first-order guess of their inner structure (see Section 1.2.4). Finally, spectroscopic observations of transiting planets during the primary transit and shortly before/after the secondary eclipse offer the ability to constrain the composition, the temperature-pressure profile and the wind dynamics within planet atmospheres (see Madhusudhan, 2019, for a recent review and Chapter 5 for more details).

1.2.4 The diversity of exoplanetary worlds

Occurrence and statistical properties of planetary systems

The large variety of exoplanets unveiled so far is a real mine of information for understanding the physical processes driving planet formation and evolution. By confronting the observed planet properties to the predictions of theoretical models, one can identify the most likely planet formation and evolution scenarios (e.g., in the so-called population synthesis framework; Alibert et al., 2005; Mordasini et al., 2012a,b,c; Alibert et al., 2011; Mordasini, 2018). Figure 1.8 shows the distribution of confirmed exoplanets in the orbital period-mass diagram. Several groups of planets can be identified in this diagram. The most massive close-in planets (at the upper left of Figure 1.8) are the hot Jupiters introduced in Section 1.1.4. Since they are the easiest planets for both transit photometry and velocimetry to detect, they appear widely represented in Figure 1.8, whereas their occurrence rate is only of 0.5-1% around Sun-like stars (e.g., Mayor et al., 2011; Howard et al., 2012; Petigura et al., 2017). Warm and cold Jupiter-like planets (at the upper right of Figure 1.8) are actually more frequent than their close-in counterparts, with occurrence rates of ranging from $6.2^{+2.8}_{-1.6}$%, for Jupiter-mass planets orbiting within 7 au (Wittenmyer et al., 2016; Santerne et al.,

[6] https://exoplanetarchive.ipac.caltech.edu/docs/counts_detail.html

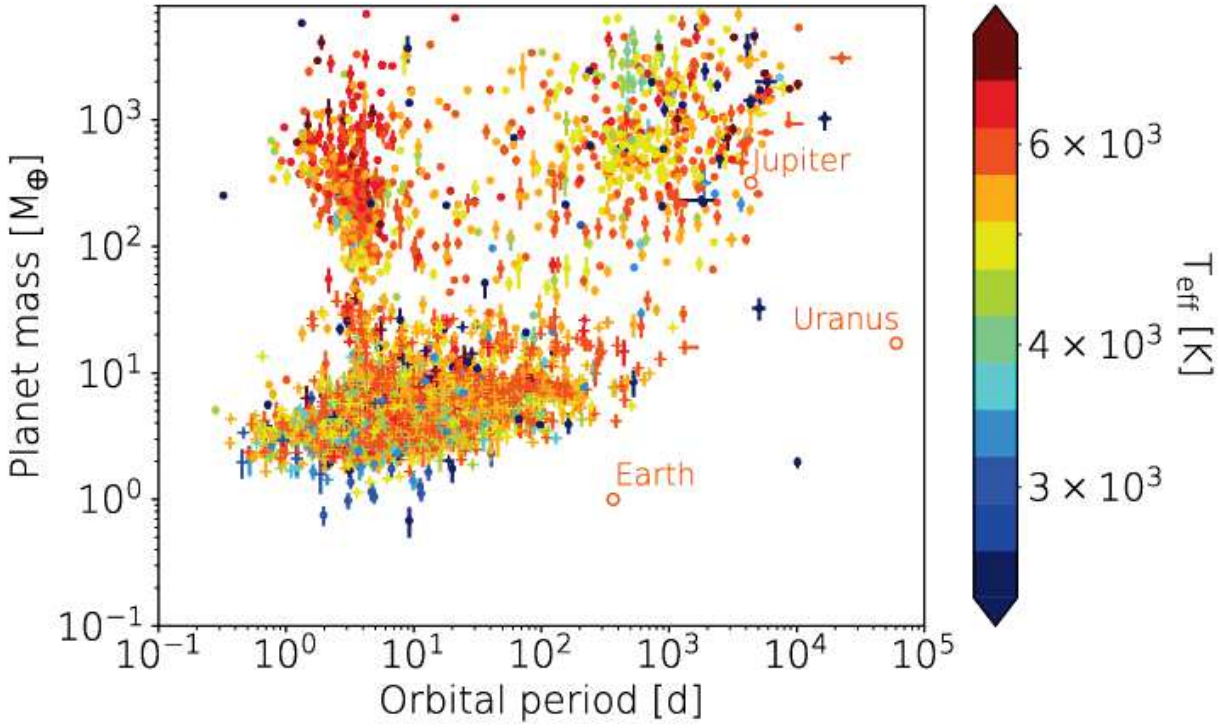

Figure 1.8 – Orbital period-mass diagram of the confirmed exoplanets with relative uncertainties on the mass and orbital period lower than 33%, computed from https://exoplanetarchive.ipac.caltech.edu/. The color scale depicts the effective temperature of the host star. For the planets detected with Doppler spectroscopy, we plot the minimum planet mass, $M_{\rm p} \sin i_{\rm orb}$, instead of $M_{\rm p}$. Planets labelled by crosses are planets detected by transit photometry only. Their masses are thus unknown yet and are inferred here using the empirical mass-radius relation of Weiss & Marcy (2014). For comparison purposes, I indicate the position of the Earth, Jupiter and Uranus by open circles.

2016), to $52 \pm 5\%$ for further companions (Bryan et al., 2016), and increasing with stellar metallicity (Fischer & Valenti, 2005; Petigura et al., 2017). As illustrated in Figure 1.8, Earth-to-Neptune mass planets are the most frequent types of planets accessible via Doppler spectroscopy and transit photometry (with an occurrence rate of 50% around Sun-like stars; Mayor et al., 2011; Howard et al., 2012). In particular, these planets are often found in compact systems (i.e., $P_{\rm orb} < 100\,{\rm d}$) where planet orbital periods are either far from resonance, or close to, but not in resonance. This observation is pretty hard to reconcile with predictions from theoretical models (e.g., disk-migration scenarios tend to find multi-planet systems in resonant orbits) and is still under investigation (see Section 3.3.2 of Baruteau et al., 2016).

Gaps in the distributions of observed exoplanet properties are also valuable information for our understanding of planet formation and evolution. For example, very few close-in Neptunes are found in both Doppler and transit surveys (see Figure 1.8 and, e.g., Mazeh et al., 2016). This so-called *hot Neptune desert* is often interpreted by the fact that contrary to hJs, migrating Neptune-mass planets crossing the inner edge of the disk are not massive enough to maintain their highly irradiated envelope which therefore rapidly evaporate (see also the discussion of Mazeh et al., 2016; Dong et al., 2018). Another gap, not visible in Figure 1.8 though, is observed in the radius distribution of close-in planets ($P_{\rm orb} < 100\,{\rm d}$), between 1.5 and 2 $R_{\rm p}$ (Fulton et al., 2017). This so-called *evaporation valley* was first anticipated theoretically from simultations of the photo-evaporation of the atmosphere of small close-in planets (Owen & Wu, 2013; Lopez & Fortney, 2013; Jin & Mordasini, 2018; Mordasini, 2020) and then confirmed from Kepler observations (Fulton et al.,

2017). Under the effect of a large stellar irradiation, close-in sub-Neptune planets see their H/He envelope escaping. As their envelope represents a low fraction of their total mass, this evaporation does not have a significant impact on the diagram shown in Figure 1.8. In contrast, this effect is expected to be seen in the mass-mean density diagram of exoplanets (Jin & Mordasini, 2018), although no young planet was yet observed in the evaporation valley.

The composition of exoplanets

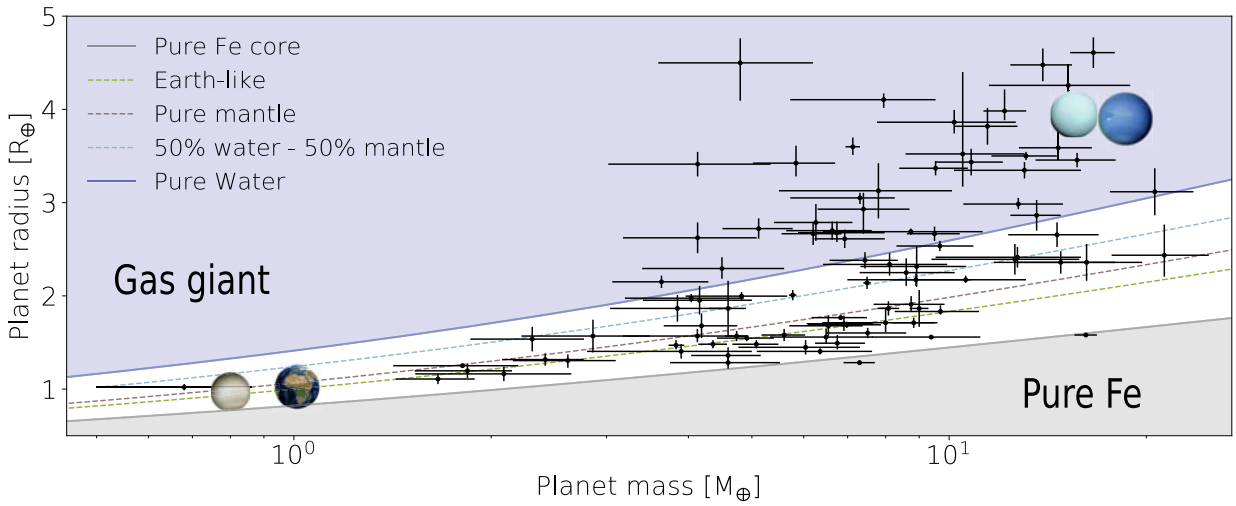

Figure 1.9 – Mass-radius diagram of planets of mass lower than $20\,M_\oplus$ and radius lower than $5\,R_\oplus$ with relative uncertainties smaller than 30% computed from the NASA Exoplanet Archive (https://exoplanetarchive.ipac.caltech.edu/). The contours correspond to different planet inner compositions computed using Zeng et al. (2019) models (see also https://www.cfa.harvard.edu/~lzeng/planetmodels.html#h2oplanets). For information, we also indicate the location of the Earth, Venus, Uranus and Neptune on the diagram.

The inner composition of exoplanets is key information that constrains planet formation and evolution models and precedes the characterisation of the planetary surface. Measuring the mass and radius of a given exoplanet allows one to access its mean bulk density, which offers a first order constraint on its inner composition (see Fortney & Nettelmann, 2010; Baraffe et al., 2014; Dorn et al., 2015). The mass-radius (MR) diagram is therefore of particular interest for planet formation and evolution models as it directly reflects the processes undergone by the planetary structure throughout its life (e.g., nature of the accreted materiel, orbital migration, atmospheric escape; Mordasini et al., 2012c). While the MR diagram is relatively well constrained for super-Earths and Neptune-mass planets (see Figure 1.9), it clearly lacks Earth-like planets, due mostly to the fact that the masses of the known transiting Earth-sized planets are plagued by large uncertainties given the small amplitude of their RV signature (often drowned into stellar activity signals as described in Section 1.4). The same goes for close-in planets orbiting stars younger than ∼30 Myr. Populating their MR diagram would greatly help understanding the evolution of planet inner densities in the early stages of their life, refining thereby planet formation and evolution models.

Observing exoplanets using low- and high-resolution spectrometers yields precious constraints on the chemical abundances of their atmosphere (see the review of Madhusudhan, 2019, and the introduction of Chapter 5). These abundances enclose information on the composition of the protoplanetary disk at the location of the planet at the time of its formation. In particular, the C/O ratio (measured using mostly H_2O, CO abundances) is widely used as a proxy to estimate the distance at which a given planet accreted the gas. Under the effect of the radial decrease in the

temperature of the disk, the snow lines of H_2O, CO_2, CO (and so on) occur at different distances from the star, which affects the radial distribution of the C/O ratio in the disk gas, and thus the atmospheric composition (Öberg et al., 2011). Note however, that various processes at work in exoplanet atmospheres (e.g., atmospheric circulation, cloud formations) may affect the measured C/O ratio (see Chapter 5).

1.2.5 The quest for habitable planets

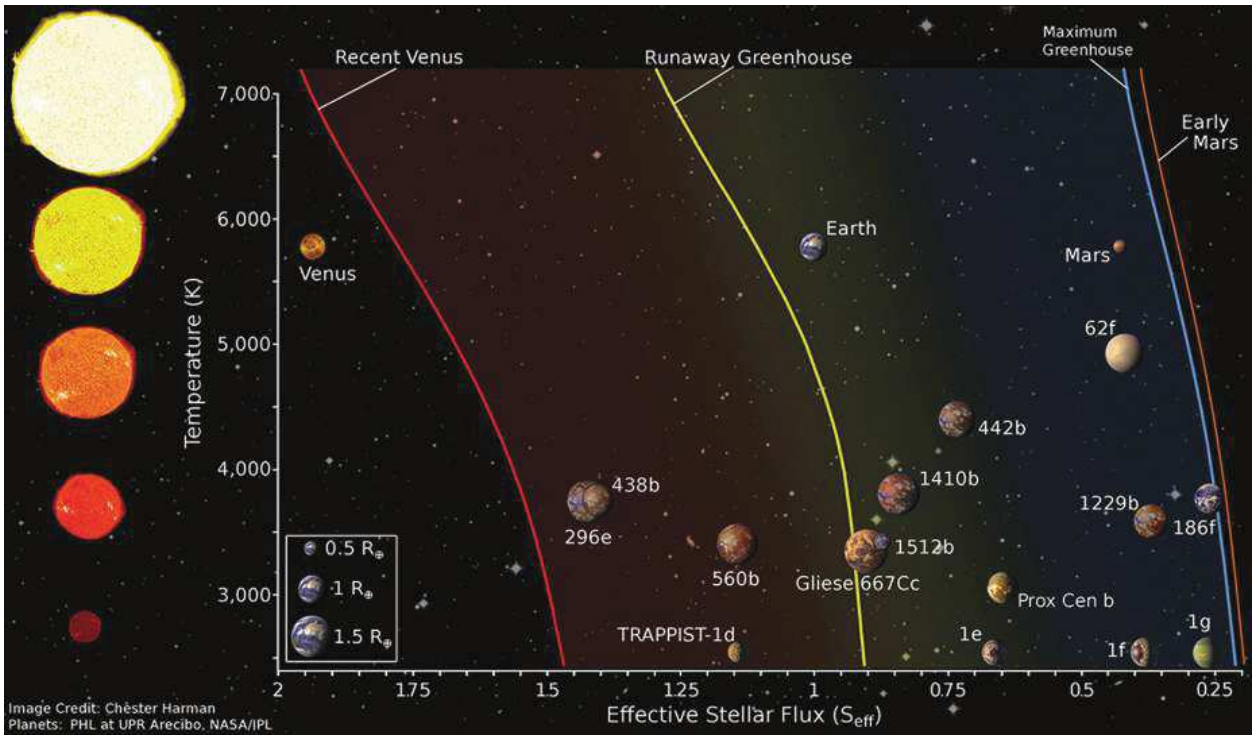

Figure 1.10 – Diagram of effective stellar flux vs stellar effective temperature for the Earth-like exoplanets (i.e., $0.5\,R_\oplus < R_\mathrm{p} < 1.5\,R_\oplus$ and $0.1 < M_\mathrm{p} < 5.0\,M_\mathrm{p}$) that are the most likely to harbour surface liquid water. An artistic view of each planet is shown next to each planet name. The HZ is delimited by the yellow and blue solid lines. For comparison, a more conservative HZ based on Venus and Mars positions is delimited by two red solid lines (Source: PHL at UPR ARECIBO, see http://phl.upr.edu/home).

The quest for extraterrestrial life is one of the main driver of the search for exoplanets. The conditions for a planet to host life are defined from our experience on Earth (see the review of Cockell et al., 2016). It requires carbon, i.e. the bedrock molecule for Earth biochemistry, liquid water, thought to be the most adapted solvent to create organic molecules, and a source of energy to drive metabolic reactions[7] (e.g., star light or planet geothermal flux). Acquiring substantial amounts of water and carbon is not challenging as both components are generally well represented in protoplanetary disks, especially beyond their snow lines, where they condensate and can be accreted by planet embryos (Lecar et al., 2006; Ros & Johansen, 2013).

In contrast, sustaining liquid water at the planetary surface requires stringent conditions. The planet surface must indeed receive the right amount of stellar flux through its atmosphere for surface liquid water to exist. This motivated the definition of the so called habitable zone (HZ; Kasting

[7] A stable surface is sometimes added to the fundamental conditions required for life to emerge as dynamical processes in non-solid mediums such as planetary atmospheres make it difficult to maintain liquid water on time scales long enough for life to develop.

et al., 1993), as the range of radial distances from the star for which planets can sustain liquid water at their surface[8]. The HZ primarily depends on the stellar flux received by the planet and thus on the effective temperature of the star. Moreover, the composition of the planet atmosphere will affect the amount of stellar flux reaching the surface. The inner edge of the HZ is generally defined as the lowest orbital distance at which a planet featuring a completely opaque atmosphere (i.e., reflecting all incoming stellar flux) cools sufficiently in its surface so that liquid water can be sustained thereon (in the so-called *runaway greenhouse limit*; Kopparapu et al., 2013). In contrast, the outer edge of the HZ is defined for a planet atmosphere dominated by greenhouse gases (in the so-called *runaway greenhouse limit*, generally defined assuming a CO_2 atmosphere; Kopparapu et al., 2013). Finally, the surface liquid water must be maintained against evaporation in the planet atmosphere. External factors such as stellar irradiation, magnetized wind, and flares affect atmospheric escape mechanisms which, in turn, affect the climate at the surface of the planet (see the book of Pierrehumbert, 2010).

A dozen of HZ exoplanets of mass/radius similar to the Earth have been detected over the past few years (e.g., Proxima Centauri b; TRAPPIST-1 e, f and g; LHS 1140 b; Luyten b reported respectively in Anglada-Escudé et al., 2016; Gillon et al., 2017; Dittmann et al., 2017; Astudillo-Defru et al., 2017b, see the illustration in Figure 1.10). These planets are primary targets for the search for patterns of biological origin (a.k.a. biosignatures) in their atmospheres. Various potential species have been identified as potential biomarkers from our experience on Earth, although abiotic origins cannot be ruled out for any of these indicators (see the reviews of Des Marais et al., 2002; Schwieterman et al., 2018). For example, the molecular oxygen (O_2) generated by photosynthetis processes, and the ozone (O_3) produced by the photochemical dissociation of O_2 in the stratosphere of Earth-like planets, induce complementary signatures thought to be among the most accessible biomarkers from the Earth (Leger et al., 1993; Schwieterman et al., 2018). The James Webb Space Telescope (JWST), due to launch in 2021, is expected to be able to detect such biosignatures in the atmosphere of terrestrial planets transiting very-low-mass stars located within 10 pc from the Sun (Deming et al., 2009; Barstow & Irwin, 2016; Morley et al., 2017). However, as things stand, only a handful of HZ planets meet the conditions required for an atmospheric characterization with the JWST (TRAPPIST-1e, f, g; LHS1140 b; Luyten b). In the longer term, ambitious projects aimed at combining high-resolution spectroscopy with high-contrast imaging facilities may bring decisive constraints on the presence of biosignatures in the atmosphere of nearby planets (Snellen et al., 2013, 2015; Mennesson et al., 2016; Snellen et al., 2019). Detecting new nearby temperate terrestrial planets is therefore an essential goal in the quest for biosignatures with new generation telescopes.

1.3 The search for planets around M dwarfs and low-mass PMS stars

1.3.1 The case of very-low-mass stars

M dwarfs (0.08-0.6 $M_\odot$), the lowest-mass stars of the main-sequence (see Figure 1.1), are the most promising targets to unveil Earth-like exoplanets. First, they largely outnumber stars of earlier spectral type in the solar neighborhood. The all-sky volume limited survey RECONS (Henry et al., 1994) has indeed demonstrated that M dwarfs represent at least 75% of the stars within 25 pc from the Sun (Henry et al., 2006), and probably more than 90% within 10 pc from the Sun (Winters et al., 2015, 2019). Second, they feature both the smallest masses and radii of the main

[8] Note that planets hosting liquid water in their interior (i.e., habitability of classes II, III and IV like Europe or Enceladus see Lammer et al., 2009) are not considered in the definition of the HZ, as probing the inner structure of exoplanets is far beyond the reach of current and future instruments.

sequence. A planet at a given orbital location will thus induce larger transit depths and RV wobbles on a M dwarf than on its solar-like counterpart (see equations 1.4 and 1.2, respectively). Thanks to their enhanced transit depths, transiting planets around M dwarfs are primary candidates for the characterization of their atmosphere with forthcoming missions such as the JWST and the ELTs (Morley et al., 2017). In addition, M dwarfs feature lower effective temperatures and thus closer-in HZ than solar-like stars, making temperate Earth-like planets around them more likely to transit and easier to detect in velocimetry. For example, the amplitude of the RV signature induced by a HZ Earth-like planet increases from about $0.1\,\mathrm{m\,s^{-1}}$, on a solar analog, to $\sim$$1\,\mathrm{m\,s^{-1}}$ on a mid M dwarf. Finally, the planet occurrence rate around M dwarfs exceeds by a factor 2-3 that of stars with earlier type (Dressing & Charbonneau, 2015; Gaidos et al., 2016). Early-to-mid M dwarfs host about two planets of radii lower than $\sim$$2\,R_\odot$ per star, and probably more for later spectral types (e.g., Gillon et al., 2017).

Over the last decade, increasing attention has been paid to the search for planets around M dwarfs. In particular, the most favourable candidates to further investigate habitability orbit stars with spectral types later than M4 (e.g., Berta-Thompson et al., 2015; Anglada-Escudé et al., 2016; Gillon et al., 2017; Dittmann et al., 2017; Astudillo-Defru et al., 2017b). However, if we consider the 320 evolved stellar systems within 6.6 pc from the Sun, only 12% of them are known to host planets. Given that M dwarfs represent 70% of this sample and that they host 2 planets in average, we conclude that the vast majority of the planets in the immediate solar neighborhood still remains to be discovered.

1.3.2 The case of low-mass PMS stars

Studying the processes driving planet formation and evolution is key to explain the large diversity in the observed exoplanet distribution and understand the evolution of the surface conditions of potentially habitable exoplanets (Raymond et al., 2014; Bolmont et al., 2017; Bolmont, 2018). This requires to detect and characterize planetary systems in the very first moments of their lives, i.e., orbiting young (i.e., younger than $\sim$30 Myr) low-mass PMS stars.

Directly detecting exoplanets in the accretion disk surrounding cTTSs is a tricky process as the accretion disk outshines planetary emissions. As a result, only two massive planets around a cTTS have been imaged so far (Keppler et al., 2018; Haffert et al., 2019). On the other hand, the presence of massive planets leaves characteristic signatures in the protoplanetary disk which can be used to indirectly unveil them. These signatures are particularly heightened in the so-called *transition disks*, defined by they reduced nIR excess compared to the median SED of PMS stars with accretion disks (Strom et al., 1989). Observations of transition disks with the Atacama Large Millimeter Array (ALMA) have revealed various structures such as gaps and rings (ALMA Partnership et al., 2015; Andrews et al., 2016) or spirals (Benisty et al., 2015) that could be induced by forming planets (Bae et al., 2016; Takahashi & Inutsuka, 2016; Wafflard-Fernandez & Baruteau, 2020), but also by other planet-independent mechanisms (e.g., Flock et al., 2015). The disk dissipation leaves a clearer field for the search for planets around PMS stars. The relatively high equilibrium temperatures (1000-2000 K) of newborn planets provide them with a relatively high flux contrast with respect to the star which favors their direct detections. As a result, a handful of planets of a few Jupiter masses have been directly imaged at a few tens of au from wTTSs and pTTSs (e.g., Lafrenière et al., 2008; Currie et al., 2014; Bohn et al., 2020).

Close-in planets orbiting within a few 0.1 au from young PMS stars are complementary targets to improve our understanding on how planets evolve shortly after their formation. The recent detections of close-in giant planets around wTTSs and pTTSs (Donati et al., 2016; David et al., 2016; Yu et al., 2017; David et al., 2019a,b; Plavchan et al., 2020b) demonstrate that planets can migrate on time scales of a few Myr in the disk. Beyond adding valuable constraints to planet

formation/migration theories, these planets are expected to have a major dynamical impact on the architecture of the system. Moreover, measuring the mass of the few known transiting planets around PMS stars such as K2-33 b (David et al., 2016; Mann et al., 2016), V1298 Tau b,c,d,e (David et al., 2019a,b), and AU Microscopii b (Plavchan et al., 2020b) will yield precious information about how the planet bulk densities vary in the early stages of their lives and constrain planet formation and evolution models (e.g., Mordasini et al., 2012c, 2015). Finally, these planets are primary targets for a spectroscopic characterization of their atmosphere, whose composition may bring insights on the planet formation (Öberg et al., 2011; Madhusudhan et al., 2017, through the C/O ratio;), and whose interactions with the star (e.g., atmospheric evaporation) could provide information on the origin of the evaporation valley (Jin & Mordasini, 2018; Mordasini, 2020).

However, both M dwarfs and low-mass PMS stars are faint in the optical domain and exhibit intense magnetic activity inducing photometric and RV signals that hamper the search for planets around them. As a consequence, most of the planets unveiled around M dwarfs so far involve stars of early spectral types (up to M3; Bonfils et al., 2013; Dressing & Charbonneau, 2015), and the exoplanet population in the solar vicinity remains poorly constrained. Similarly, only a handful of close-in giant planets have been detected around wTTSs and none of them have a well-measured bulk density. CTTSs, which are both fainter and more active than their more evolved counterparts (e.g., Johns-Krull et al., 1999a), have no planet confirmed around them, the existence of the planet candidate CI Tau b claimed in Johns-Krull et al. (2016) being currently debated in the recent literature Donati et al. (2020b); Biddle et al. (2021). In the next section, we give a phenomenological approach to the different activity phenomena of M dwarfs and low-mass PMS stars while their magnetic origin is described in Chapter 3.

1.4 Stellar activity and its impact on RV curves

1.4.1 Dynamo processes, stellar activity

1.4.1.1 Activity and rotation of low-mass stars

Young low-mass PMS stars exhibit magnetic fields of a few kG, for cTTSs (Johns-Krull et al., 1999a; Donati et al., 2010, 2012), and of a few 100 G, for wTTSs and pTTSs (Donati et al., 2014, 2015; Yu et al., 2019). In a similar way, M dwarfs frequently host magnetic fields whose strength varies from a few tens of G, for early spectral types (i.e., for $M_s \gtrsim 0.5\,M_\odot$), to the kG level for fully-convective (FC) late-type stars (Johns-Krull & Valenti, 1996; Donati et al., 2006a; Morin et al., 2008b; Reiners & Basri, 2009; Morin et al., 2010). These magnetic fields induce various characteristic phenomena (grouped under the term of magnetic activity) that are observed at the surface and in the atmosphere of low mass stars of any spectral type. Dark and bright inhomogeneities come and go at the stellar photosphere on time scales ranging from a few days to several years depending on the star (see the review of Berdyugina, 2005). Low-mass stars are surrounded by a shallow ($\sim 10^3$ km) optically thin layer of gas, called chromosphere, which is locally heated up by the particle flux carried by emerging magnetic field lines. This heating induce the reversal of prominent resonant absorption lines such as Ca or Mg in emission (see the review of Hall, 2008). Beyond the chromosphere, a low-density coronal plasma at the MK level extending up to several millions of kilometers from the star (see Figure 1.2) induces signatures at various wavelengths, especially in the X-ray and radio domains (Narain & Ulmschneider, 1996), and are associated with frequent flaring events, coronal mass ejections and magnetized winds. Active low-mass stars also exhibit prominences trapped in large-scale magnetic loops at the chromospheric/coronal level, detected either in absorption, when the confined cloud crosses the stellar disk, or in emission, through the scattering of the stellar light (Collier Cameron & Robinson, 1989; Donati et al., 2000). All these activity phenomena are induced by stellar magnetic fields powered by dynamo processes in the

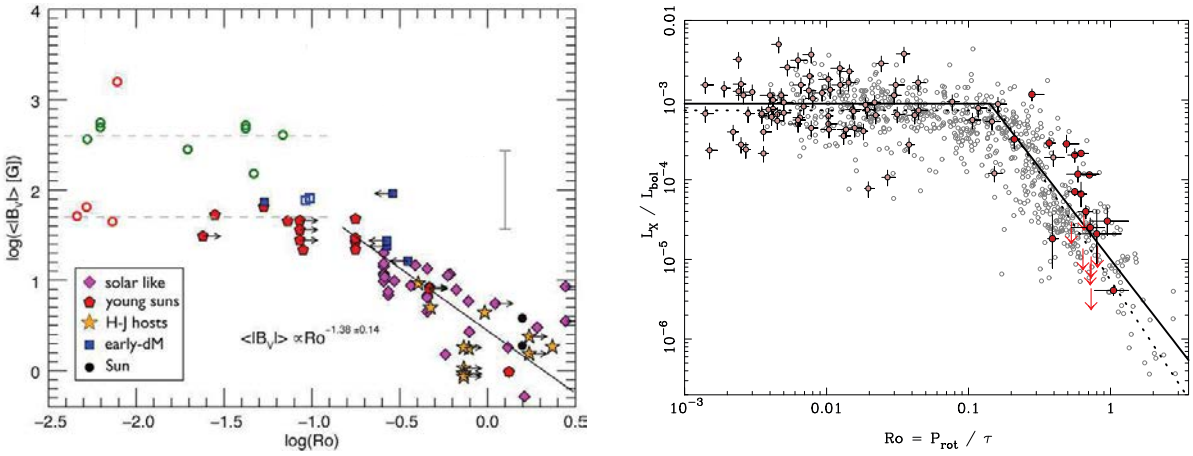

Figure 1.11 – Relationships between magnetic activity and Rossby number for stars of various spectral types. *Left panel:* correlation between the average surface large-scale magnetic field and Rossby number for various stars. The open symbols are M dwarfs in the saturated dynamo regime: blue squares stand for M dwarfs of mass $M_s > 0.4\,M_\odot$, green circles, for stars with $0.2 < M_s/M_\odot < 0.4$, and red circles for stars with $M_s < 0.2\,M_\odot$. The gray error bar indicates the typical uncertainty on the strength of the large-scale magnetic field. Right/left arrows denote cases with lower/upper limit on *Ro*. Finally, the Sun is indicated at activity minimum and maximum. The double plateau observed for late M dwarfs is discussed in Section 3.1. This panel is adapted from Vidotto et al. (2014b). *Right panel:* X-ray to bolometric luminosity ratio $\log L_X/L_{bol}$ as a function of the Rossby number for fully-convective stars (red and brown filled dots) and partly-convective stars (open circles). Red arrows indicate stars with undetected X-ray flux. The best-fitting activity-rotation relations from Wright et al. (2011) and Wright et al. (2018) are indicated by the solid and dashed lines, respectively. Source of the figure: Wright et al. (2018).

stellar interior (detailed in Chapter 3.1). To understand this activity, it is therefore required to study stellar magnetic fields, which is possible with high-resolution spectropolarimetry as discussed in more details in Chapter 3.

The activity of cool stars scales up with stellar rotation rate. In particular, the Rossby number *Ro*, defined as the ratio between the stellar rotation period P_{rot} and the convective turnover time scale of the granules in the convective zone[9], has shown to be an excellent proxy of the efficiency of the magnetic field generation (Noyes et al., 1984; Pizzolato et al., 2003; Kiraga & Stepien, 2007). Observations of low-mass stars (of any spectral type) have shown that their magnetic field properties and the associated activity (e.g., chromospheric and coronal emissions) follow similar relations with the Rossby number (see Figure 1.11 and Reiners et al., 2009; Wright et al., 2011; Vidotto et al., 2014b; Wright & Drake, 2016; Shulyak et al., 2017; Astudillo-Defru et al., 2017a; Wright et al., 2018; See et al., 2019). For $Ro \gtrsim 0.1$, magnetic activity decreases with increasing Rossby number. In contrast, the activity indicators reach a plateau in stars with $Ro \lesssim 0.1$. In this regime, the magnetic field retroacts on the fluid from which it was born, blocking therefore its amplification: the regime is said to be saturated. As a result of their relatively low effective temperatures and large convective zones, young PMS stars and M dwarfs exhibit turnover time scales of a few hundred on days (compared to ∼10 d for the Sun) and are thus more active than evolved G, K stars, at a given rotation rate. The phenomena induced by this activity produce RV signals hampering the search for planets around these stars which are listed in the forthcoming sections.

[9] Note that the Rossby number defined in this way (sometimes referred to as the empirical or effective *Ro*) is a global stellar property which differs from the Rossby number usually defined in fluid dynamics which relates to local hydrodynamical properties of the medium.

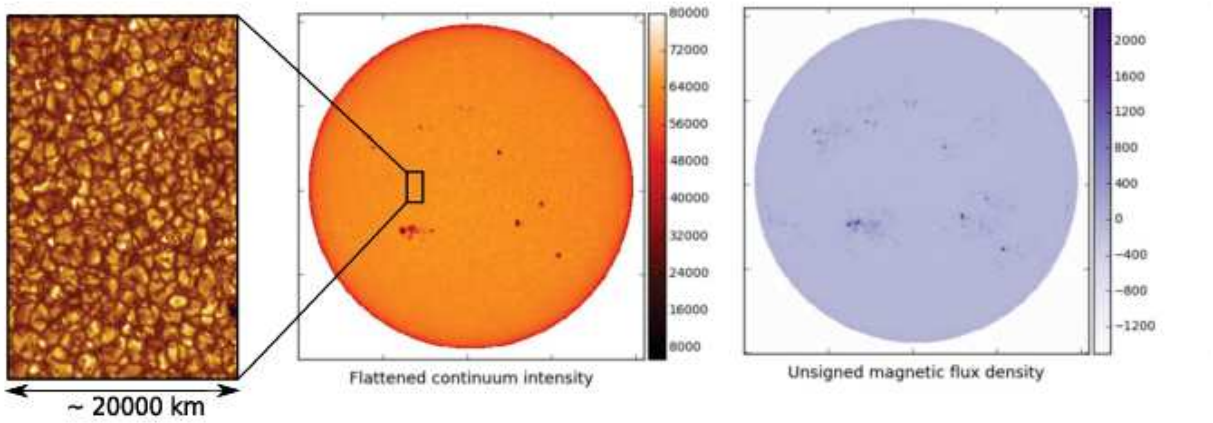

Figure 1.12 – Illustration of granulation, inhomogeneities and magnetic field at the solar surface. *Middle panel:* SDO image of the intensity at the solar disk and zoom on the stellar surface to resolve the granulae at the solar surface (left panel). *Right panel:* same as middle panel, but for the unsigned magnetic flux density (the color scale is in G). Sources of the figures: NASA/SDO (left panel) and Haywood et al. (2016) (middle and right panels).

1.4.1.2 Surface inhomogeneities

Under the effect of the local magnetic pressure, magnetic field tubes emerge at given locations above the stellar photosphere (Hale, 1908). The strong magnetic field (typically a few kG) locally suppresses the convective motion which cools down the plasma. If the flux tube is large enough, the region will appear darker than the quiet photosphere and will be referred to as a spot (see the example shown in the middle panel of Figure 1.12). In contrast, for narrow field tubes, radiative heating dominates the energy budget and the regions, called faculae, appear brighter than the quiet photosphere. The flux conveyed in the emerging field tubes heats the chromospheric plasma, resulting in the formation of small bright regions (called plages) therein. These dark and bright inhomogeneities are carried across the stellar disk by stellar rotation and thus modulate the total stellar brightness at the rotation period of the star (see Figure 1.13). As a given spot crosses the visible hemisphere of the stellar disk, it successively occults its blueshifted and redshifted halves, resulting respectively in a redshift (positive RV) and a blueshift (negative RV) of the disk-integrated spectral line (see the middle and bottom panels of Figure 1.13). The resulting RV signature roughly scales with the first derivative of the opposite of the spot-induced photometric curve (and inversely for a bright feature). In practice, several time-evolving spots surrounded by faculae and plages are distributed at the surface of the Sun (see the middle panel of Figure 1.12), which induces complex fluctuations in both photometry and velocimetry. These signals are particularly affecting the velocimetric search for planets around solar-like stars as they reach several $\mathrm{m\,s^{-1}}$ of amplitude (e.g., $5\,\mathrm{m\,s^{-1}}$ for the Sun at activity maximum Haywood et al., 2016; Collier Cameron et al., 2019), i.e., enough to completely occult and even mimic the planet RV signatures (e.g., Saar & Donahue, 1997; Queloz et al., 2001; Desort et al., 2007; Lagrange et al., 2010; Meunier et al., 2010).

The effective temperature of bright and dark surface features defines their relative contrast with respect to the quiet photosphere and the amplitude of the photometric/velocimetric signatures that they induce. The typical temperature difference between a spot and the photosphere decreases for stars with later spectral types (e.g., $\sim$1500 K for the Sun vs $\sim$300 K for a mid-M dwarf; see Berdyugina, 2005, for a review) and so does the brightness contrast b (75% for the Sun vs 40% for a mid-M dwarf). This apparent decrease in contrast is however compensated for M dwarfs that tend to be more magnetically active than their solar counterparts (as mentioned in Section 1.4.1.1; see also Basri et al., 2010; West et al., 2011; Figueira et al., 2016), implying activity RV signals of a

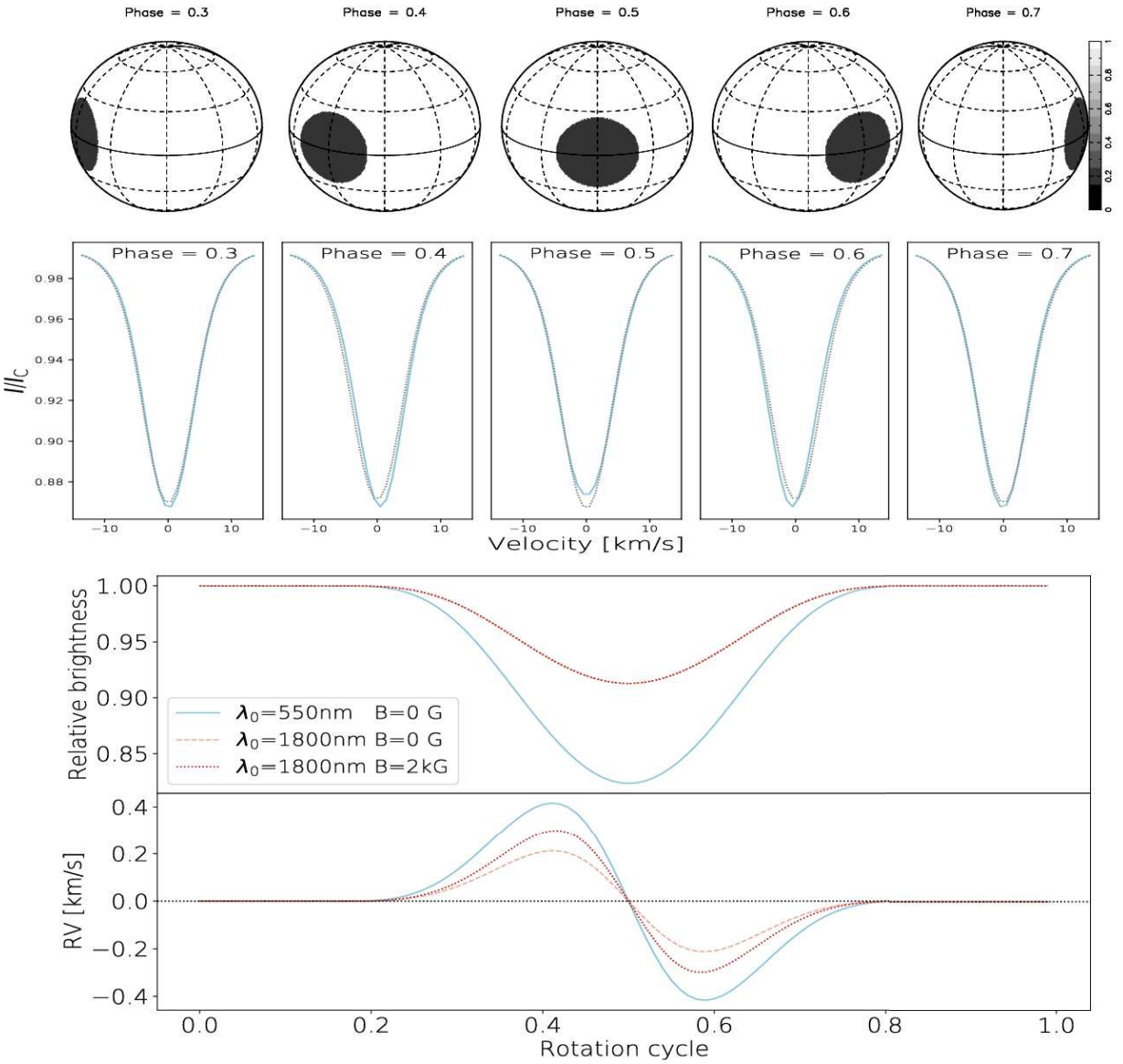

Figure 1.13 – Illustration of the photometric and RV signals induced by a dark spot at the surface of a star modeled with Zeeman-Doppler imaging (see Appendix A.1). In the top panel, the surface of the star is shown at different rotation phases (the color scale refers to the relative brightness at the stellar surface in the optical spectral domain). The spot is chosen to be 450 K cooler than the quiet photosphere consistently with Berdyugina (2005). In the middle panel, we show the effect of the spot on the average line profile (blue solid lines) with respect to the unspotted line profile (black dotted line) for all rotation phases at which the star is displayed in the first panel. In the lower two panels, we show the respective effects of the spot crossing the star disk on the relative brightness and RV, respectively. In each of the two panels, the blue solid line is obtained at a wavelength $\lambda_0 = 550$ nm, while the red lines are computed at $\lambda_0 = 1800$ nm (SPIRou maximum efficiency). In particular, dashed and dotted lines are obtained by assuming a magnetic field of 0 and 2 kG within the modeled spot.

few $\mathrm{m\,s^{-1}}$, i.e., enough to significantly hamper the search for temperate Earth-like planets around them. This effect is much more spectacular for young PMS stars that exhibit large long-lived dark spots inducing high-amplitude quasi-periodic fluctuations in their photometric curves (of up to 0.4 and 0.6 mag for cTTS and WTTS; Grankin et al., 2007, 2008) and RV curves (at the $\mathrm{km\,s^{-1}}$ level

in the optical; e.g., Bouvier & Bertout, 1989; Mahmud et al., 2011; Donati et al., 2016; Johns-Krull et al., 2016; Yu et al., 2017). Moreover, in cTTSs, the accretion shocks produced from the impact of the accreted disk material on the stellar surface locally heat the chromosphere up to temperatures of $\sim 10^4$ K (Bally, 2016). These so-called hotspots veil small parts of the stellar disk and their rotation with the star induces RV signatures similar to those produced by dark spots. However, as these accretion spots typically cover no more than a few percent of the stellar surface, their RV contribution is by far weaker than that of brightness inhomogeneities at the stellar photosphere (e.g., Valenti & Johns-Krull, 2004; Donati et al., 2007, 2008b, 2020b).

Moreover, latitudinal differential rotation can shear the surface distribution of bright and dark features. As spots come and go at the stellar surface, stellar activity photometric and RV curves can potentially lose their periodic coherence for stars featuring a high DR. This might be a problem for early M dwarfs which exhibit relatively strong solar-like DRs (i.e., the equator rotates faster than the pole) at the solar level (i.e., difference in rotation rate between the pole and the equator of the order of 0.07 rad/d; Donati et al., 2008b; Hébrard et al., 2016). In contrast, largely and fully convective M dwarfs tend to rotate as solid bodies (Donati et al., 2006a; Morin et al., 2008b, 2010). The same goes for cTTSs which exhibit low solar-like DR levels (Johns-Krull, 1996; Donati et al., 2007) by virtue of their fully convective interiors (Kuker & Rudiger, 1997). The situation is more uncertain for wTTSs and pTTSs whose DR parameters vary significantly from one star to another, some stars rotating as solid-bodies (Skelly et al., 2010; Donati et al., 2015) whereas others exhibit solar-like DR at the solar level or more (Donati et al., 2014; Yu et al., 2017, 2019).

1.4.1.3 Magnetic fields

The Zeeman effect

The magnetic field itself affects the spectral lines through the Zeeman effect (Zeeman, 1897). In short, spectral lines split into different components in the presence of a magnetic field (see the description of the effect in Section 3.1.1). The intensity of this splitting depends on the sensitivity of the spectral line to magnetic fields, on the magnetic strength, and on the square of the reference wavelength λ_0 of the line. For example, under a magnetic field of 1 kG (typical within active regions like spots at the surface of M dwarfs and low-mass PMS stars), the wavelength shift of a line moderately sensitive to magnetic fields is about 1.4 pm (i.e., 0.84 km s^{-1}), at $\lambda_0 = 500$ nm, and 22.4 pm (3.36 km s^{-1}) at $\lambda_0 = 2\,\mu$m (Donati & Landstreet, 2009). This splitting is generally not resolved by the current velocimeters in operation (although nIR high-resolution spectrometers should be able to resolve the splitting of magnetically-sensitive lines) and, instead, the spectral line is broadened (Zeeman broadening).

Magnetically active low-mass stars exhibit a finite number of so-called *active regions* featuring kG-magnetic fields, generally associated with, but not limited to, bright and dark surface inhomogeneities (as shown the right panel of Figure 1.12). The local line profile within these regions is splitted through the Zeeman effect. As a result, the disk-integrated line profile is distorted, which affects the position of its centroid and thus the measured RV (see the bottom panel of Figure 1.13). The amplitude of the RV variations induced by magnetic fields at the stellar surface is generally very low (i.e., at the sub-m s^{-1} level) for low-mass stars at visible wavelengths but can increase by one order of magnitude in the nIR (Reiners et al., 2013). This effect is stronger for slow rotators (i.e., of projected rotational velocity $v \sin i$ lower than $\sim$10 km s^{-1}), whose line profile is not dominated by Doppler broadening (Hébrard et al., 2014). As a result, low-mass PMS stars, which exhibit relatively large $v \sin i$ (Bouvier et al., 1997), are generally poorly impacted by this effect and their profile distortions are mostly induced by spots crossing the stellar disk. This effect is more pronounced for M dwarfs featuring relatively low $v \sin i$ as a result of their small radii. Moreover, the intensity of the Zeeman effect associated with the strong magnetic fields present within surface

features depends on the difference in temperature ΔT (and thus on the relative brightness contrast b) between the features and the quiet photosphere. For large values of b, the contribution of the flux emitted within star spots to the global line profile becomes negligible and the profile distortions are dominated by the veiling of the stellar disk by the spots rather than by the Zeeman effect. This condition is typically fulfilled if b is larger than ∼40% for a mid M dwarf observed in the nIR (Hébrard et al., 2014). However, due to (i) the relatively low ΔT of the features at the surface of M dwarfs and (ii) the decrease in b from optical to nIR wavelengths (b lies typically around 0.2 for a mid M dwarf; see Figure 1.14), the Zeeman effect is expected to be a major contributor of nIR stellar activity RV signals for M dwarfs.

Evolution of the magnetic field

The evolution of the magnetic field affects the distribution of bright and dark features at the stellar photosphere. In the case of the Sun, the large-scale magnetic field oscillates between an aligned magnetic dipole with few spots at moderate latitudes (at solar minimum) and a more complex dominantly toroidal field with numerous features preferentially located near stellar equator (at solar maximum), on a ∼11-yr time scale. By affecting the number and latitudinal distribution of spots on the stellar photosphere, magnetic cycles induce long-term RV variations for solar-like stars (Dumusque et al., 2011a). Activity cycles have been detected on early M dwarfs (e.g., Gomes da Silva et al., 2012) suggesting that these stars might also exhibit long-term RV shifts, provided that the dynamo processes powering these magnetic cycles are similar to those at work in the Sun. More recently, the putative detections of long-term fluctuations in the photometric curve and radio emission of very-low-mass stars (Route, 2016; Suárez Mascareño et al., 2016; Wargelin et al., 2017) suggest that these stars might also exhibit magnetic cycles. As things stand, no magnetic cycle was detected on a cTTS/wTTS yet. However, long-term variations in the shape, amplitude and period of the light curves of a few wTTSs associated to changes in the surface distribution of brightness features might be a hint that magnetic cycles could be at work in young PMS stars (Sokoloff et al., 2008; Hambálek et al., 2019; Yu et al., 2019).

1.4.1.4 Other sources of stellar activity RV signals

Flares and coronal mass ejections

Flares are impulsive released of energy associated with magnetic field line reconnections in stellar corona (see Benz, 2017, for a review). Flares can be accompanied by the ejection of coronal prominences trapped in the reconnecting field lines. Both low-mass PMS stars and M dwarfs are notorious for their frequent flaring events (separated by a few days typically; e.g., Stelzer et al., 2007; Vida et al., 2017, 2019; Mondrik et al., 2019; Günther et al., 2020). In particular for M dwarfs, the energy released by flares and the associated coronal mass ejections likely contribute to the atmospheric erosion of close-in planets (Lammer et al., 2007; Lingam & Loeb, 2017) and progressively make their surface not suitable for life (e.g., Khodachenko et al., 2007; Tilley et al., 2017). From an observational point of view, flares produce sudden increases in flux observable at various wavelengths. In particular, frequent flaring events can hamper the detectability of planetary transits and RV signatures.

Acoustic oscillations and granulation

Other phenomena not related to magnetic field contribute to photometric and RV variability. At the surfaces of solar-like stars, oscillations induced by the propagation of acoustic waves in the convective zone (Leighton et al., 1962) produce RV fluctuations of the order of the $m\,s^{-1}$ on time scales of a few minutes (Kjeldsen & Bedding, 1995; Bouchy & Carrier, 2002). The amplitude of these

oscillations roughly scales with the ratio of the stellar luminosity over the stellar mass (Kjeldsen & Bedding, 1995; Christensen-Dalsgaard, 2004). The typical luminosity-to-mass ratio of M dwarfs vary from 0.1, for a M0, to 0.001, for an ultracool dwarf. This strong decrease in the amplitude of oscillation-induced RV signals is further confirmed by the fact that these oscillations remain undetected for M dwarfs (Rodríguez-López et al., 2015), implying that they will likely not affect the search for temperate Earth-like planets (at the $m\,s^{-1}$ level). On the other hand, low-mass PMS stars exhibit self-sustained acoustic (delta scuti type) and gravity (gamma Doradus type) oscillations inducing mmag-photometric and $m\,s^{-1}$-RV variations on time scales ranging from a few minutes (for acoustic waves) to a few days (for gravity waves; see Aerts et al., 2010).

Granulation at the surface of the Sun (see the left panel of Figure 1.12) induces RV signatures that vary on time scales of a few minutes (for small granules) to a few days (for supergranules). The hot ascending and cold descending granules tend respectively to blueshift and redshift spectral lines. As a consequence of the larger flux carried by hot granules, the disk-integrated spectral line appears blueshifted (this effect is generally called *convective blueshift*). Stochastic variations of the granulation process induce $m\,s^{-1}$-RV fluctuations for solar-like stars (e.g., Dumusque et al., 2011b; Meunier et al., 2017). The amplitude of these signals scales with the velocity at which the convection operates. M dwarfs exhibit a significantly slower convection than their solar counterparts and therefore lower convective blueshifts and RV pertubations (Meunier et al., 2017; Baroch et al., 2020).

1.4.2 Modeling and filtering techniques

Accurately filtering stellar activity RV signals is one of the main challenges faced by high-precision velocimetry. In particular, the surface distribution of bright and dark features being unresolved, the resulting RV signals cannot be fitted using deterministic models. During the last decades, different techniques have been implemented to get rid of rotationally-modulated activity RV signals in observations (see Dumusque et al., 2017, for an overview). In short, one can distinguish between (i) multiple sine-wave fits to the RV data at the stellar rotation period, (ii) methods using correlations between the stellar activity RV curve and planet-independent activity indicators (Queloz et al., 2001; Boisse et al., 2009; Aigrain et al., 2012; Hébrard et al., 2014), (iii) data-driven methods aimed at using statistical properties of the stellar activity RV curve to filter it (using red-noise models or Gaussian Process Regression; e.g., Tuomi et al., 2013; Feroz & Hobson, 2014; Haywood et al., 2014; Rajpaul et al., 2015; Faria et al., 2016) and (iv) methods using the different sensitivities of spectral lines to stellar activity in order to minimize its RV contribution (Anglada-Escudé & Butler, 2012; Dumusque, 2018). We detail below methods (ii) and (iii) that we use in this manuscript.

Activity indicators

Stellar activity indicators have been used to constrain activity RV jitter since the beginning of the velocimetric search for exoplanets. Contrary to planet-induced Doppler shifts, brightness features at the stellar surface distort spectral lines. Quantities related to the shape of the average line such as its width (or FWHM) and asymmetry (measured by the bisector inverse slope; see Section 3.2.4) are thus often used to characterize stellar activity (e.g., Queloz et al., 2001, 2009). The stellar photometric curve (and its modulation by spots) comes naturally as an indicator of activity, especially if contemporaneous photometric observations are available (Aigrain et al., 2012; Haywood et al., 2014). Optical chromospheric emission is known to be well-coupled to bright and dark features in the case of the Sun. For active low-mass stars, the emission fluxes of a few resonant lines such as Ca II H & K, He I D3, Na I D1 & D2 and Hα correlate with other activity indicators like X-ray coronal emission as well as photometric and RV signals, and are thus widely used to model the activity jitter of stars of various spectral types (e.g., Bonfils et al., 2007; Boisse et al., 2009; Gomes da Silva

et al., 2011). The longitudinal magnetic field measured from circularly-polarized Zeeman signatures has also been shown to be a reliable indicator of the rotation period of active stars (Donati et al., 1997, 2006c; Hébrard et al., 2016). Directly filtering stellar activity RV signals using linear correlations with ancillary indicators is however risky as the sensitivity of these indicators to stellar activity might vary from one indicator to the other (Hébrard et al., 2016; Haywood et al., 2020). On the other hand, these indicators provide complementary information on the stellar activity that can be used as a prior for modeling the RV jitter.

Gaussian-Process Regression

More recently, Gaussian Process Regression (GPR; Rasmussen & Williams, 2006) demonstrated its ability to accurately model stellar activity RV signals (Haywood et al., 2014; Rajpaul et al., 2015; Jones et al., 2017). In short, the stellar activity RV signal $\boldsymbol{V_j}$ is modeled by a Gaussian Process (GP), i.e., by a collection of random variables drawn from a joint centered Gaussian distribution of covariance matrix $\boldsymbol{K}$. In other words, $\boldsymbol{V_j}$ is regarded as a correlated noise (or red noise) entirely defined by the statistical properties imprinted in the GP covariance matrix. From a given matrix $\boldsymbol{K}$, one can compute the mean value and dispersion of each random variable of the GP and thus predict the value of the stellar activity RV signal with its uncertainty at each time of observation (see the detailed explanation in Appendix A.3). The difficulty of GPR is that $\boldsymbol{K}$ is unknown and one must assume a covariance kernel k adapted to the description of the signal that we want to model. This kernel is often described by a certain number of so-called hyperparameters $\boldsymbol{\theta}$ estimated in the Bayesian framework through Markov chain Monte Carlo (MCMC) processes (see Appendix A.3). Activity-driven RV variations follow a pattern modulated by stellar rotation which evolves according to the growth and decay of surface features. This pattern has been shown to be well described by quasi-periodic covariance kernels (see Eq. 2.5 and Haywood et al., 2014; Delisle et al., 2018) even though other types of kernels are sometimes preferred (e.g., Hara et al., 2020). GPs provide a very flexible framework for performing Bayesian inference of stochastic signals of unknown functional form. This flexibility is controlled by the prior densities assumed on the hyperparameters which ensure that the GP fit to the stellar activity signal remains physically realistic. In particular, ancillary activity indicators can be included in the GP modeling to guarantee that the latter focuses on stellar activity-driven variations and leaves potential planet Doppler shifts intact (Rajpaul et al., 2015; Jones et al., 2017).

Doppler imaging and Zeeman-Doppler imaging

Another way to model activity-driven RV variations is to investigate feature-induced distortions on the average stellar line profile. The average line profile of fast rotators (i.e., of $v \sin i \gtrsim 10\,\mathrm{km\,s^{-1}}$) is dominated by stellar rotation. A given brightness inhomogeneity at the stellar surface occults a small fraction of the rotational RV field of the stellar surface. As a consequence, the distortion induced by this inhomogeneity on the disk-integrated line profile is located at the rotational RV of the feature at the stellar disk. Doppler imaging (DI; Vogt & Penrod, 1983; Vogt et al., 1987) is a technique using the RV dependence of feature-induced distortions to invert a time series of disk-integrated line profiles into a distribution of brightness inhomogeneities at the stellar surface. This problem is ill-posed as several brightness topologies can fit equally-well a set of observations. This degeneracy is raised by choosing the maximum-entropy solution, i.e., the one which contains the least information content (Skilling & Bryan, 1984). From a given maximum-entropy brightness map, one can compute a set of synthetic line profiles (using the forward approach described in Appendix A.1.1) whose RVs are used to filter stellar activity RV contributions. The application of this method to two wTTSs, V830 Tau and Tap 26, enabled the detection of hJs around these stars (Donati et al., 2016; Yu et al., 2017). Adapting this method to slow rotators is challenging

as feature-induced distortions are no longer resolved on the line profile. However, methods aimed at reconstructing the spot distribution at the surface of stars with $v \sin i$ as low as $1\,\mathrm{km\,s^{-1}}$ have recently yielded promising results (Hébrard et al., 2016) which are further explored in Chapter 3.

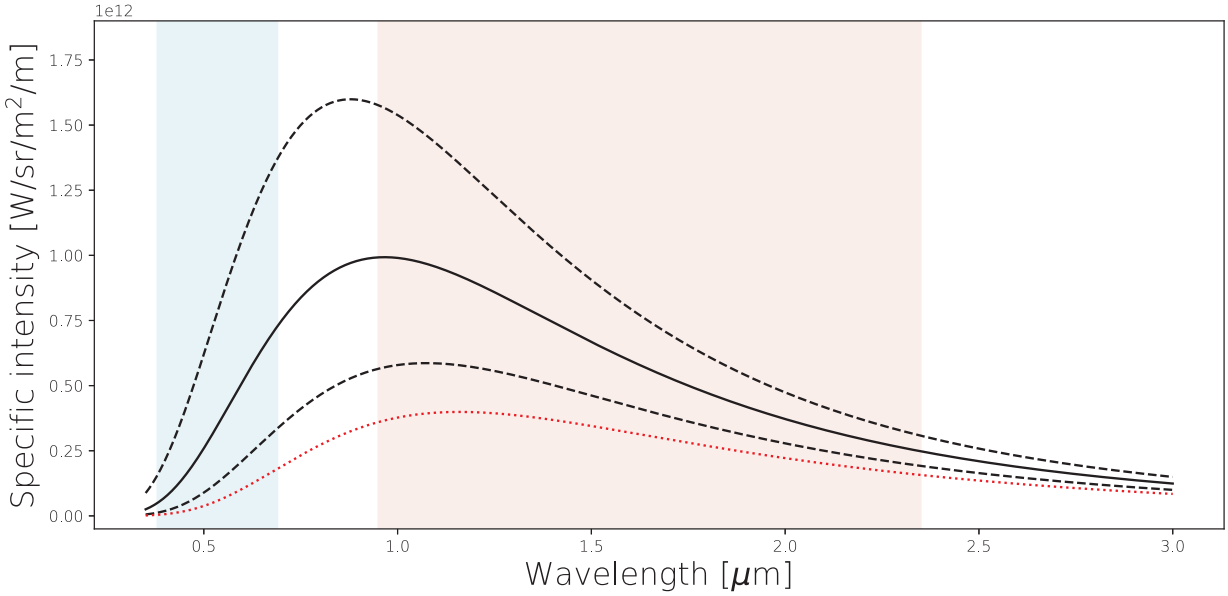

Figure 1.14 – Distribution of specific intensities of a star of effective temperature 3000 K (mid-M dwarf; black solid line) and 2500 K (ultra-cool M dwarf; red dotted line). The two black dashed lines show the distribution of specific intensities within spots and plages at the photosphere of the mid-M dwarf (respective effective temperatures of ±300 K relative to the quiet photosphere Berdyugina, 2005). The blue and red vertical bands indicate respectively the HARPS and SPIRou spectral ranges.

1.5 Observing M dwarfs and young stars with nIR velocimeters

Observing in the near-infrared (nIR; $JYHK$ spectral bands), where both M dwarfs and young PMS stars emit most of their light, is crucial to assess the potential presence of planets around them. Another advantage of observing in the nIR, is the decrease in the contrast of dark and bright features at the stellar photosphere from visible to nIR wavelengths (see the illustration in Figure 1.14), which is expected to lower the amplitude of the stellar activity RV signals, making it easier to disentangle planetary and stellar activity RV contributions (Mahmud et al., 2011; Crockett et al., 2012). As a consequence, the past few years have witnessed a flowering of nIR high-precision velocimeters[10] aimed at searching for planets around these types of stars. For example, iSHELL at the NASA IRTF (YJH and LM bands, $\mathscr{R} = 75\,000$; Rayner et al., 2012), CARMENES at the Calar Alto observatory ($VYJH$ bands, $\mathscr{R} = 80\,000$; Quirrenbach et al., 2014), IRD at the SUBARU telescope atop Mauna Kea (YJH bands, $\mathscr{R} = 70\,000$; Kotani et al., 2014), HPF at the 10-m Hobby Ebberly telescope (zYJ bands, $\mathscr{R} = 50\,000$; Mahadevan et al., 2014), GIANO at Telescopio Nazionale Galileo ($YJHK$ bands, $\mathscr{R} = 50\,000$; Claudi et al., 2017), SPIRou at the Canada-France-Hawaii telescope (CFHT; $YJHK$ bands, $\mathscr{R} = 70\,000$; Donati et al., 2018, 2020a) and its upcoming twin SPIP at Pic du Midi Observatory[11], or soon NIRPS at La Silla Observatory (YJH bands, $\mathscr{R} = 100\,000$; Wildi et al., 2017; Bouchy et al., 2017) are expected to revolutionize our knowledge of M dwarfs and their close-in planets.

[10] See the list of nIR high-precision velocimeters in https://carmenes.caha.es/ext/instrument/index.html.
[11] https://tbl.omp.eu/instruments/spip/

1.5.1 SPIRou: un spectropolarimètre infrarouge

Figure 1.15 – Presentation of the SPIRou instrument. *Top left:* SPIRou optical bench before its first cryogenic cycle (courtesy: S. Chastanet and the SPIRou team, February 2018). *Top right:* Logo of SPIRou (and SPIP) projects. *Bottom left:* Picture of the CFHT (courtesy: S. Chastanet and the SPIRou team, February 2018). *Bottom right:* Comics of the SPIRou instrument (courtesy: Jean-Yves Duhoo; see the full comic strip in http://spirou.irap.omp.eu/Gallery2/Comics).

Instrument description

SPIRou[12] (SpectroPolarimètre InfraRouge; see Donati et al., 2018, 2020a, for complete reviews of the instrument capabilities and related science, and the illustrations shown in Figure 1.15) is a nIR high-resolution spectropolarimeter and high-precision velocimeter located at the CFHT atop Mauna Kea. SPIRou is composed of three main units: the Cassegrain module, the calibration unit and the spectrometer (see the computer-aided design views of the modules in Figure 1.16). The light incoming from the telescope reaches first the Cassegrain module featuring an atmospheric dispersion corrector, a tip-tilt plate (to stabilize the image of the star at the instrument aperture), and the achromatic polarimeter that splits the incoming light into two beams of orthogonal polarization (see Section 3.2.1). The two polarized beams are conveyed to the cryogenic spectrograph using fluoride fibers (Micheau et al., 2018). The spectrograph is located in a vacuum vessel stabilized in temperature at 75 K to the mK level (Reshetov et al., 2012). The two science beams are dispersed by the échelle spectrograph (see the optical design shown in Figure 1.6 and Thibault et al., 2012, for more details), before being acquired by a H4RG detector (Artigau et al., 2018). Simultaneous calibration, carried out using both a stabilized Fabry-Perot etalon and a U/Ne hollow-cathode lamp fiber-linked to the spectrograph, delivers a RV reference precise at 0.1-0.2 $\mathrm{m\,s^{-1}}$ (see Donati et al., 2020a, and Hobson et al., in prep.). Additionally, the recently installed laser frequency comb has

[12] http://spirou.irap.omp.eu/

the potential to decrease the RV calibration error down to the $\mathrm{cm\,s^{-1}}$ level (Probst et al., 2020), once technical limitations related to the adaptation of the module to SPIRou spectral domain have been addressed (Donati et al., 2020a).

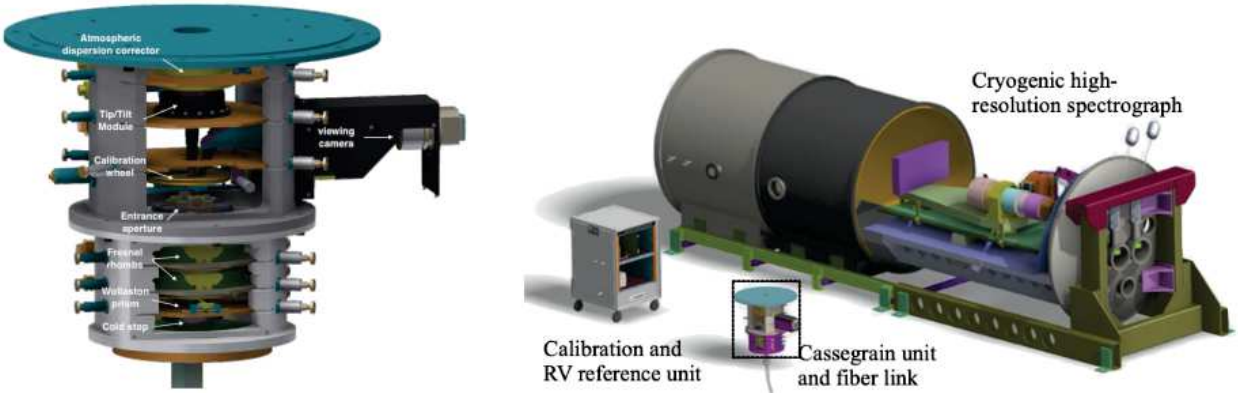

Figure 1.16 – Computer-aided design (CAD) views of of the main SPIRou units (right panel) and zoom on the Cassegrain unit (left panel). The optical view of SPIRou is shown

SPIRou has been developed in the framework of an international collaboration (involving mostly France, Canada, Hawaii, Taiwan, Brazil, Portugal and Switzerland). After its validation at OMP/IRAP, it was installed at the CFHT in February 2018 (see the pictures in Figure 1.15), where it was extensively tested until passing its acceptance review in January 2019 (first light in mid 2018).

Performances

SPIRou provides a continuous spectral coverage of the $YJHK$ bands (0.95 to 2.50 μm, 49 diffraction orders) at a resolving power of $\mathscr{R} = 70 \pm 3\mathrm{k}$ (pixels of $2.28\,\mathrm{km\,s^{-1}}$; see Donati et al., 2020a). It currently reaches a peak S/N per pixel (i.e., in the H band around 1.8 μm) of 110 at a magnitude $H = 8$ for a M4 dwarf in an exposure time of 300 s[13]. SPIRou's relative velocimetric precision is currently about 1-2 $\mathrm{m\,s^{-1}}$ for a mid-M dwarf at a peak S/N of 200 (Donati et al., 2020a). The RV error budget is dominated by instrumental effects (e.g., light injection stability and, to a lesser extent, instrument intrinsic stability), regularly reduced with instrument upgrades, and the pollution from telluric lines which is a very active research topic for high-precision nIR velocimetry (see Section 1.5.3).

1.5.2 The SPIRou legacy survey and science goals

SPIRou's main science goals are outlined by the SPIRou Legacy Survey (SLS), a 300-night large program spread over ∼4 yr involving a large international consortium of 150 scientists. The SLS is divided into five components, called work packages (WPs), associated to different key questions regarding M dwarfs and low-mass PMS stars:

- **WP 1:** The planet search component of the SLS (SLS-PS; 150 nights) consists in carrying out a blind search for planets around about 70 nearby weakly-active M dwarfs selected from the input catalog of Moutou et al. (2017) and Fouqué et al. (2018). The goal of the SLS-PS is to unveil a statistically significant number of planets in order to understand how planet formation and evolution operate at the lower end of the main-sequence, and constrain the occurrence rates of planets around mid to late M dwarfs. Realistic Monte-Carlo simulations

[13] See the SPIRou exposure time calculator: http://etc.cfht.hawaii.edu/spi/

of the nearby M dwarf population and properties have shown that SPIRou should be able to detect about 60 new exoplanets including 25 Earth-mass planets, 6 of which orbiting in the HZ of their host stars (Cloutier et al., 2018). These planets will be photometrically monitored from the ground with ExTrA (Bonfils et al., 2015) or NGTS (Wheatley et al., 2018) in order to identify potential transit events and thereby pin down the most exciting targets for a characterization with the JWST and the ELTs.

- **WP 2:** The transit follow-up component (SLS-TF; 75 nights) is dedicated to the observations of ∼20 exciting transiting planets (around M dwarfs and PMS stars) unveiled with space-based telescopes like TESS (or Kepler/K2, to a lesser extent) and ground-based facilities (e.g., ExTrA, NGTS, TRAPPIST/SPECULOOS, MEarth). SPIRou will provide a RV follow-up of these targets in order to pin down the planet mass, which is a key parameter for atmospheric characterizations (Batalha et al., 2019), and constrain the MR diagram (thus inner structure) of young and low-mass planets. Moreover, velocimetric observations of the planetary transits will provide measurements of the projected spin-orbit obliquity of the planet orbits (through the RM effect), yielding constraints on the formation and evolution processes of the star-planet systems (Winn & Fabrycky, 2015). Finally, spectroscopic observations of planetary transits and secondary eclipses will enable to probe the chemical abundances, temperature, and even dynamical processes in the planet atmospheres, improving thereby our knowledge of planetary atmospheres in preparation for future missions like JWST and ARIEL (Madhusudhan, 2019).
- **WP 3:** The Magnetized star/planet formation (SLS-MP; 75 nights) component is aimed at using SPIRou spectropolarimetric capabilities to investigate the impact of the magnetic field on star/planet formation. The goal of this program is to carry out a spectropolarimetric monitoring of ∼55 nearby PMS stars (of classes I, II, and III), reconstruct the surface distribution of the large-scale magnetic field using ZDI, search for hJs in their vicinity (similarly to Donati et al., 2016; Yu et al., 2017) and, ultimately, improve our understanding of how stellar dynamo processes and magnetospheric accretion behave throughout star/planet formation.

1.5.3 The challenges of nIR spectroscopy

Despite the advantages of nIR observations for the search for planets around M dwarfs and low-mass PMS stars, nIR high-precision spectroscopy faces various challenges that need to be addressed in order for this technique to be used to its full potential. This first of these challenges is on the instrumental side. For example, the development of SPIRou required the development of state-of-the-art devices (e.g., 4k×4k H4RG detector, high-throughput fibers with large scrambling, ZnSe rhombs for polarimeters, calibration lamps are etalons, thermal stabilization solution) on which considerable efforts have been invested over the past decade. Although minor instrumental upgrades are expected to increase the instrument RV precision (e.g., use of the laser frequency comb, increase in the fiber scrambling), SPIRou is now operational and the main challenges lie on the post-analysis side.

Another major challenge of nIR high-precision velocimetry is to correct for the forest of telluric absorption and emission lines. As shown in Figure 1.17, the whole SPIRou spectral range is affected by Earth atmosphere absorption lines (typically H_2O, CO_2, CH_4, O_2), especially in the water absorption bands where telluric absorption largely blocks the stellar light. The Earth atmosphere contribution has to be accurately filtered from high-resolution spectra since it could bias the RV measurement process (Moutou et al., 2020) and yield spurious signatures in exoplanet atmospheric characterizations (Brogi et al., 2018). Filtering this contribution is however challenging especially as the depth of H_2O absorption lines relies on the water vapor content along the line of sight which may vary from one observation to the next. For SPIRou, nightly observed telluric standards (generally hot stars) are stored in a data base of telluric spectra covering a wide range of atmospheric

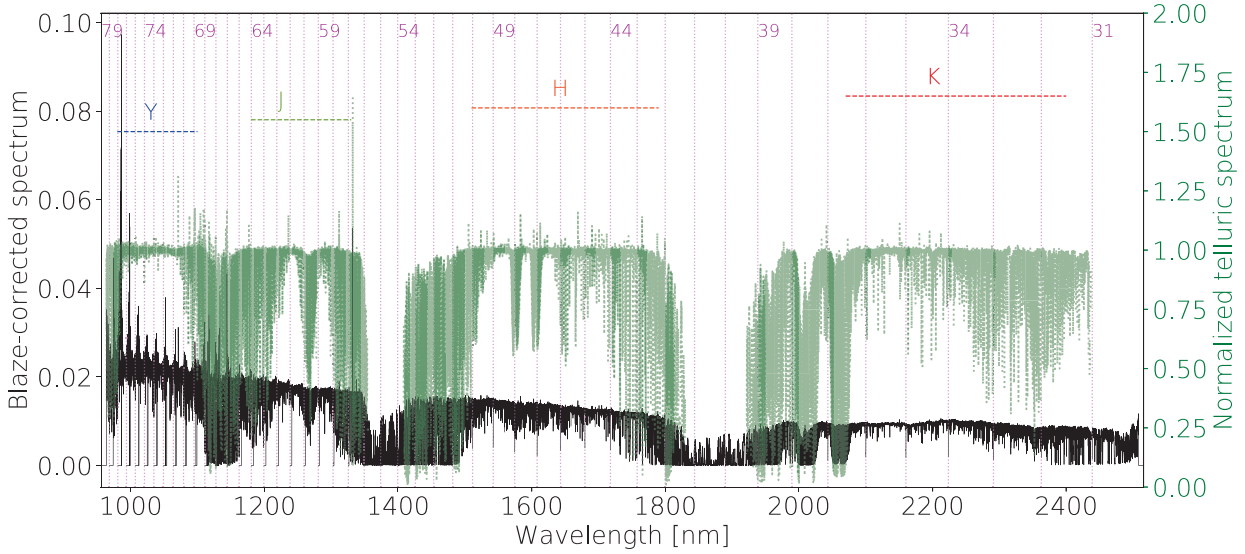

Figure 1.17 – Example of a blaze-corrected SPIRou spectrum (black lines) of the K2 star HD 189733 obtained in September 2018. For comparison, the Earth atmosphere spectrum, computed using the method presented in Artigau et al. (2014), is shown in green (note that the associated Y-axis is shown to the right of the plot). The gaps in the Earth atmosphere spectrum correspond to regions so polluted by telluric absorption lines that no reliable estimate of the spectrum could be made using the method of Artigau et al. (2014). The $YJHK$ bands are indicated in blue, green, orange and red at the top of the plot. Finally, the starting wavelengths of each SPIRou order are indicated by the vertical magenta dashed lines and the corresponding order number is given for every five orders.

conditions. The telluric contamination spectrum associated to each SPIRou observation is then obtained by matching a master telluric spectrum, computed from the library of standard telluric spectra (using a principal component analysis-based approach; Artigau et al., 2014), to the science spectrum. Residuals of telluric correction contributes to $\sim$1 m s^{-1} to the RV error budget (Donati et al., 2020a, Artigau et al., in prep.).

1.6 Overview of the Ph.D. Thesis

The goal of this Ph.D. thesis is to investigate the magnetic activity of M dwarfs and low-mass PMS stars, as well as model their activity-driven RV signals in order to prepare for future search and characterization of exoplanets with SPIRou. As this project took place a year before the first SPIRou observations, I started by conducting simulations of nIR RV follow-up of representative active M dwarfs and PMS stars hosting transiting planets. The goal was to assess (i) the evolution of stellar activity RV signals from visible to nIR wavelengths in presence of magnetic fields, and (ii) the impact of these signals, but also of the observational strategy and noise level, on the planet detection. These simulations are described in Chapter 2. In Chapter 3, I describe spectropolarimetric analyses of a versatile range of low mass stars (i.e., AU Mic, Proxima Centauri, EPIC 211889233 and V471 Tau) using different instruments (SPIRou, HARPS-Pol, and ESPaDOnS), in order to better understand their magnetic activity. The use of SPIRou velocimetric capabilities to measure the mass of the young Neptune-sized planet AU Mic b is then described in Chapter 4. On another front, SPIRou, thanks to its high-resolution spectroscopic capabilities, has the potential to probe the atmosphere of transiting giant planets. In Chapter 5, I present a preliminary benchmark analysis of the atmosphere of the hot Jupiter HD 189733 b with SPIRou. I finally conclude and outline the perspectives of the thesis in Chapter 6.

2 | Simulating nIR RV observations of low-mass stars with transiting planets

Contents

2.1 Motivation and strategy

2.1.1 Motivation

The central goal of the SPIRou Legacy Survey - Transit Follow-up (SLS-TF) is to carry out nIR RV observations of the most interesting transiting planets around late K and M dwarfs unveiled from various ground- and space-based surveys (e.g., K2, TESS, ExTrA, NGTS, MEarth, TRAPPIST). Transit photometry yields key properties on planet orbits (e.g. orbital periods and phases), that can be used to optimize the sampling strategy of velocimetric follow-ups (Ford, 2008; Burt et al.,

2018; Damasso et al., 2019) and enhance the significance of the planet detection in the RV time-series. Coming up with dedicated sampling strategies for the different types of targets within the SLS-TF is all the more important as SPIRou faces a strong time allocation pressure (due to different instruments in use at CFHT). Hence the need, for each target of the SLS-TF, to find a balance between maximising the accuracy on the planet mass measurement and minimising the telescope time.

The targets of the SLS-TF are mainly (i) M dwarfs hosting Earth-sized planets (e.g., Kepler-138, TRAPPIST-1; Rowe et al., 2014; Gillon et al., 2017), and (ii) PMS stars hosting transiting planets (e.g., K2 33, V1298 Tau; David et al., 2016; Mann et al., 2016; David et al., 2019a,b). Precise planet mass measurements for both types of targets are crucially needed to constrain the MR diagram of Earth-mass planets and young close-in giants. The SLS-TF targets exhibit stellar activity RV signals whose amplitude in the optical domain exceeds that of the planet-induced RV signatures, making them extremely challenging to filter. Observing in the nIR rather than in the optical reduces the brightness contrast of features at the stellar surface, on the one hand, but increases their sensitivity to surface magnetic fields, on the other hand. As shown in Chapter 1, these two effects have opposite consequences on the amplitude of stellar activity RV signals at nIR wavelengths, the first tending to reduce it (Mahmud et al., 2011; Crockett et al., 2012) whereas the second is expected to increase it (Reiners et al., 2013; Hébrard et al., 2014). However, the way the stellar activity RV curves vary between optical and nIR domains is not well known, especially for M dwarfs, and is worth detailed simulation studies as it will play a major role in the choice of the follow-up sampling strategy.

In this chapter, I detail simulations of nIR velocimetric observations of TRAPPIST-1 and K2-33, two typical representatives of the M dwarfs and PMS targets of the SLS-TF. The application of the methods developed for these simulations to the planet-hosting pTTS AU Mic has made it possible to obtain 7 h of SPIRou telescope time dedicated to the RV follow-up of the star. The systems are described below in Sections 2.1.2, 2.1.3 and 2.1.4. I then detail the method implemented to carry out realistic simulations of planet mass measurements in Section 2.2, before presenting the main results and their implications in Section 2.3.

2.1.2 TRAPPIST-1

TRAPPIST-1 is an ultracool dwarf hosting at least seven transiting Earth-sized planets, including three HZ planets (Gillon et al., 2017). Since the first detection of transiting planets around the star with the ground-based TRAPPIST-South telescope (Gillon et al., 2016), an extensive photometric monitoring of the system with, among others, K2 and Spitzer space telescopes, allowed to obtain precise estimates of the planet orbital parameters and radius (Gillon et al., 2017; Luger et al., 2017; Delrez et al., 2018; Ducrot et al., 2020). The uniqueness of the TRAPPIST-1 system paves the way for exciting studies on diverse topics. First, this super compact system forms the longest resonant chain known to date (Luger et al., 2017; Papaloizou et al., 2018), which gives the opportunity to perform detailed studies of the formation and migration of the planets within the protoplanetary disc (e.g., Ormel et al., 2017; Schoonenberg et al., 2019; Coleman et al., 2019). Moreover, the strong mutual interactions between the planets result in large TTVs, making it possible to estimate the planet masses (Grimm et al., 2018; Agol et al., 2020). The measured masses suggest rocky compositions for the planets with an enrichment of volatiles compare to the Earth (Grimm et al., 2018; Dorn et al., 2018). Second, the star exhibits magnetic activity evidenced by 10 mmag-quasi-perdiodic fluctuations modulated at $P_{\rm rot} = 3.3$ d in its K2 light curve (Luger et al., 2017), frequent flaring events (Vida et al., 2017), and persistent XUV emission (Wheatley et al., 2017), that have likely impacted the planet atmospheres, especially during the PMS phase (see Bolmont et al., 2017; Bourrier et al., 2017; Fleming et al., 2020; Turbet et al., 2020). Finally, the TRAPPIST-1 planets

are currently among the best Earth-sized candidates for a nIR atmospheric characterization in transmission with the JWST (using NIRSPEC; e.g., Barstow & Irwin, 2016; Fauchez et al., 2019; Lustig-Yaeger et al., 2019; Gillon et al., 2020). In particular, TRAPPIST-1 e is one of the most likely planet to harbor liquid water on its surface (Wolf, 2017; Turbet et al., 2018; Fauchez et al., 2019). The main properties of the planetary system and its host star are given in Table 2.1.

As a magnetically active star hosting well constrained transiting Earth-sized planets, TRAPPIST-1 is representative of the SLS-TF targets. The system itself is currently observed with SPIRou in order to provide direct estimates of the planet masses. The latter will indeed play a crucial role in JWST characterizations of planetary atmospheres (Batalha et al., 2019), and TTV mass estimates remain strongly model-dependent and often differ from their velocimetric counterparts (Mills & Mazeh, 2017). Providing an independent mass measurement of just one planet of the system would already allow to confirm or adjust the TTV mass estimates and is worth the observing time. I thus simulated SPIRou RV observations of this system as a typical SLS-TF target, but also to assess our ability to provide a direct mass measurement of at least one planet of the system.

Table 2.1 – Main properties of the TRAPPIST-1 (columns 2 and 3), K2-33 (column 4 and 5) and AU Mic (columns 6 and 7) systems considered in these studies. We taken from the literature, the reference of each parameter is indicated on the right on its value†. For TRAPPIST-1 and K2-33, the projected rotational velocity and surface gravity are respectively computed from the stellar radius, $P_{\rm rot}$, and planet transit inclination, and from the mass and radius of the star. For TRAPPIST-1, we simply give the minimum and maximum values of the parameters of the planet in the system. In the last 6 lines, we give the evolution parameters of the surface feature properties used to generate the stellar activity curve using the method described in Section 2.2.1.

Properties	TRAPPIST-1	Reference	K2-33	Reference	AU Mic	Reference
Stellar parameters						
Spectral type	M8	Li06	M3.3	M16	M1	Ke89
Distance [pc]	12.4299 ± 0.0187	Gaia18	139.8 ± 1.5	Gaia18	9.7248 ± 0.0046	Gaia18
Age [Gyr]	7.6 ± 2.2	Bu17	$8\text{-}11 \times 10^{-3}$	D16; M16	$22 \pm 3 \times 10^{-3}$	Ma14
Effective temperature $T_{\rm eff}$ [K]	2557 ± 47	D20	3475 ± 100	D16; M16	3700 ± 50	Af19
Stellar mass [$M_\odot$]	0.0898 ± 0.0024	D20	0.31-0.56	D16; M16	0.50 ± 0.03	P20
Stellar radius [$R_\odot$]	0.1197 ± 0.0017	D20	1.1 ± 0.1	D16	0.75 ± 0.03	P20
Surface gravity [log g]	5.234 ± 0.003	–	3.8-4.1	D16; M16	4.39 ± 0.03	–
Rotation period $P_{\rm rot}$ [d]	3.30 ± 0.14	Lu17	6.3 ± 0.2	D16; M16	4.86 ± 0.01	P20
Projected rotational velocity [km/s]	1.84 ± 0.08	–	8.2 ± 1.8	M16	7.8 ± 0.03	–
Planet parameters						
Number of confirmed transiting planets	7	Gi17	1	D16; M16	1	P20
Planet orbital periods [d]	1.51 - 18.77	D20	5.425	D16; M16	8.46321 ± 0.00004	P20
SMA [au]	0.012 - 0.062	D20	0.053	D16; M16	$0.066^{+0.007}_{-0.006}$	P20
Planet radius [$R_\oplus$]	0.752 - 1.161	D20	4.7 ± 0.1	M16	4.2 ± 0.2	P20
Eccentricity	0.002 - 0.01	Gr18	–	–	$0.10^{+0.17}_{-0.09}$	P20
Transit inclination [°]	89.28 - 89.76	D20	$89.1^{+0.6}_{-1.1}$	M16	89.5 ± 0.4	P20
Planet mass [$M_\oplus$]	0.297 - 1.156	Gr18	–	–	< 58.3	P20
Feature properties in synthetic light curves						
Typical number of features	60	–	15	–	10	–
Apparition rate [d^{-1}]	6	–	0.15	–	0.125	–
Total lifetime [$P_{\rm rot}$]	$\mathcal{N}(3.0, 0.5)$	–	$\mathcal{N}(18.0, 0.5)$	–	$\mathcal{N}(18.0, 0.5)$	–
Effective temperature [$\pm T_{\rm eff}$]	$\mathcal{N}(\pm 150, 50)$	Ber05	$\mathcal{N}(\pm 450, 50)$	Ber05	$\mathcal{N}(\pm 600, 50)$	Ber05
Latitude	$\mathscr{U}$(-90°,90°)	–	$\mathscr{U}(-90°,90°)$	–	$\mathscr{U}(-90°,90°)$	–
$\log_{10}$ maximum size	$\mathcal{N}(-3.0, 0.3)$	–	$\mathcal{N}(-2.6, 0.3)$	–	$\mathcal{N}(-1.8, 0.3)$	–

† To gain some space in the table, we use aliases of the references. ***TRAPPIST-1:*** Li06, Gaia18, Bu17, D20, Lu17, Gi17, Gr18 and Ber05 stand respectively for Liebert & Gizis (2006), Gaia Collaboration et al. (2018), Burgasser & Mamajek (2017), Ducrot et al. (2020), Luger et al. (2017), Gillon et al. (2017), Grimm et al. (2018) and Berdyugina (2005). ***K2-33:*** D16 and M16 stand respectively for David et al. (2016) and Mann et al. (2016). ***AU Mic:*** Ke89, Ma14, Af19 and P20 stand respectively for Keenan & McNeil (1989), Mamajek & Bell (2014), Afram & Berdyugina (2019) and Plavchan et al. (2020b).

2.1.3 K2-33

K2-33 is a 8-11 Myr M3 PMS star located in the Upper Scorpius star forming region. The star was recently shown to host a 4.7-$R_\oplus$ close-in transiting planet (David et al., 2016; Mann et al., 2016, hereafter D16 and M16, respectively). The 80 d continuous K2 light curve of the star, from which the planet was unveiled, exhibits ∼3% fluctuations modulated at $P_{\rm rot} = 6.3$ d ($v \sin i = 8.2\,{\rm km\,s^{-1}}$) induced by active regions at the stellar surface, suggesting stellar activity RV signals of 100-200 $\rm m\,s^{-1}$ in the optical domain (M16), likely significantly larger than the semi-amplitude of the planet RV signature (likely $\lesssim 20\,{\rm m\,s^{-1}}$)[1]. As a consequence, and given the faintness of the star in the V band (∼14 in Kepler spectral domain; D16), any attempt to measure the planet mass with currently operating optical velocimeters is doomed. In contrast, K2-33 represents a target of choice for nIR high-precision velocimeters that will benefit from both its larger brightness in the nIR ($H = 10.3$; Cutri et al., 2003), and the likely weaker stellar activity RV signal. Besides, this star is a good representative of the PMS stars hosting transiting planets observable with SPIRou. Simulating SPIRou RV observations of K2-33 will therefore inform us about (i) the detectability of such planets in the nIR and (ii) potential optimal sampling strategies to maximise the precision on the planet mass while minimizing the telescope time.

2.1.4 AU Mic

AU Microscopii[2] (AU Mic, GJ 803) is an active nearby M1 dwarf located in the 22 Myr-old β Pictoris moving group (see Mamajek & Bell, 2014; Malo et al., 2014; Bell et al., 2015; Messina et al., 2016, and the detailed presentation of the star in Section 3.3.1). AU Mic is notorious for its intense magnetic activity evidenced by the 0.1 mag quasi-periodic photometric fluctuations modulated at a period of 4.86 d (e.g., Torres & Ferraz Mello, 1973; Rodono et al., 1986; Plavchan et al., 2020b) and frequent flaring events (e.g., Robinson et al., 2001; MacGregor et al., 2020). A close-in transiting Neptune-sized planet was recently unveiled from TESS and Spitzer observations of the star (see Plavchan et al., 2020b, and the planet properties listed in Table 2.1). In order to pin down the mass of AU Mic b, Plavchan et al. (2020b, hereafter P20) conducted a velocimetric follow-up of the star using HIRES and HARPS optical spectrometers and iSHELL nIR spectrograph. However, given (i) the high-amplitude activity-driven fluctuations in their RV time-series (dispersions of 175 and 115 $\rm m\,s^{-1}$ RMS in HIRES and HARPS RVs, respectively) and (ii) the sparseness of their sampling (∼75 data points collected on a ∼15 yr-period), P20 reported no more than an upper limit of $M_{\rm p} < 58.3\,M_\oplus$ (corresponding to $K_{\rm s} < 28\,{\rm m\,s^{-1}}$) for the mass of AU Mic b.

SPIRou appears well suited to provide precise RVs for as bright a star as AU Mic ($H = 4.831$). Moreover, nIR RV time-series of AU Mic were found to be 2 to 3 times less dispersed than their optical counterparts (dispersion of about 50 $\rm m\,s^{-1}$ rms in the nIR; Gagné et al., 2016; Plavchan et al., 2020b), making it easier to separate the stellar activity RV contribution from the planet signature. Conducting simulations of a RV follow-up of AU Mic with SPIRou will allow us to (i) assess the detectability of the close-in planet and (ii) pin down the number of observations needed to obtain an accurate measurement of the planet mass. The results of these simulations will be used as a basis of a Director's Discretionary Time (DDT) proposal aimed at observing the star with SPIRou.

[1] Assuming a Neptune density for K2-33 b, the semi-amplitude of the planet RV signature will be ∼20 $\rm m\,s^{-1}$. However, given the youth of the system, the planet is likely still contracting and, thus, less dense than Neptune.

[2] See the simbad page http://simbad.u-strasbg.fr/simbad/sim-id?Ident=%402356387&Name=V*+AU+Mic&submit=display+all+measurements#lab_meas

2.2 Method

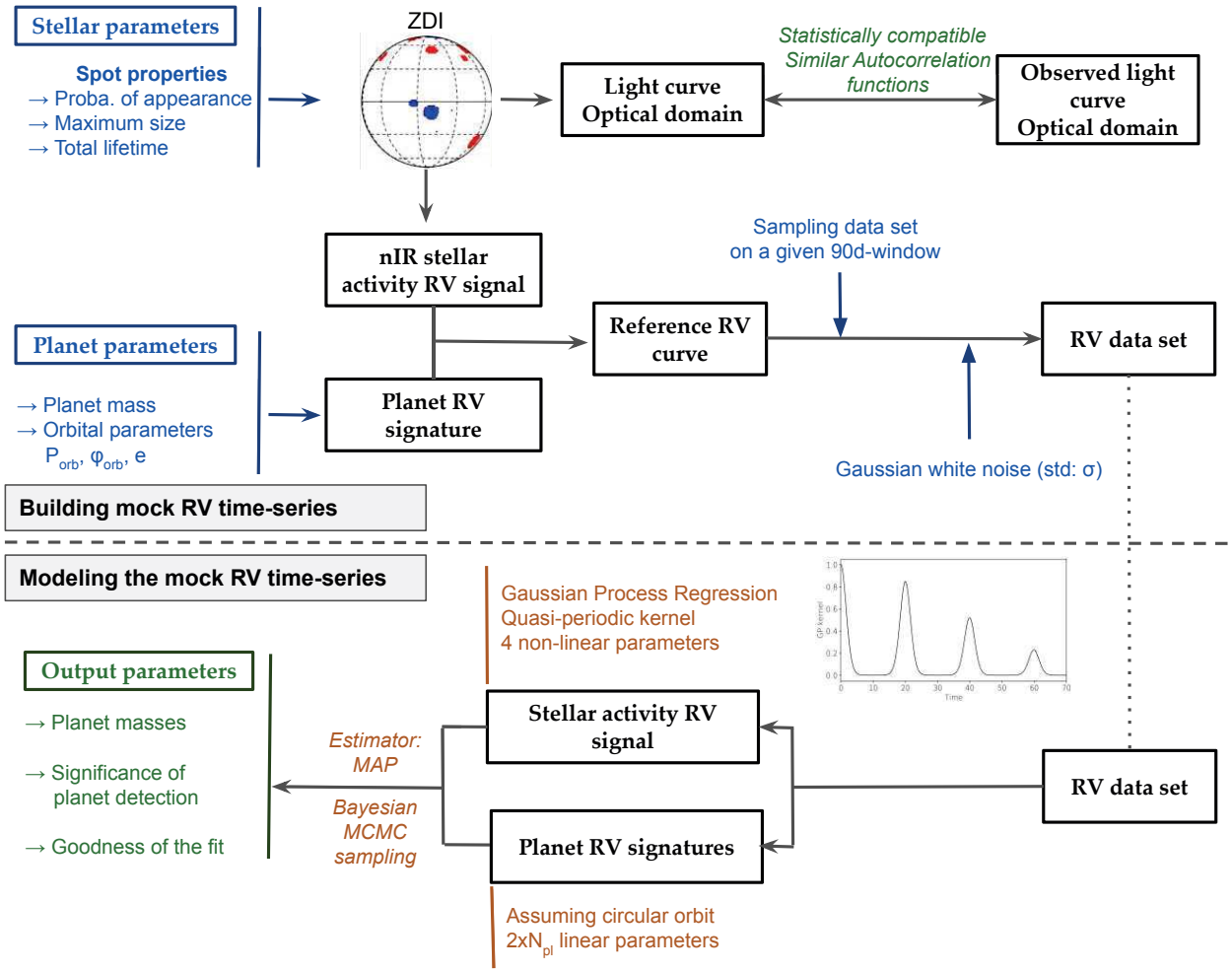

Figure 2.1 – Illustration of the procedure to simulate nIR velocimetric follow-up of transiting targets.

The procedure used to simulate nIR RV observations of transiting targets is illustrated in Figure 2.1. Note that this procedure is similar to that used in the SOAP/SOAP2.0 algorithms in the optical domain (Boisse et al., 2012; Dumusque et al., 2014). First of all, we need to generate a reference densely-sampled stellar RV curve containing both the expected planet signatures and a realistic nIR stellar activity signal. Mock RV time-series are then created by (i) sampling the reference curve according to various strategies and (ii) adding random noise to the resulting data sets. The second step consists in modeling each RV time-series in order to recover the planet mass and quantify the significance of the planet detection. By comparing how the recovered planetary signals depend on the observation scheme, stellar activity RV signals and level of white noise, we conclude on the best strategies for SPIRou to observe SLS-TF targets.

2.2.1 Generating realistic stellar activity RV signals

TRAPPIST-1, K2-33 and AU Mic were observed as part of K2 or TESS space-based missions, and, as a result, a nearly continuous densely-sampled light curve is available for each star. This curve encloses valuable information about the evolution properties of bright and dark features on the stellar photosphere. I present below a method to generate a stellar activity RV curve whose

statistical properties are consistent with those of the photometric curve of the star.

2.2.1.1 Modelling the stellar surface with ZDI

The quasi-periodic fluctuations in the light curves of the three stars of interest are induced by evolving dark and bright surface inhomogeneities, as introduced in Section 1.4.1.2. These inhomogeneities are expected to be found at all latitudes for both very-low-mass stars like TRAPPIST-1 (Delrez et al., 2018; Morris et al., 2018a; Ducrot et al., 2018) and young PMS stars like K2-33 and AU Mic (Strassmeier, 2009; Donati et al., 2014; Yu et al., 2017). The stellar brightness topology evolves over time as features appear, grow/decay, and disappear from the surface of the star. The time scale on which the distribution of inhomogeneities changes at the stellar surface corresponds to the time on which photometric and RV curves lose their coherence. In our case, we use the forward modeling approach of ZDI to model the surface of each star of interest and to compute the corresponding photometric and RV curves. Our ZDI code was adapted in order to include time-evolving surface features in the stettar model as described below.

In its forward modeling approach, ZDI (see the description Appendix A.1.1) samples the stellar surface into typically $N = 100\,000$ cells of identical projected area with crossing the meridian. Each cell n features a brightness factor relative to the quiet photosphere, b_n (1 for the quiet photosphere, > 1 for a brighter region and < 1 for a darker region), and a radial magnetic field $B_{\mathrm{r,n}}$. For a given configuration of the stellar surface (i.e., a given realisation of $\{b_n, B_{\mathrm{r,n}}\}_{n<N}$), ZDI computes a local intensity profile, $\boldsymbol{I_n}$, for each cell, using the Unno-Rachkovski analytical solution of the radiative transfer equation in a plane-parallel Milne–Eddington atmosphere, which depends, among others, on $B_{\mathrm{r,n}}$. Each local profile is then Doppler-shifted by $\Delta v_n = v \sin i \sin \phi_n \cos \theta_n$, where θ_n and ϕ_n are respectively the colatitude and the azimuth of cell n. To account for stellar limb darkening, the local profiles are weighted according to a linear law in $\cos\theta$. The local profiles are finally combined into a global Stokes I profile, $\boldsymbol{I}$, such that

$$\boldsymbol{I} = \sum_{n=0}^{N-1} b_n \boldsymbol{I}_n(\Delta v_n, B_{\mathrm{r,n}})[1 - \epsilon(1 - \cos\theta)], \tag{2.1}$$

where ϵ is the linear limb darkening coefficient. The RV of the star at any given rotational phase is finally measured by fitting a Gaussian profile to $\boldsymbol{I}$. For the same configuration of the stellar surface, it is also possible to compute the relative photon flux, F, using

$$F = \sum_{n=0}^{N-1} b_n[1 - \epsilon(1 - \cos\theta)]. \tag{2.2}$$

2.2.1.2 Generating realistic densely-sampled stellar activity RV curves

The synthetic star is assumed to rotate at a given rotation period P_{rot}. Using an arbitrarily low time step of 0.01 d (14.4 min), we use the process detailed above to generate densely-sampled photometric and RV curves for the star for both optical and nIR domains. At each time step t, a new bright or dark feature is added to a random location at the stellar surface with a probability $p(t)$, drawn from a Bernoulli density law of parameter p. The newly-created feature is randomly chosen to be either dark or bright. We regard both the quiet stellar photosphere and the feature as black bodies emitting respectively at T_{eff} and $T_{\mathrm{eff}} \pm \Delta T$, where T_{eff} is the effective temperature of the star and, ΔT, the temperature contrast of the feature, obtained from Berdyugina (2005)[3]. The

[3] In practice, ΔT is drawn from from a Gaussian density low centered on the value reported in Berdyugina (2005) and using a typical standard deviation of 50 K.

resulting brightness contrast relative to the quiet photosphere at a wavelength λ, b_λ, is computed as the ratio of the spectral irradiance $\mathscr{B}$ within the feature to that of the quiet photosphere:

$$b_\lambda = \frac{\mathscr{B}(\lambda, T_{\rm eff} \pm \Delta T)}{\mathscr{B}(\lambda, T_{\rm eff})}. \tag{2.3}$$

The spot/plage is assumed to have a circular shape at the surface of the star. Its radius is set to zero when it appears at the stellar surface, and linearly increases until reaching its maximum size, $s_{\rm max} \sim \log \mathscr{N}(s_{\rm r}, s_{\rm r}/10)$, where $s_{\rm r}$ is a generic parameter that controls the average maximum relative area of the features in our simulation. Then, the radius of the circular feature linearly decays until the spot/plage is removed from the stellar surface. When a long-lived spot appears at the surface of the Sun, it first rapidly grows from the emergence of magnetic flux that increasingly inhibits the local convection and, then, undergoes a slower decay controlled the diffusion of the magnetic flux (Meyer et al., 1974; Howard, 1992). We thus impose the growing phase of surface features to last one third of their lifetime, which turns out to be a reasonable assumption given Dumusque et al. (2011c). Starspot lifetimes appear roughly proportional to their maximum areas for late-type and PMS stars (e.g. Hall & Henry, 1994; Hatzes, 1995; Berdyugina, 2005; Strassmeier, 2009). We thus rescale the total lifetime of the feature, $t_{\rm f}$, by $s_{\rm max}/s_{\rm r}$ in our simulation. The code also includes differential rotation and latitudinal/longitudinal migration of features due to magnetic cycles.

We simultaneously generate stellar photometric and RV curves over a 400-500 d period, and remove a burn-in period significantly longer that the typical feature lifetime (100 d and 200 d for TRAPPIST-1 and K2-33/AU Mic, respectively), so that the stellar surface is more or less stable in time, with the disappearance of old features being compensated by the appearance of new ones. The global parameters of the simulation, p, $s_{\rm r}$, and $t_{\rm f}$, are tuned so that the synthetic light curve in the optical domain statistically mimics the observed light curve of the star (see the following paragraph). From this synthetic curve, we select the 90 d-period during which the amplitude of the fluctuations is closest to that of the observed light curve. The corresponding 90 d-nIR RV curve, which originates from the same realization of features at the stellar surface, is taken as the reference stellar activity RV curve for our simulations.

2.2.1.3 Measuring the statistical properties of light-curves

As the distribution of features at the stellar surface is unknown, directly comparing our synthetic light curves to the observed one would be pointless. However, activity-induced fluctuations in photometric curves can be seen as the combination of roughly similar quasi-periodic patterns induced by evolving dark and bright inhomogeneities at the stellar photosphere. Comparing the average feature-induced patterns of synthetic and observed light curves is an effective way to ensure that these curves share similar statistical properties.

We first compute the auto-correlation function (ACF) of the light curve. For a discrete data set $\boldsymbol{y}$, the ACF between two positions m and n is given by (Edelson & Krolik, 1988):

$$a_{m,n} = \frac{(y_m - \bar{y})(y_n - \bar{y})}{\sigma_m \sigma_n}, \tag{2.4}$$

where σ_n is the 1σ-uncertainty on y_n, and $\bar{y}$ is the inverse-variance weighting average of the data set. As an example, the ACFs of TRAPPIST-1 and K2-33 light curves are shown in top panels of Figure 2.2. They both feature quasi-periodic shapes that enclose information on the average evolution properties of the features at the stellar surface. The position of the second most prominent peak of the ACF yields the recurrence time scale of the signal, which corresponds, here, to

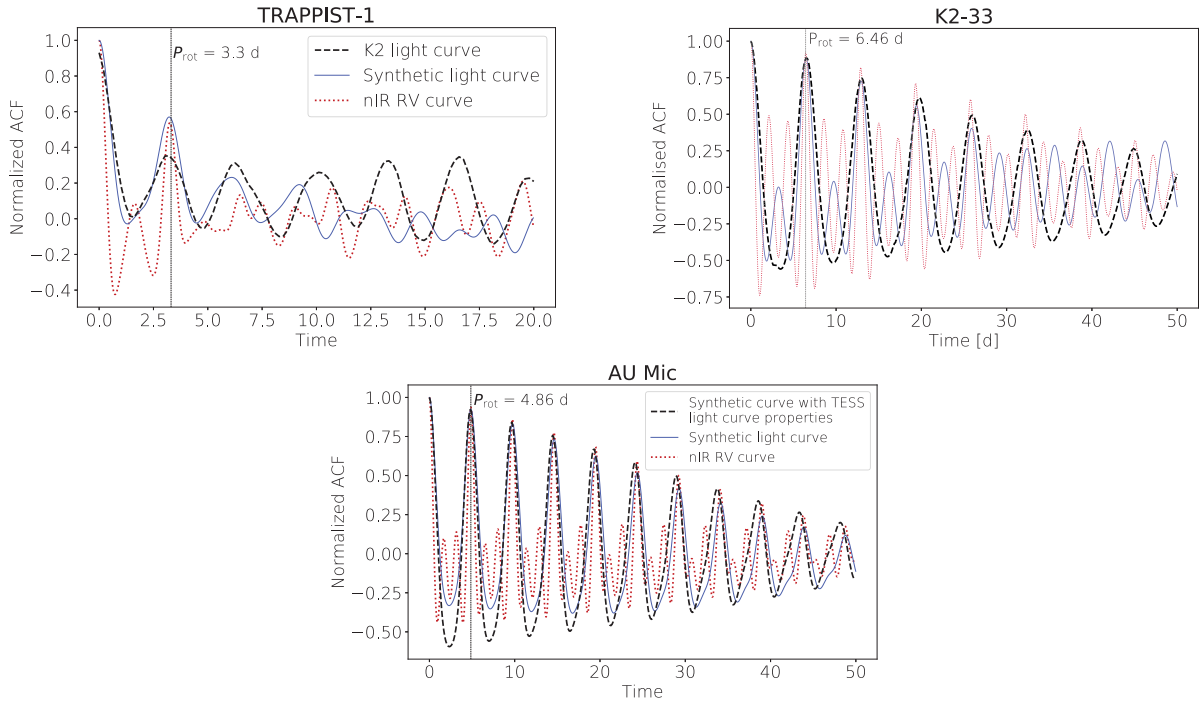

Figure 2.2 – Normalized autocorrelation functions (ACFs) of TRAPPIST-1 (top left), K2-33 (top right) and AU Mic (bottom) light and RV curves. In each plot, the ACF of the detrended K2 light curve is shown as the black dashed line, while the ACF of the synthetic photometric and RV curves are plotted in blue solid lines and red dotted lines, respectively. The rotation period of the star is indicated by the vertical dashed line in each panel. The TESS light curve of AU Mic only covers a period of 27 d, much shorter than the typical evolution time-scale of surface features reported in P20 (∼100 d). Instead of showing the ACF of the TESS light curve, we plot the ACF of a synthetic curve with the statistical properties of AU Mic's light curve. This synthetic curve is drawn from a GP with quasi-periodic covariance kernel (see Eq. 2.5) whose parameters are taken from P20 analysis (i.e., decay time of 100 d and smoothing parameter of 1.0).

the rotation period of the stars. The decrease in the amplitude of the successive peaks gives us information on the time scale on which inhomogeneities evolve at the stellar surface. For example, TRAPPIST-1's ACF suggests that the surface features evolve on time scales of the order of the stellar rotation cycle, while K2-33 exhibits a much more periodic ACF, symptomatic of features that are long-lived compared to the stellar rotation cycle. Finally, the FWHM of the peaks informs us on the longitudinal distribution of the features at the stellar surface. For example, the FWHM of the peaks will be smaller if the features are preferentially located at a given longitude rather than homogeneously arranged at the surface surface. The ACF of the stellar light curve acts as a reference to tune the global parameters of features in our simulation.

Another way to compare the statistical properties of the observed light curves to their synthetic counterparts is to model them with GPs (see Appendix A.3). The characteristic shapes of the ACFs of the light curves makes it natural to adopt a quasi-periodic covariance kernel k for the GP, defined by (Haywood et al., 2014):

$$\mathrm{k}(t_i, t_j; \boldsymbol{\theta}) = \theta_1^2 \exp\left[-\frac{(t_i - t_j)^2}{\theta_2^2} - \frac{\sin^2 \frac{\pi(t_i - t_j)}{\theta_3}}{\theta_4^2}\right], \tag{2.5}$$

where t_i is the time associated to observation i. This quasi-periodic kernel relies on four hyper-parameters, $\boldsymbol{\theta} = (\theta_1, \theta_2, \theta_3, \theta_4)$, whose components are respectively the amplitude, decay time,

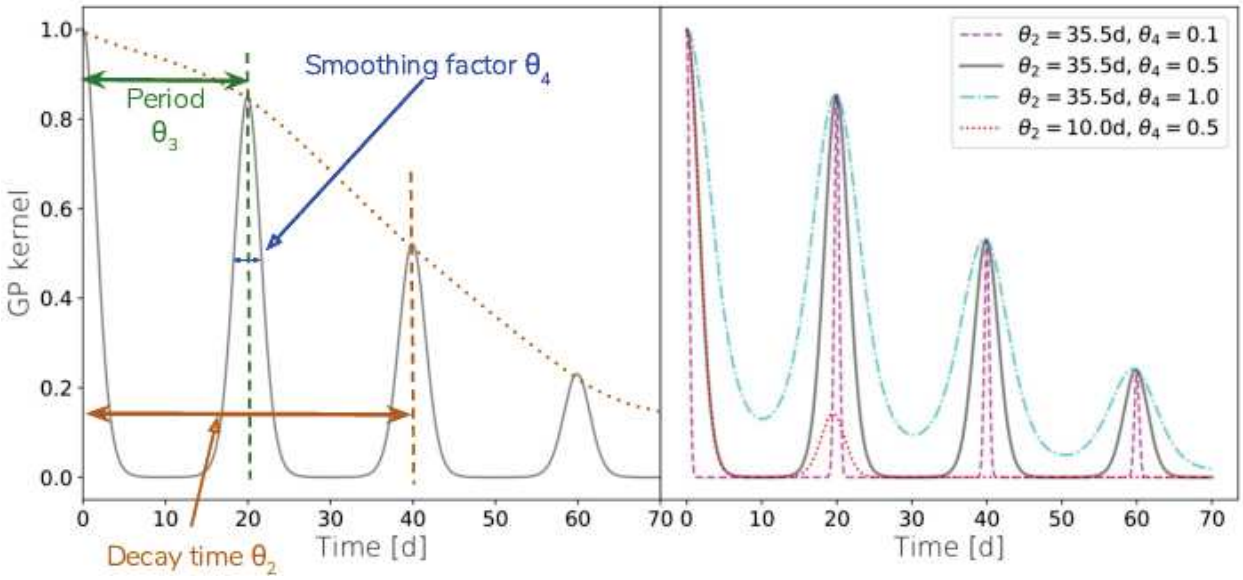

Figure 2.3 – *Left panel:* Schematic of a normalized quasi-periodic GP kernel. Note that the smoothing factor is a dimensionless parameter, falsely represented here by the FWHM of the main peak of the kernel which is, in fact, approximatively equal to $\theta_3/\pi \arcsin \theta_4 \sqrt{-\ln(1/2)}$ for quasi-periodic signals. *Right panel:* Evolution of the GP kernel as a function of its decay time and smoothing parameter.

recurrence time scale, and smoothing parameters of the GP (see the illustration of the hyperparameters and their effect on k in Figure 2.3). When we model a light curve using GPR, we somehow parameterize its ACF with the GP hyperparameters. Therefore, $\boldsymbol{\theta}$ must be roughly similar in both synthetic and observed light curves, provided that both curves feature similar S/Ns. For a given data set $\boldsymbol{y}$, $\boldsymbol{\theta}$ is estimated by maximising the so-called posterior density of parameters, i.e., the probability density law followed by the parameters of our model $\mathscr{M}$ given the data: $p(\boldsymbol{\theta}|\boldsymbol{y}, \mathscr{M})$. In the Bayesian framework, the posterior density is proportional to the product of the prior density law, $\pi(\boldsymbol{\theta}|\mathscr{M})$, and the likelihood $\mathscr{L}(\boldsymbol{y}|\boldsymbol{\theta}, \mathscr{M})$, given by:

$$2 \ln \mathscr{L}(\boldsymbol{y}|\boldsymbol{\theta}, \mathscr{M}) = -N_{\rm pt} \ln 2\pi - \ln |\boldsymbol{K} + \boldsymbol{\Sigma}| - \boldsymbol{y}^{\rm T} (\boldsymbol{K} + \boldsymbol{\Sigma})^{-1} \boldsymbol{y}, \tag{2.6}$$

where $N_{\rm pt}$ is the number of data points, and $\boldsymbol{K}$ and $\boldsymbol{\Sigma}$ are the covariance matrices associated respectively to the GP kernel (i.e., $\boldsymbol{K}_{i,j} = k[t_i, t_j; \boldsymbol{\theta}]$) and to the white noise in the data (i.e., $\boldsymbol{\Sigma}_{i,j} = \sigma_i^2 \delta_{i,j}$, where $\delta_{i,j}$ is the Kronecker delta and σ_i is the uncertainty on y_i). The posterior density is sampled using the EMCEE affine-invariant sampler (Foreman-Mackey et al., 2013), which is an efficient MCMC process (see the description in Appendix A.2.5).

For the systems of interest, GPR is used to double check that the statistical properties of the synthetic light and RV curves are consistent with those of the observed light curve. Modeling our 90 d-synthetic stellar activity photometric (or RV) curves is straightforward, as it just requires to sub-sample the densely-sampled curves into typically 200-250 evenly-sampled data points covering the rotation cycle of the synthetic star, and to add a realistic random noise (typically equal to the noise of the observed data). In contrast, the GP modeling of the observed light curves needs to be more carefully done, as the latter are often affected by shorted-lived phenomena like flares, planet transits, and uncorrected systematics (e.g., of instrumental origin). By simply under-sampling the observed light curves, we risk to include structures of higher frequencies than those produced by quasi-periodic patterns, which would result in decreasing θ_2 and/or $\theta 4$. We therefore propose a specific method to extract the rotationally-modulated signal from a given light curve. We first divide

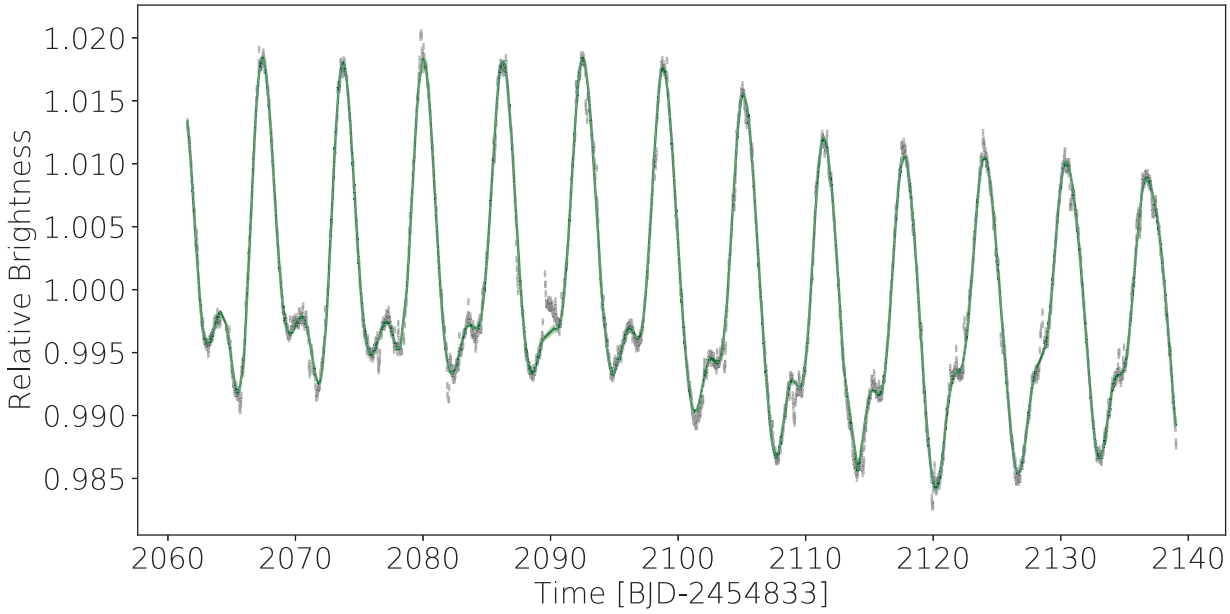

Figure 2.4 – K2 light curve of K2-33 (gray dots) detrended using the EVEREST software (Luger et al., 2016, 2018), and best prediction of its rotationally-modulated component using GPR (green solid line with $\pm 1\sigma$ error bands.)

the observed light curve into M consecutive time intervals (M is generally equal to 200 for a 80-d K2 light curve), and build an under-sampled light curve of M points, $\boldsymbol{y_{sub}}$, by taking the median of all points within each interval. We then train a GP, assuming a quasi-periodic covariance kernel for $\boldsymbol{y_{sub}}$, using the MCMC process described above. Thanks to the GP properties, we predict the values (and uncertainties) of the modeled rotationally-modulated photometric signals at all the observation times of the light curve, and reject the points deviating by more than 5σ from the prediction. We then repeat the process until no more point is rejected. This procedure is illustrated for K2-33 in Figure 2.4 and the best hyper-parameters for both systems are given in Table 2.2.

Table 2.2 – Results of the GP modeling of the observed light curve $\boldsymbol{Y_{obs}}$, and of the synthetic light and RV curves, $\boldsymbol{Y_{syn}}$ and $\boldsymbol{V_{syn}}$ for TRAPPIST-1 and K2-33. The first column gives the prior density law adopted for each hyperparameter of the GP[†]. **For the photometric time-series, the RMS of the time-series (line 1), the typical level of error bars, $\bar{\sigma}$, and the GP amplitude are multiplied by 1000 for clarity purposes.**

Param.	$\pi(\boldsymbol{\theta})$	TRAPPIST-1			K2-33			AU Mic		
		$\boldsymbol{Y_{obs}}$	$\boldsymbol{Y_{syn}}$	$\boldsymbol{V_{syn}}$	$\boldsymbol{Y_{obs}}$	$\boldsymbol{Y_{syn}}$	$\boldsymbol{V_{syn}}$	$\boldsymbol{Y_{obs}}$	$\boldsymbol{Y_{syn}}$	$\boldsymbol{V_{syn}}$
RMS	–	4	5	$6\,\mathrm{m\,s^{-1}}$	9	9	$17\,\mathrm{m\,s^{-1}}$	14	14	$42\,\mathrm{m\,s^{-1}}$
$\bar{\sigma}$	–	1.1	1.0	$1.0\,\mathrm{m\,s^{-1}}$	0.3	0.2	$2\,\mathrm{m\,s^{-1}}$	0.2	0.2	2.0
θ_1	Mod. Jeffreys ($\bar{\sigma}$)	3.3 ± 0.5	5.3 ± 0.5	$5.9 \pm 0.3\,\mathrm{m\,s^{-1}}$	10 ± 2	7 ± 2	$18 \pm 4\,\mathrm{m\,s^{-1}}$	13 ± 2	12 ± 1	30 ± 3
$\theta_2[d]$	$\log \mathscr{U}(1,7)$	4.1 ± 0.8	4.3 ± 0.3	$4.4^{+0.5}_{-0.4}$	19 ± 1	26 ± 2	36 ± 3	15 ± 2	100 ± 10	70 ± 7
θ_3 [d]	$\mathscr{U}(0.9,1.1)P_{\mathrm{rot}}$	3.6 ± 0.1	3.36 ± 0.04	$3.30^{+0.05}_{-0.03}$	6.35 ± 0.04	6.36 ± 0.02	6.35 ± 0.01	4.84 ± 0.02	4.86 ± 0.01	4.86 ± 0.01
θ_4	$\mathscr{U}(0.1,5.0)$	$1.1^{+0.2}_{-0.1}$	0.81 ± 0.06	$0.26^{+0.04}_{-0.05}$	1.01 ± 0.1	0.71 ± 0.06	0.33 ± 0.02	0.57 ± 0.04	0.8 ± 0.1	0.41 ± 0.03

[†] In this manuscript, $\mathscr{U}(a,b)$ stands for the Uniform density low between a and b while *Mod. Jeffreys* ($\bar{\sigma}$) refers to the modified Jeffreys prior density of knee $\bar{\sigma}$, as defined in Gregory (2007) (see also Table 4.1).

2.2.1.4 Application to TRAPPIST-1, K2-33 and AU Mic

We generate stellar activity photometric and RV curves for TRAPPIST-1, K2-33 and AU Mic using the process described above, and compare their statistical properties to those of the observed light curves. The properties of the stellar features assumed for each star are given in the bottom panel

of Table 2.1, and the resulting light and RV curves are shown together with their corresponding surface brightness topology in Figure 2.5. TRAPPIST-1's photosphere is covered by small features of average relative area 0.06 % with respect to the whole stellar surface, roughly consistent with the upper limit on the spot relative area found in Morris et al. (2018b). In contrast, the surfaces of K2-33 and AU Mic only exhibit a few large slowly-evolving inhomogeneties inducing much more periodic light and RV curves. For K2-33 (and probably AU Mic), the decrease in the brightness contrast of the features from 70% to 40% from visible to nIR wavelengths induces a substantial reduction of the amplitude of the stellar activity RV signal (from $\sim$150 m s^{-1} to $\sim$60 m s^{-1} peak-to-peak for K2-33), even when assuming that surface spots/plages host magnetic fields. This is not the case for TRAPPIST-1 nIR RV curve, whose fluctuations are dominated by the Zeeman broadening rather than the brightness contrast of surface features. Note however that this observation depends on the strength of the assumed magnetic field within the star spots/plages, which remains poorly-constrained for as cold a star as TRAPPIST-1.

Using the method described in Section 2.2.1.3, we modeled the synthetic stellar activity curves with GPR. The best GP hyperparameters are given in Table 2.2, and appear roughly similar to those of the observed light curves for K2-33 and TRAPPIST-1. In the K2-33 synthetic light curve, θ_2 and θ_4 are found respectively larger and smaller than their counterparts in the observed light curve, indicating respectively (i) slightly longer evolution time scales for the modeled features (but may also be due to uncorrected high frequency structures in the observed light curve, as both ACFs are consistent in terms of evolution time scale; see Figure 2.2), and (ii) that the distribution of inhomogeneities at the stellar surface in this realization induces photometric/RV variations of higher frequencies than in the observed light curve. We also note that θ_2 is found to be larger in the RV curve than its photometric counterpart for K2-33 whereas the two curves exhibit similar decay times for TRAPPIST-1. The RV signatures induced by small rapidly-evolving features at the surface of K2-33 are partly drowned in the injected noise, and, as a consequence, its RV curve is dominated by larger slowly-evolving features. For K2-33 and AU Mic, whose RV curves are dominated by the brightness contrast of the inhomogeneities at the stellar surface, θ_4 is roughly twice as large in photometry than in RV, as a feature at the stellar surface produces a RV signature evolving roughly twice as fast as its photometric counterpart (see Aigrain et al., 2012). In the case of TRAPPIST-1, the RV curve is dominated by the impact of Zeeman broadening on spectral lines which has no more than a marginal impact on the light curve. As a consequence, θ_4 decreases by a factor of $\gtrsim 3$ from TRAPPIST-1's photometric curve to its RV counterpart.

For AU Mic, the GP decay time and smoothing parameters of our synthetic photometric and RV curves are consistent with the values reported in the RV analysis of the star by Plavchan et al. (2020b) ($\theta_2 \approx 100$ d and $\theta_4 \approx 0.4$). In particular, the dispersion of our synthetic nIR RV time-series is consistent with the $\sim$50 m s^{-1} RMS found in Gagné et al. (2016) and Plavchan et al. (2020b) to the first order. However, θ_2 is found to be surprisingly low in the TESS light curve of the star. This light curve is plagued by frequent flares of various intensity (up to 2%) occurring on a daily basis (see the bottom panels of Figures 2.5 and 4.1) whose contributions have likely not been precisely removed by our iterative cleaning process. The uncorrected short-lived phenomena have likely biased our estimate of the GP decay time, especially since TESS observations cover only $\sim$5 rotational cycles of the star.

2.2.2 Building mock RV time-series

2.2.2.1 Planetary signals

We build a reference densely-sampled curve, $\boldsymbol{V}_{\mathbf{ref}}$, by adding planet signatures to the synthetic stellar activity RV curve. Consistently with transit light curve analyses (Mann et al., 2016; Grimm et al., 2018; Plavchan et al., 2020b), the planet orbits are assumed to be circular for the each system

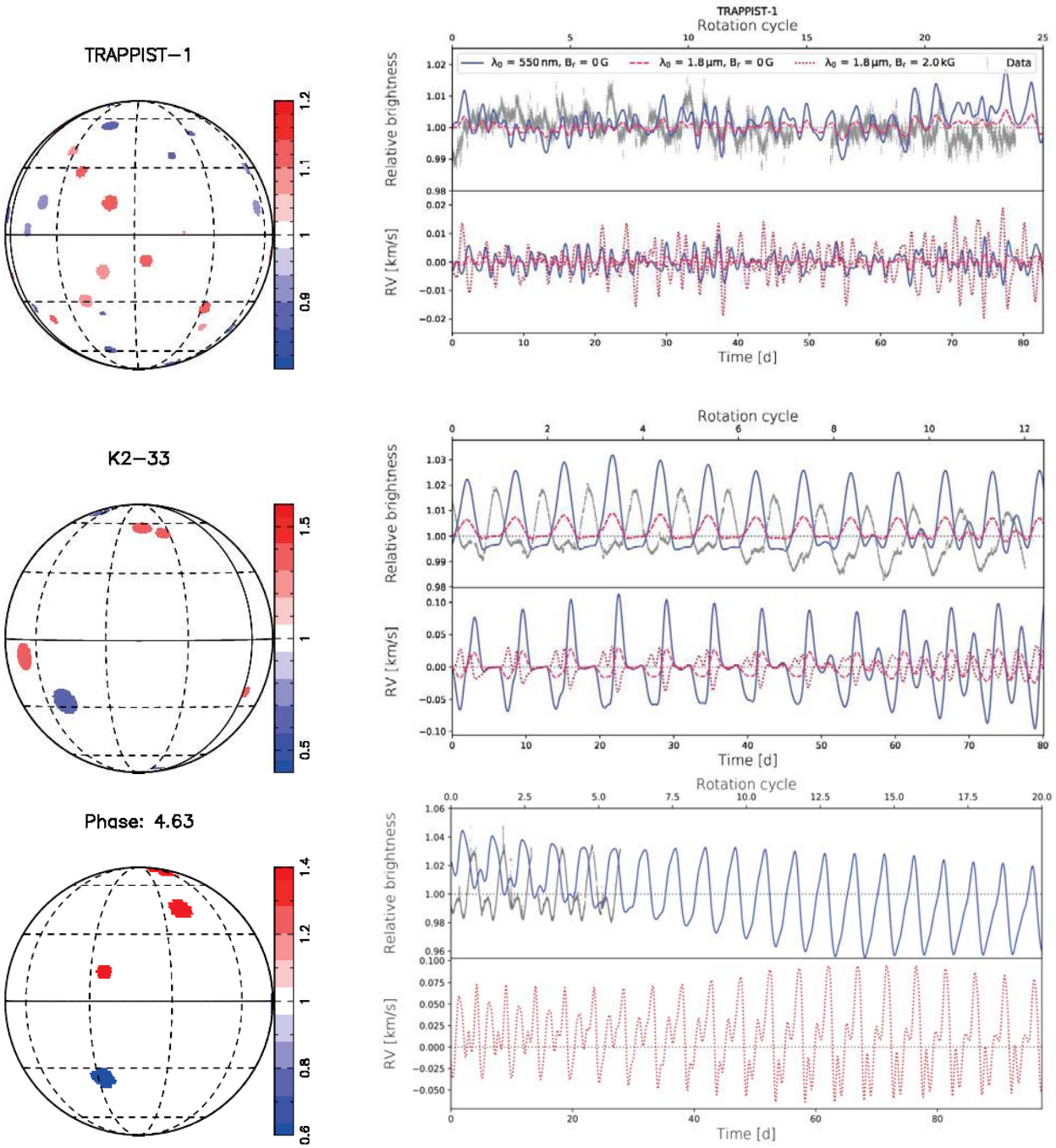

Figure 2.5 – Illustration of the modeled stellar surfaces (left panels) and resulting synthetic light and RV curves (right panel) for TRAPPIST-1 (top line), K2-33 (middle line) and AU Mic (bottom line). The color of the inhomogeneities on the left panels indicates their relative brightness with respect to the quiet photosphere (note the different color scale for each star). On the right panels, the synthetic light curves generated in the optical domain (blue solid lines), and in the nIR assuming a magnetic field of 0 and 2 kG within each feature (resp. pink dashed lines and red dotted lines) are shown in the top panel of each line, whereas their RV counterparts are shown in the bottom panels. For comparison purposes, we also plot the detrended K2 light curve of each star in gray dots. For AU Mic, we only computed a light curve in the optical domain and the corresponding RV curve in the nIR, assuming a magnetic field of 2 kG within the features.

of interest and, therefore, each planet produces a RV signature V_p on the host star given by

$$V_\mathrm{p}(t) = -K_\mathrm{s} \sin\left[2\pi \frac{t - T_0}{P_\mathrm{orb}}\right], \tag{2.7}$$

where K_s is the semi-amplitude of the planet RV signal, defined in Eq. 1.2, and P_orb and T_0, the orbital period and mid-transit time of the planet orbit, which are generally well-constrained from transit analyses. The global planetary RV signature is then simply the sum of all individual planet RV signals[4]. The computation of K_s requires the knowledge of the planet mass M_p. For TRAPPIST-1, we use the planet masses obtained from TTVs (Grimm et al., 2018, see the TRAPPIST-1 planetary RV signature shown in Figure 2.6). Not that using both ground- (e.g., SPECULOOS, TRAPPIST-North / -South) and space-based (Spitzer, K2, HST) observations, Agol et al. (2020) significantly refined the TTV mass estimates of all TRAPPIST-1 planets, improving their precision by a factor ranging from ∼2 (for planets b and c) up to 3.5 (planet e). Except planets e and h, all planets are found more massive than the estimates that we consider in this study. For K2-33 b, for which no TTV has been observed, we assumed different values of K_s in the range 5-20 $\mathrm{m\,s^{-1}}$ corresponding to M_p of 6-37 $M_\odot$ and bulk densities of 0.3-1.9 $\mathrm{g\,cm^{-3}}$ (i.e., 0.2-1.2 Neptune bulk density; less massive planets are also predicted to exist at the age of K2-33 by the population synthesis model of Mordasini et al., 2012c, but their RV signature would likely be undetected). The same goes for AU Mic b for which only an upper limit on the mass is available.

Moreover, the ellipticity of the planet orbit is generally poorly constrained by transit light-curves. For TRAPPIST-1, this limitation is overcome by the significant TTVs of the planets in the system, whose dynamical modeling yields eccentricities smaller than 0.01 for all planet orbits (see Grimm et al., 2018). The situation is trickier for K2-33 b and AU Mic b for which low-to-moderate orbit ellipticities are not excluded as a result of potential past interactions with putative outer planets in the system (Chatterjee et al., 2008; Jurić & Tremaine, 2008). The impact of elliptical planet orbits on our simulations is detailed in Section 2.3.2.

Scheduling of the observations

From the reference RV curve, we create mock RV time-series using various sampling schemes. In practice, a given synthetic data set $\boldsymbol{V_\mathrm{r}}$, is simply given by

$$\boldsymbol{V_\mathrm{r}} = \boldsymbol{V_\mathrm{ref}}(\boldsymbol{t_\mathrm{obs}} \subset \boldsymbol{t}), \tag{2.8}$$

where $\boldsymbol{t}$ and $\boldsymbol{t_\mathrm{obs}}$ are the time vectors respectively associated to the reference curve (i.e., evenly-sampled vector of step 0.01 d) and to the observations. The observation strategies considered for the two systems of interests are listed in Table 2.3 and differ significantly from one another.

TRAPPIST-1 is a complex system featuring rapidly-evolving activity and many close-in low-mass planets. Recovering the mass of each planet in this system will likely require a dense coverage of the star on its visibility period, probably not achievable with a single telescope. Given the complexity of the system, we first need to define a fiducial sampling scheme $\mathrm{T_A}$, consisting in taking evenly-spaced data points at a frequency of $2\,d^{-1}$ (i.e., larger than twice the maximum frequency of the planet signals to ensure that the Shannon-Nyquist condition is fulfilled). This scheme will

[4] Note this model does not account for dynamical interactions between the planets of the system. However, even in the case of TRAPPIST-1 where the planets strongly interact which each other, the orbital phase shift induced by dynamical planet-planet interactions are expected to be lower than 10^{-3} from the modeled TTVs of Grimm et al. (2018) and Agol et al. (2020). As this value is significantly lower than the typical uncertainties that we obtain on planet orbital phases from the RV modeling, planet-planet interactions are neglected in this study.

Table 2.3 – List of the different sampling schemes considered for TRAPPIST-1 (lines 2 to 5) and K2-33 (lines 7 to 10) simulated observations. The first column gives the name of the configuration while columns 2 and 3 indicate respectively the typical number of observations, $N_{\rm pt}$, and the sampling frequency. More details on the telescopes in use and the conditions of observations are given in column 4. Unless otherwise specified, CFHT bright time periods are assumed to last 15 d.

Scheme	$N_{\rm pt}$	Freq. [$\rm d^{-1}$]	Comments
TRAPPIST-1			
$\rm T_A$	180	2	Fiducial case - even sampling
$\rm T_B$	$\sim$120	$\sim$2	CFHT (all nights) & TBL
$\rm T_C$	$\sim$85	$\sim$2	CFHT (bright time only) & TBL
$\rm T_D$	$\sim$76	$\sim$1	CFHT (all nights)
K2-33			
$\rm K_A$	50	1	CFHT (bright time periods of 20 d)
$\rm K_B$	40	1	CFHT (bright time only)
$\rm K_C$	35	1	CFHT (bright time only)
$\rm K_D$	30	1	CFHT (bright time only)
AU Mic			
–	30	1	CFHT (2 bright time slots)

provide an upper limit on the achievable precision on the planet masses. We then consider a second more realistic case where the star is observed from both the CFHT, with SPIRou, and the TBL, with SPIP, at airmass $\lesssim$1.5 and at a rate of one point per night per telescope. To account for stochastic weather conditions, the observations are successfully carried out with probabilities of 0.85 and 0.5 at Mauna Kea and Pic du Midi de Bigorre, respectively. In practice, SPIRou observes mostly during bright-time slots, i.e., $\sim$15 d windows centered on full Moon periods. We account for this specificity in Scheme $\rm T_C$, while scheme $\rm T_B$ allows observations during both bright and dark time periods. Finally, as SPIP is not yet available for observations, we define scheme $\rm T_D$, similar to scheme $\rm T_B$, but assuming that TBL is not available. Schemes $\rm T_C$ and $\rm T_D$ are illustrated in Figure 2.6. Given that the orbital parameters of the planets are well-constrained from transit photometry, a promising observing strategy would be to take the nightly observation only at the times that maximise the absolute value of the planetary signal (see the red crosses in Figure 2.6). In principle, this scheme maximises that the information of the planet RV curve which should then be easier to unveil (e.g., Ford, 2008; Burt et al., 2018). However, the impact of stellar activity RV signals on the recovered planet signatures is unclear and worth a dedicated test in this study.

For K2-33, the main question is whether the mass of the close-in planet can be measured under realistic observation conditions with SPIRou. In order to keep the coherence of the stellar activity signal throughout the run, one needs to carry out the monitoring on a $\sim$90 d-period where the star is visible under good airmass conditions (typically $\lesssim$1.5). Hence typically 3 consecutive 15 d-bright time periods centered on full moons where the star can be observed with SPIRou. Among the 45 observable nights, we build data sets containing 30, 35 and 40 randomly-selected data points (cases $\rm K_A$, $\rm K_B$ and $\rm K_C$). We also consider a more advantageous case where 50 data points are collected among 3 bright time periods of 20 d (scheme $\rm K_D$). To get rid of potential biases induced by the observation scheme, we typically generate a dozen of data sets with different observation times for each sampling schemes considered in this study.

The goal is slightly different for AU Mic, since we want to determine the minimum semi-amplitude of the signature of AU Mic b that can be measured with a given sampling scheme. At the time where the simulations were carried out (in the end of 2018), SPIRou was just starting observing and the allocations of its observing periods were not secure. The goal was to ask for 30

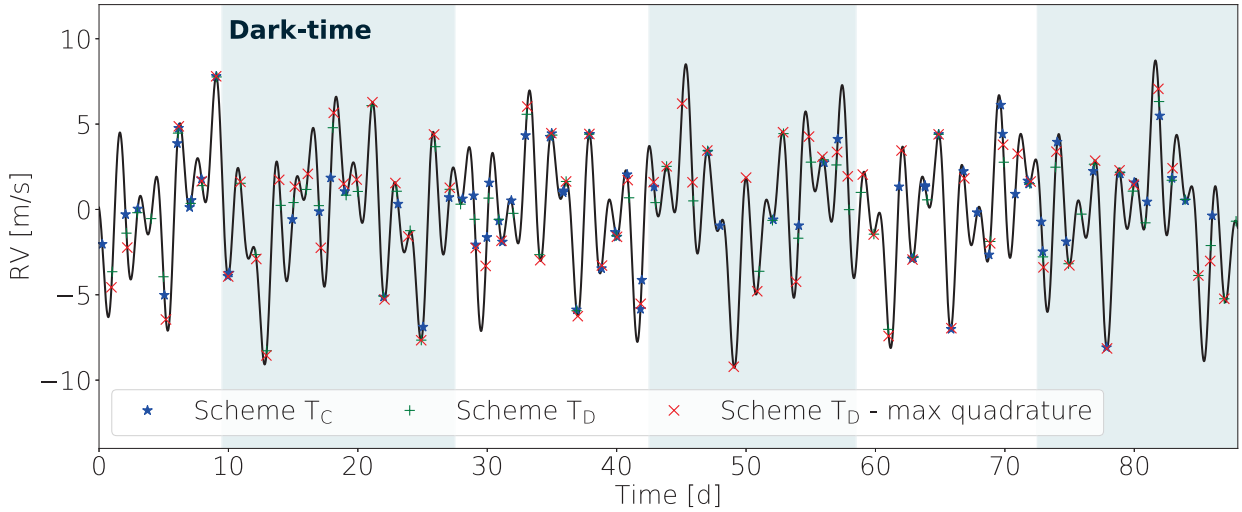

Figure 2.6 – Synthetic planet RV curve of the TRAPPIST-1 system (black solid line). We illustrate different samplings used to build TRAPPIST-1 RV time-series: the blue stars are obtained in cases T_C (i.e., SPIRou observations during bright-time periods only and SPIP observations), T_D (one point per night from SPIRou) and T_D at maximum quadrature (only points that maximize the absolute value of the planet RV curve taken every night). The dark time assumed for scheme T_C are indicated by the blue vertical bands.

visits spread over two consecutive 15-d bright time periods in the first semester of 2019.

Adding noise to the data

For each sampling strategy considered, we build a large number (typically 50) of RV time-series with different realizations of white noise accounting for the various sources expected to pollute the data set (e.g., photon noise, stellar variability, instrumental noise). This is done by adding a centered Gaussian noise of standard deviation σ_n to the mock time-series. We assume that the level of noise is known and well-estimated, i.e., that there is no excess of uncorrelated noise nor systematics in our data set. We also assume that the injected noise is uncorrelated as, when these simulations were carried out, no precise quantification of SPIRou's systematics was available. We thus decided to assume an uncorrelated RV noise as the simulation study focuses on assessing the general impact of stellar activity and sampling strategy on the recovered planet signature rather than on providing realistic prescriptions on the performances for a given system. Note that a preliminary analysis of SPIRou systematics is available in Donati et al. (2020a). Two levels of white noise are considered for TRAPPIST-1 and K2-33, one optimistic reference value basically assuming photon noise to be the dominant error contribution ($\sigma_n = 1\,m\,s^{-1}$ for TRAPPIST-1 and $\sigma_n = 2\,m\,s^{-1}$ for K2-33), and a more conservative one ($\sigma_n = 2\,m\,s^{-1}$ for TRAPPIST-1 and $\sigma_n = 5\,m\,s^{-1}$ for K2-33). Due to higher $v \sin i$ of K2-33, the noise level on the RV time-series of the star is expected to be larger than that of TRAPPIST-1. For AU Mic, we impose a conservative noise level of $5\,m\,s^{-1}$.

2.2.3 Modeling the mock RV time-series

Description of the model

The goal is now to recover the planet signatures from each synthetic RV time-series and, ultimately, to estimate the associated planet mass. To do so, we model each RV time-series as the sum of a planetary signature, V_p, and a stellar activity signal, V_j, such that

$$V_{\rm r}(t) = V_{\rm p}(t) + V_{\rm j}(t) + \epsilon(t), \tag{2.9}$$

where $\epsilon(t) \sim \mathscr{N}(0, \sigma_{\rm n})$. The planet RV signature produced by $N_{\rm p}$ planets is simply modeled by

$$V_{\rm p}(t) = \sum_{n=1}^{N_{\rm p}} \alpha_n \cos\left(\frac{2\pi}{P_{\rm orb,n}} t\right) + \beta_n \sin\left(\frac{2\pi}{P_{\rm orb,n}} t\right) \tag{2.10}$$

which is simply a linearized version of Eq. 2.7, where $\alpha_n = K_{\rm s,n} \sin\phi_n$ and $\beta_n = \text{-}K_{\rm s,n} \cos\phi_n$, where $\phi_n = 2\pi T_{0,n}/P_{\rm orb,n}$ is the orbital phase of planet n. The planet orbital periods are frozen to their best photometric estimates, leaving α_n and β_n as the only parameters be recovered for each planet n. The modeled planet signature can thus be simply expressed by $\boldsymbol{V_{\rm p}} = \boldsymbol{X}\,\boldsymbol{\omega}$, where $\boldsymbol{\omega} = (\alpha_1, \beta_1, ..., \alpha_{N_{\rm p}}, \beta_{N_{\rm p}})$ is the vector of planet parameters and $\boldsymbol{X}$ is a matrix of size $(N_{\rm pt}, N_{\rm p})$ independent of $\boldsymbol{\omega}$. We model the stellar activity RV signal using GPR assuming the 4-parameter quasi-periodic kernel defined in Eq. 2.5. As a result, a model searching for $N_{\rm p}$ planetary signatures in the RV time-series will contain $4 + 2N_{\rm p}$ free parameters, 4 of which are non-linear. In the case when the orbital phases of the planets are frozen to their best estimates from transit photometry, only one free linear parameter, $K_{\rm s,n}$, remains for each planet n.

Estimation process

Our model regards each RV time-series $\boldsymbol{V_{\rm r}}$ as planet signatures embedded into correlated noise of covariance matrix $\boldsymbol{K}(\boldsymbol{\theta}) + \boldsymbol{\Sigma}$, where, this time, $\boldsymbol{\Sigma}_{i,j} = \sigma_{\rm n}^2\,\delta_{i,j}$. Our estimation process consists in maximising the posterior density of the model, $p(\boldsymbol{\omega}, \boldsymbol{\theta}|\boldsymbol{V_{\rm r}})$, written in the Bayesian framework, as

$$p(\boldsymbol{\omega}, \boldsymbol{\theta}|\boldsymbol{V_{\rm r}}) = \pi(\boldsymbol{\theta})\pi(\boldsymbol{\omega})\mathscr{L}(\boldsymbol{V_{\rm r}}|\boldsymbol{\omega}, \boldsymbol{\theta}), \tag{2.11}$$

where we assumed that $\boldsymbol{\omega}$ and $\boldsymbol{\theta}$ are independent, and where $\mathscr{L}(\boldsymbol{V_{\rm r}}|\boldsymbol{\omega}, \boldsymbol{\theta})$ is expressed as in Eq. 2.6, but replacing $\boldsymbol{y}$ by $\boldsymbol{V_{\rm r}} - \boldsymbol{V_{\rm p}}$. We use a MCMC process to sample the posterior density of the model. However, jointly sampling $\boldsymbol{\omega}$ and $\boldsymbol{\theta}$ would be time-consuming especially for TRAPPIST-1 (given the large number of model free parameters). Given the large number of mock RV time-series to model, we propose a method to gain time in the estimation process. The posterior density of the model is analytically integrated over the linear free parameters (i.e., the planet parameters):

$$p(\boldsymbol{\theta}|\boldsymbol{V_{\rm r}}) = \pi(\boldsymbol{\theta}) \int_{\omega} \mathscr{L}(\boldsymbol{V_{\rm r}}|\boldsymbol{\omega}, \boldsymbol{\theta})\pi(\boldsymbol{\omega}){\rm d}\boldsymbol{\omega}. \tag{2.12}$$

The analytical derivation of Eq. 2.12 is given in Appendix A.2.6. We adopt a non-informative prior density on $\boldsymbol{\omega}$ (e.g., uniform law on $\mathbb{R}$) and the prior densities given in Table 2.2 for $\boldsymbol{\theta}$. The marginalized posterior density $p(\boldsymbol{\theta}|\boldsymbol{V_{\rm r}})$ is sampled using the EMCEE affine-invariance process (5000 iterations of 100 walkers; i.e., significantly longer that the typical autocorrelation times of the chain Foreman-Mackey et al., 2013), and the best hyperparameters $\boldsymbol{\theta_{\rm b}}$ of the model and their associated uncertainties are estimated from the posterior distribution obtained after removing a burn-in period of 2000 iterations from the chain. For a given value of $\boldsymbol{\theta}$, the posterior distribution of the planet parameters is simply given by a least-squares estimator (see Appendix A.2.3), such that

$$p(\boldsymbol{\omega}|\boldsymbol{V_{\rm r}}, \boldsymbol{\theta}) \sim \mathscr{N}\left(\boldsymbol{A}^{-1}(\boldsymbol{\theta})\boldsymbol{b}(\boldsymbol{\theta}), \boldsymbol{A}^{-1}(\boldsymbol{\theta})\right) \tag{2.13}$$

where

$$\left\{ \begin{array}{rcl} \boldsymbol{A}(\boldsymbol{\theta}) & = & \boldsymbol{X}^{\mathrm{T}}[\boldsymbol{K}(\boldsymbol{\theta}) + \boldsymbol{\Sigma}]^{-1}\boldsymbol{X} \\ \boldsymbol{b}(\boldsymbol{\theta}) & = & \boldsymbol{X}^{\mathrm{T}}[\boldsymbol{K}(\boldsymbol{\theta}) + \boldsymbol{\Sigma}]^{-1}\boldsymbol{V}_{\mathbf{r}}. \end{array} \right. \tag{2.14}$$

The planet parameters and their error bars are estimated by applying Eq. 2.13 at $\boldsymbol{\theta} = \boldsymbol{\theta}_{\mathbf{b}}$ and by convolving the resulting Gaussian density with the distribution of $\boldsymbol{\omega}$ obtained by computing Eq. 2.13 for all the samples of the joint posterior distribution on $\boldsymbol{\theta}$. As shown in Appendix A.2.6, this estimator yields results consistent with those obtained with jointly sampling the planet and stellar activity parameters with a MCMC process.

2.2.3.1 Quantifying the significance of each planet RV signature

Which criterion to use to claim that a planet is firmly detected in a given RV time-series? Although apparently basic, answering this question is far from trivial and there is no simple way to address this issue. The first intuitive answer to this question would be to compute the ratio between the estimate of the planet mass and its 1σ-error bar. However, this quantity does not tell us how robust the recovered planet mass is (e.g., how it is affected by the realization of the noise, the sampling strategy, or the model itself). Over the past decade, numerous tools aiming at robustly quantifying the statistical significance of a planetary signal in a data set have been implemented (e.g., Zechmeister & Kürster, 2009; Haywood et al., 2014; Díaz et al., 2014; Mortier et al., 2015; Faria et al., 2016; Hara et al., 2017, see Appendix A.4 for an overview).

To quantify the significance of planet signatures in our mock RV time-series, we use the method introduced by Chib & Jeliazkov (2001) and applied by Haywood et al. (2014) for the search of planets in RV data sets. Let us call M_n the model described in Eq. 2.9 searching for n planet RV signatures in the data. To quantify whether planet n is detected from a given data set $\boldsymbol{V}_{\mathbf{r}}$, we compute the so-called posterior odds ratio $p(M_n|\boldsymbol{V}_{\mathbf{r}})/p(M_{n-1}|\boldsymbol{V}_{\mathbf{r}})$ (see Díaz et al., 2014, for a detailed introduction to model comparison). In the Bayesian framework, the posterior odds ratio can be expressed as

$$\frac{p(M_n|\boldsymbol{V}_{\mathbf{r}})}{p(M_{n-1}|\boldsymbol{V}_{\mathbf{r}})} = \frac{p(M_n)}{p(M_{n-1})} \frac{p(\boldsymbol{V}_{\mathbf{r}}|M_n)}{p(\boldsymbol{V}_{\mathbf{r}}|M_{n-1})}, \tag{2.15}$$

where the first term of the right-handed side of Eq. A.48 is known as the prior odds ratio (set to 1 in our case) and the second term, known as the Bayes factor BF_n, is the ratio of the so-called marginal likelihoods (MLs) of models containing n and $n-1$ planets, where

$$p(\boldsymbol{V}_{\mathbf{r}}|M_n) = \int_{\boldsymbol{\theta}} \pi(\boldsymbol{\theta}|\mathrm{M_n})\, \mathrm{p}(\boldsymbol{V}_{\mathbf{r}}|\boldsymbol{\theta}, \mathrm{M_n})\, \mathrm{d}\boldsymbol{\theta}. \tag{2.16}$$

Chib & Jeliazkov (2001) proposed a numerical method to compute MLs when $\boldsymbol{\theta}$ is sampled using a MCMC process (see Appendix A.4.1 for practical details about the implementation of the method). In practice, we run our MCMC process searching for 0 to N_{p} planets in each synthetic RV time-series (N_{p} =7 for TRAPPIST-1, and 1 for K2-33), estimate the ML of each model using the method of Chib & Jeliazkov (2001), and compute BF_n for $n=1$ to $n=N_{\mathrm{p}}$. Following Jeffreys (1961) and Kass & Raftery (1995), BFs larger than 150 (5 in log) will be interpreted as a definite planet detection. The evidence in favour of a planet will then be regarded as strong if BF lies in ∼150-20 (5-3 in log), positive if BF falls in 20-3 (3-1 in log) and inconclusive otherwise. Note however that the recent extensive simulations of Nelson et al. (2020) indicate that $\log \mathrm{BF} \sim 10$ seems to be a more reliable threshold to claim definite detection. Chib & Jeliazkov (2001)'s method has the advantage of being computationally fast and well suited to MCMC sampling.

2.3 Results and perspectives

We model each synthetic RV time-series of Section 2.2.2 using the process described in Section 2.2.3. The results of the parameter estimation are extensively described in Klein & Donati (2019) and Klein & Donati (2020) for TRAPPIST-1 and K2-33, respectively. In this section, we give the main results of these two studies and their implications for future observations.

2.3.1 Results for TRAPPIST-1

At the time when the simulations of RV monitoring of TRAPPIST-1 were carried out, our algorithm to generate realistic stellar activity RV curves did not include the possibility to change the wavelength of observation nor to add magnetic field within surface features. The following results are thus based on mock time-series assuming a stellar activity RV curve generated in the optical domain, without magnetic field. As shown in Figure 2.5, the smaller brightness contrast of features is more or less compensated by the increased Zeeman effect on the spectral lines in the nIR (depending on the assumed magnetic field though), making the stellar activity RV curve generated in the optical domain a relatively good first order approximation of its nIR counterpart. To strengthen this conclusion, we ran our estimation process on a couple of data sets with different sampling strategies listed in Table 2.3 and noise levels and found similar estimates for the planet parameters. We conclude that the results presented below will not be significantly affected by computing the stellar activity RV curve in the nIR rather than in the optical domain.

Case 0: planetary signals alone

We consider a first ideal case of data sets containing only the planet RV signatures and white noises of $\sigma_n = 1\,m\,s^{-1}$ or $\sigma_n = 2\,m\,s^{-1}$. The RV signature of the planets is described using Eq. 2.10 and their parameters are estimated using a least-squares estimator. For all sampling schemes and levels of white noise, the masses of all Earth-sized planets in the system (i.e., planets b,c,e,f,g) are recovered at better than 10σ precision, and those of Mars-sized planets (i.e., planet d and h), at $\sim 5\sigma$ precision, except for samplings T_C and T_D at $\sigma_n = 2\,m\,s^{-1}$, where they are barely recovered at 3σ.

Fiducial sampling case T_A

We now include stellar activity in our RV time-series. In the ideal configuration of sampling scheme T_A ($\sim$180 evenly-sampled data points) and $\sigma_n = 1\,m\,s^{-1}$, we find that the masses of the Earth-sized planets in the system are still recovered at $\sim 10\sigma$. Unsurprisingly, the BF in favour of these planets is systematically larger than 10, implying that these planets are firmly detected. In contrast, the Mars-sized planets, completely drowned into stellar activity, are already undetected. The conclusion is that these planets are likely not detectable with current nIR high-precision velocimeters. An example of the fit to a given RV time-series in this case is shown in Figure 2.7. If we increase the noise level to $\sigma_n = 2\,m\,s^{-1}$, we interestingly note that the precision on the recovered planet mass is not affected in the same way for all planets. The precision on the mass of some planets is limited by the white noise and, thus, linearly decreases with increasing σ_n (planets c, e and f). In contrast, the precision on the mass of the other planets is weakly impacted by the increase in σ_n, and is thus limited by the stellar activity itself.

Impact of the sampling strategy

The precision of the recovered planet signatures is unsurprisingly degraded for RV time-series sampled from schemes T_B, T_C and T_D. With SPIRou as the only available instrument for the

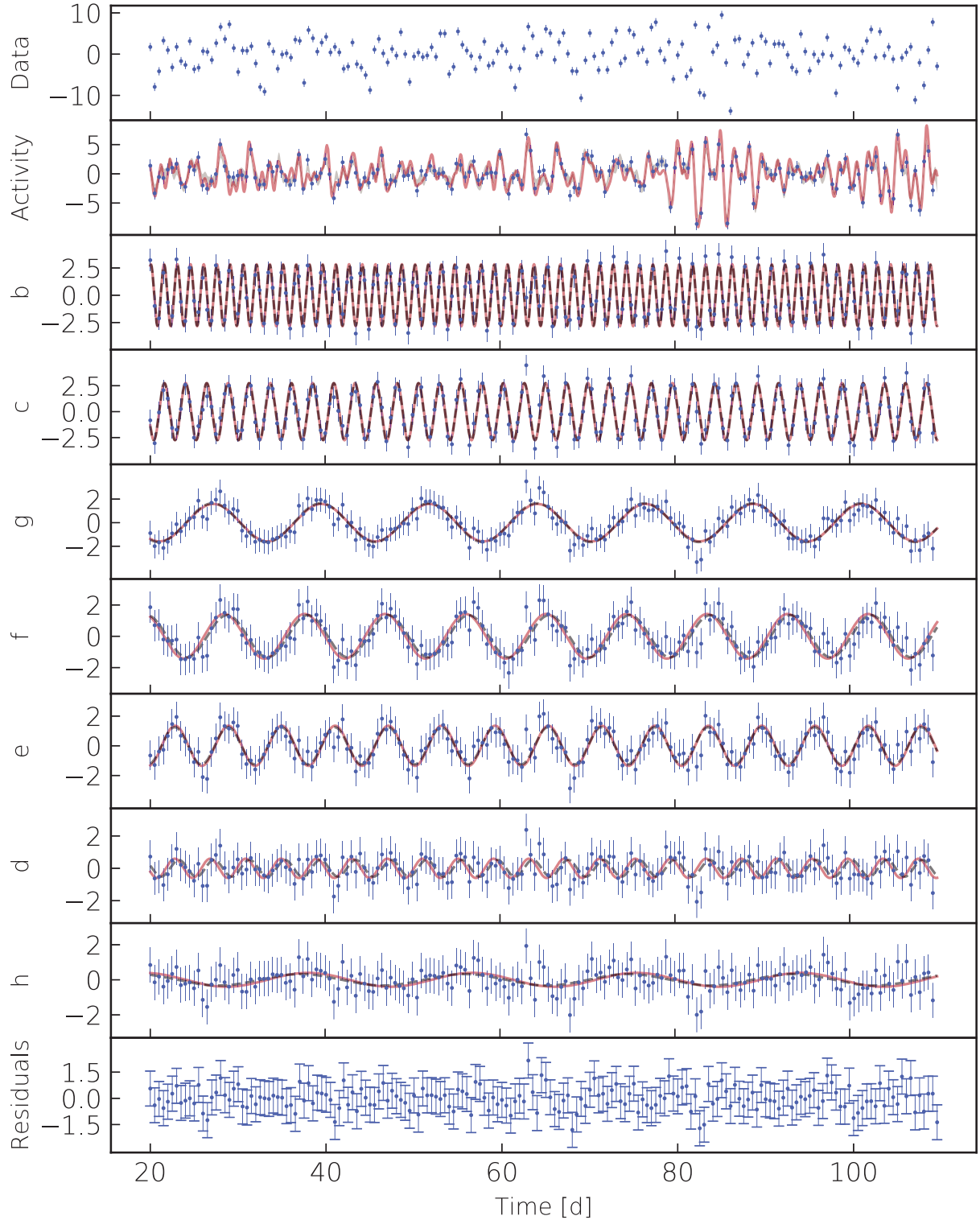

Figure 2.7 – Example of a fit to a given synthetic RV time-series of TRAPPIST-1 sampled with scheme T_A at a white noise of $1\,m\,s^{-1}$. All RVs are expressed in $m\,s^{-1}$. From top to bottom: raw RV data set, stellar activity RV signal (in the optical domain), RV signatures from planets b to h (sorted by decreasing semi-amplitudes) and residuals. In each panel, the red dotted line is the injected RV curve while the gray solid line is the best-fitted prediction of the model. For stellar activity and planet RV signals, the blue dots are obtained by subtracting all components of the model except the one shown in the panel. Source of the figure: Klein & Donati (2019).

RV monitoring of TRAPPIST-1 yields insufficient coverage of the stellar rotation cycle, forcing us to freeze the decay time and smoothing parameter of the GP to their best estimates of Table 2.2 so that the MCMC process can converge. At $\sigma_n = 2\,m\,s^{-1}$, the precision of the mass estimates of planets e, f, and g still lies above 3σ, but their masses are strongly over-estimated (similarly to what was found in Damasso et al., 2019). As discussed in Klein & Donati (2019), this strong over-estimation is most likely due to an incomplete coverage of the stellar activity signal in the regions where the latter is particularly dispersed. The full-amplitude of the stellar activity RV component is not well captured by the observations and, as a consequence, the MCMC process injects power in the semi-amplitude of the planet signatures and decreases the GP amplitude to reach a higher likelihood level. However, we still note that the RV signals induced by the closest planets of the system (planets b and c) are still accurately recovered at precisions larger than 5σ (probably because their orbital cycle is still well covered by the considered sampling schemes).

Freezing the planet orbital phases to their best photometric estimates yields similar estimates of the planet parameters. The same goes for data sets sampled by taking the nightly observation that maximises the planetary signal. Moreover, collecting two points spaced by more than 2 h every night with SPIRou alone (scheme T_D) no more than marginally increases the precision on the planet masses and does not significantly decrease the observed biases on planets e, f and g. The planet mass estimates are however found to be increasingly accurate when modeling data sets sampled in cases T_C and T_B. Using two telescopes located at complementary longitudes provides a more regular coverage of both planet and stellar activity curves that turns out to be critical to accurately recover the planet masses (similarly to the conclusions of Burt et al., 2018).

Perspectives for TRAPPIST-1

The RV follow-up of TRAPPIST-1 with SPIRou has already started at a rate of one point per night. A total of 26 spectropolarimetric observations of TRAPPIST-1 were obtained from 2019 June 16 to November 14. Given the results of our simulations, there is no chance of detecting any of the planets in as sparse a data set. However, observing as faint a target as TRAPPIST-1 is challenging due for example to detector persistence. The observations collected so far could be used as a benchmark to test efficient methods to correct for instrumental effects affecting SPIRou observations of faint targets. In the longer term, SPIRou and SPIP should be able to achieve a dense enough sampling of TRAPPIST-1 stellar activity RV curve, and therefore to accurately recover the masses of some of the planets in the system which will help adjusting their TTV estimates.

2.3.2 K2-33

Main results

For K2-33, we first note that 20 to 30% of data sets of 30 points (scheme K_D in Table 2.3) are rejected, due to the fact that the MCMC process tends to minimize the smoothing parameter of the GP. In this case, the posterior distribution of the smoothing parameter appears bound to the lower limit of the uniform prior (and would result in over-fitted data if the lower bound of the prior was set to 0). Note also that, in our case, the prior density chosen is relatively wide (i.e., $\mathscr{U}(0.1, 5.0)$), but could have been narrowed using the best GP parameters estimated from the densely-sampled curve (shown in Table 2.2). However, in the cases where the MCMC process does not converge, preliminary tests showed that adopting a more informative prior of the smoothing parameter barely affect the results of the estimation process. For the remaining data sets, the semi-amplitude of the planet RV signature is systematically over-estimated (up to a factor 2, consistently with what is found in Damasso et al., 2019, for signals containing too few observations). Surprisingly, the BF in favour of K2-33 b is found $\gtrsim 10$, which would in principle be interpreted as a fair detection of

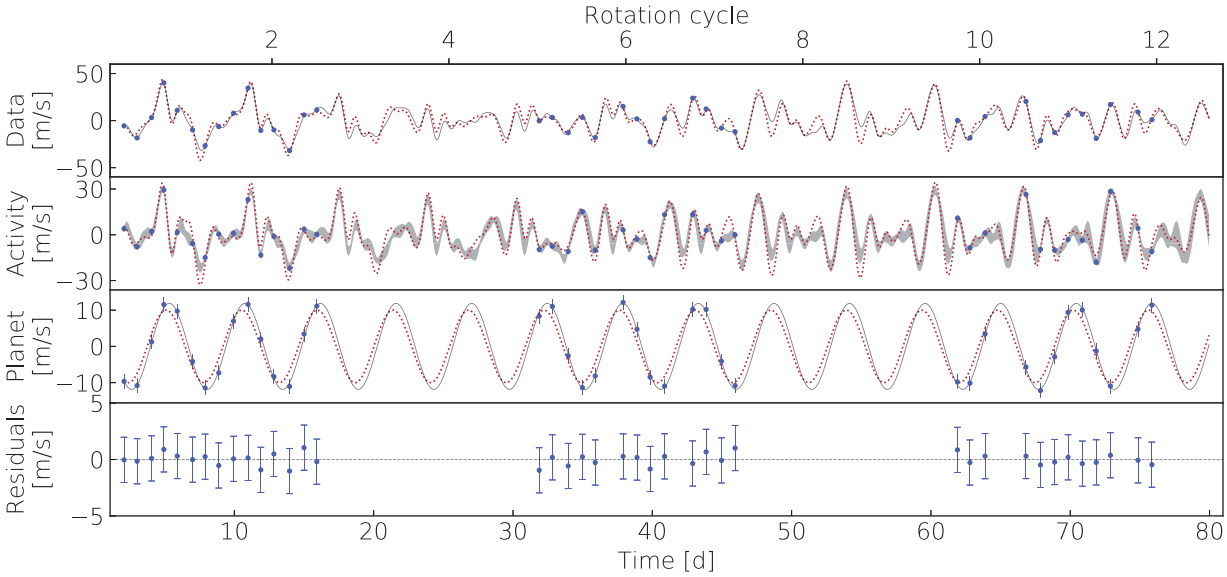

Figure 2.8 – Best fit to one of the synthetic data sets generated for K2-33 with scheme K_B (i.e., 40 points) assuming $K_s = 10\,m\,s^{-1}$ and $\sigma_n = 2\,m\,s^{-1}$. The figure properties are the same as in Figure 2.7.

the planet. However, as its mass estimate is systematically inaccurate, we conclude that 30 visits of K2-33 on its visibility window will probably not be enough to provide reliable estimates of the mass of its close-in planet.

The accuracy of the recovered planet mass progressively increases when the number of observations goes from 30 to 40, where the planet mass is no longer over-estimated, as evidenced by the fit shown in Figure 2.8. For 40 observations, we find that planet signatures $\gtrsim 10\,m\,s^{-1}$ are reliably recovered at 5 and 4σ for respective σ_n of 2 and $5\,m\,s^{-1}$. Finally, we note that 50 observations would allow to detect a semi-amplitude of $5\,m\,s^{-1}$ for the planet, while it would have only be marginally detected for lower number of points. Finally, we here again note that imposing the planet orbital phase to be that derived from photometric analyses only marginally impact the mass estimates.

Constraining the eccentricity of the planet orbit

Even though the transit curve of K2-33 b is compatible with a circular orbit, moderately eccentric orbits (resulting from, e.g., past interactions with putative outer planets in the system cannot be excluded; Chatterjee et al., 2008; Jurić & Tremaine, 2008). In order to quantity the impact of elliptic planet RV signatures on the recovered planet mass from our estimation process, we generate planet RV curves using Eq. 1.1 assuming an eccentricity of 0.2. By running the estimation process described in Section 2.2.3 (that assumes circular planet orbits) on 50 signals with different noise realizations, we find that the recovered K_s and associated error bars are only marginally impacted by the process.

Constraining the eccentricity of moderately elliptical planet orbits will require significantly more measurements that what we assumed for K2-33. As a preliminary test, we built a synthetic 90-d RV curve containing the stellar activity signal and a planet RV signature assuming $K_s = 10\,m\,s^{-1}$, an eccentricity of $e_p = 0.2$, and $\omega = 1$ rad. Using three consecutive 20-d bright time periods (i.e., sampling K_D of Table 2.3), we built data sets of 60 and 100 points, assuming respectively that 1 and 2 observations can be obtained every night. We added a white oise of $2\,m\,s^{-1}$ and then ran our estimation process on data sets with different noise realizations. This time, the planet signature is modeled using Eq. 1.1 and freezing both orbital period and phase their photometric estimates. The

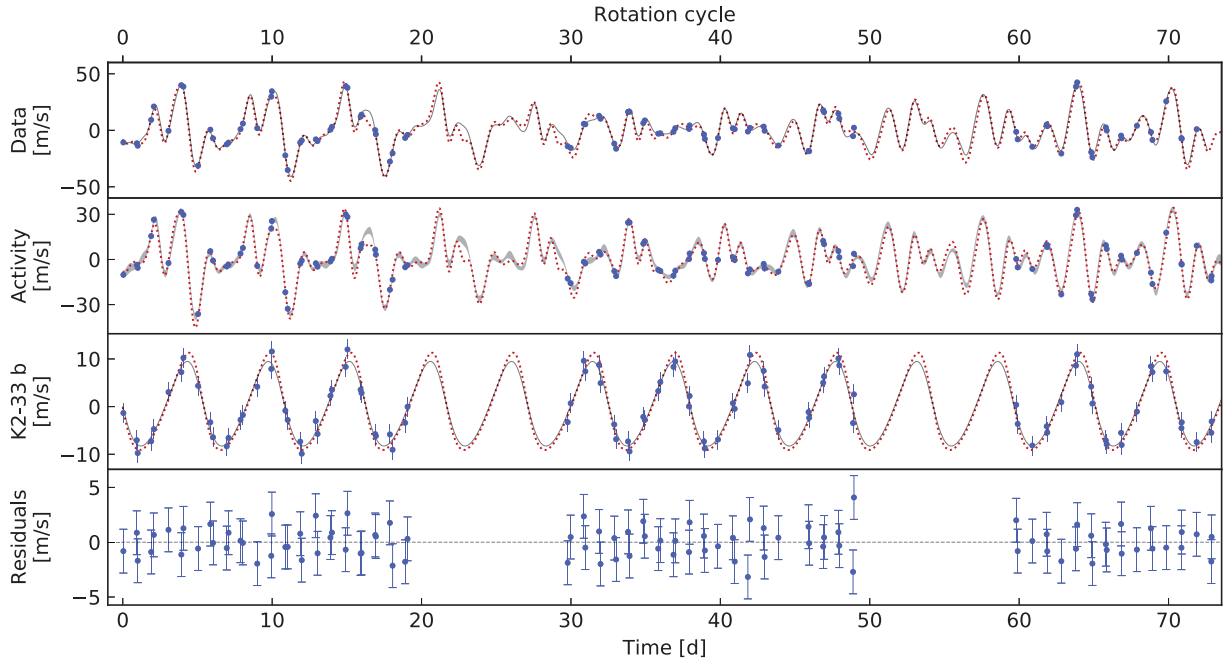

Figure 2.9 – Best fit to a RV time-series of K2-33 assuming an eccentric planet orbit and $K_s = 10\,m\,s^{-1}$. The figure properties are the same as Figure 2.8.

free parameters of the planet RV signature (K_s, e_p and ω from Eq. 1.1) are jointly sampled with the stellar activity parameters in the MCMC process. The best fit to the RV time-series is given in Figure 2.9. We find that data sets of 100 points yield estimates of the eccentricity of the planet orbit with error bars of the order of 0.07, whereas 60 visits over the visibility window of the star would have yielded uncertainties as large as 0.2 on e_p. This confirms that constraining the ellipticity of the planet orbit is expensive in terms of telescope time over one observing season. Hence the choice to focus on the planet mass measurement and to leave the eccentricity measurement for longer-term studies.

Perspectives for K2-33

Two sets of ∼10 spectropolarimetric sequences (i.e., 4 observations) of K2-33 were respectively collected with SPIRou in July-September 2019 and 2020. Each exposure is carried out with an integration time of 675 s, implying that each set of four observations have a S/N[5] of ∼120. A preliminary analysis of the average line profiles measured for K2-33 indicates that the RV error budget is dominated by a photon noise of $\sim 10\,m\,s^{-1}$. Measuring the planet mass from as sparse and noisy a data set as that obtained so far seems challenging. Note that this relatively large value of the photon noise was not anticipated when the simulations were carried out, as SPIRou had barely started observing at the time. The first SPIRou observations allowed us to empirically refine the exposure time requested, especially for faint targets like K2-33. Hence the interest in focusing on brighter stars like AU Mic, more favourable for a RV monitoring with the current capabilities of SPIRou, or in increasing the exposure time of K2-33 observations. This second more ambitious option is confronted with the high pressure on SPIRou's instrument, on the one hand, and with the number of SPIRou observing runs limited by other CFHT instruments that cannot simultaneously observe.

[5] Using the SPIRou exposure time calculator: http://etc.cfht.hawaii.edu/spi/.

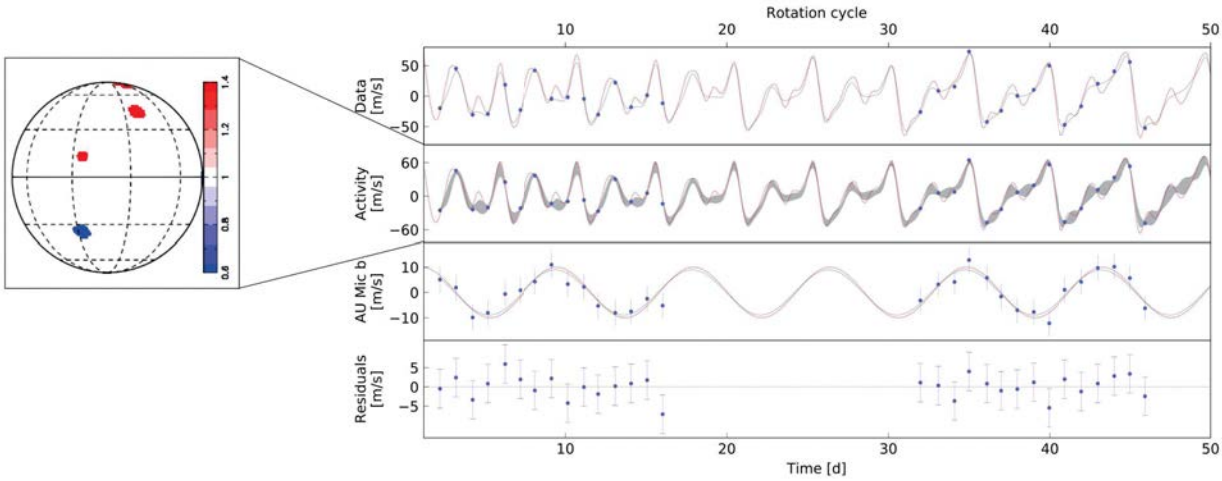

Figure 2.10 – Best fit to a given synthetic RV time-series of AU Mic assuming a circular planet orbit at $K_s = 10\,\mathrm{m\,s^{-1}}$ and a white noise level of $5\,\mathrm{m\,s^{-1}}$ (RMS of the residuals: $3\,\mathrm{m\,s^{-1}}$). The figure properties are the same as Figure 2.8.

2.3.3 Application to AU Microscopii

For AU Mic, we find that 30 visits spread over two consecutive bright time slots will allow to reach a 4σ detection of a planet RV signature of $10\,\mathrm{m\,s^{-1}}$ (i.e., $M_p \sim 20\,M_\oplus$ corresponding to a Neptune bulk density). An example of the best fit to the synthetic RV time-series is shown in Figure 2.10. This encouraging simulation allowed us to obtain 7h of telescope time dedicated to the RV monitoring of AU Mic (PI: Klein). In total, 27 spectropolarimetric observations of AU Mic where collected with SPIRou between September and November 2019. The spectropolarimetric and velocimetric analyses of these observations are respectively described in Section 3.3.1 and Chapter 4.

3 | Modelling the magnetic field and activity of low-mass MS and PMS stars

Contents

Understanding the processes driving the generation and temporal evolution of the magnetic fields of low-mass MS and PMS stars is a prerequisite to study the activity phenomena that they induce. High-resolution spectropolarimetry is the best way to constrain the surface distributions of dark/bright features and magnetic fields of stars and how these distributions are linked to various activity proxies. After reviewing our knowledge of the magnetic fields of low-mass MS and PMS stars in Section 3.1, we describe how optical and nIR spectropolarimetry can be used to constrain surface distributions of magnetic fields and relative brightness as well as study magnetic activity in Section 3.2. We then present our spectropolarimetric analysis of four low-mass MS and PMS stars, AU Mic (with SPIRou), Proxima Centauri (from HARPS-Pol data), EPIC 211889233 (from HARPS-Pol/ESPaDOnS data), and V471 Tau (from ESPaDOnS data) in Section 3.3.

3.1 Context: magnetic field and activity of low-mass stars

3.1.1 Measuring magnetic fields

The activity indicators listed in Section 1.4.1.1 (e.g., chromospheric and coronal emissions) provide us with indirect information on the stellar magnetic field. On the contrary, the Zeeman effect on spectral lines provides us with direct measurements of the strength and geometry of magnetic fields at surface of stars. After describing the physical properties of the Zeeman effect, we briefly introduce its measurement from both unpolarized and polarized spectra as well as the magnetic properties to which it gives access.

3.1.1.1 The Zeeman effect

In this section, we give a brief introduction on the Zeeman effect (Zeeman, 1897) relevant for this study and redirect the reader towards the book of Landi Degl'Innocenti & Landolfi (2004) for a detailed explanation. Under the action of a magnetic field vector $\boldsymbol{B}$, each excitation level E_J of a given element splits into $2J+1$ sublevels of energy[1]:

$$E_{J,M} = E_J + \mu_0 g B M \tag{3.1}$$

where $M \in \{-J, -J+1, ..., J-1, J\}$, μ_0 is the Bohr magneton, and g is the so-called Landé factor of transition J which quantifies its sensitivity to the magnetic field. A transition between an energy level $E_{J,M}$ and another level $E_{J',M'}$ is only possible if $M' - M = \Delta M \in \{-1, 0, 1\}$. As a result, instead of observing a given transition between levels E_J and $E_{J'}$, we observe a total of $4J + 2J' + 1$ transitions referred to as π transitions, when $\Delta M = 0$, and as σ_b and σ_r, when $\Delta M = 1$ and $\Delta M = $-1, respectively.

The mean shift in wavelength $\Delta\lambda_\mathrm{B}$ of a σ component to the reference wavelength λ_0 is given by

$$\Delta\lambda_\mathrm{B} = \frac{\lambda_0^2 e B}{4\pi m_\mathrm{e} c_0^2} = 4.67 \times 10^{-12} \lambda_0^2 g_\mathrm{eff} B \tag{3.2}$$

where B is the magnetic field strength, c_0 the speed of light in the vacuum, and e and m_e, the charge and mass of the electron. The so-called effective Landé factor g_eff (adimensional) quantifies the sensitivity of each line to magnetic fields. This parameter varies from line to line between 0 (no Zeeman splitting) and 3 (highly-sensitive line), and generally lies around 1.2 for usual optical lines (see the illustration of the dependency of the Zeeman splitting on g in Figure 3.1). In the right-handed part of Eq. 3.2, λ_0 is expressed in nm and B in G.

The Zeeman splitting also involves the emission of circularly- and linearly-polarized lights. The light associated to a π transition vibrates along with the magnetic field vector whereas that associated to $\sigma_\mathrm{b,r}$ transitions vibrates circularly in a plane orthogonal to $\boldsymbol{B}$. As a consequence, if the magnetic field vector is parallel to the line of sight, two circularly-polarized signatures of opposite polarities (i.e., the two σ transitions) will be observed (see Figure 3.1). On the other hand, if the magnetic field vector is orthogonal to the line of sight, one will observe one signature linearly-polarized in one direction (associated to the π transition) and two signatures linearly-polarized in the orthogonal direction (associated to the σ transitions).

Diatomic molecules (e.g., FeH, TiO, MgH) can also be sensitive to magnetic fields. They are present in the atmosphere of cold stars (Afram & Berdyugina, 2019), but also in the spots of hotter

[1] Note that this expression is only true in the so-called weak-field approximation, where the spin-orbit interaction dominates over the strength of the external magnetic field, which is the case for the kG fields present at the surface of low-mass stars (Landi Degl'Innocenti & Landolfi, 2004).

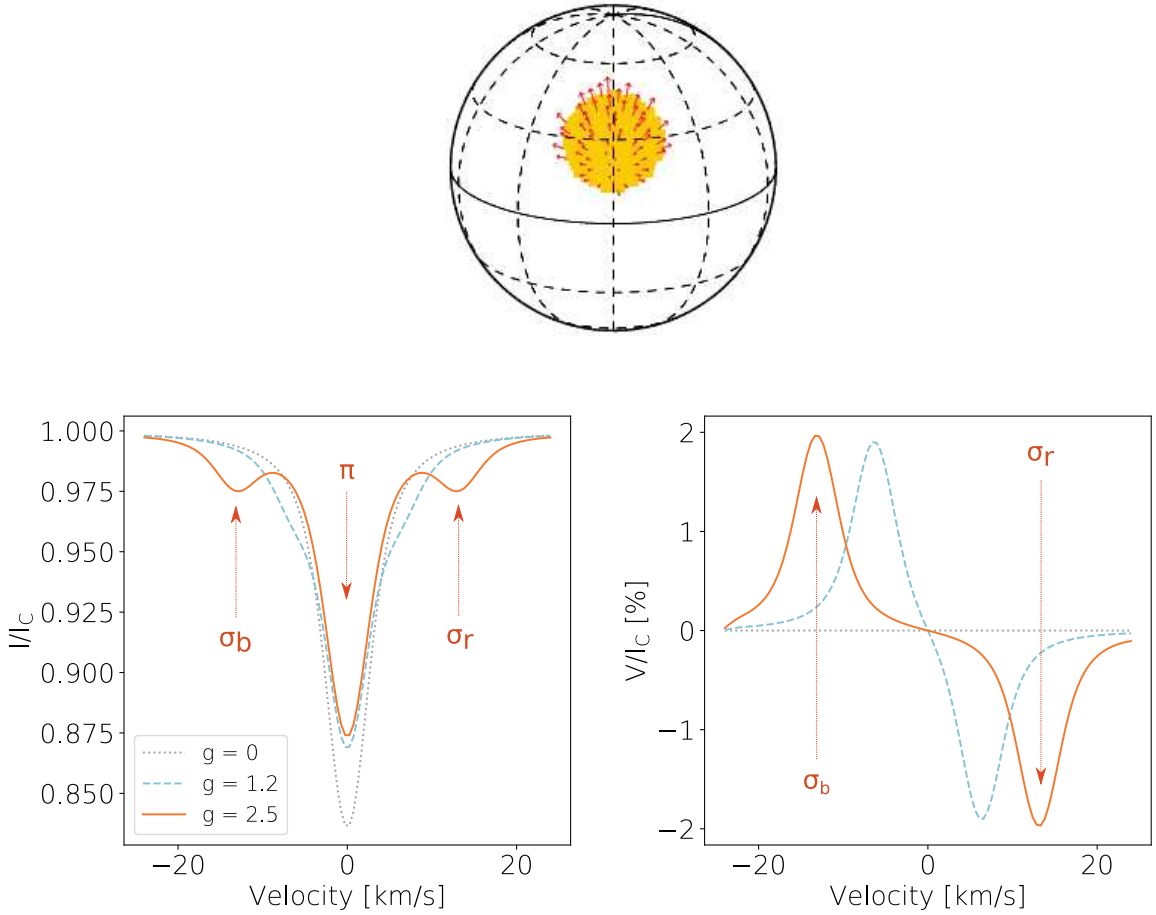

Figure 3.1 – Effect of a 6 kG radial field spot (shown in the top panel; credit: http://www.ast.obs-mip.fr/article.php3?id_article=457) on intensity (Stokes I; bottom left) and circularly-polarized (Stokes V; bottom right) line profiles with Landé factors of 0 (gray dotted line), 1.2 (blue dashed line) and 2.5 (orange solid line).

low-mass stars and can be used to constrain their physical and magnetic properties (e.g., Schadee, 1978; Afram & Berdyugina, 2015). The sensitivity of molecular lines to magnetic fields remains however poorly constrained although progresses in the modeling of these lines have been made on both experimental and theoretical sides (Berdyugina & Solanki, 2002; Berdyugina et al., 2003; Virgo et al., 2005; Afram et al., 2008; Zhang & Steimle, 2014; Afram & Berdyugina, 2015).

3.1.1.2 Measuring magnetic fields from unpolarized spectra

The first way to study the Zeeman effect consists in measuring the Zeeman splitting of unpolarized spectral lines sensitive to magnetic fields. For example, the splitting of the Fe I line at 630.25 nm ($g_{\rm eff} = 2.5$) under a kG-magnetic field is about 2 km s^{-1}. Resolving such a separation on a slowly-rotating star would require an échelle spectrograph with a resolving power as high as 130 000, i.e., larger than the resolving power of most high-resolution spectrographs currently in operation. What is usually done instead is to study how the width of stellar lines with similar formation conditions varies with the magnetic sensitivity (i.e., $g_{\rm eff}$) in order to measure the Zeeman broadening. This method provides the average magnetic field strength B and the fraction f of the stellar surface covered by magnetic regions (Robinson, 1980; Saar, 1988). As these two quantities are somewhat

degenerate, the magnetic flux density Bf is more accurately recovered than those two parameters taken individually.

The extension of this technique to molecular lines, well represented in the spectra of very-low-mass stars, offers an interesting alternative to study the magnetic fields of these stars. In particular, the FeH bands at 0.99 μm (a.k.a. the *Wing-Ford* bands) is composed by several lines with different magnetic sensitivities, which prodives us with an appealing framework to study magnetic fields (Valenti et al., 2001). As mentioned in the previous section, these lines lack precise measurements of their effective Landé factor. To overcome this challenge, Reiners & Basri (2006) proposed to compare the observed FeH forest to the spectra of two reference stars known for their respectively strong and weak magnetic fields. This technique has been successfully applied to very-low-mass stars (Reiners & Basri, 2007, 2008; Reiners et al., 2009), providing us with a first order measurement of the magnetic flux density for a statistically significant number of stars. Detecting stellar magnetic fields is also easier in the nIR where the Zeeman broadening is enhanced. For example, a line with $g_{\rm eff} = 2.5$ under a magnetic field of 1 kG exhibits a Zeeman splitting of 7.7 km s^{-1} at 2.2 μm (i.e., 3 times larger than at 630 nm). This technique is all the more interesting for cold stars emitting mostly in the nIR (i.e., M dwarfs and low-mass PMS stars; e.g., Saar & Linsky, 1985; Valenti et al., 1995; Johns-Krull et al., 1999b; Johns-Krull, 2007).

However, note that magnetic field measurements from the Zeeman broadening of unpolarized spectral lines essentially inform us about the disk-integrated magnetic field strength and are no more than weakly sensitive to the geometry of the field at the stellar surface.

3.1.1.3 Measuring polarized Zeeman signatures

The study of polarized Zeeman signatures provides us with complementary magnetic properties to those obtained from the broadening of unsigned spectral lines. The detection of circularly- and linearly-polarized Zeeman signatures allows us to unambiguously detect stellar magnetic fields (contrary to the broadening of unpolarized spectral lines which can be induced by various non-magnetic effects). Moreover, Zeeman signatures in circular and linear polarization are sensitive to the direction of the magnetic field vector with respect to the line of sight, allowing one to access the magnetic field geometry at the stellar surface. However, magnetic regions of opposite polarities induce Zeeman signatures that cancel out. As a result, the observed polarized Zeeman signatures probe no more than the largest spatial scales of the magnetic field and are weakly sensitive to the disk-integrated magnetic flux density.

The amplitude of circularly-polarized Zeeman signatures is generally small for low-mass stars (of the order of 0.1% in general for active low-mass stars) and requires dedicated high-resolution spectropolarimeters (e.g., ESPaDOnS, NARVAL; Donati et al., 2006b) to be firmly detected. Even then, individual polarized signatures remain generally drowned into the noise and one must combine all the available individual lines into an average profile in order to unveil circularly-polarized Zeeman signatures (see Section 3.2.1). Linear polarization signatures, whose amplitude is generally an order of magnitude lower than that of circularly-polarized Zeeman signatures, are generally undetected for low-mass stars (Donati et al., 1997).

By collecting high-resolution polarized spectra densely sampling the rotation cycle of a star, one can access the distribution of the large-scale field vector at its surface. This is done using Zeeman-Doppler Imaging (ZDI; Semel, 1989; Donati et al., 1989; Semel et al., 1993; Brown et al., 1991; Donati & Brown, 1997; Donati, 2001; Donati et al., 2006c), a tomographic technique inspired from DI, which is described in Section 2.2 and Appendix A.1.

3.1.2 Magnetic fields of M dwarfs and low-mass PMS stars

The processes describing how the magnetic fields of low-mass stars are generated and sustained against turbulent magnetic dissipation are described by the so-called dynamo theory (see Rincon, 2019, for a comprehensive review of stellar and planet dynamo theories). In the case of the Sun, the evolution of the magnetic field vector, described by its poloidal and toroidal components (Chandrasekhar, 1961), is best explained by the so-called $\alpha\Omega$ paradigm (Parker, 1955; Babcock, 1961; Leighton, 1969). Starting from a purely poloidal large-scale field at the minimum of the solar magnetic cycle, differential rotation (DR) shears the field lines until the large-scale magnetic field is largely toroidal, at solar maximum (Ω effect). Under the effect of helical turbulence (i.e., the field lines rising with ascending convective cells get twisted by stellar rotation under the Coriolis force), the toroidal field is progressively converted into a poloidal field of opposite polarity (α effect). By mapping the internal rotation structure of the Sun, asteroseismology has unveiled a thin layer of intense shear separating the convective zone (sheared by DR) from the radiative zone (Spiegel & Zahn, 1992). This zone, called *the tachocline*, is thought to play a critical role in the generation of sustainable toroidal fields by the Ω effect (e.g., Brun et al., 2004; Browning et al., 2006). Note however that the role of the tachocline in the Solar dynamo processes still remains actively debated in the literature (e.g., Brown et al., 2010; Wright & Drake, 2016). Other types of dynamo exist (e.g., α^2, $\alpha^2\Omega$; see Rincon, 2019) but do not describe the Sun's magnetic field generation and evolution as well as the $\alpha\Omega$ dynamo theory.

By analogy with the Sun, the existence of magnetically-driven activity phenomena (e.g., chromospheric emission in Ca H & K, and Hα cores, X-ray/radio coronal emissions, surface inhomogeneities, flares) along with strong surface magnetic fields suggests that M dwarfs and low-mass PMS stars are able to generate and maintain magnetic fields through dynamo processes. This is further confirmed by the fact that the activity and surface magnetic fields of these stars scale up with the Rossby number, as predicted by dynamo theories (see Section 1.4.1.1 and Figure 1.11, and Wright et al., 2011; Vidotto et al., 2014b; Folsom et al., 2016; Shulyak et al., 2017; Wright et al., 2018). The magnetic fields of partly-convective low-mass stars, which possess a tachocline, are thought do be driven by $\alpha\Omega$ dynamo processes. In contrast, fully-convective (FC) stars (i.e., M dwarfs less massive than $0.35\,M_\odot$ and PMS stars on the Hayashi track) do not possess a tachocline and both observational and theoretical studies suggest that they rotate almost as solid bodies[2] (e.g., Johns-Krull, 1996; Kuker & Rudiger, 1997; Barnes et al., 2005; Küker & Rüdiger, 2005; Morin et al., 2008a; Donati et al., 2015). If this hypothesis is valid, the Ω effect can no longer twist the field lines and the magnetic field of these stars must be generated by another type of dynamo process.

Non-solar dynamo processes mostly based on the α effect have been invoked to explain the generation of magnetic fields in low-mass FC stars. Assuming that these stars rotate as rigid bodies, Küker & Rüdiger (1999) and Chabrier & Küker (2006) found that α^2 dynamo processes (i.e., purely turbulent) could generate a non-axisymmetric poloidal large-scale field for FC PMS stars and M dwarfs, respectively. Subsequent global simulations found that this non-axisymmetric poloidal large-scale field could be associated with a significant antisolar surface DR (Dobler et al., 2006), whereas Browning (2008) found a strong toroidal component along with a weak surface DR. These predictions were hard to reconcile with the mostly poloidal axisymmetric large-scale field found spectropolarimetric observations of FC M dwarfs (Donati et al., 2006a; Morin et al., 2008a,b).

Further spectropolarimetric observations of FC M dwarfs in the saturated dynamo regime have revealed a bimodal distribution of their magnetic properties with either strong axisymmetric dipoles, or weaker non-axisymmetric complex fields[3] (see Morin et al., 2010, and the period-mass diagram shown in Figure 3.2). Tentative explanations of this distribution involve either a bistable

[2] Note that the lack of DR highlighted for FC stars only relate to the stellar surface though.

[3] The topology of the magnetic field is called complex when configurations of smaller scale than the dipole (e.g., quadripolar, octupolar or higher order components) occupy a significant fraction of the reconstructed magnetic energy.

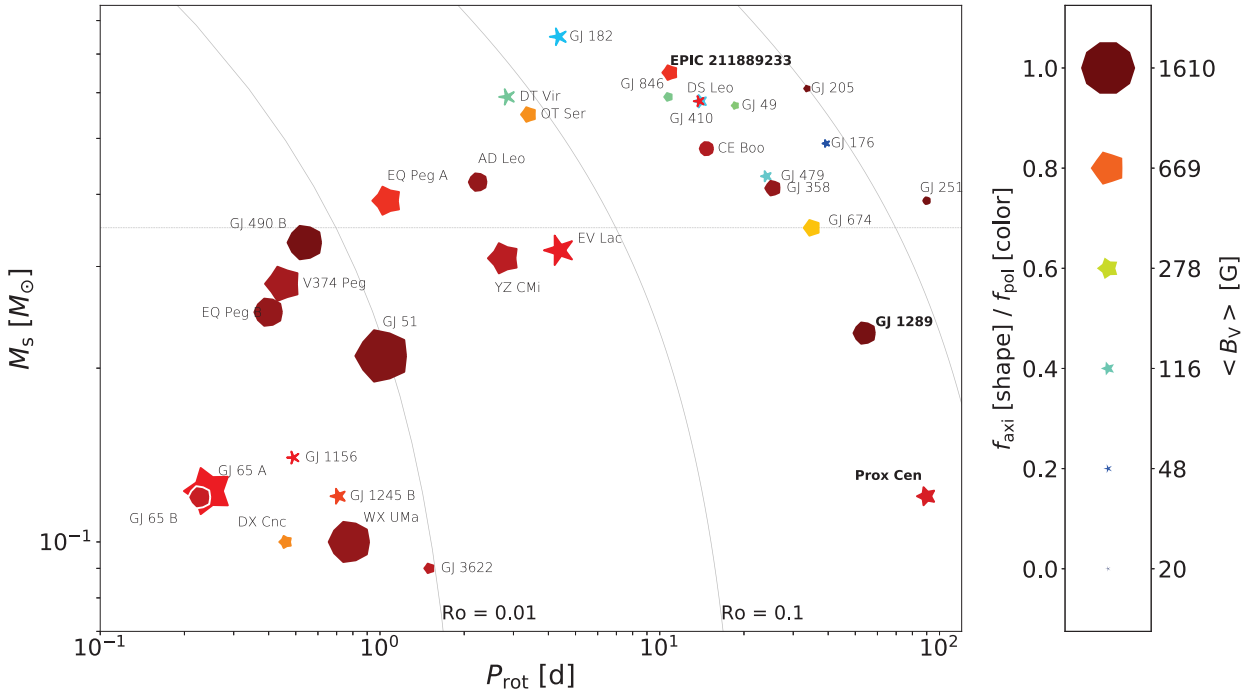

Figure 3.2 – Rotation period-mass diagram of M dwarfs with reconstructed magnetic topologies. The size and shape of the symbols indicate the strength and degree of axisymmetry of the reconstructed magnetic field (with decagons and stars standing respectively for purely axisymmetric and purely non-axisymmetric topologies). The color of the symbols depicts the fraction of poloidal field in the reconstructed magnetic energy (with dark red and dark blue standing respectively for pure poloidal and pure toroidal large-scale magnetic fields). The horizontal dotted line indicates the theoretical full-convection threshold ($\sim$0.35 $M_\odot$; Baraffe et al., 1998, 2015). Contours of constant Rossby numbers of 0.01, 0.1 and 1, computed using the empirical relation of Wright et al. (2018) (based on FC M dwarfs), are shown in gray solid lines. Except for Proxima Cen and EPIC 211889233, the magnetic properties of the stars shown in the diagram originate from Donati et al. (2008b); Morin et al. (2008b); Phan-Bao et al. (2009); Morin et al. (2010); Hébrard et al. (2016); Kochukhov & Lavail (2017); Moutou et al. (2017)

dynamo process depending on the density stratification in the stellar interior (Morin et al., 2011; Gastine et al., 2012, 2013), or an oscillatory dynamo that would alternate between the two observed topologies (Kitchatinov et al., 2014). As shown in Figure 3.2, most of the available observational results relate to stars in the saturated dynamo regime and the large-scale fields of slowly-rotating FC M dwarfs are poorly-constrained. As things stand, the dynamo processes powering the magnetic fields of low-mass FC stars remain unclear and additional spectropolarimetric observations of FC M dwarfs with different *Ro* are needed to constrain theoretical models.

Spectropolarimetric observations have revealed that M dwarfs more massive than 0.5 $M_\odot$ exhibit relatively weak large-scale magnetic fields (of a few tens to hundreds of Gauss), preferentially weakly axisymmetric and featuring a strong toroidal component (sometimes dominant), along with significant DR (see Figure 3.2 and Donati et al., 2008b; Hébrard et al., 2016). Partly-convective stars of mass lower than $\sim$0.5 $M_\odot$ exhibit a dominant axisymmetric poloidal field with increasing strength as the stellar mass decreases (Morin et al., 2008b). This transition is likely due to a change in the dynamo process, switching from a regime where the magnetic field generation takes place at the base of the convective zone, for early M dwarfs, to a regime where dynamo processes are distributed in the whole convective zone, as stellar interiors get largely/fully convective. Further spectropolarimetric observations of early M dwarfs with mass between 0.35 and 0.5 $M_\odot$ are needed to investigate how this transition operates.

Large-scale magnetic topologies of cTTSs and wTTSs were reconstructed as part of the *Magnetic Protostars and Planets* (MaPP; e.g., Donati et al., 2011a, 2010, 2012) and of the *Magnetic Topologies of Young Stars and the Survival of massive close-in Exoplanets* (MaTYSSE; e.g., Donati et al., 2014; Yu et al., 2017; Hill et al., 2017) programs. Most of the studied FC PMS stars were found to harbor strong (at the kG level) mainly poloidal and axisymmetric large-scale fields[4] (Donati et al., 2008a, 2012, 2015), resembling those of FC M dwarfs (Gregory et al., 2012). Older mostly radiative PMS stars harbor much more complex topologies, preferentially non-axisymmetric and often with a strong toroidal component (Folsom et al., 2016; Yu et al., 2017). This difference in topology is thought to arise from a change in the dynamo process induced by the development of a radiative core when stars leave the Hayashi tracks (Donati et al., 2011b; Gregory et al., 2012), even though this assumption has been lately questioned in Hill et al. (2019). As things stand, due to a lack of observational constraints on the evolution of stellar magnetic topologies during the early PMS stages, the physical mechanisms driving the transition in the dynamo processes between FC and partly-convective stars remain unclear.

3.1.3 Magnetic interactions between stars and close-in planets

Close-in planets strongly interact with their host star. In addition to the large irradiation that they endure (e.g., Lammer et al., 2009; Bourrier et al., 2016; Ribas et al., 2016), they experience tidal forces (e.g., Bolmont & Mathis, 2016; Bolmont et al., 2017) and evolve in a highly-magnetized environment (e.g., Strugarek et al., 2014, 2015; Folsom et al., 2020). Star-planet interactions (SPIs) can cause the star to exhibit enhanced magnetic activity (e.g., tidal interactions, superflares, stellar hotspots, or even a change in the stellar dynamo; see Cuntz et al., 2000; Rubenstein & Schaefer, 2000; Shkolnik et al., 2005; Abreu et al., 2012; Strugarek et al., 2019). Detectable effects of SPI on the planetary side are much less numerous. For example, intense stellar flares and coronal mass ejections could induce detectable signatures on the planet atmosphere such as auroral radio emissions, allowing one to constrain the planet magnetic field (Zarka, 2007; Vidotto et al., 2012; Vidotto & Donati, 2017; Vidotto et al., 2019).

Stellar winds and flares affect the atmospheric and habitability conditions of HZ planets orbiting very-low-mass stars (Selsis et al., 2007). The interaction between the stellar wind and a close-in planet depends on whether the magnetic field lines of the stellar magnetosphere are open or not at the position of the planet. This relies on the so-called Alvèn surface, i.e., the location where the velocity of the stellar wind reaches the local Alvèn velocity $v_{\rm A} = B\sqrt{4\pi\rho}$, ρ being the density of the wind particles. Outside the Alvèn surface, the magnetic field lines are expected to open under the effect of the wind ram pressure. For rapidly rotating stars with corotation radius $r_{\rm co}$ significantly smaller than the typical radius $r_{\rm A}$ of the Alvèn surface, field lines open under the effect of centrifugal forces, leading the wind particles to quickly drag the magnetic field beyond $r_{\rm co}$ and reducing thereby the size of the Alvèn surface. If the planet orbits inside the Alvèn surface, the star and the planet magnetospheres are connected and, as a result, any change in stellar magnetic field will be propagated to the planet magnetosphere and vice versa (in the so-called sub-afvenic regime; see Strugarek et al., 2015). Beyond the Alvèn surface, wind particles reach the planet atmosphere at a supersonic speed (relative to $v_{\rm A}$) and no direct connection between the two magnetospheres exists. In this case, the high kinetic energy of the wind particles may drive the evaporation of the planet atmosphere with an efficiency depending on whether the planet harbours a magnetosphere large-enough to deflect the incoming wind particles. The Alfvèn surface of a star can be computed using 3D magnetohydrodynamical simulations from the surface distribution of the large-scale magnetic field reconstructed with ZDI (e.g., Vidotto et al., 2009, 2011; Vidotto & Donati, 2017; Folsom et al.,

[4] Note that a couple of FC PMS stars, LkCa 4 (Donati et al., 2014) and V410 Tau (Yu et al., 2019), exhibit a strong toroidal component whose origin remains unclear.

2018, 2020).

3.1.4 Modeling stellar activity to improve the filtering of the RV jitter

Understanding the origin of the stellar activity RV signals exhibited by low-mass stars is a key goal to detect Earth-like planets and obtain an accurate determination of their mass. Inverting the fluctuations of the RV jitter into the activity phenomena that generate the latter is degenerated as the stellar surface is not resolved. The properties and inner structure of G-K stars is relatively similar to those of the Sun which thus represents a prime laboratory to identify the activity phenomena producing RV activity signals and come up with a solution to correct them in RV observations (e.g., Lagrange et al., 2010; Meunier et al., 2010; Meunier & Lagrange, 2013; Haywood et al., 2016; Collier Cameron et al., 2019; Haywood et al., 2020; Dumusque et al., 2020). M dwarfs and low-mass PMS stars feature different properties than their solar-like counterparts (e.g., rotation rate, size of the convective zone, convective turnover times) that likely affect the balance of the various RV contributions of the activity phenomena they exhibit (e.g., Beeck et al., 2015). This is especially true for largely- of fully-convective stars (i.e., M dwarfs of mass lower than $0.5\,M_{\odot}$ and young PMS stars) whose magnetic properties likely result from processes other than those of their partly-convective counterparts (as shown in Section 3.1.2).

Hence the need to carry out simultaneous long-term measurements of various activity indicators of low-mass MS/PMS stars, in order to compare their evolution and come up with optimized methods to model and correct their activity-driven RV signals. Combining photometry, spectroscopy and velocimetry succeeds in yielding accurate models for stellar activity RV signals of G-K stars (e.g., Aigrain et al., 2012; Haywood et al., 2014; Rajpaul et al., 2015; Santerne et al., 2018; Lopez et al., 2019). Spectropolarimetry and Zeeman-Doppler imaging has the additional potential to simultaneously probe the distribution of the brightness and large-scale magnetic field at the stellar surface, making it possible to remove some degeneracies in the RV reconstruction process (Hébrard et al., 2016). Hence the goal of a project, led by Théo Lopez (at LAM), consisting in observing targets of various spectral types in the TESS continuous viewing zone using velocimetry with SOPHIE and spectropolarimetry with ESPaDOnS/NARVAL.

In this chapter, we describe how spectropolarimetry can help to improve our understanding of the dynamo processes at work in the interior of low-mass MS/PMS stars and of the various manifestations of stellar activity and their velocimetric contributions. The spectropolarimetric analysis of low-mass stars present a few specificities that are detailed in the next section. We then describe the spectropolarimetric analysis of four K2 to M5.5 dwarfs and their implications on our understanding on the magnetic activity of low-mass stars.

3.2 Spectropolarimetric analysis of low-mass stars

3.2.1 Spectropolarimetric measurements and data reduction

Collecting spectropolarimetric data

A spectropolarimeter is the combination of a module that analyses the polarisation of the incoming light (the polarimeter) and a spectrograph. The general principle of a spectropolarimeter is illustrated in Figure 3.3. In the polarimeter, the light travels first through an *achromatic retarder waveplate* (e.g., Fresnel rhombs; see Donati et al., 2006b) that imposes a phase change between the two components of orthogonal polarization and, thus, alters the polarization of the light. In a second step, the light beam passes through the so-called *analyser* (e.g., Wollaston prism), that splits the beam into light waves of orthogonal polarization states, $I_{\parallel}$ and $I_{\perp}$. Both light beams are then directed to the spectrograph where they are decomposed in the wavelength space.

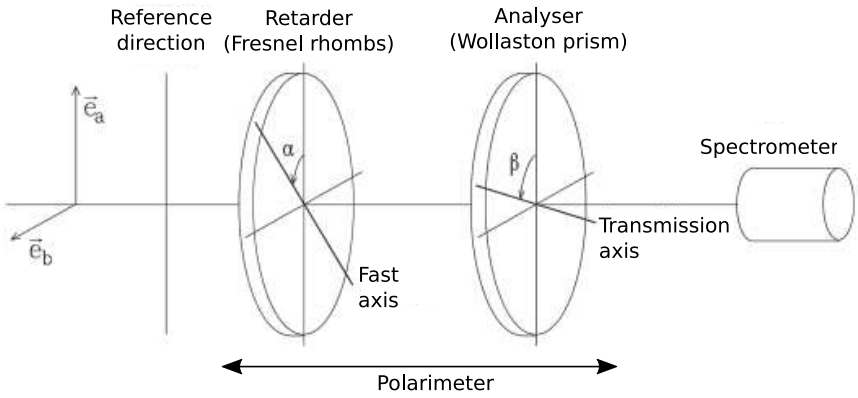

Figure 3.3 – Schematic representation of the polarimetric module of a spectropolarimeter (adapted from Landi Degl'Innocenti & Landolfi, 2004).

Table 3.1 – Main features of the spectropolarimeters used in this chapter.

Instrument	Telescope	Spectral range [nm]	Resolving power	Throughput	RV precision [m s^{-1}]	Reference
ESPaDOnS	CFHT (3.6 m)	350 - 1050	68 000	10-15% at 550 nm	20	Ma03, Do06
NARVAL	TBL (2 m)	350 - 1050	68 000	10-15% at 550 nm	20	–
HARPS-Pol	La Silla (3.6 m)	378 - 691	100 000	2-3% at 550 nm	1	Ma03, Sn11
SPIRou	CFHT (3.6 m)	980 - 2350	70 000	3.5% (Y) to 12% (K)	2 (goal 1)	Do18, Do20

A spectropolarimetric sequence consists of four successive sub-exposures, each characterized by a different angle of the retarder waveplate (45°,135°,225°,315°). The four Stokes parameters I, Q, U and V are obtained by combining together the subexposures in a way to remove systematics and correct for the most prominent spurious signatures in polarized spectra (Donati et al., 1997; Bagnulo et al., 2009). In particular

$$\left\{ \begin{array}{rcl} I & = & \sum_{i=1}^{4} I_{i,\parallel} + I_{i,\perp} \\ V & = & I \frac{R-1}{R+1} \end{array} \right. \tag{3.3}$$

where I and V refers to intensity and circularly-polarized spectra, and where

$$R^4 = \frac{I_{1,\parallel}/I_{1,\perp}}{I_{2,\parallel}/I_{2,\perp}} \frac{I_{4,\parallel}/I_{4,\perp}}{I_{3,\parallel}/I_{3,\perp}}. \tag{3.4}$$

The spectropolarimeters used in this manuscript are listed in Table 3.1. Note that, contrary to HARPS and SPIRou, ESPaDOnS and NARVAL are not designed to measure precise RVs (typical relative RV precision of 20-30 m s^{-1}, see Moutou et al., 2007). In practice, the data reduction and optimal combination of the four subexposures within each polarization sequence is carried out using the fully automated pipeline Libre ESpRIT (Donati et al., 1997, 2006b), which was originally designed and implemented for ESPaDOnS and NARVAL spectropolarimeters, then adapted for HARPS-Pol (Hébrard et al., 2016) and SPIRou (Donati et al., 2020a). The spectra obtained by combining sub-exposures corresponding to identical azimuths (in terms of polarimetric analysis) of the retarder waveplate (positions (1,2) and (3,4)) are called Null spectra as, in principle, they only contain white noise (e.g., Donati et al., 1997).

Least-squares deconvolution

The observed spectra feature a wealth of spectral lines which enclose information about brightness inhomogeneities (through the distortions of line profiles) and magnetic fields (through the Zeeman signatures in Stokes I and V profiles) at the stellar surface. However, as mentioned in Section 3.1.1, the typical signatures produced by surface active regions on individual lines are generally drowned in the noise (e.g., Donati et al., 1992). Hence the need to combine information from a large number of individual lines in order to boost the S/N of Stokes I and V line profiles. This is done by applying Least-Squares Deconvolution (LSD; Donati et al., 1997; Kochukhov et al., 2010) to the intensity and circularly-polarized spectra.

This cross-correlation technique is based on the fact that spectral lines show more or less the same profiles, in particular in the case of moderate to rapid rotators ($v \sin i_{\rm rot} > 10\,{\rm km\,s^{-1}}$, where $i_{\rm rot}$ is the stellar inclination). From a given template of $N_{\rm l}$ line profiles, the observed spectrum $\boldsymbol{Y}$ (Stokes I or V) is thus approximated by

$$\boldsymbol{Y} = \boldsymbol{M}\boldsymbol{F} \tag{3.5}$$

where $\boldsymbol{M}(v) = \sum_{i=1}^{N_{\rm l}} \omega_i \delta(v - v_i)$ is a line mask, ω_i and v_i being respectively the weight and position associated to line i, and v, the velocity coordinate. The line profile $\boldsymbol{F}$ is simply estimated using a linear least-squares estimator (see Appendix A.2.3).

The choice of the line mask depends on the kind of information to be extracted from the line profile. For magnetic analyses, one must know the sensitivity of each line to the magnetic field (i.e., its Landé factor). Hence the choice of atomic line masks generally computed using an ATLAS9 local thermodynamical equilibrium (LTE) stellar atmosphere model (e.g., Kurucz, 1993; Gustafsson et al., 2008) using the values of $T_{\rm eff}$ and $\log g$ of the star of interest[5]. As mentioned in Donati et al. (1997), only moderate-to-strong lines are included in the mask (typically with depth larger than 40%), in order for shallow lines (numerous in the spectra low-mass stars) not to be over-represented in the line list. In contrast, high-precision velocimetric analyses require the use of denser mask of atomic and molecular lines, generally empirically built for M dwarfs (e.g., Bonfils et al., 2013). For nIR high-precision velocimetric analyses (e.g., with SPIRou), one has to ensure that the lines of the template are not contaminated by telluric lines (see Moutou et al., 2020).

As a safety check, LSD is also applied to the Null spectra in order to identify uncorrected systematic noise in polarized spectra. Spurious signatures in Null LSD profiles will be falsely interpreted as signatures of toroidal magnetic field, resulting in an erroneous magnetic analysis. When identified, we thus filter the correlated signatures in the Null LSD profile by modelling the median Null profile using a Gaussian function, linearly adjusting the amplitude of this Gaussian function to match the spurious signatures observed in each NULL LSD profile, and subtracting the best model from the corresponding Stokes V LSD profile.

3.2.2 Mapping brightness inhomogeneities at the surface of low-mass stars with Doppler Imaging

We first consider intensity spectra alone, and, in particular, the line profiles extracted using LSD (called Stokes I LSD profile in the following). As introduced in Section 1.4.2, DI (carried out with our ZDI code) allows one to invert the time series of observed Stokes I LSD profiles, $\boldsymbol{I}$, into a maximum-entropy brightness distribution at the surface of the star (see the detailed description of the process in Appendix A.1). For moderate to fast rotators ($v \sin i_{\rm rot} \gtrsim 10\,{\rm km\,s^{-1}}$), the Stokes I

[5] We generally compute the line mask using the VALD3 data base: http://vald.astro.uu.se/~vald/php/vald.php.

LSD profiles are dominated by the Doppler broadening of the star and, therefore, the contribution of each feature of the stellar disk to the line profile is well-recovered under standard DI approximations. In contrast, the intrinsic profile at the surface of the star significantly contributes to the width of the Stokes I LSD profiles for slowly-rotating stars. In this case, the imaging code will likely concentrate on trying to correct systematic differences between observed and synthetic intrinsic profiles rather than on modeling the profile variations, which contain the genuine material we aim at modeling. Here, we present two independent methods to get rid of most of the systematics between observed and synthetic profiles.

Method 1: Residuals method

This first method, introduced in Hébrard et al. (2016), focuses on reconstructing profile distortions induced by non-axisymmetric spots (i.e., dark features) rotating with the star. This assumption seems legitimate for early M dwarfs, that tend to be dominated by dark features (Beeck et al., 2015; Baroch et al., 2020; Panja et al., 2020), whereas it remains unclear for late fully-convective M dwarfs (e.g., Barnes et al., 2015; Yadav et al., 2016; Morris et al., 2018a). In the ZDI reconstruction process, the relative brightness b of the spots is assumed constant for all spots, and we reconstruct the fraction C_i of photosphere within each cell i ($C_i = 0$ corresponding to a entirely spotted cell), such that the local profile is given by

$$\boldsymbol{I}_i = C_i \boldsymbol{I}_i^{(p)} + b(1 - C_i)\boldsymbol{I}_i^{(s)} \tag{3.6}$$

where $\boldsymbol{I}^{(p)}$ and $\boldsymbol{I}^{(s)}$ are the local profiles respectively associated to quiet and spotted regions of the stellar surface. $\boldsymbol{I}^{(s)}$ has the possibility to be redshifted to simulate the inhibition of the convective blueshift in active regions of Solar-like stars (even though this effect is expected to be small for M dwarfs, as shown in Meunier et al., 2017; Baroch et al., 2020).

To get rid of systematic differences between observed and synthetic line profiles, the median line profile $\bar{\boldsymbol{I}}$ is computed in the stellar rest frame and subtracted from each line profile, resulting in a time series of residual Stokes I LSD profiles $\boldsymbol{I_r}$. In principle, most of the profile distortions are retained as they vary from one observation to the other. We empirically build a synthetic intrinsic line $\bar{\boldsymbol{I}}'$ profile by adjusting the parameters of the line profile (e.g., depth and width) until $\bar{\boldsymbol{I}}'$ matches $\bar{\boldsymbol{I}}$. Finally, we build a new set of profiles $\boldsymbol{I}' = \bar{\boldsymbol{I}}' + \boldsymbol{I_r}$ that we now can reconstruct with ZDI as $\boldsymbol{I}'$ is now perfectly know.

Method 2: Iterative procedure for systematics removal

In this second method lately implemented in Klein et al., (2020b), we use an iterative process to ensure that the average observed and synthetic line profiles perfectly match so that the ZDI reconstruction concentrates on the profile variations rather than on systematic differences between the model and the observations. We perform a maximum-entropy brightness reconstruction of $\boldsymbol{I}$ with ZDI which generates a time series of synthetic profiles $\boldsymbol{I_s}$. We then subtract the median difference between $\boldsymbol{I}$ and $\boldsymbol{I_s}$ from $\boldsymbol{I}$ and repeat the procedure until the median difference between $\boldsymbol{I}$ and $\boldsymbol{I_s}$ is flat. Note that this method no longer assumes that only dark spots are present at the stellar surface and reconstructs the brightness distribution at the surface of the star rather than the spot occupancy.

Comparison of the two methods

The performance of the two methods for reconstructing the distortions induced by stellar inhomogeneities on the line profiles of slowly-rotating stars is evaluated on synthetic data. We created

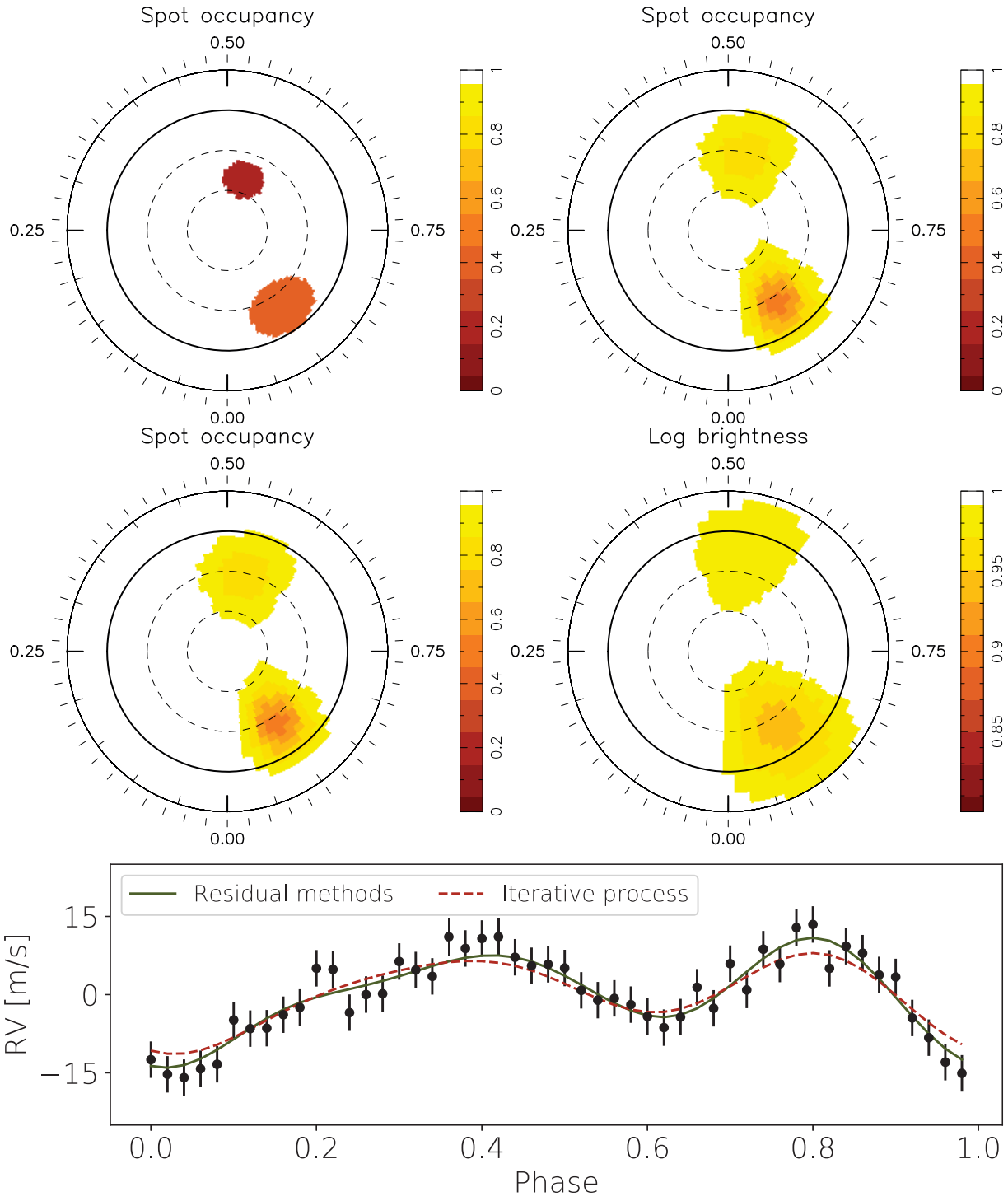

Figure 3.4 – Reconstructed spot distributions at the surface of a synthetic star of $v \sin i_{\rm rot} = 1\,{\rm km\,s^{-1}}$ and $i_{\rm rot} = 60°$. *Upper left:* synthetic spot distribution to reconstruct (total equivalent area of 1.5%). *Upper right:* Reconstruction of the spot occupancy (i.e., filling factor, see Eq. 3.6) assuming that the intrinsic profile of the Stokes I LSD profiles to reconstruct is known. *Middle left:* Same but using the residuals method (i.e., method 1) to reconstruct the spot distribution. *Middle right:* Distribution of surface brightness (note the change in the color scale) reconstructed with ZDI assuming an intrinsic profile 1% narrower than the line profile of the simulated star, and using method 2 to iteratively correct for systematic differences between observed and synthetic line profiles. Note that we assume that only dark spots are present at the stellar surface for the reconstruction. *Bottom:* Comparison of the RVs of the lines profiles modeled using method 1 (green solid line) and method 2 (red dashed line). The black points are obtained by measuring the RVs of the synthetic line profiles computed from the brightness maps using ZDI.

a synthetic star assuming $v \sin i_{\rm rot} = 1\,{\rm km\,s^{-1}}$ and $i_{\rm rot} = 60°$ to which we added two spots of relative brightness $b = 0.5$ and relative area of 3% and 1.5% with filling factors of 60% and 80% at latitudes 20° and 50°, respectively (the surface of the synthetic star is shown in the upper left panel of Figure 3.4). The synthetic star thus features an equivalent spot coverage of 1.5%[6]. From the simulated stellar surface, we create a time series of 50 synthetic line profiles (see the detailed process in Appendix A.1.1) assuming a regular coverage of the stellar rotation cycle. We finally add a random noise to the data so that the S/N of each profile is ∼4000, which is typically what is obtained for our HARPS Stokes I LSD profiles of EPIC 211889233 (see Section 3.3.3).

To ensure that our simulated data set is exploitable by ZDI, we first carry out a reconstruction of the spot coverage at the stellar surface assuming that the intrinsic profile of the star is perfectly known (see the upper right panel of Figure 3.4). We then apply the two methods described above to reconstruct the surface distributions of spot coverage and relative brightness with ZDI, assuming this time that the intrinsic profile of the star is unknown. To ensure that method 2 is accurately correcting for systematic differences between observed and synthetic profiles, we decrease the width of the intrinsic profile used in the brightness reconstruction process by 1%. The resulting spot coverage maps are shown in the middle panels of Figure 3.4. Both methods yield similar spot distributions with equivalent spot coverages of 1.4%. Note that method 2 provides a slightly different brightness distribution than method 1, which might be attributed to the fact that we reconstruct the brightness rather than spot occupancy. The consistency between methods 1 and 2 is further evidenced by the similar RV curves associated to the two reconstructed stellar surfaces. Note that method 2 is significantly easier to implement and less time-consuming than method 1.

3.2.3 Reconstructing large-scale magnetic topologies of low-mass stars with ZDI

We use ZDI to invert a time series of circularly-polarized Zeeman signatures into a distribution of the large-scale magnetic field vector at the surface of a given star. In this section, we summarize the application of the inversion process to low-mass stars and redirect the interested reader to the detailed description of ZDI in Appendix A.1. In short, ZDI decomposes the large-scale magnetic field into its poloidal and toroidal components, both expressed as weighted sums of spherical harmonics as described in Donati et al. (2006c). The weights are chosen to favour the magnetic structures at the largest spactial scales (e.g., dipole). As a result of their small radii, M dwarfs usually have low $v \sin i_{\rm rot}$ which limits the resolution (i.e., the number of cells) of the reconstructed maps[7] and, thus, the order $l_{\rm max}$ of the spherical harmonic expansion ($l_{\rm max}$ is typically of the order of 5 for slowly-rotating M dwarfs; see Morin et al., 2008b, 2010).

Circularly-polarized Zeeman signatures are characterized by their amplitude (linked to the large-scale magnetic flux density B_V), and their overall width, which depends on the magnetic strength B. For slowly-rotating low-mass stars (especially late M dwarfs), assuming that $B = B_V$ in the reconstruction process often yields too narrow synthetic Stokes V line profiles unable to fit the width of the observed signatures to the noise level. Following Morin et al. (2008b), we introduce two filling factors f_I and f_V, constant over the stellar surface, defined as the fraction of each cell containing small- and large-scale magnetic field, respectively (see Appendix A.1.1 for the mathematical expressions of f_I and f_V). As a result, inverting the observed Stokes V LSD profiles with ZDI yields a large-scale magnetic flux density $B_V = B f_V$, meaning that a magnetic field B is present on a relative area f_V with respect to the whole stellar surface. f_V and f_I are

[6] The equivalent spot coverage is defined as $b \sum_{i=1}^{n_{\rm spot}} s_i\, C_i$, where $n_{\rm spot}$ is the number of spots and s_i is the relative size of spot i. Note that C_i is set to 1 when the relative brightness is reconstructed instead of the spot occupancy (i.e., in method 2).

[7] The longitudinal resolution at the equator is given by $2\pi v \sin i_{\rm rot}/W$, where W is the width of the intrinsic Stokes I LSD profile.

respectively measured from the Stokes V and I profiles. However, f_I is partly degenerated with other parameters of the line and, in general, cannot be precisely determined from Stokes I line profiles. However, in some cases where the modulation in the width of the observed Stokes I LSD profiles matches the large-scale magnetic topology, one can constrain f_I by using the map of large-scale field to generate synthetic Stokes I profiles that can be compared to the observed ones (see the application to Proxima Centauri in Section 3.3.2). The increase in the Zeeman broadening from optical to nIR domains should allow one to carry out simultaneous inversions of small- and large-scale fields, which is further discussed in Chapter 6.

3.2.4 Proxies for magnetic activity

As introduced in Section 1.4.2, several proxies can be computed in order to study the connection between surface distributions of bright/dark features and large-scale magnetic field with stellar activity. In particular, the phase-folded curve of these proxies informs us on how they are linked to the structures unveiled with ZDI reconstructions. In addition, the period $P_{\rm ind}$ at which each time series of activity proxy is modulated informs us about the stellar rotation period. Moreover, when the star exhibits differential rotation, this period also tells about preferential latitudes of emission of the indicator. $P_{\rm ind}$ can be determined using frequentist analysis tools such as Lomb-Scargle periodograms (Lomb, 1976; Scargle, 1982; Zechmeister & Kürster, 2009; Mortier et al., 2015, see the description of periodograms in Appendix A.4.0.1) or by GPR (see Appendix A.3), provided that the GP parameters are finely-tuned to only model the rotationally-modulated component in the time series of each indicator. In this section, we describe the activity indicators that we consider for our studies while their application to real data is detailed in Section 3.3.

Longitudinal field

The longitudinal field B_ℓ is directly related to circularly-polarized Zeeman signatures. It corresponds to the first-order moment of the Stokes V LSD profile, such that (e.g. Donati et al., 1997):

$$B_\ell = -2.14 \times 10^{11} \frac{\int vV(v)dv}{\lambda_0 g_{\rm eff} c_0 \int (I_{\rm c} - I(v))dv} \tag{3.7}$$

where I and V are the Stokes parameters described in Section 3.2.1, $I_{\rm c}$ the unpolarized continuum, c_0 the speed of light (in $\mathrm{km\,s^{-1}}$) and $g_{\rm eff}$ the effective Landé factor of the LSD line profile. Although it encloses less information than the Zeeman signatures themselves, B_ℓ is closely related to the surface distribution of the large-scale magnetic field and, thus, can be used for preliminary analyses of the stellar magnetic topology. Moreover, B_ℓ has been shown to be a reliable proxy of stellar rotation periods for various types of stars (e.g., Donati et al., 2006c; Hébrard et al., 2016).

FWHM and small-scale magnetic field

Bright and dark features at the surface of a star induce variations in the width of intrinsic Stokes I LSD profiles (see Section 1.4). If the observed line profiles are not dominated by stellar rotation (i.e., $v \sin i_{\rm rot} \lesssim 10\,\mathrm{m\,s^{-1}}$), and in absence of strong magnetic fields, the variation of their FWHM is expected to probe the distribution of bright and dark inhomogeneities at the stellar surface and to correlate well stellar activity RV signals, at least for low-mass stars observed in the optical domain (e.g., Queloz et al., 2001; Dumusque et al., 2014; Hébrard et al., 2016).

The effect induced by surface inhomogeneities on the intrinsic stellar line profile decreases from optical to nIR wavelengths. Although weaker, this effect might still be observable on Stokes I profiles computed from nIR lines poorly-sensitive to magnetic field (e.g., most of the molecular

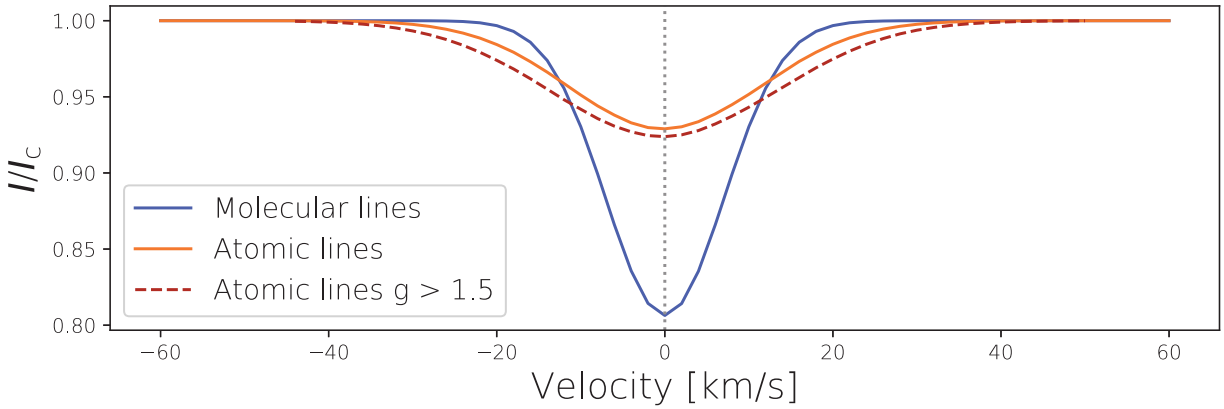

Figure 3.5 – Median Gaussian fits to SPIRou line profiles of AU Mic computed using an empirical line mask (dominated by molecular lines, blue solid line), atomic lines ($g_{\rm eff} = 1.2$; orange solid line) and atomic lines of Landé factor larger than 1.5 only (red dashed line). In each case, we fitted a Gaussian function on top of a linear continuum to each line profile and computed the median of the resulting Gaussian function (corrected for the slanted continuum). The vertical dotted line indicate the line center of the line profile computed with the empirical line mask (-4.45 km s^{-1}).

lines). However, as soon as the effective Landé factor of the average line profile increases, its FWHM also reflects the Zeeman broadening now probing as well the small-scale magnetic field at the surface of the star (see Figure 3.5 for an illustration of the dependency of FWHM on the magnetic field in the nIR). This is all the more interesting as the small-scale magnetic field turns out to be an excellent proxy for rotationally-modulated stellar activity RV signals for the Sun as the solar activity RV signals are dominated by the suppression of the convective blueshift, closely-linked to the distribution of small-scale magnetic field (e.g., Haywood et al., 2016, 2020). NIR high-precision spectrometers like SPIRou offer a unique opportunity to investigate the evolution of the Zeeman broadening throughout $YJHK$ bands, and characterize (and possibly image) the small-scale magnetic field at the surface of the star.

Asymmetry of the line profile

The bisector of the CCF allows to measure the asymmetry of the line profile to the first order. Originally introduced to characterize the granulation at the solar surface (Gray, 1982), it has shown to be a good indicator of distortions induced by dark and bright features (e.g., Gray, 1997; Queloz et al., 2001) or magnetic fields (Hébrard et al., 2014) at the surface of low-mass stars. In particular, the so-called velocity span (or bisector inverse slope), i.e., the difference $V_{\rm s}$ of RVs between the top and bottom parts of the Stokes I LSD profile (resp. within 20-40% and 60-95% of the full depth counting from the continuum; the computation of velocity span is illustrated in Figure 4.2), correlates well with stellar activity RV signals and, thus, is a good probe of the surface distribution of spot/plages. However, this correlation is not observed for slow rotators ($v \sin i_{\rm rot} \lesssim 2$ km s^{-1}, e.g., Desort et al., 2007; Hébrard et al., 2014), whose profiles are too narrow.

Chromospheric indicators

The non-thermal emission in a few chromospheric lines of low-mass stars was shown to correlate well with other activity indicators such as X ray emission, and photometric and RV signals (e.g., Noyes et al., 1984; Lockwood et al., 2007; Skelly et al., 2008). In particular, six resonant optical lines have been identified as potential probe of the distribution of active regions at the surface of low-

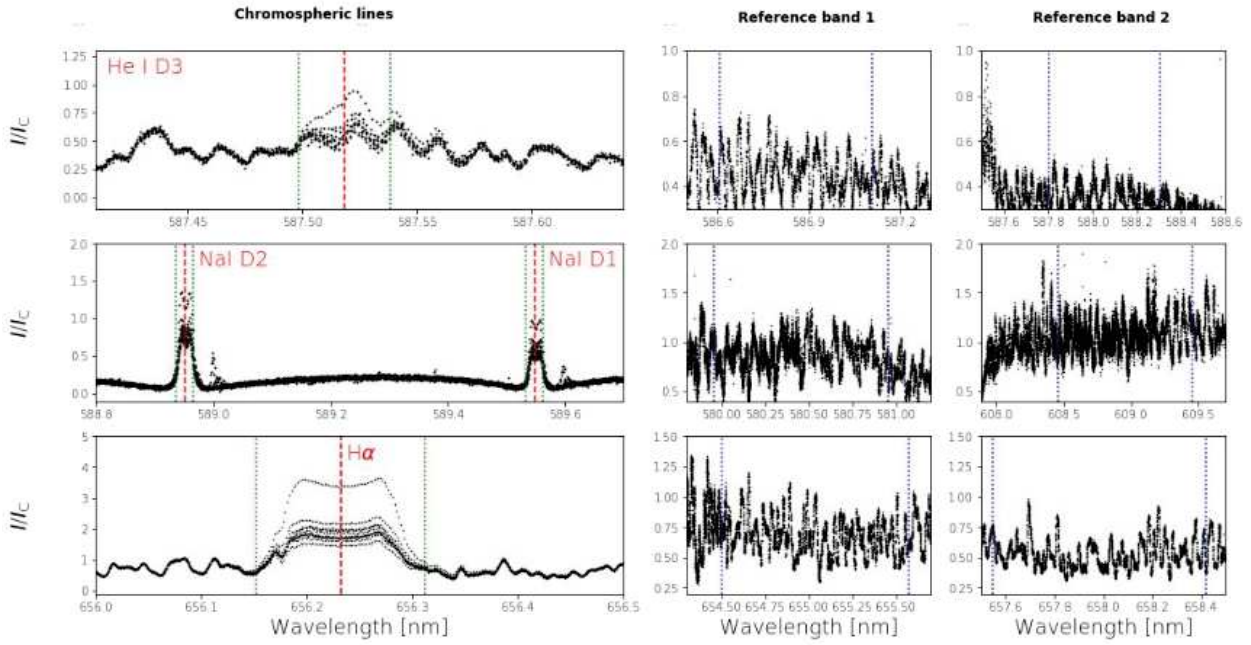

Figure 3.6 – Chromospheric emission lines in the optical domain used to compute stellar activity proxies of Proxima Centauri. *Left column:* normalized HARPS spectra of Proxima Cen in the stellar rest frame centered on He I D3 (top), Na I D1 & D2 (middle) and Hα (bottom). The reference wavelength of each line is indicated by the red vertical dashed line, while the interval used to compute the emission flux within each line is delimited by the two green dotted lines. *Last 2 columns:* reference continuum bands (delimited by the blue vertical dotted lines) used to compute the activity proxy associated with the emission line(s) shown in the left-handed panel).

mass stars (e.g., Bonfils et al., 2007; Boisse et al., 2009; Gomes da Silva et al., 2011): Ca II H & K, He I D3, Na I D1 & D2 and Hα (see the corresponding wavelengths in Table 3.2). For each line (or doublet) of interest, we compute the associated activity index by dividing the total normalized emission flux within the line, by a reference flux, computed from two continuum regions located on the blue and red sides of the lines (see the method described in Gomes da Silva et al., 2011). The wavelength ranges used to compute the activity indices associated to the aforementioned lines are given in Table 3.2 and illustrated in Figure 3.6.

In the nIR, only a few chromospheric lines have been identified as potential probes of stellar activity (e.g. Zirin, 1982; Short & Doyle, 1998): He I triplet (1083 nm), Paβ (1282 nm) and Brγ (2165 nm). However, the way they connect to the stellar brightness/magnetic topologies remains unclear (Sanz-Forcada & Dupree, 2008; Schmidt et al., 2012; Schöfer et al., 2019; Moutou et al., 2020). Thank to its continuous coverage of the Y to K bands, SPIRou has the ability to compute the three aforementioned indicators, using the method described in Moutou et al. (2020). Each telluric-corrected SPIRou spectrum is shifted into the stellar rest frame and then divided by the median observed spectrum. The activity proxy is defined as the average of each median-divided spectrum computed in intervals centered on the line(s) of interest (see the intervals delimited by green vertical dashed lines in the right-handed panel of Figure 3.2 and Table 3.2). The error bars are computed from the average dispersion of 0.5 nm continuum regions at in the blue and red sides of the lines (see Table 3.2).

Table 3.2 – Wavelength ranges used to compute various chromospheric activity indicators. Column 2 gives the wavelengths of the chromospheric lines while columns 3 and 4 list the wavelengths of the reference blue and red continuum regions, respectively. Note that the flux in the reference regions is used as a normalizing constant for optical indicators, while it is only use to assess the error bars on the indice in the nIR. For each wavelength, we indicate in brackets the total width of the window on which the indicator is computed.

Indicator	λ_0 ($\Delta\lambda$)	λ_b ($\Delta\lambda$)	λ_r ($\Delta\lambda$)
–	[nm]	[nm]	[nm]
Ca II H & K (S index)	396.847 (0.06) 393.366 (0.06)	390 (1)	400 (1)
He I D3	587.562 (0.06)	550.0 (0.5)	650 (0.5)
Na I D1 & D2	589.592 (0.05) 588.995 (0.05)	580.5 (1.0)	609.0 (1.0)
Hα	656.2808 (0.16)	655.087 (1.075)	658.031 (0.875)
He I (1083 nm)	1082.9081 - 1083.0250 - 1083.0341 (0.25)	1082.25 (0.5)	1083.75 (0.5)
Paβ	1281.81 (0.18)	1280.75 (0.5)	1282.75 (0.5)
Brγ	2165.5 (0.5)	2164.75 (0.5)	2166.25 (0.5)

3.3 Application to a sample of low-mass stars

We now present a spectropolarimetric analysis of four low-mass stars: AU Mic (SPIRou), Proxima Centauri (HARPS-Pol), EPIC 211889233 (ESPaDOnS/NARVAL) and V471 Tau (ESPaDOnS). The four stars are shown on an HR diagram in Figure 1.4 and their properties and the main results of their spectropolarimetric analyses are shown in Table 3.3. The studies Proxima Cen and AU Mic were published in two first-author papers (Klein et al., 2021, 2020, for Prox Cen and AU Mic, respectively), whereas the analyses of EPIC 211889233 (ESPaDOnS) and V471 Tau (ESPaDOnS) will be respectively published in *Lopez, Klein et al., 2020* (in prep.) and *Zaire, Donati & Klein, 2020* (submitted).

3.3.1 AU Microscopii

AU Mic: an active star

As already mentioned in Section 2.3.3, the post-T Tauri M1 dwarf AU Mic ($v \sin i_{\rm rot} = 7.8\,{\rm km\,s^{-1}}$, $Ro = 0.15$) has been widely studied over the past decades for its intense magnetic activity evidenced by the 0.1 mag activity-driven fluctuations in its light curve (Torres & Ferraz Mello, 1973; Rodono et al., 1986; Plavchan et al., 2020b) and frequent flares of variable intensity (e.g. Robinson et al., 2001; MacGregor et al., 2020). AU Mic harbours a strong small-scale magnetic field of $\sim$2 kG (Berdyugina et al., 2006; Afram & Berdyugina, 2019; Kochukhov & Reiners, 2020) which could potentially impact its close-in planet AU Mic b (Carolan et al., 2020). The star also hosts a resolved edge-on debris disk extending from roughly 35 to 210 au from the star Kalas et al. (2004), widely investigated with infrared and submilimetric imagers over the past decade (e.g., Wilner et al., 2012; MacGregor et al., 2013; Boccaletti et al., 2015). In particular, SPHERE observations have revealed a few fast moving features exhibiting non-keplerian motions within AU Mic's debris disk (Boccaletti et al., 2015, 2018; Daley et al., 2019). The origin of these features, tentatively explained by disk-wind interactions in a titled stellar magnetic field (Chiang & Fung, 2017; Wisniewski et al., 2019), or the presence of a massive body within the disk (Sezestre et al., 2017), is still unclear.

Given how bright AU Mic is ($H = 4.831$; Cutri et al., 2003), the star appears as a prime target for a spectropolarimetric analysis with SPIRou. SPIRou has the potential to reconstruct the large-scale magnetic topology of AU Mic and investigate the underlying dynamo processes. Knowing the geometry of the large-scale magnetic field will also help constraining the extended magnetosphere of the star and thus the interactions between stellar wind and the close-in planet (Vidotto et al.,

Table 3.3 – Properties of V471 Tau (columns 2-3) , AU Mic (columns 4-5), EPIC 211889233 (columns 6-7) and Proxima Centauri (columns 8-9) useful for the spectropolarimetric analyses. When taken from the literature, the reference of each parameter is indicated to the right of it†. When available, the 1σ uncertainty of the last two digits is shown within brackets.

Parameter	AU Mic		Prox. Cen.		EPIC 211		V471 Tau	
–	Val.	Ref.	Val.	Ref.	Val.	Ref.	Val.	Ref.
Stellar parameters								
ST	M1	Ke89	M5.5	Be91	M0	Hu16	K2	Hu06
d [pc]	9.7248 (46)	Gaia18	1.3012 (03)	Gaia18	50.46 (22)	Gaia18	47.70 (10)	Gaia18
Age [Gyr]	0.022 (03)	Ma14	4.8	Ba16	–		0.625 (50)	Pe98
$T_{\rm eff}$ [k]	3700 (50)	Af19	2980 (80)	Ri17	4083 (110)	Spectro.	5066 (04)	Va15
$L_{\rm s}[L_\odot]$	0.09 (02)	Pl09	1.51 (08) $\times 10^{-3}$	Ri17	0.09	$T_{\rm eff}$ and $R_{\rm s}$	-0.282 (01)	$T_{\rm eff}$ and $R_{\rm s}$
$M_{\rm s}$ $[M_\odot]$	0.50 (03)	P20	0.120 (03)	Ri17	0.65	De00	0.9971 (12)	Va15
$R_{\rm s}$ $[R_\odot]$	0.75 (03)	P20	0.146 (07)	Ri17	0.61	Ba98	0.93709 (93)	Va15
$\log g$	4.39 (03)	–	5.02 (18)	Pa16	4.602 (28)	Spectro	4.49331 (87)	Va15
$P_{\rm rot}$ [d]	4.86 (01)	P20	89.9 (4.0)	Mag. field	10.88 (28)	Mag. field	0.52118833875 (27)	Va15
$i_{\rm rot}$ [°]	89.5	–	47 (07)	–	60 ± 10	Spectro	78.755 (30)	Va15
$v \sin i_{\rm rot}$ [km/s]	7.8 (0.3)	–	0.06 (01)	–	2.5 ± 1.0	Spectro	89.30 (11)	Va15
Ro	0.15	Wr16	0.63 (10)	Wr18	0.26	Wr11	–	–
Spectropolarimetric observations								
Nb. seasons	1		1		1		2	
Instruments	SPIRou		HARPS-Pol		ESPaDOnS,HARPS		ESPaDOnS	
$T_{\rm ref}$ [BJD]	2458651.993		2457862		2458115.95527		2445821.898291	
Dates	Sep to Nov 19		Apr to Jul 17		Dec 17 to Feb 18		Nov 04 - Dec 05	
$N_{\rm seq}$	27		10		19, 27		230 - 400	
Median S/N	678		118		184 -		147-158	
Brightness and magnetic analysis								
Median B_ℓ [G]	33 (03)		-15.4 (3.2)		4.8 (4.3)		–	
l	7		5		5		15	
$S_{\rm p}$[%]	1.4		–		1.35		14 - 17	
$<B_{\rm I}>$ [G]	2300	Ko20	600	Re08	–		–	
$<B_{\rm V}>$ [G]	475		200		109		170 - 220	
f_I	–		0.3		–		–	
f_V	0.2		0.1		–		–	
$f_{\rm pol}$ [%]	78		92		85		65 - 60	
$f_{\rm dip}$ [%]	70		57		44		15 - 35	
$f_{\rm quad}$ [%]	3		22		44		10 - 10	
$f_{\rm oct}$ [%]	11		10		3		15 - 15	
$f_{l>3}$ [%]	16		11		9		60 - 40	
$f_{\rm axi}$ [%]	65		44		81		65	
$B_{\rm dip}$ [G]	450		135		90		90 - 150	
$\theta_{\rm dip}$ [°]	19		51		30		20 - 40	
$\phi_{\rm max}$	0.18		0.28		0.76		0.08 - 0.38	
Differential rotation parameters – Brightness distribution (Stokes I)								
$\Omega_{\rm eq}$ [rad/d]	1.298 (03)		–		0.612 (03)		12.106 (01) - 12.091 (01)	
$d\Omega$ [rad/d]	0.075 (31)		–		0.19 (02)		0.099 (05) - 0.073 (02)	
$P_{\rm eq}$ [d]	4.84 (01)		–		10.26 (06)		0.51901 (04) - 0.51966 (04)	
$P_{\rm pol}$ [d]	5.10 (15)		–		14.7 (0.3)		0.52329 (22) - 0.52281 (10)	
ΔP [d]	0.26 (15)		–		4.4 (0.3)		0.00428 (22) - 0.00315 (11)	
Differential rotation parameters – Large-scale magnetic field (Stokes V)								
$\Omega_{\rm eq}$ [rad/d]	1.344 (02)		–		0.54 (06)		12.116 (04) - 12.089 (02)	
$d\Omega$ [rad/d]	0.167 (09)		–		0.21 (09)		0.130 (11) - 0.058 (05)	
$P_{\rm eq}$ [d]	4.675 (06)		–		11.6 (1.2		0.51859 (17) - 0.51974 (09)	
$P_{\rm pol}$ [d]	5.34 (05)		–		18.8 (2.1)		0.52421 (51) - 0.52224 (23)	
ΔP [d]	0.66 (05)		–		7.1 (2.4)		0.00562 (87) - 0.0025 (25)	

† talia ***AU Mic:*** Ke89, Gaia18, Ma14, Af19, Pl09, P20, Wr16 and Ko20 stand respectively for Keenan & McNeil (1989), Gaia Collaboration et al. (2018), Mamajek & Bell (2014), Afram & Berdyugina (2019), Plavchan et al. (2009), Plavchan et al. (2020b), Wright & Drake (2016) and Kochukhov & Reiners (2020). ***Proxima Cen:*** Be91, Ri17, Pa16, Wr18 and Re08 stand respectively for Bessell (1991), Ribas et al. (2017), Passegger et al. (2016), Wright et al. (2018) and Reiners & Basri (2008). ***EPIC 211889233:*** De00, Ba98, Wr11 stand respectively for Delfosse et al. (2000), Baraffe et al. (1998) and Wright et al. (2011). ***V471:*** Hu06, Pe98 and Va15 stand respectively for Hussain et al. (2006), Perryman et al. (1998) and Vaccaro et al. (2015).

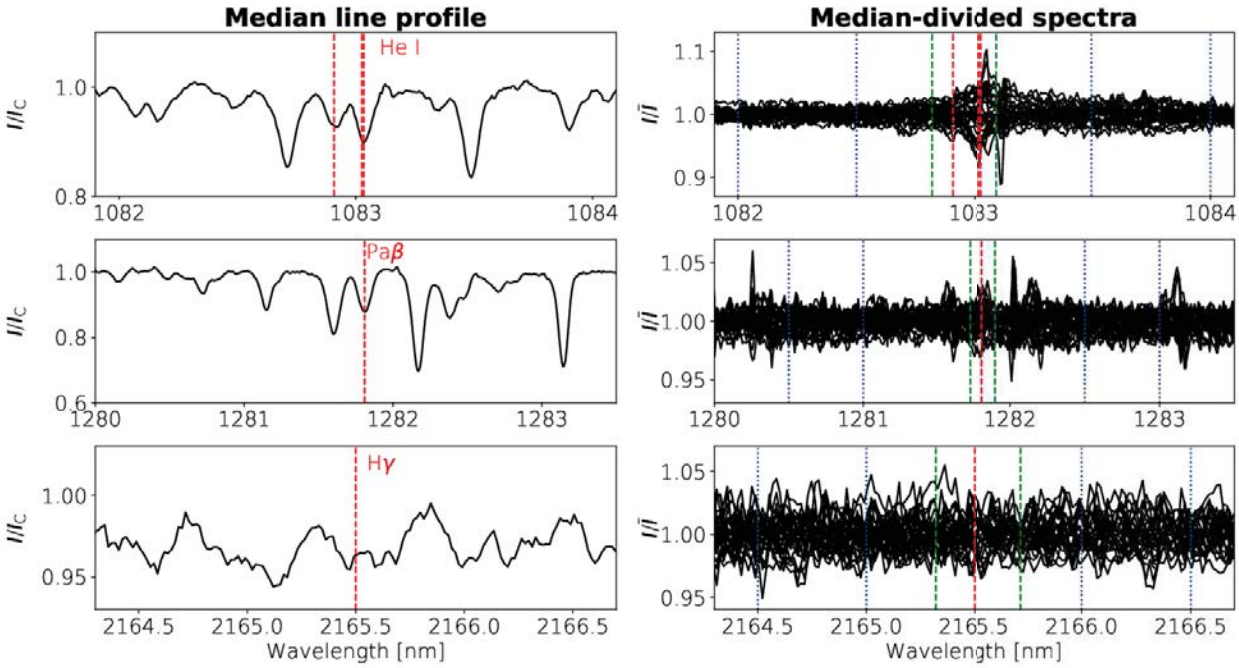

Figure 3.7 – Near-infrared chromospheric emission lines used to compute stellar activity proxies of AU Mic. The left column shows the median SPIRou spectrum centered on He I, Paβ and Brγ lines. In the right column, we show the median-divided SPIRou spectra. The intervals delimited by the green dashed and blue dotted lines are respectively used to compute the mean flux and the error bar of each value of the indicator. In all panels, the reference wavelengths of the chromospheric lines are indicated by the red vertical dashed lines.

2014a; Strugarek et al., 2015; Carolan et al., 2020). Finally, AU Mic acts as a benchmark to assess the ability of SPIRou to carry out velocimetric and spectropolarimetric analyses of early M dwarfs (following the preliminary results on low-mass stars reported in Moutou et al., 2020; Donati et al., 2020a).

AU Mic was observed between 2019 September 18 and November 14 with SPIRou as part of the proposal described in Chapter 2 (ID: 19BD97, PI: Klein). A total of 27 spectropolarimetric measurements were collected at a rate of one polarimetric sequence per night during CFHT bright-time periods. As shown in Section 2.3.3, this sampling strategy is expected to be well suited to the detection of the close-in planet AU Mic b. The SPIRou spectra are reduced using a version of the Libre-ESpRIT data reduction pipeline adapted to SPIRou spectra (Donati et al., 2020a), and corrected from telluric lines using the method described in Artigau et al. (2014). The reduced spectra feature peak S/Ns of 678 in average. We compute the Stokes I and V LSD profiles using three different line masks. For brightness and velocimetric analyses, we use an empirical weighted mask built on a SPIRou spectrum of the early M dwarf Gl 15A containing $\sim$3000 atomic and molecular lines. For the magnetic analysis, we used a mask of $\sim$3600 moderate-to-strong atomic lines of average Landé factor $\sim$1.2. To estimate the amount of Zeeman broadening in the observed Stokes I LSD profiles, we also used a third line mask containing $\sim$700 atomic lines with Landé factors larger than 1.5 (i.e., the most magnetically-sensitive lines of the reference mask of atomic lines). In the rest of this section, we describe the spectropolarimetric analysis of AU Mic, while the velocimetric analysis of the SPIRou observations of the star is detailed in Chapter 4.

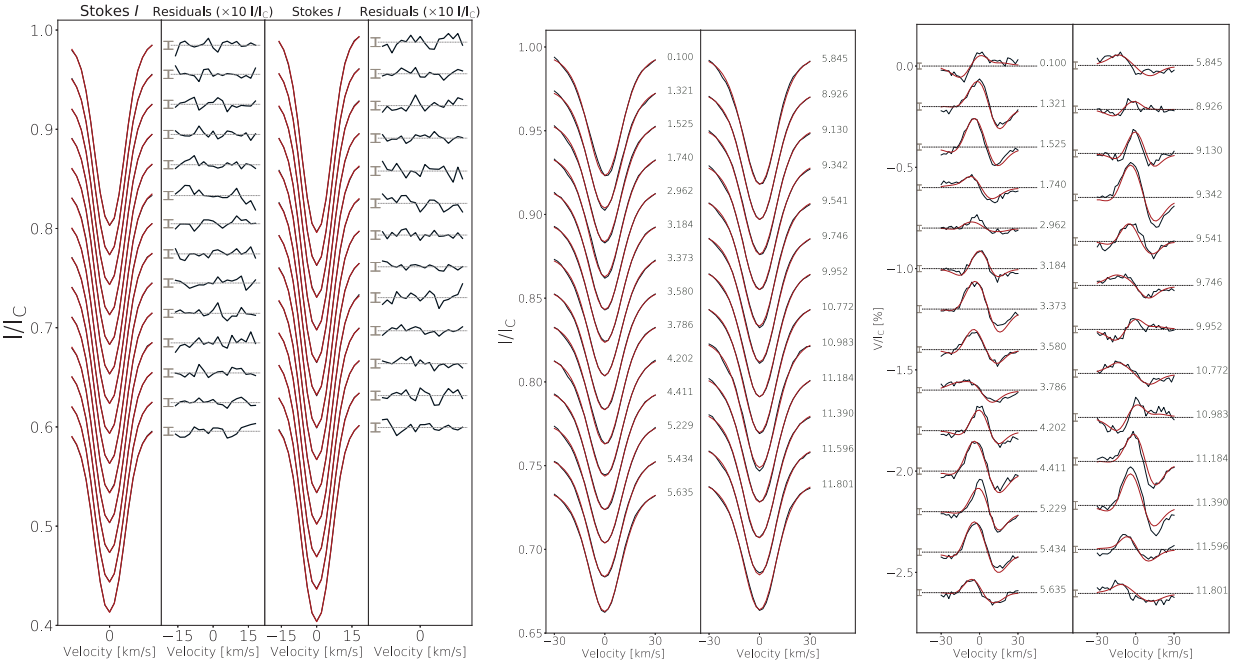

Figure 3.8 – Best ZDI fits (red lines) to the time series of observed Stokes I and V LSD profiles (black lines). *Left-handed panel:* Best fit to the Stokes I LSD profiles computed with the empirical line mask (panels 1 and 3) and residuals of the fit in unit of $10 \times I/I_C$ (panels 2 and 4). The $\pm$ 1σ error bars are indicated on the right side of each residual profile. *Middle and right-handed panels:* reconstructions of the Stokes I (middle panel) and Stokes V (right panel) computed using the atomic line mask. The rotation cycles are indicated on the right side on each line profile and the $\pm\sigma$ error bars on the Stokes V LSD profiles are shown on the right side of each profile on the right-handed panel.

The magnetic field of AU Mic

The Stokes V LSD profiles of AU Mic exhibit rotationally-modulated Zeeman signatures of full amplitude up to 0.4% (see the left panel of Figure 3.8). The corresponding longitudinal field ranges from -48 to 83 G with a median value of 33 G (typical error bar of 3 G), consistent with the values reported from previous spectropolarimetric observations of AU Mic (Berdyugina et al., 2006; Kochukhov & Reiners, 2020), and in particular, from June 2019 SPIRou observations of the transiting planet (median value of 46 G; see Martioli et al., 2020a). Assuming an inclination of 90° for AU Mic (i.e., equal to the inclination of the planet orbit, which is further evidenced by null projected spin-orbit obliquity reported in Martioli et al., 2020a; Palle et al., 2020; Hirano et al., 2020), we find that the star features a relatively low $v \sin i_{\rm rot}$ of 7.8 km s^{-1} which limits the spherical harmonic expansion to $l_{\rm max} = 7$ in ZDI reconstructions. Using the chi-square fitting procedure described in Appendix A.2.4, we find that $P_{\rm rot} = 4.80 \pm 0.01$ d matches best the modulation of the observed circularly-polarized Zeeman signatures. Note that this value is slightly lower, but still compatible at 2σ with the value of 4.83 ± 0.02 d obtained by modelling the B_ℓ time-series with GPR.

We used ZDI to model the time series of Stokes I and V LSD profiles simultaneously (see the results of the magnetic analysis in Table 3.3). The maximum-entropy fit to the time series is shown in the two right-hand panels of Figure 3.8 while the corresponding surface distribution of brightness and large-scale magnetic field are shown in the bottom panel of Figure 3.9. We find a large-scale magnetic field of 475 G with a filling factor $f_V = 0.2$, meaning that a $\sim$2.4 kG is present on $\sim$20% of the stellar surface, consistent with typical field strengths reported in the literature (Saar, 1994; Berdyugina et al., 2006; Reiners et al., 2012; Afram & Berdyugina, 2019; Kochukhov & Reiners,

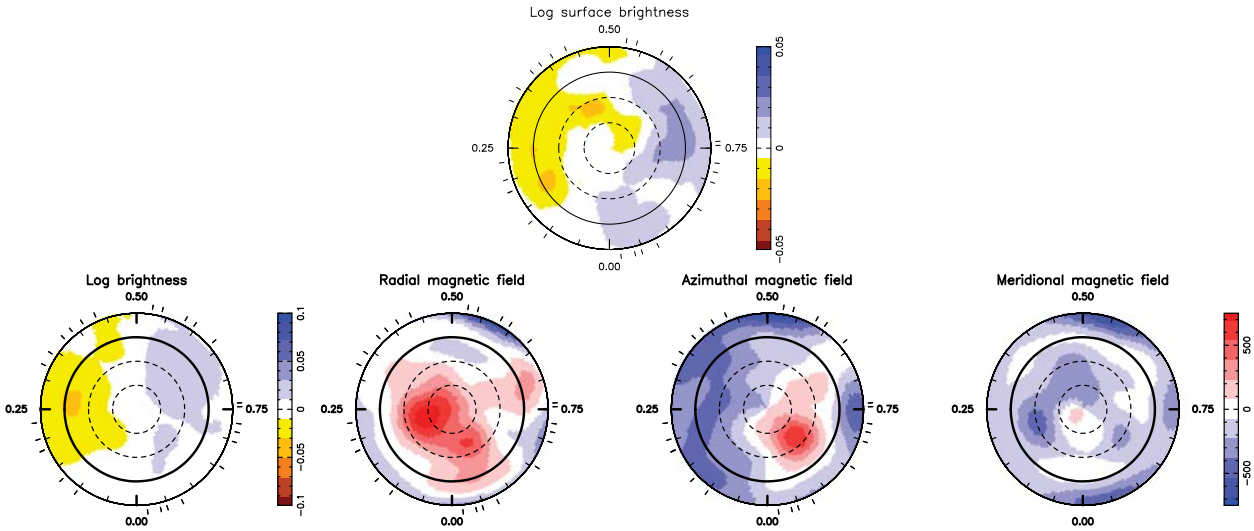

Figure 3.9 – Flattened polar views of the reconstructed distribution of logarithmic brightness (left panel) and radial, azimuthal and meridional large-scale magnetic field (panels 2 to 4) at the surface of AU Mic. On each panel, the circles indicate the equator (solid line) and the -30°, 30°, and 60° parallels (dashed lines). The ticks around the star mark the spectropolarimetric observations. Magnetic fields are expressed in G. The rotation cycle of the star is computed from the stellar rotation period $P_{\rm rot} = 4.86$ d with the reference time BJD = 2458651.993.

2020). The reconstructed field is mainly poloidal and axisymmetric contrary to what Kochukhov & Reiners (2020) obtained (based on only a few spectropolarimetric observations taken at different epochs, though). In particular, the topology of the large-scale field is dominated by a dipole of 450 G tilted at 19° to the rotation axis towards phase 0.18. AU Mic is respectively predicted fully and largely convective by the evolutionary tracks of Siess et al. (2000) and Baraffe et al. (2015) (with a radiative core occupying ∼10% of the total mass). The relatively strong axisymmetric poloidal large-scale field obtained in this study is in good agreement with the typical magnetic topologies obtained for largely-/fully-convective young PMS stars (Folsom et al., 2016; Hill et al., 2019) and M dwarfs (Morin et al., 2008b, 2010) featuring similar *Ro*.

The properties of AU Mic are relatively similar to those of the more evolved M dwarf AD Leo (effective temperature, mass, magnetic geometry; see Morin et al., 2008b; Lavail et al., 2018). Using Baraffe et al. (2015) evolutionary tracks, we find that AU Mic is expected to contract until reaching a radius of 0.4 $R_{\rm s}$ at the ZAMS, compatible with that of AD Leo. Assuming conservation of the angular momentum, this would imply that AU Mic will feature a rotation period of ∼2 d, consistent again with the 2.2-d rotation period of AD Leo (Morin et al., 2008b). One may thus wonder whether AU Mic will resemble to AD Leo at the beginning of the main-sequence. Assuming the conservation of stellar magnetic flux, AU Mic would harbour an average large-scale magnetic field of about 1 kG, significantly stronger than that of AD leo ($\lesssim$ 300 G). This demonstrates that, unlike fossil magnetic fields (e.g., Landstreet et al., 2007), the conservation of magnetic flux does not apply to magnetic fields generated by dynamo processes (which are rather driven by energy exchanges within stellar convective zones).

Brightness imaging

We use ZDI to reconstruct the brightness distribution at the surface of AU Mic from the Stokes I LSD profiles extracted using the empirical line mask. Given the relatively low $v \sin i_{\rm rot}$ of the star, we correct for systematic differences between observed and synthetic profiles using the iterative procedure described in Section 3.2.2 (Method 2). The process is converging well after a few iterations

and yields the brightness map shown in the top panel of Figure 3.9. The brightness distribution is roughly similar to that obtained from the magnetic analysis and features a spot coverage of 1.4% almost equally distributed into bright and dark features.

Surface differential rotation of AU Mic

Using the method described in Appendix A.1, we find that both the surface distribution of inhomogeneities and the large-scale field of AU Mic are sheared by solar-like DR respectively 1.5× and 3× larger than that of the Sun. The values of the rotation rate $\Omega_{\rm eq}$ at the equator and the difference $\mathrm{d}\Omega$ in rotation rates between the equator and the pole are given in Table 3.3. We find a net difference between the equatorial rotation periods derived from Stokes I and Stokes V profiles, suggesting that both observables probe different layers of the convective zone. This strong DR is somewhat unexpected for a largely-convective star like AU Mic. One possible interpretation is that the radiative core of AU Mic is sufficiently developed for the magnetic field generation to be similar to that of more-evolved partly-convective stars. This speculation is consistent with the putative chromospheric cycle reported for the star in Ibañez Bustos et al. (2019) and attributed to an $\alpha\Omega$ dynamo process at work in its convective interior.

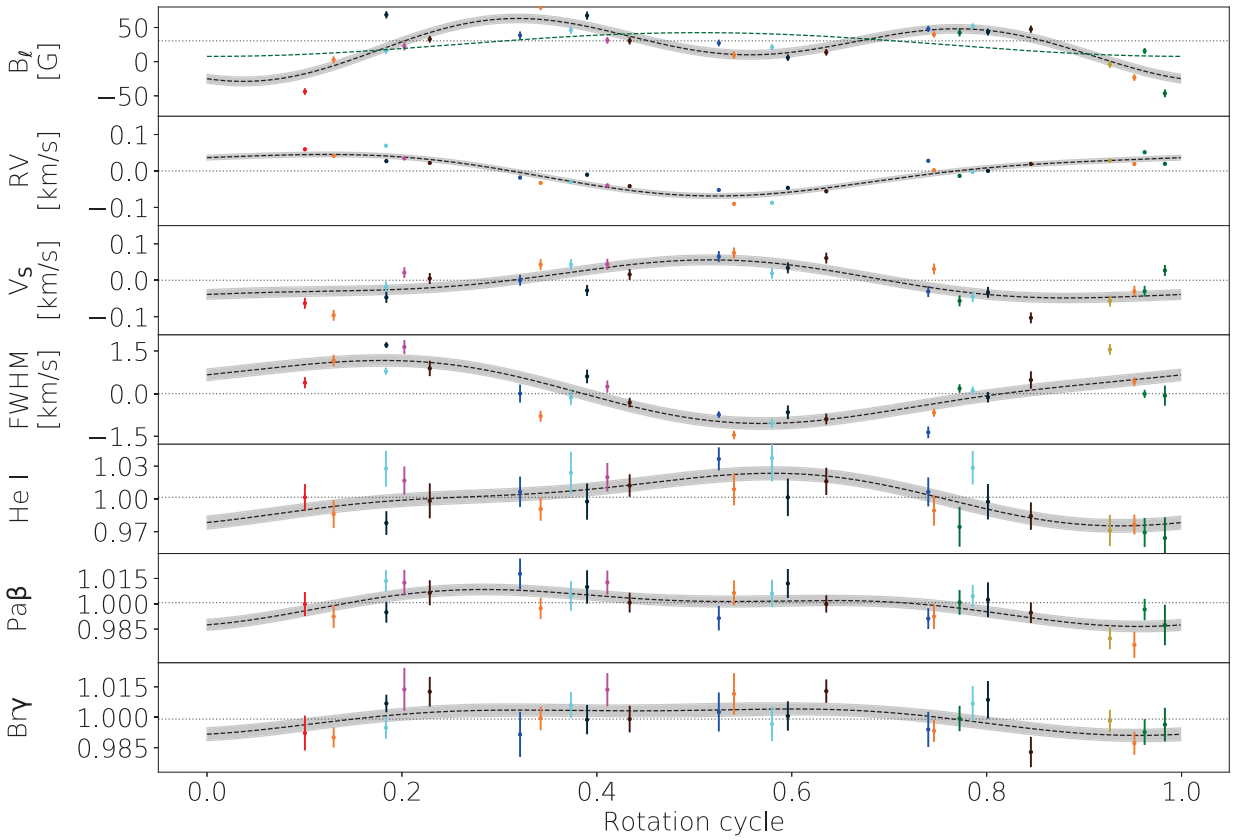

Figure 3.10 – *From top to bottom:* Time series of B_ℓ, RV, VS, FWHM of the Stokes I LSD profiles computed from lines of landé factor larger than 1.5, He I, Paβ and Brγ folded at AU Mic's rotation period (i.e., 4.86 d). In each panel, the black dashed line show the double-sine wave that matches best the data (with $\pm1\sigma$ error bands). Points of different colors belong to different rotational cycles. In the top panel, the green dashed line shows the best simple sine-wave fit to B_ℓ at $P_{\rm rot} = 4.86$ d.

Investigating the magnetic activity of AU Mic

To study the way nIR chromospheric indicators are linked to the stellar photosphere, we computed indices based on He I (1083 nm), Paβ (1282 nm) and Brγ (2165 nm) using the method described in Section 3.2.4 (see the different lines computed from AU Mic spectra in Figure 3.7). By modeling the resulting time series with GPR[8] (see Table 4.3), we find that He I and Paβ are modulated at respective rotation periods of $4.87^{+0.06}_{-0.05}$ d and $4.99^{+0.11}_{-0.09}$ d. Given the DR parameters obtained from the Stokes I LSD profile, this would suggest that He I emission rather concentrates close to the stellar equator ($\sim$20°) while Paβ is mostly emitted at higher latitudes ($\sim$50°). This speculation is further evidenced on the phase-folded plot shown in Figure 3.10. Paβ appears more correlated with B_ℓ, with a maximum when the magnetic pole faces the observer (around phase 0.3; see Figure 3.9). In contrast, He I is maximum when the magnetic equator faces the observer (around phase 0.6). Note however that no conclusion can be drawn at this stage, as the rotation periods derived from both time series of chromospheric indicators differ by barely more then 1$sigma$. Brγ shows no significant rotational modulation and is thus not considered as a reliable activity indicator for AU Mic.

We also note that the FWHM of the Stokes I LSD profiles computed from atomic lines with Landé factors larger than 1.5 correlates well with RVs (and V_s) in Figure 3.10. This correlation decreases with decreasing effective Landé factors of the Stokes I LSD profiles until being marginal for the line profiles computed from the empirical line mask. This suggests that the profile distortions producing the fluctuations in the RV time-series are at least partly of magnetic origin, further suggesting that small-scale magnetic fields are promising proxies to model stellar activity RV signals for exoplanet searches (see also Chapter 4). To break the degeneracy between surface brightness and small-scale field, one would have to simultaneously invert Stokes I LSD profiles of spectral lines with different Landé factors so that the impact of the two respective components can be unambiguously identified.

Next steps for AU Mic

AU Mic was re-observed with SPIRou as part of the SLS-TF in 2020 in order to achieve a thorough study of the magnetic properties of the star (and their evolution with time), and to better constrain the properties of its close-in planet (see Section 4.4). On the longer term, investigating how the magnetic and DR parameters of AU Mic vary on time scales of 5-10 yr should help finding out whether the 5-yr chromospheric activity cycle recently reported by Ibañez Bustos et al. (2019) is real or not, and if yes, whether it is attributable to an underlying $\alpha\Omega$-dynamo process. The topology of the large-scale magnetic field vector shown in Figure 3.9 is used as an input to compute the geometry of the Alfvèn surface of AU Mic using 3d magnetohydrodynamical simulations and study its interaction with the close-in planet of the system (Kavanagh, Vidotto, Klein et al., in prep.).

3.3.2 Proxima Centauri

Proxima Centauri: a target of choice for a spectropolarimetric analysis

Our closest neighbor, Proxima Centauri[9], is an active FC M5.5 dwarf hosting a close-in HZ planet, Proxima b (Anglada-Escudé et al., 2016; Suárez Mascareño et al., 2020), and potential outer com-

[8] We assumed a quasi-periodic GP kernel (see Appendix A.3) for the fit. The decay time and the smoothing parameters are respectively fixed to 100 d and 1.0. These values are compatible with that obtained in Plavchan et al. (2020b) RV analysis. The smoothing parameter is about twice as large than in RVs since active regions produce RV signatures that evolve roughly twice as fast than their counterpart in activity proxy.

[9] http://simbad.u-strasbg.fr/simbad/sim-id?Ident=Proxima+Centauri

panions (Damasso et al., 2020; Damasso & Del Sordo, 2020). The habitability of Proxima b has been widely studied in the recent literature (e.g., Ribas et al., 2016; Turbet et al., 2016; Barnes et al., 2016; Meadows et al., 2018). In particular, given its proximity to the star (0.05 au), the planet atmospheric and surface properties are likely affected by the various manifestations of the magnetic activity of the star and in particular by the stellar wind (e.g., Garraffo et al., 2016; Garcia-Sage et al., 2017; Vidotto et al., 2019) and intense flares (e.g., Davenport et al., 2016; Pavlenko et al., 2017; Vida et al., 2019). Constraining the magnetic activity of the star and, in particular, the magnetic field driving it, is crucial to better understand the interaction between the star and the planet.

Ten spectropolarimetric observations of Proxima Cen were collected with HARPS-Pol from April to July 2017 (ESO program 099.C-0334(A), PI: Hébrard). The data were reduced using the version of the LIBRE-ESpRIT pipeline adapted to HARPS-Pol as described in Hébrard et al. (2016). The resulting spectra feature a median peak S/N per pixel of 118. The Stokes I and V LSD profiles were computed from a mask of ∼4000 atomic lines covering the HARPS spectral range. Spurious signatures are observed in the Null LSD line profiles and corrected using the method described in Section 3.2.1.

Magnetic analysis of Proxima Cen

As shown in the left panel of Figure 3.11, Zeeman signatures of full-amplitude up to 0.3% are detected in the time series of Stokes V LSD profiles. These Zeeman signatures appear modulated with stellar rotation with a sign switch occurring between phases 0.310 and 0.687, during the gap in our observations. We find that this modulation is best reproduced by ZDI for a rotation period of $P_{\rm rot} = 89.8 \pm 4.0$ d and a stellar inclination of $47 \pm 7°$. A similar rotation period is obtained when we model the B_ℓ time-series using a simple sine-wave (and the chi-square fitting procedure described in Appendix A.2.4). The best fit to the observed circularly-polarized Zeeman signatures and the corresponding magnetic topology are shown in Figures 3.11 and 3.12, respectively. We find a large-scale field of 200 G with a filling factor $f_V = 0.1$, implying a typical field strength of 2 kG covering 10% of the surface of the star. The field is found to be mainly poloidal, with a dominant dipole of 135 G tilted at 51° to the rotation axis towards phase 0.28. Still, we note that higher order magnetic structures correspond to a significant fraction of the reconstructed magnetic energy (e.g., 22% of the poloidal energy lies in the quadripolar component, see Table 3.3). Finally, the reconstructed field is only moderately axisymmetric (44% of the reconstructed energy).

As shown in the right panel of Figure 3.11, the Zeeman broadening of the observed Stokes I LSD profiles varies as a function of the rotation cycle, reaching it maximum around phase 0.3, when the magnetic pole faces the observer. We used the magnetic topology reconstructed with ZDI (see Figure 3.12) to compute a time series of synthetic Stokes I LSD profiles that we compare to the observed ones for a range of f_I/f_V values. We find that $f_I/f_V \sim 3$ minimizes the χ^2 of the residuals in the central regions of the profiles (i.e., within $\pm 6\,{\rm km\,s^{-1}}$, where the modulation of the Zeeman broadening is largest). This yields an unpolarized magnetic flux density of 600 G, consistent with the value reported in Reiners & Basri (2008). If the value of f_I/f_V that we measured is confirmed, this would imply that Proxima Cen has the highest ratio $f_I/f_V = B_I/B_V$ reported so far (found, in general, lower than 0.15; e.g., Reiners & Basri, 2009; Morin et al., 2010; See et al., 2019), which suggests that the dynamo processes at work in Proxima Cen's convective interior are efficient at injecting magnetic energy into the largest spatial scales. Note however that, as it assumes that the small-scale field is distributed as the large-scale field, our estimate of f_I/f_V is to be taken with caution.

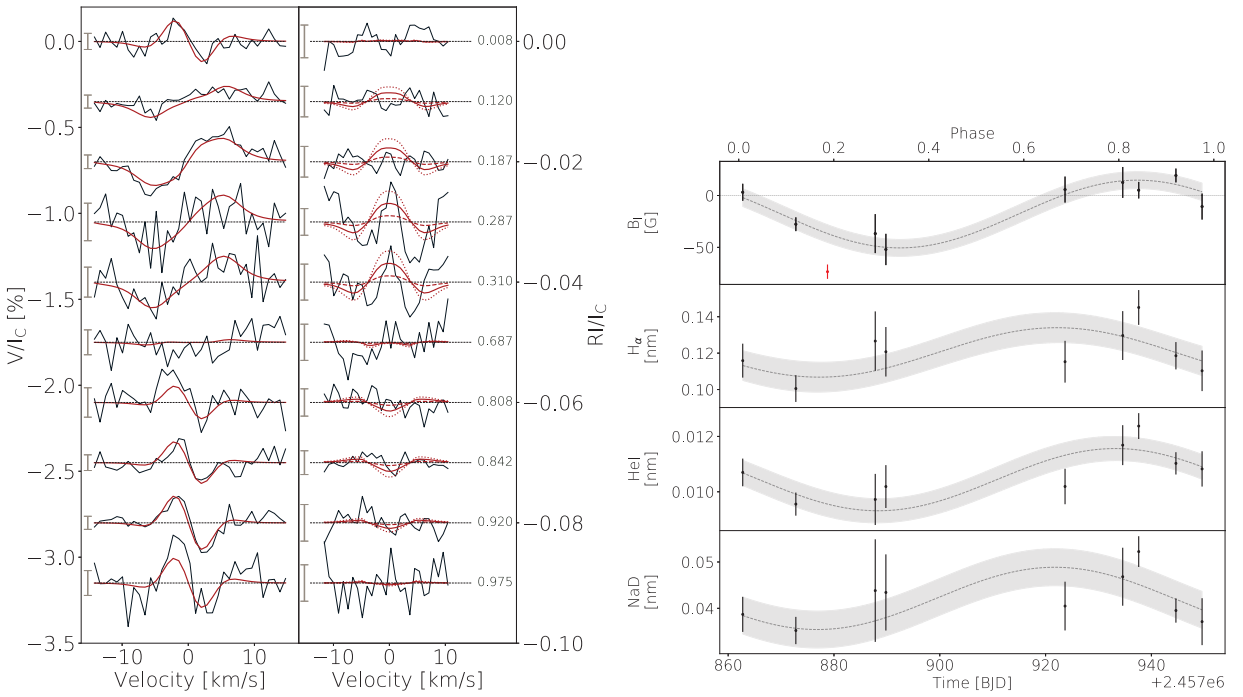

(a) Fit to the observed LSD profiles

(b) Activity indicators

Figure 3.11 – ***Panel 3.11a:*** *Left panel:* Time series of the observed Stokes V LSD profiles of Proxima Cen (thin black lines) and maximum-entropy fit with ZDI (thick red lines). *Right panel:* Median-subtracted Stokes I LSD profiles, RI (thin black lines), and predictions using the magnetic maps of Figure 3.12 assuming f_I/f_V of 1 (red dashed lines), 3 (red solid lines) and 5 (red dotted lines). The figure elements and notations are the same as in Figure 3.8. ***Panel 3.11b:*** Time series of B_ℓ, Mount Wilson S index, and Hα, He I, and Na D activity indices. In each panel, the best sine-wave fit to the time series is shown with the gray dashed line (with $\pm1\sigma$ error bands). Due to a flare occurring before the observation, the chromospheric indices are significantly larger than the mean observed value at phase 0.187, and are thus not displayed here for clarity purposes (this value was also discarded from the sine-wave fit to each time series of indicator displayed here).

Implications for magnetic activity and star-planet interactions

In order to investigate how the reconstructed magnetic topology correlates with the chromospheric activity of Proxima Cen, we computed indices[10] based on Hα, He I and Na D emission flux using the method described in Section 3.2.4 (see the different chromospheric lines in Figure 3.6). The resulting time series, shown in Figure 3.11b, appear modulated with the stellar rotation. He I correlates well with B_ℓ, with minimum emission reached at phase 0.29 ± 0.06 when the magnetic pole faces the observer, and maximum emission when the magnetic equator faces the observer, around phase 0.8. In contrast, non-thermal emissions in the cores of Hα and Na D lines are shifted by $\sim$0.2 in phase with respect to the magnetic field, reaching their respective minimum at phases 0.17 ± 0.07 and 0.17 ± 0.08 (consistent within 2σ with the phasing of the magnetic field). This shift is most likely due to a complex distribution of the chromospheric material differently probed by the two indicators. The overall modulation of the chromospheric indices might reflect the presence of coronal hole associated to open field lines that would be mostly visible when the magnetic pole faces the observer, around phase 0.3.

The recovered magnetic topology can be used to constrain the interaction between Proxima

[10] Note that the activity index based on Ca H & K emission (i.e., the S index) could not be reliably estimated from our observations given the low S/N of the reference continuum regions of Gomes da Silva et al. (2011).

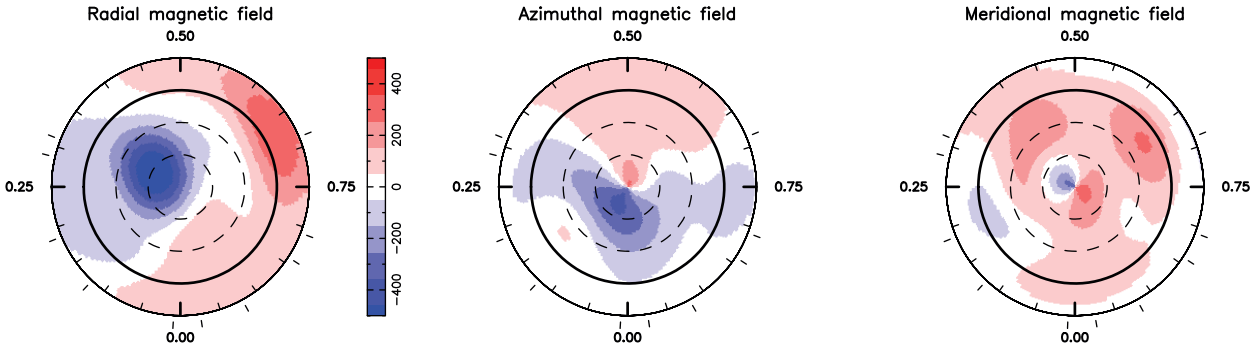

Figure 3.12 – Surface distribution of the radial (left panel), azimuthal (middle panel) and meridional (right panel) components of the large-scale magnetic field of Proxima Cen. The star is described as a flattened polar view featuring the same symbols and notations as Figure 3.9. The rotation cycle of the star is computed from the stellar rotation period $P_{\rm rot} = 89.9\,$d with the reference time BJD = 2457862.

Cen's stellar wind and its close-in planet Proxima b. Given the large corotation radius of Proxima Cen ($\sim$285 $R_{\rm s}$), field lines are expected to open under the effect of wind ram pressure rather than under centrifugal forces (see Section 3.1.3). Although 3D magnetohydrodynamical simulations are needed to determine the shape of the Alfvèn surface of the star, we can obtain a first order estimate of the radius $R_{\rm A}$ of an hypothetically spherical Alfvèn surface under simple assumptions. Proxima Cen features X-ray emission suggesting the presence of a hot corona, likely able to largely ionize the stellar wind (as demonstrated for M dwarfs of earlier types in Mesquita & Vidotto, 2020). Under this assumption, we can compute the so-called magnetic confinement parameter η, defined as the ratio between magnetic and stellar wind kinetic energy densities, such that (ud-Doula & Owocki, 2002)

$$\eta = \frac{B_{\rm s}^2 R_{\rm s}}{\dot{M} v_\infty} \tag{3.8}$$

where $B_{\rm s}$ is the typical strength of the stellar magnetic dipole, equal to 135 G for Proxima Cen, and $\dot{M}$ and v_∞ are the wind mass loss rate and terminal velocity, respectively taken as $2\times10^{-15}\,M_\odot\,{\rm yr}^{-1}$ and $400\,{\rm km\,s}^{-1}$ for Proxima Cen (Wood et al., 2001). We find that $\eta = 8.5\times10^5$ for Proxima Cen. As shown in Figure 3.13, the extended magnetic field B of Proxima Cen is mainly dipolar at large distance and, thus, weakens with the distance r to the star as

$$B(r) = B{\rm s}\left(\frac{\rm R_s}{\rm r}\right)^3. \tag{3.9}$$

Using equation 8 of ud-Doula & Owocki (2002), we find that the equatorial Alfvèn radius of the star is about 25 $R_{\rm s}$. Proxima b orbits at a distance of $\sim$70 $R_{\rm s}$ and is thus expected to lie in the super-alfvenic region of the stellar wind. Moreover, changes in the size of the magnetosphere with the magnetic cycle of the star could potentially affect the alfvenic regime of the stellar wind at the distance of the planet, as suggested in Garraffo et al. (2016). Finally, our magnetic topology confirms the strength of the magnetic field assumed in Ribas et al. (2016), suggesting that the close-in planet could host a magnetosphere of 2-3 planetary radii. Moreover, as suggested in Vidotto et al. (2014a), non-axisymmetric magnetic fields favour axisymmetric distributions of stellar wind mass fluxes. In our case, the moderately non-axisymmetric magnetic topology recovered with ZDI suggests that the wind mass flux is relatively homogeneously distributed and, thus, that the

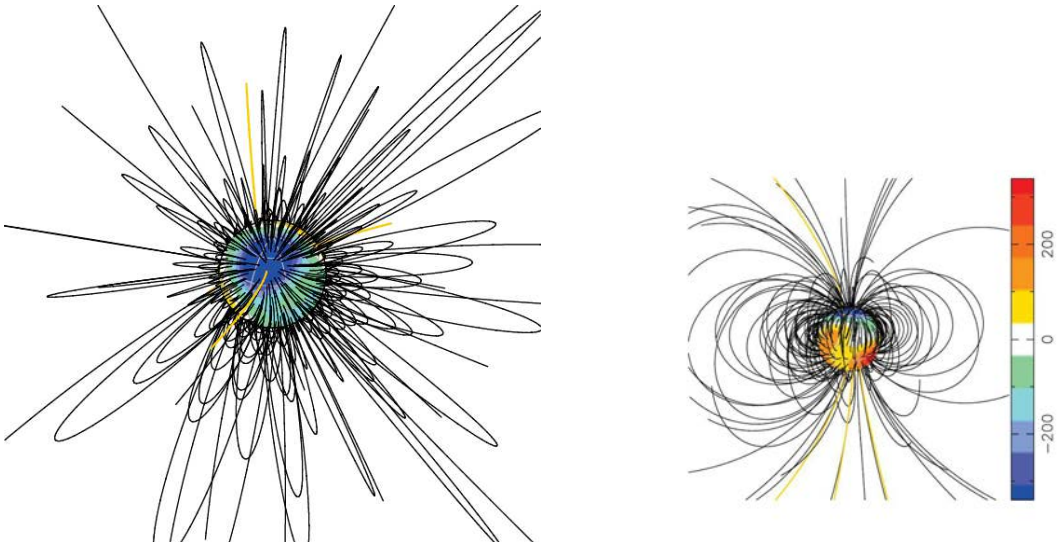

Figure 3.13 – Potential magnetic field of Proxima Cen, extrapolated from the reconstructed magnetic topology of Figure 3.12 using the method of Jardine et al. (1999), shown at phases 0.3 (left panel) and 0.8 (right panel). The color scale depict the strength of the magnetic field at the stellar surface. Open/closed field lines are respectively shown in yellow/black lines. The source surface at which the field lines become radial (and thus open) is set to 25 R_s. For clarity purpose, the star is shown as seen from a distance of 5 R_s.

planet magnetosphere does not undergo significant variations in size as the planet orbits around the star. Extensive magnetohydrodynamical simulations are being carried out by Robert D. Kavanagh (Trinity College Dublin) using the magnetic topologies shown in Figure 3.12 in order to obtain a more precise shape for the Alfvèn surface and study its interaction with Proxima b in more details (Kavanagh, Vidotto, Klein et al., in prep.).

Next steps for Proxima Cen

This study demonstrates that the large-scale magnetic field of Proxima Centauri can be detected with optical spectropolarimeters like HARPS-Pol and that its modulation can be inverted into a surface distribution of large-scale magnetic field. Proxima Cen is one of the first FC M dwarf in the unsaturated dynamo regime (with a Rossby number of 0.63 and $\log L_X/L_{bol} = -3.94$; see Figure 1.11 and Wright et al., 2018) to have its large-scale field reconstructed with ZDI. Its large-field properties appear similar to those of the group of FC M dwarfwith saturated dynamo exhibiting weak multipolar large-scale fields (see Morin et al., 2010, and Figure 3.2). On the other hand, the ratio $<B_V>/<B_I>$ is generally found much weaker for FC M dwarfs in the multipolar large-scale field regime (∼about 6%) than for M dwarfs in the dipole-dominated group (∼15%). If confirmed by new spectropolarimetric observations, the high value of $<B_V>/<B_I>$ measured for Proxima Cen is hard to reconcile with its complex large-scale magnetic topology.

Moreover, our spectropolarimetric observations take place about one year after the activity maximum of the putative 7 yr-photometric cycle reported in Suárez Mascareño et al. (2016) and Wargelin et al. (2017). If the star's magnetic cycle is indeed powered by an $\alpha\Omega$ dynamo as suggested in Yadav et al. (2016) and Wargelin et al. (2017), its magnetic field may oscillate between a strong axisymmetric dipole, at activity minimum, and a weaker non-axisymmetric complex field, at activity maximum. The fractions of axisymmetric and poloidal magnetic energies reconstructed by ZDI have been shown to be excellent proxies of solar-like activity cycles (Lehmann et al., 2021). Hence the need to keep monitoring them throughout the activity cycle, which could give rise to a 7 yr-long large HARPS-Pol program in a near future.

3.3.3 EPIC 211889233

Context and goals

EPIC 211889233 is a M0 dwarf observed with K2 from April to July 2015. It was simultaneously observed with HARPS (27 observations), SOPHIE (15 observations), and ESPsDOnS+NARVAL (21+2 observations) between December 2017 and February 2018. The star was identified as a spectroscopic binary SB1 whose RV signature is fitted and corrected using our velocimetric observations. The residual RVs exhibit a modulation of 11 d probably induced by brightness inhomogeneities crossing the stellar disk, confirming the active nature of the star. EPIC 211889233 is a prime target of choice to prepare the future campaign of spectroscopic and spectropolarimetric observations of TESS targets in the continuous viewing zone (see Section 3.1.4). This work, led by T. Lopez (LAM), is still ongoing. In this section, I only focus on the reconstruction of the surface distributions of large-scale magnetic field and relative brightness that I made from ESPaDOnS/NARVAL and HARPS spectra, respectively.

Our ESPaDOnS and NARVAL sequences of spectra were reduced with the Libre-ESpRIT package and feature a typical S/N of 184 per pixel (of $1.8\,\mathrm{km\,s^{-1}}$ velocity bin). Due probably to bad weather conditions, all the NARVAL spectra and two ESPaDOnS observations exhibit significantly lower S/Ns (of ∼70-90) and are thus discarded from the analysis. The Stokes I and V LSD profiles of each observation were computed from a VALD3 atomic line mask of ∼4000 lines. Spurious signatures are almost systematically seen in our time series of Null LSD profiles. We correct for them using the method described in 3.2.1.

Magnetic analysis

EPIC 211889233 is a slow rotator ($v \sin i_{\mathrm{rot}} = 2.5 \pm 1.0\,\mathrm{km\,s^{-1}}$ from the width of the observed Stokes I LSD profiles, which yields a stellar inclination of $i_{\mathrm{rot}} = 60 \pm 10°$), limiting the order of the spherical harmonic expansion to $l_{\mathrm{max}} = 5$. Circularly-polarized Zeeman signatures of full-amplitude up 0.4% are detected in our time series of Stokes V LSD profiles. Using ZDI, we find that the Zeeman signatures are modulated at a rotation period of 10.88 ± 0.28 d, consistent with that obtained from the RV analysis. The maximum-entropy fit to the observed Stokes V LSD profiles is shown in Figure 3.14. We find a large-scale field of average surface strength 110 G, mainly poloidal (at 85%) and axisymmetric (at 80%), appearing in particular dominated by dipolar and quadripolar contributions (see Table 3.3 and the resulting magnetic topologies shown in Figure 3.15). The time series of observed Stokes V LSD profiles cannot be strictly reproduced to the noise level (χ^2_{r} of 1.15). One possible explanation for this is that the magnetic field has evolved during the gap of almost 2 rotational cycles separating the last three observations from the bulk of our data. The search for potential differential rotation shearing the magnetic field will help reinforcing this speculation.

Brightness reconstructions

Given its small $v \sin i_{\mathrm{rot}}$, EPIC 211889233 appears as a good benchmark to validate the brightness reconstruction methods described in Section 3.2.2 to very slowly-rotating stars. We used methods 1 and 2 described in Section 3.2.2 (respectively, the residuals method of Hébrard et al., 2016, and the iterative process to correct for systematic differences between observed and synthetic line profiles) to map the surface brightness of the star. EPIC 211889233 is an early M dwarf which is thus likely to exhibit dark inhomogeneities at its photosphere (see Beeck et al., 2015, and Section 3.2.2), which is reinforced by the fact that the average value of the K2 relative brightness curve is visually located below 1[11]. For method 1, the spot local brightness is set to 0.5.

[11] https://www.cfa.harvard.edu/~avanderb/k2c5/ep211889233.html

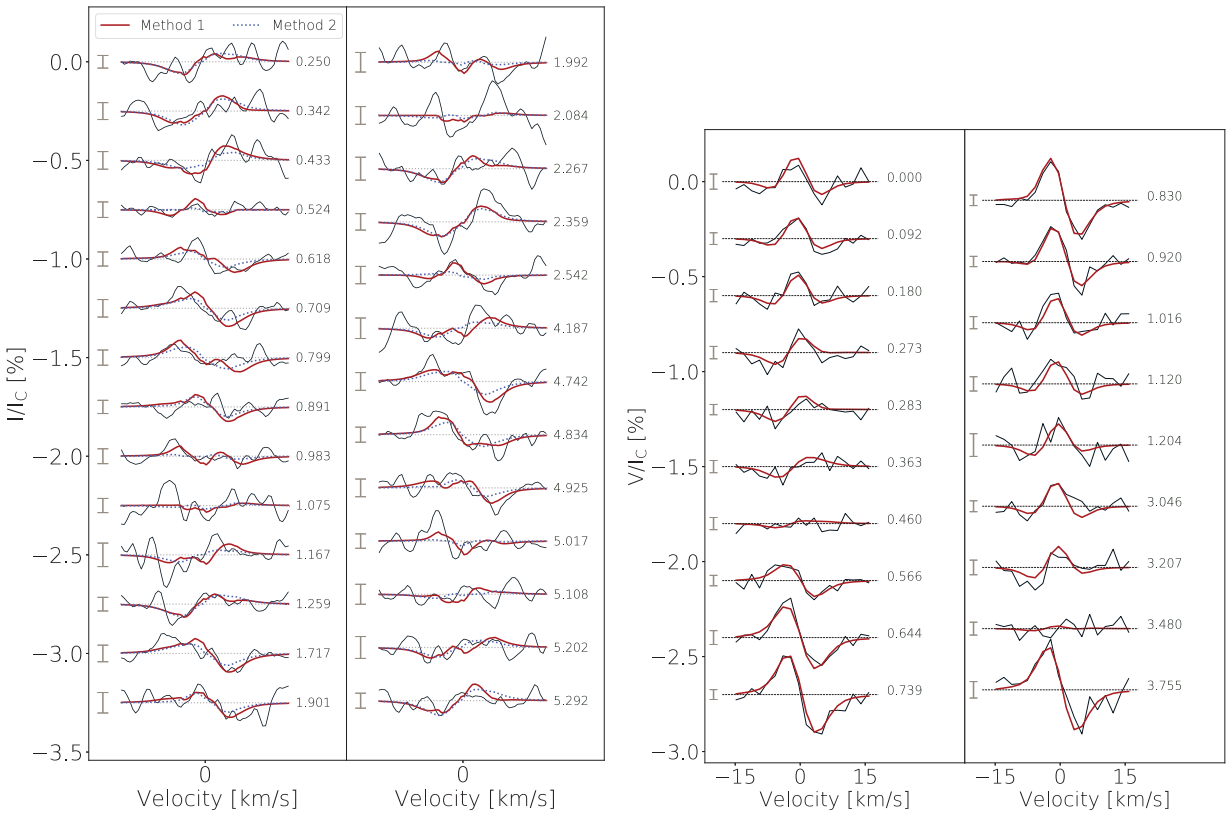

Figure 3.14 – *Left panel:* Median-subtracted Stokes I LSD profiles of EPIC 211889233 (black solid lines) and best reconstructions using Methods 1 and 2 described in Section 3.2.2. *Right panel:* Maximum-entropy fit to the observed Stokes V LSD profiles of EPIC 211889233. The figure elements are the same as in Figure 3.8. The rotation cycle of the star is computed from the stellar rotation period $P_{\rm rot} = 10.88$ d with the reference time BJD = 2458115.95527.

Both maximum entropy reconstructions are shown in the middle panels of Figure 3.15 and the best fits to the median-subtracted Stokes I LSD profiles are shown in Figure 3.14. Both methods yield roughly similar reconstructions featuring consistent equivalent spot coverages of 1.35%. When compared to the magnetic topology, we note that the largest brightness inhomogeneities roughly follow the magnetic equator (e.g., around phases 0.15, 0.3, 0.95). As a safety check, we tried to include bright features in the brightness reconstruction using method 2 and found that the recovered brightness topology is marginally impacted by the assumption, confirming that the surface of the star is preferentially populated by dark spots. In order to quantify how accurate the reconstructions of the activity-induced distortions in the observed profiles are, we generate time-series of synthetic Stokes I LSD profiles from the two brightness distributions shown in Figure 3.15, from which we deduce the RVs. As illustrated in the bottom panel of Figure 3.15, both methods yield accurate modelling of the stellar activity RV signal, down to a $\chi^2_{\rm r}$ of 1.4, comparable to the goodness of the fit obtained when the RVs are modeled using a sine-wave at a period of 10.88 d and its first two harmonics. We note that the fit cannot be pushed further as the star has evolved during our observations (the last 3 RV measurements, shown in magenta in Figure 3.15, appear visually shifted from the other data points). As intrinsic variability of stellar activity is not yet included in our ZDI reconstruction algorithm, the fit cannot be pushed further for now.

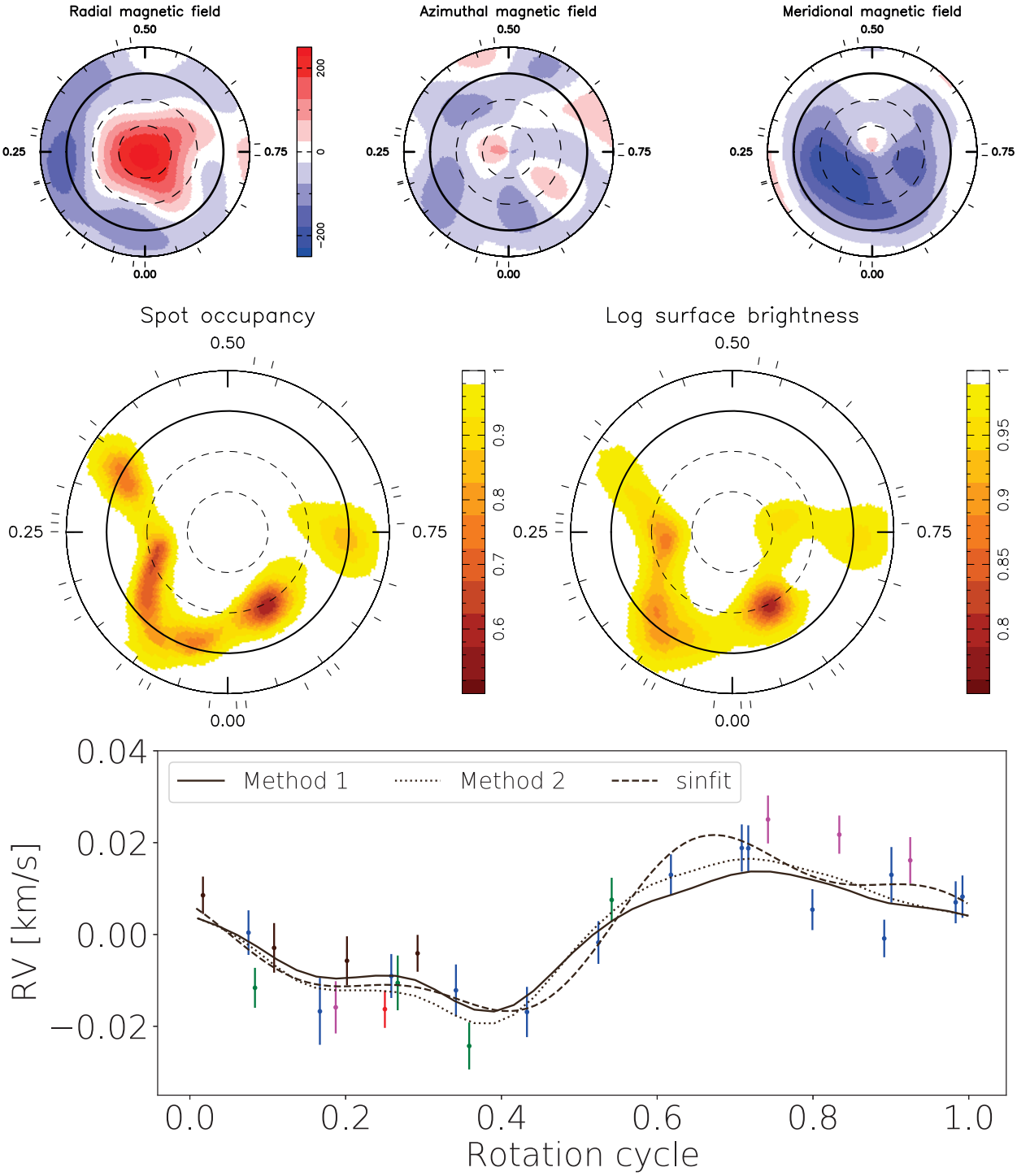

Figure 3.15 – *Top line:* Flattened polar views of the surface distribution of the radial, toroidal and azimuthal components of the large-scale magnetic field of EPIC 211889233. *Middle line:* Surface distribution of the spot coverage (left panel) and relative brightness (right panel) obtained by respectively applying methods 1 and 2 of Section 3.2.2 to carry out the maximum-entropy reconstructions of the time series of HARPS Stokes I LSD profiles. *Bottom line:* Phase folded HARPS RV time-series (black points) and best sine-wave fit including the first two harmonics of $P_{\rm rot}$ (dashed line) and the brightness distributions obtained with methods 1 (residuals method, solid line) and 2 (iterative removal of systematics, dotted line). The RMS of the residuals is 5.5, 5.3 and 5.4 m s^{-1} for the sine-wave fit, method 1 and method 2. Data points of the same color belong to the same rotational cycle. The rotation cycle of the star is computed from the stellar rotation period $P_{\rm rot} = 10.88$ d with the reference time BJD = 2458115.95527.

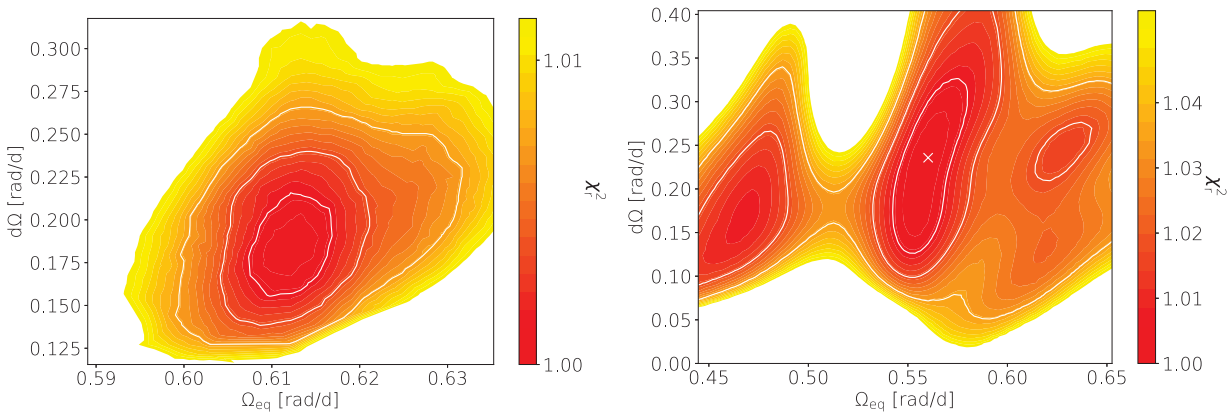

Figure 3.16 – Distribution of χ^2 as a function of the stellar DR parameters $\Omega_{\rm eq}$ and $d\Omega$ obtained by performing brightness reconstructions of HARPS Stokes I LSD profiles (left panel; method 2 for brightness reconstruction) and magnetic reconstructions of ESPaDOnS Stokes V LSD profiles (right panel). In each panel, the white contours indicate the 1, 2 and 3σ levels from the minimum value.

Differential rotation

We find that both surface distributions of spots and large-scale field are sheared by solar-like DR of similar levels within the error bars (see the $\chi^2_{\rm r}$ maps shown in Figure 3.16). However, the DR shearing the large-scale field remains poorly-constrained by as sparse a data set as ours. Note however that one local minimum is found at similar DR parameters as those obtained for the brightness distribution. A dense coverage of 2-3 consecutive stellar rotation cycles will likely allow us to more accurately pin down the DR shearing the large-scale field of EPIC 211889233.

Next steps for EPIC 211889233

The spectropolarimetric analysis of EPIC 211889233 is ongoing and will be published in the months to come (Lopez, Klein et al., in prep.). The goal is now to determine how the surface distribution of spots and large-scale field can be combined with activity indicators such as K2 light curve or chromospheric emission in order to accurately model the observed stellar activity RV signals. Ultimately, synthetic planet signatures could be added to observed Stokes I LSD profiles in order quantify their detectability around stars of similar spectral types and activity levels.

3.3.4 V471 Tau

The pre-cataclysmic variable binary system V471 Tau

V471 Tau is a white dwarf-K2 dwarf eclipsing binary of the 625 Myr Hyades open cluster (Perryman et al., 1998). This system is a compact ($P_{\rm orb} = 0.52$ d) pre-cataclysmic variable[12] thought to have undergone a recent common envelope phase (see Vaccaro et al., 2015, and the references therein). Starting from two MS stars separated by a few astronomical units, the post MS evolution of the most massive star triggered a mass transfer from the pre-red giant to the MS star on much shorter time scales than the typical Kelvin-Helmholtz time scale of the MS star. As a result of this unstable mass transfer, a common envelope forms between the two stars. This common envelope exerts a strong drag on the two stars that get progressively closer to each other until the common envelope is expelled (see the review of Ivanova et al., 2013). The system is thought to be a pre-cursor of cataclysmic variables, in which the white dwarf (WD) distorts its stellar companion and accretes

[12]

its material until the mass of the WD reaches the Chandrasekhar limit and explodes as a type Ia supernova (Warner, 1995). Mass transfers from the K2 dwarf to the white dwarf are expected to start in about $\sim 8 \times 10^8$ yr (Schreiber & Gänsicke, 2003).

The V471 Tau system exhibits eclipse timing variations (ETV) modulated at a 30 yr-period (e.g., Vaccaro et al., 2015), initially interpreted by the presence of a distant third body in the system (O'Brien et al., 2001). However, this assumption was recently questioned in Hardy et al. (2015) and Vanderbosch et al. (2017) in favour of the Applegate effect (Applegate, 1992), in which stars harbouring cyclic magnetic fields might be capable of modifying their inner mass distribution by redistributing angular momentum in their convective envelope. In the V471 Tau system, the cyclic gravity change induced by the Applegate effect in the K2 dwarf interior might explain the periodic ETVs.

Spectropolarimetric observations of the K2 dwarf of the V471 Tau system were collected with ESPaDOnS back in November 2004 and December 2005. Our data set contains 230/400 Stokes I spectra and 56/98 Stokes V spectra for Nov 04/Dec 05 periods, respectively. These observations represent an opportunity to investigate how the strong tides undergone by the K2 dwarf affect its magnetic topology and DR. Their analysis, carried out by Bonnie Zaire, will soon be submitted to MNRAS (Zaire, Donati & Klein, in prep.). In the following, we refer to K2 dwarf of the V471 Tau system as V471 Tau.

Temporal fluctuations in the surface differential rotation of V471 Tau

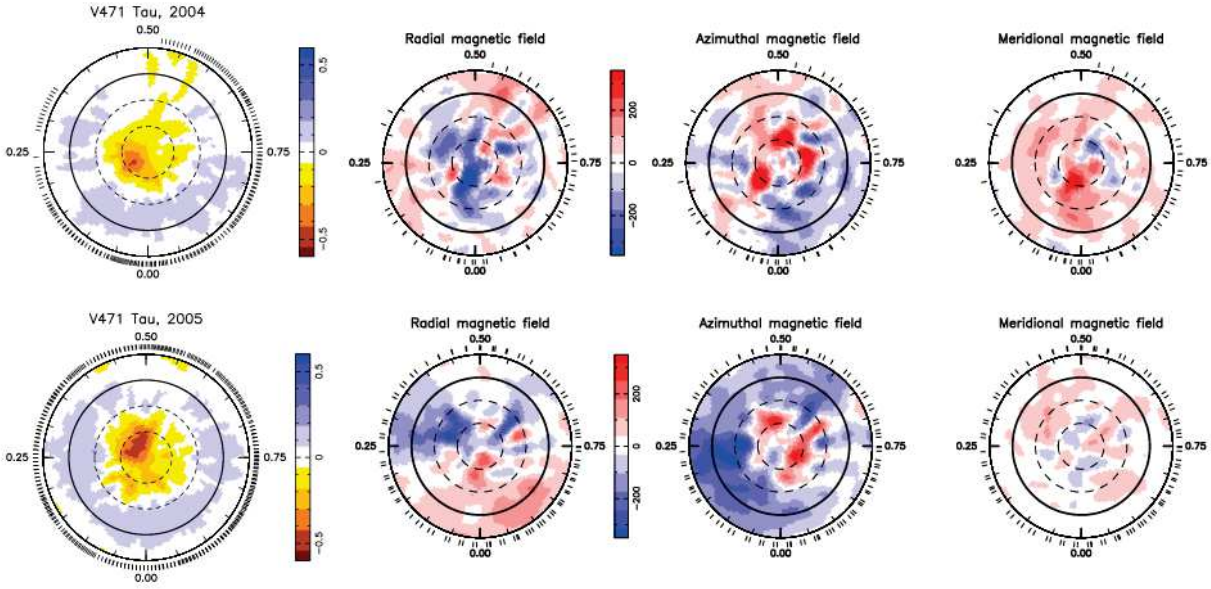

Figure 3.17 – Flattened polar views of the logarithm of the relative brightness (first column) and radial, azimuthal, and meridional components of the large-scale magnetic field (resp. columns 2, 3, and 4) at the surface of V471 Tau. The maps shown in the top/bottom lines were obtained by fitting the line profiles observed in Nov 2004/Dec 2005. The figure properties are the same as in Figure 3.9. The rotation cycle of the star is computed from the stellar rotation period $P_{\rm rot} = 0.52118833875$ d (Vaccaro et al., 2015) with the reference time BJD = 2445821.898291. Source: Zaire, Donati & Klein, submitted.

After applying LSD to our reduced set of spectra (using a VALD3 atomic line mask assuming $T_{\rm eff} = 5000$ K and $\log g = 4.5$), we estimate the orbital period, phase and semi-amplitude of the binary barycentric motion by reconstructing the observed Stokes I LSD profiles with ZDI (and using the chi-square fitting method), and align the line profiles in the stellar rest frame. We then

used ZDI to independently invert our time series of Stokes I and Stokes V line profiles into surface distributions of brightness and large-scale magnetic field for the two epochs of observations.

The maximum-entropy surface distributions of brightness and large-scale field are shown in Figure 3.17. The brightness maps are roughly consistent with each other, with spot/plage coverages of 8/6 and 10/7% for Nov 04 and Dec 05, respectively[13] and resemble those reported in previous studies (e.g., Ramseyer et al., 1995; Hussain et al., 2006), suggesting long-lived features at the stellar surface. We recover consistent magnetic field strengths of 170-160 G for both epochs. The reconstructed topologies are however slightly different: the topology recovered in Nov 04 is dominated by high-order components (60% of the reconstructed energy lie in modes with $l > 3$; see Table 3.3), whereas that of Dec 05 is dominated by the dipole component (with now only 30% of the reconstructed energy modes with $l > 3$). However, we caution that this difference in magnetic topologies could just be an artefact induced by the 0.15 phase gap (between phases 0.35 and 0.5) in Nov 04. As a consequence, we cannot formally conclude on the field evolution between the two epochs.

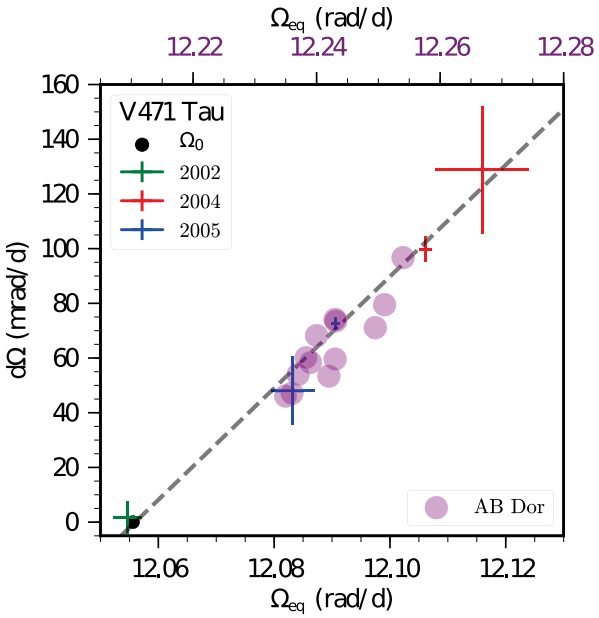

Figure 3.18 – Differential rotation at the surface of V471 Tau obtained from our Nov 2004 and Dec 2005 data sets (resp. red and blue crosses with $\pm 1\sigma$ error bars. We also indicate in green the DR parameters reported in Hussain et al. (2006). The black dot indicates the rotation rate of V471 Tau, assuming a solid-body rotation. A linear fit to all the DR parameters reported for V471 Tau is shown by the dashed gray line ($\Omega_{\rm eq} = 0.49\,{\rm d}\Omega + 12.056$ rad/d). For comparison, we include the DR parameters measured for AB Doradus, a twin single-star version of the K2 dwarf of the V471 Tau system, as purple circles (Donati et al., 2003; Jeffers et al., 2007).

As shown in Table 3.3, we report a positive solar-like DR for V471 Tau. While dΩ is found $\gtrsim 2\times$ solar from both our Stokes I and Stokes V profiles in Nov 04, it drops to a level close to solar in Dec 05. We interpreted this observation in term of redistribution of the angular momentum in the stellar convective zone using the method introduced in Donati et al. (2003). Assuming the conservation of the angular momentum in the convective, zone, one can demonstrate that $\Omega_{\rm eq} = \lambda {\rm d}\Omega + \omega_{\rm c}$, where $\omega_{\rm c}$ is a constant and λ depends on how the angular momentum is distributed within the convective

[13] The slight increase in feature coverage from Nov 04 to Dec 05 is likely due to the gap in our observations between phases 0.35 and 0.5

zone. For the Sun, where the radial evolution of the rotation rate is roughly constant, implying that $\lambda = 0.2$. In contrast, according to the Taylor-Proudman theorem, the angular rotation rate of fast rotators (i.e., $P_{\rm rot} \lesssim 0.5\,{\rm d}$) is roughly constant over axisymmetric cylinders in the convective zone, which yields $\lambda = 0.52$ for AB Doradus (Donati et al., 2003). As illustrated in Figure 3.18, by combing the DR parameters recovered for V471 Tau, we find that $\lambda = 0.49 \pm 0.02$, which is consistent with a rotation constant over cylinders.

Our results demonstrate that the high level of tides undergone by the star due to its proximity to the white dwarf is not sufficient to significantly weaken the stellar DR as initially expected (Scharlemann, 1981, 1982). However, our relative DR $\mathrm{d}\Omega/\Omega$ does not exceed 1%, implying that the observed ETVs are likely not driven by the Applegate mechanism (Völschow et al., 2018). At this stage, the mechanism producing the observed ETVs remains unclear despite promising alternative mechanisms recently proposed in the literature (Lanza, 2020). Several spectropolarimetric campaigns of the star on time scales on which the eclipsing transit time varies could greatly help probing the evolution of the magnetic field of the star and potentially identify the mechanism driving the ETVs of the system.

4 | Measuring the mass of AU Mic b with SPIRou

Contents

Close-in planetary systems transiting young PMS stars are primary targets to understand how planets form and evolve. Velocimetric follow-ups of such targets have the potential to provide a precise measurement of the planet mass, critically needed by planet formation and evolution models (Mordasini et al., 2012c) and required for robust atmospheric characterization with forthcoming space-based missions like the JWST (Batalha et al., 2019). Moreover, the planet orbital parameters accessible with high-precision velocimetry, such as the orbit ellipticity and the sky-projected spin-orbit obliquity (through the RM effect), can yield essential information about the planet formation history (Baruteau et al., 2016). No more than 3 planetary systems transiting stars younger than 30 Myr have been unveiled so far (K2-33 b; V1298 Tau b, c, d, e; and AU Mic b, c reported in David et al., 2016, 2019b; Plavchan et al., 2020b, respectively). However, due to the intense magnetic activity exhibited by their host star (see Sections 1.3 and 1.4), none of the planets of these systems has seen its mass measured. In this chapter, we analyse the 27 observations of AU Mic collected with SPIRou as part of the proposal elaborated in Chapter 2 (ID: 19BD97, PI: Klein), in order to pin down the mass of the close-in planet AU Mic b. After briefly introducing this planet in Section 4.1, we present two different methods to determine its mass in Sections 4.2 and 4.3, before outlining the implications and perspectives of this work in Section 4.4. Note that the work presented in this chapter has been the main subject of a national Press Released published on 02/02/2021 and provided in Appendix B.3.

4.1 A Neptune-sized close-in planet around the PMS star AU Microscopii

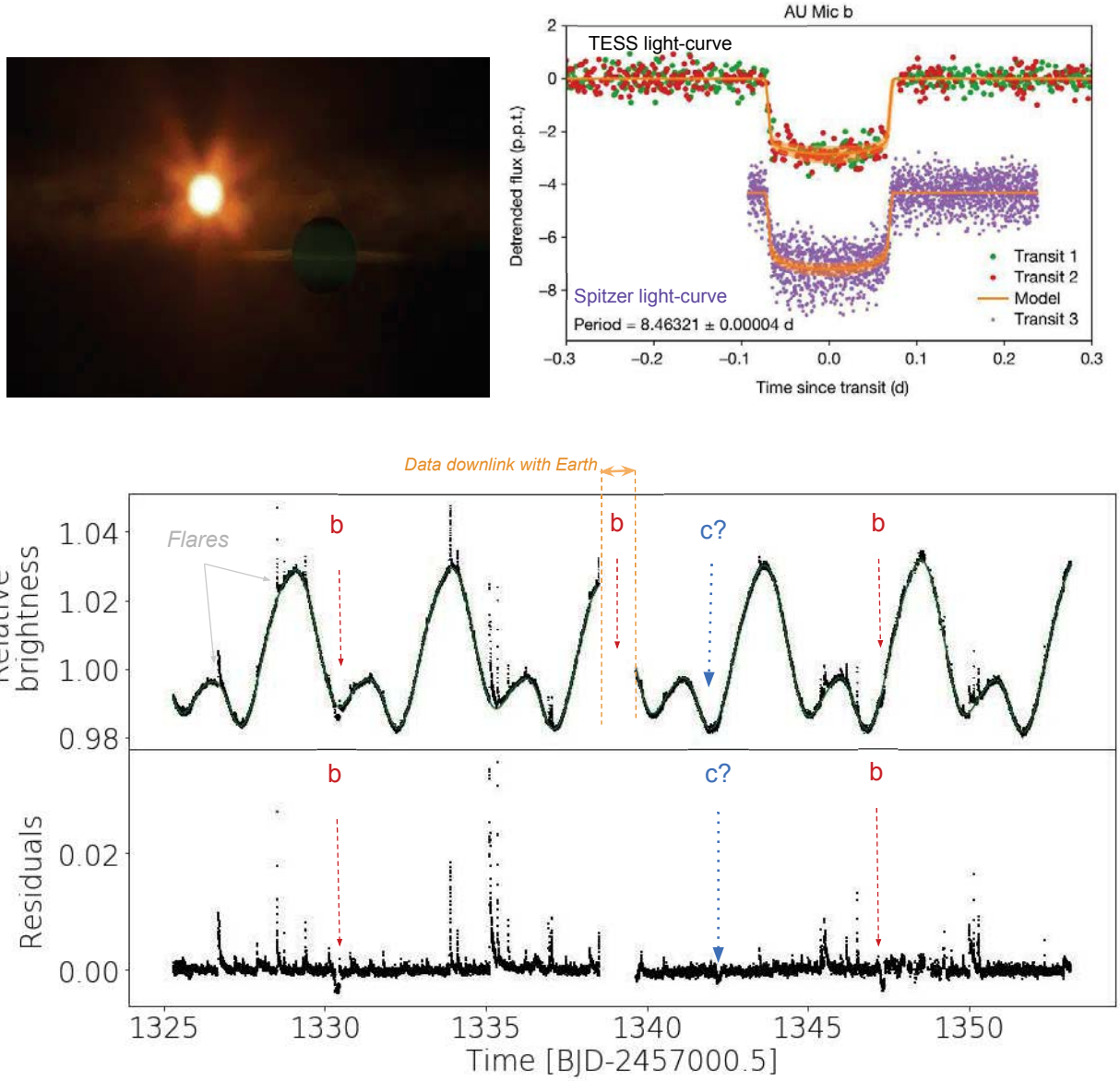

Figure 4.1 – *Upper left panel:* Artist impression of AU Mic b in front of its host star (source: : Goddard Space Flight Centre de la NASA/Chris Smith (https://svs.gsfc.nasa.gov/13648). *Upper right panel:* Folded transit light curves of AU Mic b observed in TESS light curve (top curves; green/red points corresponding to transit 1/2) and Spitzer light curve (bottom curve), and best prediction from P20 from which this plot is adapted. *Bottom panel:* TESS light curve of AU Mic (black dots) and best prediction of its rotationally-modulated component using the method described in Section 2.2.1 (green solid line) and residuals after subtracting this prediction from the data. The transit events of AU Mic b and AU Mic c are indicated by the vertical red dashed and blue dotted arrows.

AU Mic was observed in the first sector of the TESS mission (2018 July 25 to August 22). The resulting 27 d-light curve, shown in Figure 4.1 exhibits three transit-like structures identified by Plavchan et al. (2020b) (refered as P20 in the following), two of them being produced by the same planet AU Mic b, which was confirmed by observations collected with the Spitzer space telescope.

Table 4.1 – Stellar and planet parameters of the AU Mic system relevant for the velocimetric analysis of SPIRou data. When optimized with the model described in Section 4.2.2, we give the prior density used for the Bayesian MCMC process in column 5. In the table $\mathscr{U}$ stands for the uniform distribution and *Mod. Jeffreys ($\bar{\sigma}$)*, for the modified Jeffreys prior† of knee $\bar{\sigma}$, $\bar{\sigma}$ being the typical uncertainty on the RV measurements (i.e., $5\,\mathrm{m\,s^{-1}}$). P20, Ma20, Pa20 and Hi20 stand respectively for Plavchan et al. (2020b), Martioli et al. (2020a), Palle et al. (2020) and Hirano et al. (2020).

Quantity	Parameter	Value	Reference	Prior density
Stellar parameters				
H-band magnitude	H	4.831 ± 0.016	Cutri et al. (2003)	–
Stellar radius	R_s	$0.75 \pm 0.03\,R_\odot$	P20	–
Stellar mass	M_s	$0.50 \pm 0.03\,M_\odot$	P20	–
Rotation period	P_rot	4.86 ± 0.01 d	P20	–
Stellar inclination	i_rot	89.5°	Assumed equal to i_orb	–
Projected velocity	$v \sin i_\mathrm{rot}$	$7.8 \pm 0.3\,\mathrm{km\,s^{-1}}$	From R_s, P_rot and i_rot	–
Linear LD coef.	u	$0.21^{+0.20}_{-0.15}$	TESS light-curve (P20)	–
Stellar activity parameters				
GP Amplitude	θ_1	–	Optimized	Mod. Jeffreys ($\bar{\sigma}$)
GP Decay time	θ_2	110 ± 30 d	P20, B_ℓ	–
GP period	θ_3	–	Optimized	$\mathscr{U}$(4.5,5.3) [d]
GP smoothing param.	θ_4	0.37 ± 0.02	P20, B_ℓ	–
Systemic velocity	V_0	–	Optimized	$\mathscr{U}$(-100,100) [$\mathrm{m\,s^{-1}}$]
Excess of uncorrelated noise	S	–	Optimized	Mod. Jeffreys ($\bar{\sigma}$)
Close-in planet properties				
Planet orbital period	P_orb	8.46321 ± 0.00004 d	P20	–
Semi-major axis	a_p	$0.066^{+0.007}_{-0.006}$ au	P20	–
Mid transit time	T_0	BJD = 2458651.993± 0.002	P20	–
Planet radius	R_p	$4.4 \pm 0.2\,R_\oplus$	**(alias?)**	–
Semi-amplitude AU Mic b RV	K_s	–	Optimized	Mod. Jeffreys ($\bar{\sigma}$)
Orbit inclination	i_orb	$89.5 \pm 0.4°$	P20	
Orbit eccentricity	e_p	$0.10^{+0.17}_{-0.09}$	P20	–
Sky-proj. Spin-orbit incl.	λ	∼0.0	Ma20; Pa20; Hi20	
Orbital phase correction (w.r.t. the transit)	ϕ_p	0.0	Optimized	$\mathscr{U}(0,1)$

† A modified Jeffreys prior of knee κ on a parameter x acts as a uniform distribution when x is small compared to κ, and as a log-uniform density when x is large compared to κ (Gregory, 2007).

The analysis of the transit light curve yielded a radius of $4.2 \pm 0.2\,R_\oplus$ and an orbital period of 8.46321 ± 0.00004 d for the close-in planet (see the planet parameters given in Table 4.1). The Rossiter-McLaughlin effect induced by AU Mic b was independently detected with ESPRESSO, IRD, SPIRou/iSHELL and the Minerva-Australis velocimeters in June 2019 (Palle et al., 2020; Hirano et al., 2020; Martioli et al., 2020a; Addison et al., 2020), and suggests that the sky-projected spin-orbit inclination of the planet is close to zero. In order to determine the mass of AU Mic b, P20 conducted a high-precision velocimetric follow-up of AU Mic using HIRES (Vogt et al., 1994) and HARPS (Mayor et al., 2003) optical spectrometers, and iSHELL nIR spectrograph (Rayner et al., 2016). However, given (i) the high-amplitude RV fluctuations induced by stellar activity in their RV time-series (dispersion of $115/175\,\mathrm{m\,s^{-1}}$ RMS in HARPS/HIRES RVs), and (ii) the sparseness of their sampling (∼75 data points collected on a ∼15 yr-period), P20 reported no more than an upper limit of $M_\mathrm{p} < 58.3\,M_\oplus$ (corresponding to $K_\mathrm{s} < 28\,\mathrm{m\,s^{-1}}$) for the mass of AU Mic b[1]. AU Mic was again observed by TESS in July 2020 (in Sector 27), allowing Martioli et al. (2020b) to refine the transit parameters of AU Mic b and confirm the existence of an outer transiting Neptune-sized planet, AU Mic c, for which one candidate transit event had been identified in the 2018 TESS light curve (see Figure 4.1). As the existence of AU Mic c was confirmed after the submission of the present document, this chapter focuses on the characterization of AU Mic b while the mass

[1] Note that Plavchan et al. (2020b) obtained a semi-amplitude of $14.4^{4.8}_{-5.1}\,\mathrm{m\,s^{-1}}$ for AU Mic b but preferred to remain cautious and report an upper limit for the planet mass

measurement of outer planets is left for future SPIRou observations of the star.

The 27 spectropolarimetric observations of AU Mic presented in Section 3.3.1 offer a great opportunity to pin down the mass of AU Mic b. The observational sampling of our data is quite similar to that assumed in the simulated RV follow-up of AU Mic presented in 2. Provided that we achieve precise RV measurements from our spectra (what seems possible given how bright the star is in the nIR) and that the resulting RV time-series is exhibits a dispersion comparable to that of our synthetic data, we should be able to detect a planet signature of semi-amplitude down to $\sim$10 m s^{-1} for AU Mic b (see Section 2.3.3).

4.2 Unveiling AU Mic b signature from SPIRou RV time-series

4.2.1 RV measurement process

RV measurement

The RV measurement is carried out from the Stokes I LSD profiles extracted using the empirical line mask described in Chapter 3 (see Section 3.3.1 for the description of the data set). We propose three independent methods, illustrated in Figure 4.2, to measure the RVs from the Stokes I LSD profiles.

- **Gaussian fit:** We jointly fit a Gaussian function on top of a linear continuum (5 parameters in total) to each line profile truncated at $\pm$ 20 km s^{-1} from the line center, located at -4.45 km s^{-1} (i.e., the value that minimizes χ^2_r in ZDI reconstructions). The slanted continuum turns out to be critical not to bias the RV measurement process. The modeled line profiles are shown in the upper right panel of Figure 4.2.
- **Median bisector:** We calculated the bisector of each line profile truncated at $\pm$ 31 km s^{-1} from the line center and corrected from residual slopes in the continuum. As recommended by Gray (1982) and Queloz et al. (2001), the bisector is computed between 20 and 95% of the full line profile counting from the continuum and the RVs are derived by taking the median value of the resulting bisector. The latter, shown in the bottom left panel of Figure 4.2, exhibits a characteristic "C" shape symptomatic of solar-like granulation at the surface of the star (e.g. Gray, 1982, 1989; Queloz et al., 2001). We also compute the velocity span, V_s, known to be a reliable proxy of stellar activity RV signals (Queloz et al., 2001), from the average velocities on top and bottom parts of the bisector (resp. within 20-40% and 60-95% of the full line depth counting from the continuum; see Figure 4.2).
- **Variation of LSD profiles:** In this method, we start by linearly adjusting all LSD profiles $\boldsymbol{I}$ to the median line profile $\bar{I}$ (using a LS estimator), and subtract $\bar{I}$ from $\boldsymbol{I}$. Non-axisymmetric stellar features crossing the stellar disk induce small shifts on the width of $\boldsymbol{I}$ that are roughly proportional to the first derivative of the line profile (see the example in the upper right panel of Figure 4.2. We fit a Gaussian function to $\bar{I}$, and compute its first derivative that we then linearly adjust to each median-subtracted Stokes I LSD profile to obtain the corresponding RV.

The RV time-series computed using the three methods described above are shown in the lower right panel of Figure 4.2. They all exhibit similar dispersions of $\sim$45 m s^{-1} RMS, consistent with nIR RV observations of AU Mic (Gagné et al., 2016; Plavchan et al., 2020b) and with the synthetic RV curve generated in Chapter 2. Note that we however find median differences as high as 9 m s^{-1} RMS between the different RV time-series which is tentatively interpreted in Section 4.2.3.

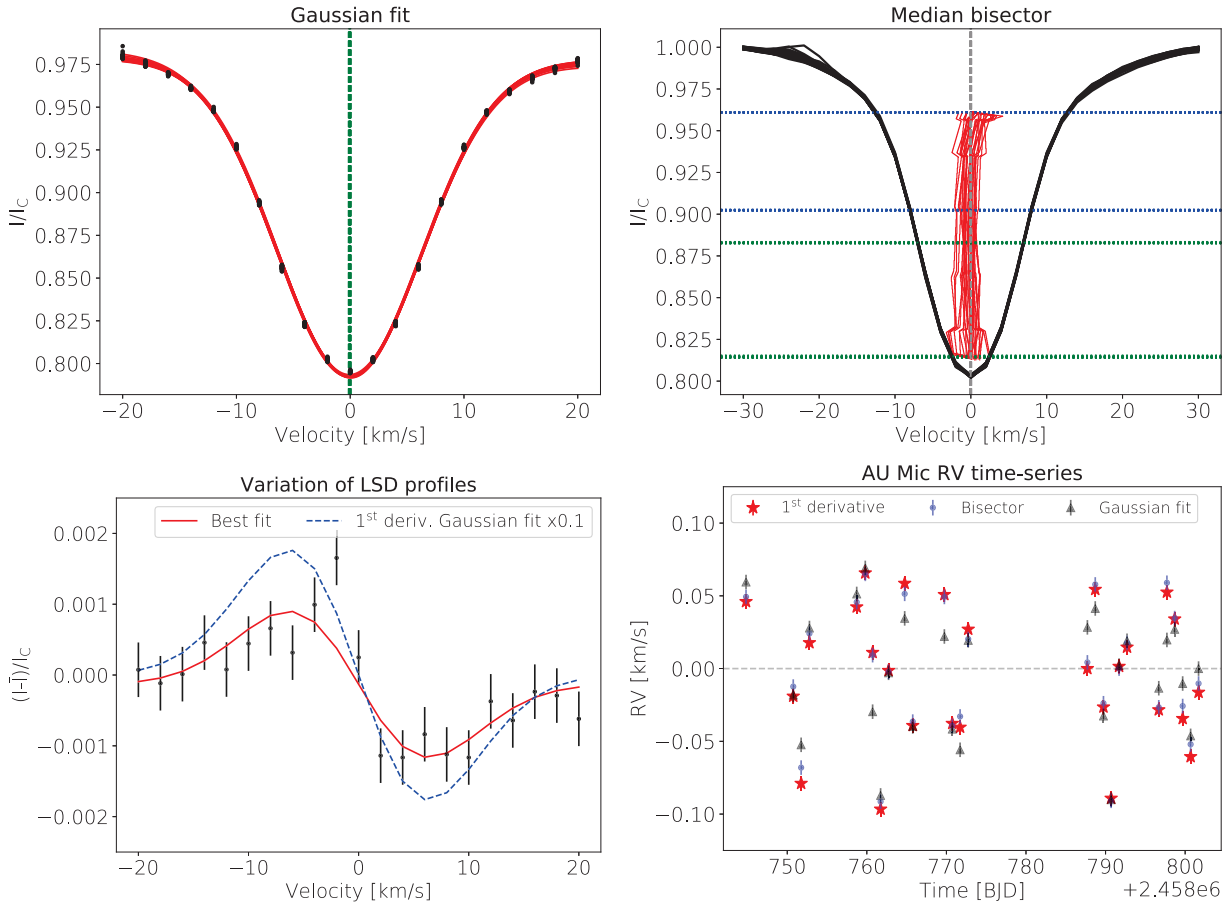

Figure 4.2 – *Upper right panel:* Best Gaussian fits on top of a linear continuum (red solid lines) to a all superimposed Stokes I LSD profiles (black solid points). The measured RVs are indicated by the vertical green dashed lines. *Upper left panel:* Stokes I LSD profiles (black solid lines) and bisectors (red solid lines, 20× enlarged). The RVs are computed by taking the median value of the bisector between the upper blue and lower green horizontal lines (respectively 20 and 95% of the full line depth). The measured RVs are indicated by the gray vertical dashed lines. The two regions delimited by the horizontal blue and green dotted lines are used to compute the velocity span. *Lower left panel:* First derivative of a Gaussian function fitted to the median Stokes I LSD profile (blue dashed line; divided by 10 for the clarity of the plot). An example of a linear fit of this derivative to a given median-subtracted Stokes I LSD profile (black points with 1σ error bars) is shown by the red solid line. *Lower right panel:* Median-subtracted RV time-series of AU Mic using the methods detailed in the three other panels of the figure. All RV time-series exhibit similar dispersion of $45\,\mathrm{m\,s^{-1}}$ RMS.

RV uncertainty

Various sources of noise contribute to the RV error budget of our observations of AU Mic (e.g., instrument and light injection stability, photon noise, pollution from telluric lines, difference of RV zero point from one observing period to the other; see Section 1.2.2.2). Estimating these contributions is a tricky process on as active a star as AU Mic. Velocimetric observations of the inactive star Gl 699 (a.k.a. Barnard's star) collected with SPIRou at almost the same epochs as our observations yield a median absolute deviation of $3\,\mathrm{m\,s^{-1}}$ and a standard deviation of $5\,\mathrm{m\,s^{-1}}$. In our analysis, we take $5\,\mathrm{m\,s^{-1}}$ as a conservative uncertainty for our RV measurements of AU Mic and check in the RV analysis that this error bar is adapted for our data (see 4.2.2).

We quantify the photon noise on our RV measurements using the following procedure. We

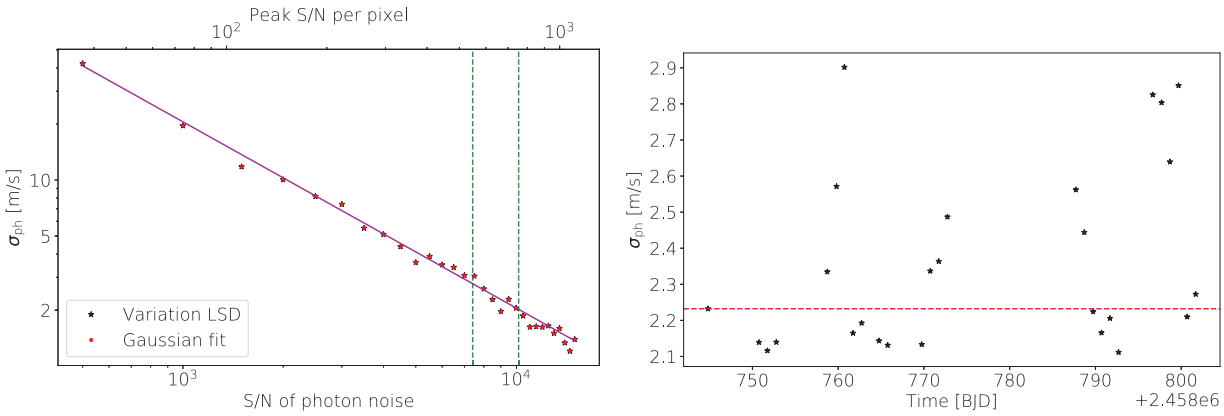

Figure 4.3 – *Left panel:* Evolution of the RV uncertainty $\sigma_{\rm RV}$ as a function of the S/N associated with photon noise in the Stokes I LSD profiles (lower X-axis), and of the peak S/N per pixel (i.e., 2.28 km s^{-1}) in the observed AU Mic spectra (the lowest and largest peaks S/N per pixel of the observed spectra is indicated by the green vertical lines). Note that both X and Y axes are in logarithmic scale. The black stars and red dots are respectively obtained by fitting a Gaussian to synthetic AU Mic line profiles and linearly adjusting the first derivative of a Gaussian the median-subtracted line profiles of AU Mic. The magenta solid line indicates the hyperbola that matches best the data. *Right panel:* RV photon noise of each observation (the median value is indicated by the red dashed line).

generate 100 unspotted synthetic line profiles for AU Mic (using the line parameters derived in Section 3.3.1) with different realizations of a random Gaussian white noise of a given level σ per pixel. We then measured the RV of each synthetic line profile by fitting a Gaussian function to it, and take the dispersion of the resulting RVs as the RV uncertainty $\sigma_{\rm ph}$. We repeat this process for different values of σ. As shown in the left panel of Figure 4.3, $\sigma_{\rm ph}$ typically varies like the inverse of the S/N in the synthetic line profiles (where S/N $= 1/\sigma$). The level of photon noise in each of our observed Stokes I LSD profile is estimated by computing the dispersion within the continuum. We then use an hyperbola linearly adjusted to the distribution of $\sigma_{\rm ph}$ (see the magenta curve in the left panel of Figure 4.3) to quantify $\sigma_{\rm RV}$. As shown in the right panel of Figure 4.3, the resulting photon noise on our RV time-series varies from 2.1 to 2.9 m s^{-1} (median/mean of 2.2/2.4 m s^{-1}). As photon noise is not the main contribution of the RV error budget, we keep using the 5 m s^{-1} dispersion of the RVs of Gl 699 to be a reasonable estimate of the 1σ error bar for our RV measurements of AU Mic (noted $\sigma_{\rm RV}$ in the following).

4.2.2 RV modeling

The observed median-subtracted RV time-series are modeled using a process similar to that used to fit synthetic RV time-series in Section 2.2.3 (we keep the same notations). We here focus on the few changes of our estimation process when applied to real data. The observed RV time-series are modeled as

$$V_{\rm r}(t) = V_{\rm p}(t) + V_{\rm j}(t) + V_0 + \epsilon(t), \tag{4.1}$$

where V_0 is a constant RV offset and $\epsilon(t) \sim \mathcal{N}(0,\sigma_{\rm RV})$, with $\sigma_{\rm RV} = 5$ m s^{-1}. As reported in P20, the eccentricity of AU Mic b's orbit is likely small. We thus assume that the planet orbit is circular, and model its RV signature by

$$V_{\rm p}^{i}(t) = -K_{\rm s} \sin\left[2\pi\left(\frac{t-T_0}{P_{\rm orb}} - \phi_{\rm p}\right)\right], \tag{4.2}$$

where $\phi_{\rm p}$ the orbital phase correction relative to the planetary transit (the values of these two quantities are given in Table 4.1) to Eq. 2.10. As shown for the similar system K2-33 in Chapter 2, constraining the orbital eccentricity of AU Mic b from only 27 data points is doomed and $\gtrsim 60$ data points on a given period would allow to constrain the orbital ellipticity with a precision better than that reported in Plavchan et al. (2020b). Both $P_{\rm orb}$ and $\phi_{\rm p}$ are fixed to their photometric estimates (see table 4.1) in our fiducial model. The stellar activity RV signal is modeled using GPR, assuming the quasi-periodic covariance kernel k defined in Eq. 2.5. Given the low number of data points in our RV time-series, we fix the values of the GP decay time and smoothing parameters, respectively θ_2 and θ_4, to 100 d and 0.4, close to the values reported in Plavchan et al. (2020b) and consistent with the values obtained by modeling the B_ℓ time-series of AU Mic with a GP (see Section 3.3.1 and Figure 4.5).

To investigate whether the 1σ-uncertainties adopted for our RV time-series are correctly estimated, we added a constant term representing a potential excess of uncorrelated noise, S, in the free parameters of the model (to account for stellar variability or residuals of telluric correction, in a way similar to Delisle et al., 2018; Suárez Mascareño et al., 2020). S is quadratically added to the covariance matrix of the red and white noise in our RV time-series, $\mathbf{\Lambda}(\boldsymbol{\theta}, S)$, given by

$$\mathbf{\Lambda}(\boldsymbol{\theta}, S) = \boldsymbol{K}(\boldsymbol{\theta}) + \mathbf{\Sigma}(S) \tag{4.3}$$

where $\mathbf{\Sigma}_{i,j}(S) = ({\sigma_{\rm RV}}^2 + S^2)\,\delta_{i,i}$. Note that, as the 1σ error bars on our RVs are presumably conservative, we do not in principle except any excess of uncorrelated noise in our RV time-series (i.e., $S = 0\,{\rm m\,s^{-1}}$). Our final model contains 5 or 4 parameters (depending on whether S is fitted or not), whose posterior density $p(K_{\rm s},\theta_1,\theta_3,V_0,S|\boldsymbol{V_{\rm r}})$, given by

$$p(K_{\rm s}, \theta_1, \theta_3, V_0, S|\boldsymbol{V_{\rm r}}) = \pi(\theta_1, \theta_3, {\rm S})\,\mathcal{N}(\boldsymbol{V_{\rm r}}; \boldsymbol{V_{\rm p}}({\rm K_s}) + {\rm V_0},\, \mathbf{\Lambda}(\theta_1, \theta_3, {\rm S})), \tag{4.4}$$

is jointly sampled in the Bayesian framework using the EMCEE affine-invariant sampler (5000 iterations of 100 walkers with a burn-in period of 2000 iterations). The prior density adopted for the model parameters are listed in Table 4.1. The parameters of the model are estimated by maximising p, and the 1σ error bars on each parameter is computed from the $16^{\rm th}$ and $84^{\rm th}$ percentiles of the distribution. Like for our synthetic RV time-series, the statistical significance of AU Mic b is estimated by computing the Bayes factor (BF) in favor of the planet using the method of Chib & Jeliazkov (2001) as described in Appendix A.4.1.

4.2.3 Detection of the planet

We fit the model described in Section 4.2.2 to the different RV time-series measured in Section 4.2.1. The main parameters provided by the MCMC process are given in Table 4.2. Note that the RV time-series obtained by fitting a Gaussian function to each Stokes I LSD profiles is chosen to be the reference case here. This is due to the fact that the amplitude of the GP estimated by our MCMC process in the two other cases is about twice as large as the dispersion of our RV time-series ($\sim$45 $\rm m\,s^{-1}$ for all methods presented in Section 4.2.1). As the GP amplitude is expected to scale with the dispersion of the stellar activity signal to model, we conclude that these two RV measurement methods are likely less reliable than the Gaussian fit (which is confirmed when S is left as a free model parameter) and choose the latter to be the reference measurement method in the following.

Table 4.2 – Results of the fit to the RV time-series measured by (i) fitting a Gaussian function to each Stokes I LSD profiles (Case *Ref.*; lines 1 to 4), (ii) computing the median value of the Bisector of each line profile (case *BIS*; lines 5 and 6) and (iii) adjusting the 1st derivative of a Gaussian function to the median subtracted line profiles (case *1st deviv.*; lines 7 and 8). The fit to the RVs measured from the reduced Stokes I LSD profiles prior to ZDI reconstruction (see Section 4.3) is given in lines 9 and 10, while the results of the ZDI reconstruction itself is indicated in line 11. Columns 2 to 8 give the best estimate of each parameter in the model (written in bold when fixed in the MCMC process) with $\pm 1\sigma$ error bars. The last two columns indicate respectively the RMS of the residuals of the fit and the BF in favour of AU Mic b in the different RV time-series.

Case	θ_1	θ_3	K_s	ϕ_p	P_{orb}	M_p	S	RMS	ln BF
	[m s^{-1}]	[d]	[m s^{-1}]		[d]	[$M_\oplus$]	[m s^{-1}]	[m s^{-1}]	
Ref.	47^{+11}_{-8}	4.836 ± 0.009	$8.5^{+2.3}_{-2.2}$	**0.0**	**8.46321**	$17.1^{+4.7}_{-4.5}$	**0.0**	3.0	5.6
Ref. (S free)	43^{+11}_{-8}	4.84 ± 0.01	$9.3^{+3.2}_{-3.0}$	**0.0**	**8.46321**	$18.7^{+6.5}_{-6.1}$	$6.0^{+3.8}_{-3.1}$	4.4	4.5
Ref. (ϕ_p free)	45^{+11}_{-8}	4.836 ± 0.009	$8.2^{+2.4}_{-2.3}$	-0.03 ± 0.04	**8.46321**	$16.5^{+4.9}_{-4.7}$	**0.0**	3.1	6.3
Ref. (P_{orb} free)	46^{+10}_{-8}	4.834 ± 0.009	8.5 ± 2.3	**0.0**	8.5 ± 0.03 d	17.1 ± 4.7	**0.0**	3.7	7.3
BIS (S free)	80^{+20}_{-15}	4.85 ± 0.01	$8.6^{+2.5}_{-2.4}$	**0.0**	**8.46321**	$17.3^{+5.1}_{-4.9}$	**0.0**	3.3	5.7
BIS (S free)	40^{+11}_{-8}	4.85 ± 0.02	5.2 ± 3.2	**0.0**	**8.46321**	10.4 ± 6.4	$15.2^{+4.1}_{-3.4}$	13.3	0.5
1st deriv.	91^{+21}_{-17}	4.85 ± 0.01	$7.8^{+2.6}_{-2.5}$	**0.0**	**8.46321**	$15.7^{+5.3}_{-5.1}$	**0.0**	3.8	4.0
1st deriv. (S free)	41^{+12}_{-8}	$4.85^{+0.03}_{-0.02}$	4.5 ± 3.3	**0.0**	**8.46321**	9.0 ± 6.6	$14.6^{+4.3}_{-3.5}$	10.9	0.1
RVs from $\boldsymbol{I_f}$	45^{+11}_{-8}	4.85 ± 0.01	10.1 ± 2.3	**0.0**	**8.46321**	20.3 ± 4.7	**0.0**	3.0	7.3
RVs from $\boldsymbol{I_f}$ (S free)	38^{+11}_{-7}	4.86 ± 0.02	$10.1^{+3.1}_{-2.9}$	**0.0**	**8.46321**	$20.3^{+6.4}_{-6.3}$	$6.4^{+3.2}_{-2.9}$	5.0	4.8
ZDI fit	–	–	9.7 ± 2.5	**0.0**	**8.46321**	19.1 ± 5.1	–	8.7	–

Case 1: fixing S to zero

In a first instance, we assume that $S = 0\,\mathrm{m\,s^{-1}}$ in the estimation process. We report a 3.9σ detection of a planetary signal of $K_s = 8.5^{+2.3}_{-2.2}\,\mathrm{m\,s^{-1}}$ at the orbital period of P20 from our reference RV time-series (see the fit shown in Figure 4.4). Leaving ϕ_p or P_{orb} as free parameters of the MCMC process yield consistent planet RV signatures, systematically well-phased with the photometric analysis of P20 (see Table 4.2 and Figure 4.5). Consistent planet masses are obtained from the RVs measured with the two methods described in Section 4.2.1 (assuming $S = 0\,\mathrm{m\,s^{-1}}$). Moreover, the values of BF lie close or above the theoretical fair detection threshold ($\ln \mathrm{BF} = 5$; see Jeffreys, 1961). Even though we can in principle conclude that the planet is formally detected from our different RV time-series, the BF values remain far from the definite detection threshold of $\ln \mathrm{BF} \sim 10$ recommended by Nelson et al. (2020), and we thus caution that more RV measurements are needed to increase our BF and claim a definite detection of the planet. Another method to quantify the statistical significance of our planet signature, is to compute the generalized Lomb-Scargle periodogram (Zechmeister & Kürster, 2009) of the activity-subtracted RV time-series. As shown in Figure 4.6, we find a prominent peak above the 0.1% false alarm probability level (FAP), which is further evidence that the planet signature is indeed well present in the data.

A significant excess of uncorrelated noise in our RV time-series?

Leaving the excess of uncorrelated noise as a free parameter of the model results in a surprisingly large value of $S = 6.0^{+3.8}_{-3.1}\,\mathrm{m\,s^{-1}}$ and a planet mass with a slightly degraded precision of 3.1σ for our reference RV time-series. A consistent value of $S = 7.2^{+3.2}_{-2.0}\,\mathrm{m\,s^{-1}}$ is obtained when using the photon noise alone as the formal RV uncertainty instead of a constant value of $\sigma_{RV} = 5\,\mathrm{m\,s^{-1}}$. Note that the total uncorrelated noise ($\sqrt{\sigma_{RV}^2 + S^2}$) is similar in both cases (resp. $7.8\,\mathrm{m\,s^{-1}}$ and $7.6\,\mathrm{m\,s^{-1}}$). We investigated the reliability of these results by running our MCMC process on synthetic data.

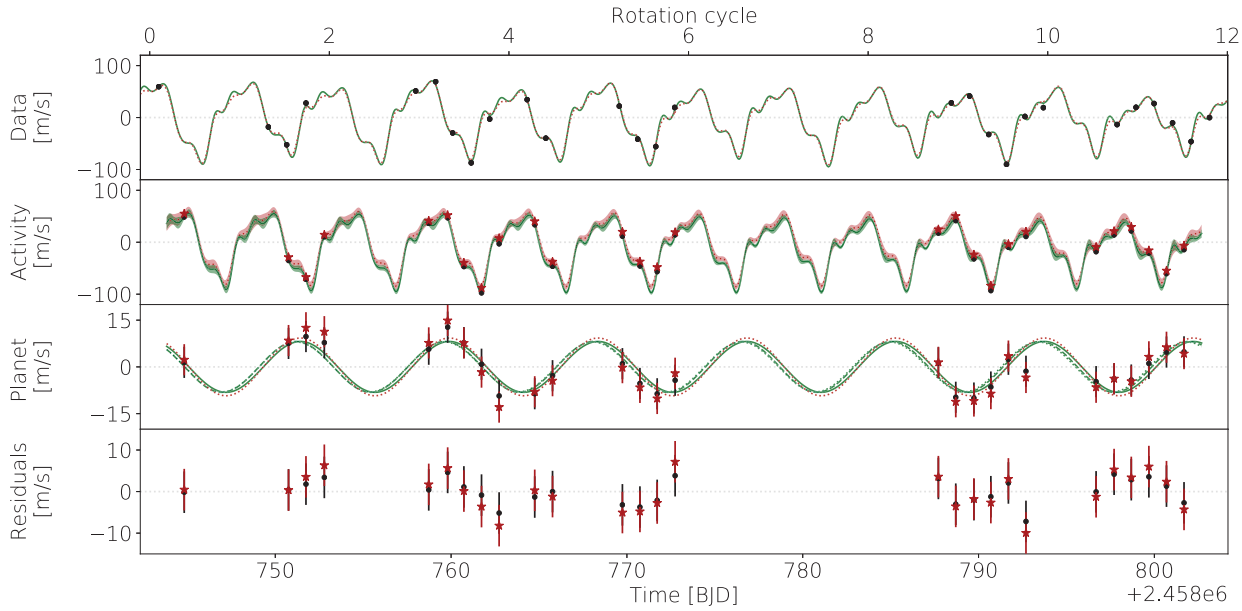

Figure 4.4 – Best fit to our reference RV time-series. *From top to bottom:* raw data, stellar activity signal, AU Mic b RV signature, and residuals after subtracting the planet and stellar activity signals from the raw RVs. In each panel, the green solid and red dotted lines show the best predictions (with $\pm 1\sigma$ error bands for the GP prediction in panel 2) when S is assumed null and fitted by the MCMC process, respectively (i.e., lines 1 and 2 of Table 4.2). In panels 2 and 3, the data points (black dots and red stars for cases with $S = 0\,\mathrm{m\,s^{-1}}$ and S optimized by the MCMC process, respectively) are obtained by subtracting all components except the one shown in the panel from the raw RV time-series. In panel 3, the planet signatures obtained when ϕ_p and P_orb are free parameters of the model are shown in dashed and green lines. The RMSs exhibited by the residuals is 3.0 and $4.4\,\mathrm{m\,s^{-1}}$ when S is assumed null and optimized by the MCMC process, respectively.

We built a synthetic RV curve containing the GP prediction of the stellar activity RV signal and a planet signature of semi-amplitude $8.3\,\mathrm{m\,s^{-1}}$ at $\phi_\mathrm{p} = 0$. We then created two data sets, S_1 and S_2 containing respectively 100 evenly-sampled data points and 27 points taken at the same epochs as our observations. In both time series, we added a photon noise of $2\,\mathrm{m\,s^{-1}}$ RMS and an additional uncorrelated Gaussian noise of $4\,\mathrm{m\,s^{-1}}$ RMS, and assumed formal RV uncertainties of $5\,\mathrm{m\,s^{-1}}$ (similarly to our reference RVs). We then ran our estimation process on 40 of these synthetic data sets with different realizations of the white noise. We thus expect the estimate of S to be consistent with 0 (or at least significantly lower than the injected RMS of the white noise).

The resulting distribution of S is shown in Figure 4.7. Whereas no significant excess of uncorrelated noise is found in case S_1 (i.e., with 100 data points), S is systematically over-estimated in case S_2 (27 data points only), with a mean value of $4.5 \pm 2.0\,\mathrm{m\,s^{-1}}$. This suggests that the value of S found in our real data, consistent with the average value of S recovered on our synthetic RV time-series, is also likely over-estimated. We note that θ_1 and S are anti-correlated in case S_2 (Pearson correlation coefficient of $\rho = -0.20 \pm 0.08$, consistent with the value of -0.3 observed in the modeling of our reference RVs), whereas no such trend is observed in case S_1. This suggests that, due to the low number of points in data sets S_2 (as in our real data), the MCMC process is not able to fully disentangle the uncorrelated noise from the stellar activity RV signal, resulting in transferring part of the GP amplitude into S.

The two alternative methods to measure the RVs of the Stokes I LSD profiles (i.e., median bisector and fit to the median-subtracted line profiles; see Section 2.2.3) yield significantly larger estimates of S than our reference RVs (see Table 4.2), suggesting that they are noisier. Moreover,

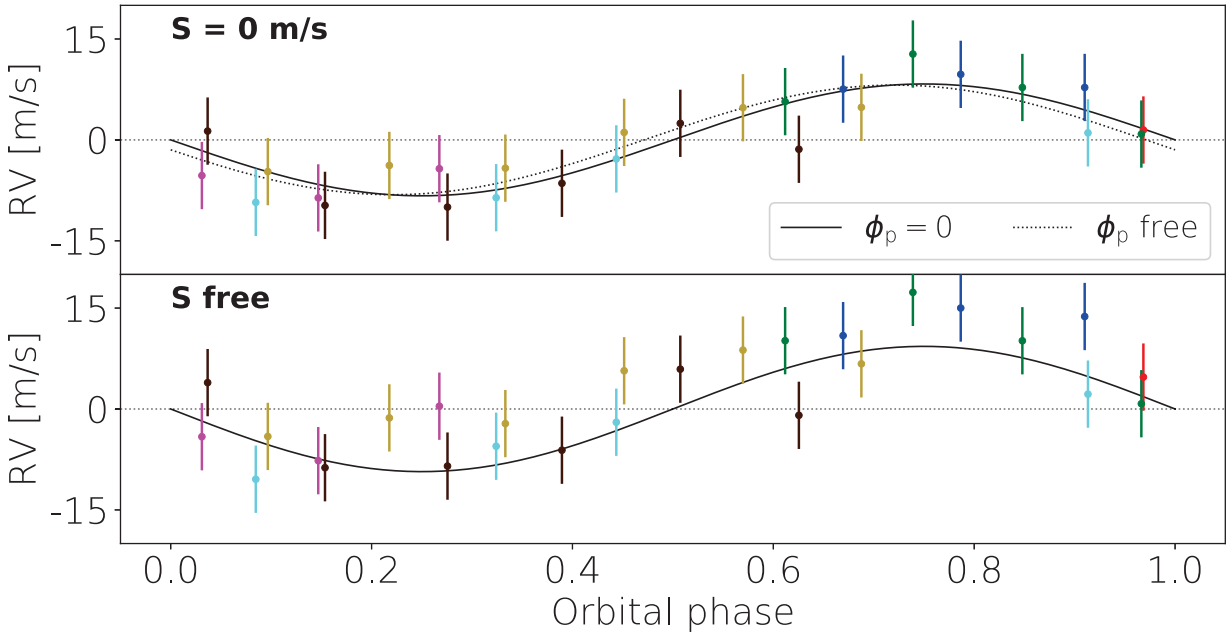

Figure 4.5 – Activity-subtracted RV time-series (in the reference case) folded to $P_{\rm orb}$ using T_0 as reference time in the case when S is assumed null (top panel) and fitted by the MCMC process (bottom panel). In the top panel, the solid and dash lines show the predicted planet RV signature when $\phi_{\rm p} = 0$ and when $\phi_{\rm p}$ is fitted by the MCMC process. Data points of same color belong to the same orbital phase.

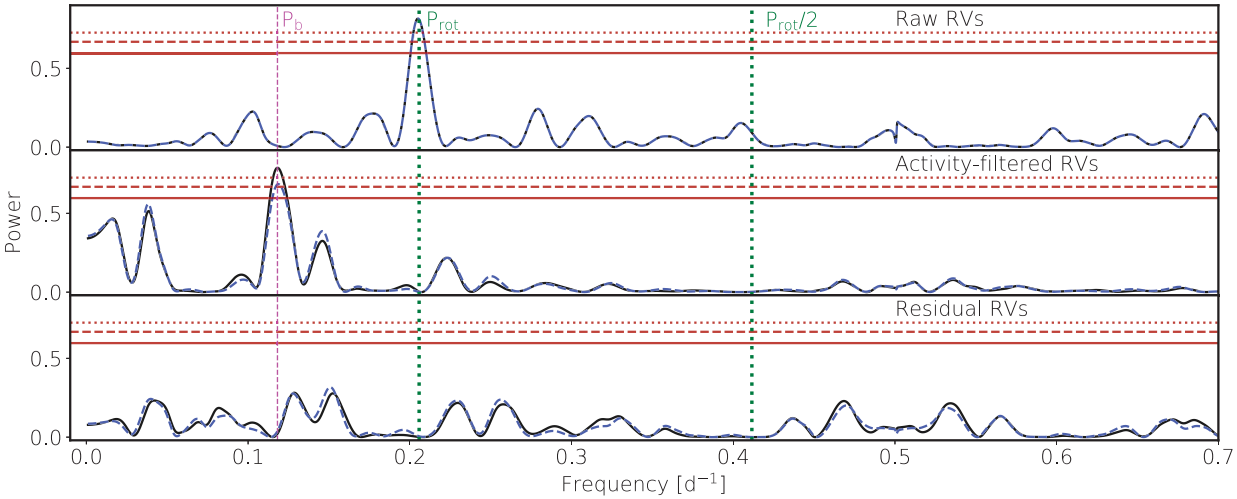

Figure 4.6 – GLS periodograms of (i) our reference RV time-series (top panel), (ii) the RV time-series obtained by subtracting the GP prediction of the stellar activity to the raw RVs (middle panel) and (iii) the residual RVs (bottom panel). In each panel, the solid black and blue dashed lines correspond respectively to cases where $S = 0\,{\rm m\,s^{-1}}$ and where S is fitted by the MCMC process. The horizontal lines indicate FAP levels of 10, 1 and 0.1% computed using the method of Zechmeister & Kürster (2009) with the PyAstronomy python package (Czesla et al., 2019). The green and magenta vertical lines indicate the frequencies corresponding respectively to the rotation period of the star (and its first harmonic) and the orbital period of AU Mic b.

when $S = 0\,{\rm m\,s^{-1}}$, the GP amplitude reaches unrealistically high values $\gtrsim 80\,{\rm m\,s^{-1}}$, typically of the order of the peak-to-peak amplitude of the observed RVs, while one would have expected θ_1 to

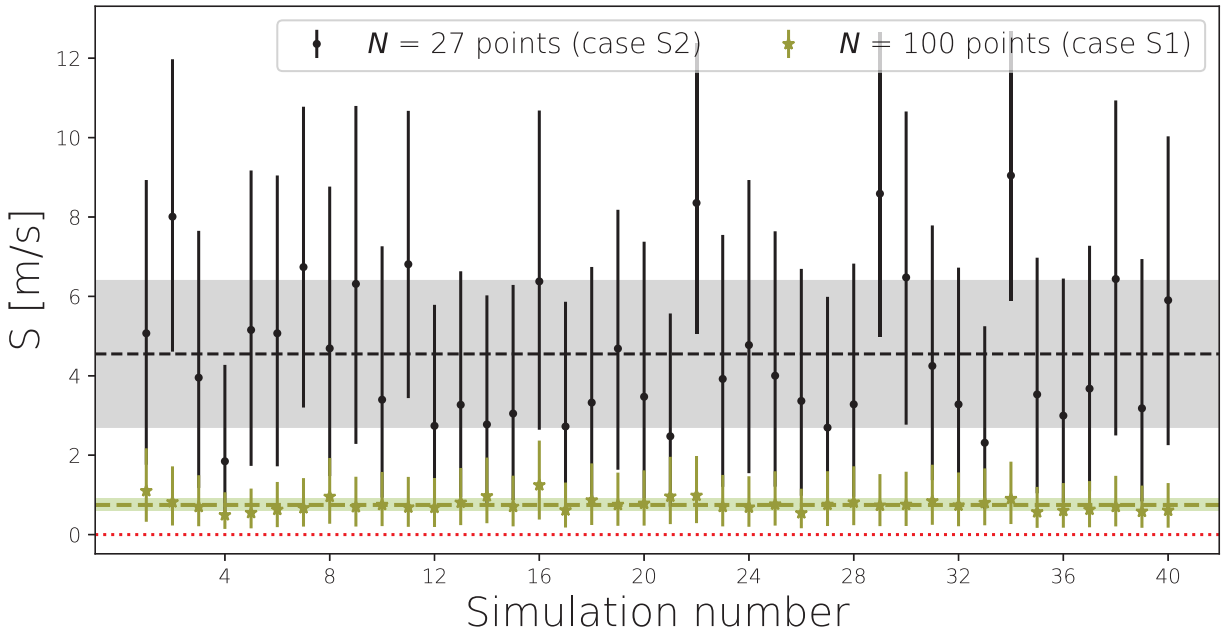

Figure 4.7 – Best estimates of S obtained by modeling 40 synthetic RV time-series of case S_1 (black points) and S_2 (green stars). The true value of S, indicated by the horizontal red dashed line, is $0\,\mathrm{m\,s^{-1}}$ as the formal RV uncertainties on the synthetic RVs are larger than the RMS of the injected noise. The mean values and standard deviation of the S estimates are indicated by the horizontal dashed lines and bands.

be more or less equal to the RMS of the RV time-series (i.e., $45\,\mathrm{m\,s^{-1}}$) as observed in the GPR modeling of the reference RVs (i.e., Gaussian fit to the line profiles). We conclude that for the specific case of AU Mic, these two alternative methods provide noisier RVs, which are expected to yield less reliable estimates of the planet mass.

4.2.4 Filtering stellar activity RV signal with ancillary indicators

SPIRou's observations of AU Mic offer the opportunity to study how the various activity proxies computed in Section 3.3.1 are linked to the stellar activity RV signals. The GLS periodogram of each of them is shown in Figure 4.8. Except for Brγ, all activity indicators are modulated at periods close to $P_{\rm rot}$ or its first harmonic. As already noted in Section 3.3.1, the FWHM of the Stokes I LSD profiles is all the more rotationally-modulated as the magnetic sensitivity of the line increases. In particular, the fact that the FWHM of the line profiles computed with the empirical line mask is weakly-modulated suggests that the stellar activity RV signal is at least partly of magnetic origin.

Table 4.3 – Best rotation periods (line 1) obtained by modeling each time series of stellar activity indicator by a GP and Pearson correlation coefficient (ρ; line 2) of each indicator with the RV time-series.

Indicator	RV	B_ℓ	$V_{\rm s}$	FWHM			He I	Pa β	Brγ
				Empirical	Atomic	$g>1.5$			
$P_{\rm rot}$ [d]	4.84 ± 0.01	4.83 ± 0.02	$4.89^{+0.04}_{-0.02}$	4.9 ± 0.4	4.9 ± 0.1	4.84 ± 0.04	$4.87^{+0.06}_{-0.05}$	$4.99^{+0.11}_{-0.09}$	4.8 ± 0.5
ρ	–	-0.214	-0.695	-0.367	0.241	0.691	-0.503	-0.281	-0.381

We use GPR with the quasi-periodic kernel of Eq. 2.5 to independently model the time series of B_ℓ, $V_{\rm s}$, FWHM (for the different line profiles considered), as well as He I and Paβ. The resulting

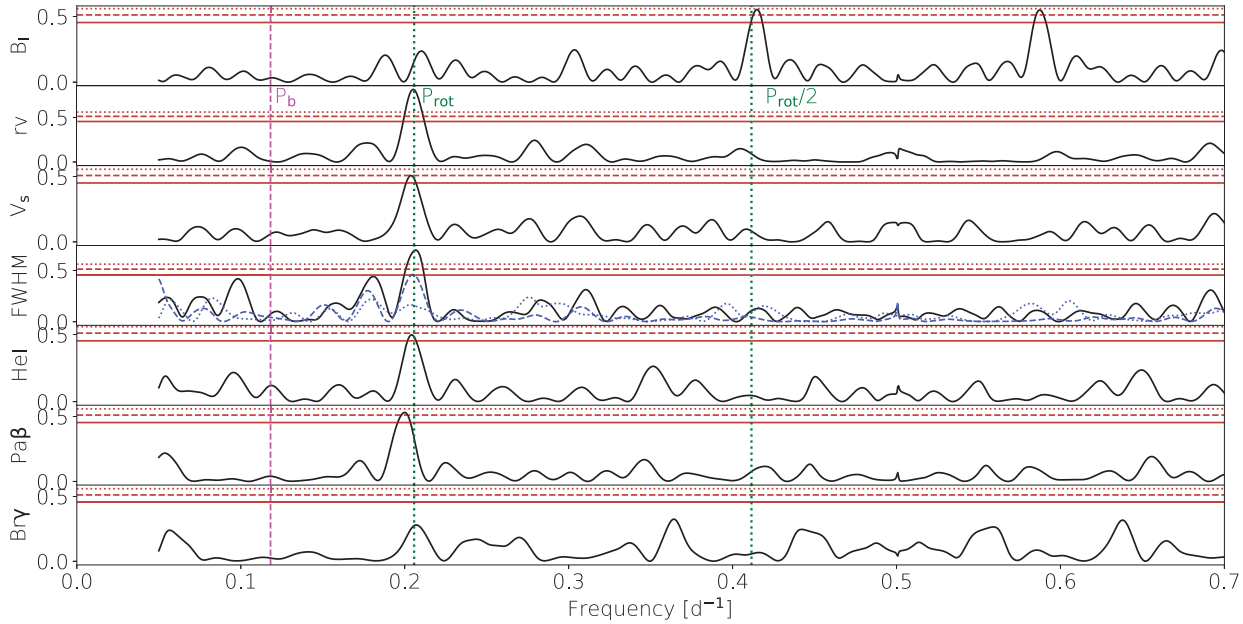

Figure 4.8 – *From top to bottom:* GLS periodograms of the time series of B_ℓ, RV, V_s, FWHM, He I, Paβ and Brγ. In panel 4, the GLS periodograms of FWHMs of the Stokes I LSD profiles computed with the atomic and empirical line masks are shown in blue dotted and dashed lines, respectively, while the black solid line corresponds to the FWHM of line profile computed from lines of Landé factors larger than 1.5. The symbols are the same as in Figure 4.6, except that we indicate FAPs of 0.3, 0.1 and 0.03.

GP periods are listed in Table 4.3. We find that B_ℓ is modulated at a period of 4.83 ± 0.02 d, consistent with the value of $P_{\rm rot}$ obtained from the RV analysis, confirming that B_ℓ is a reliable proxy of stellar rotation periods (Donati et al., 2006c; Hébrard et al., 2016). The same goes from V_s, He I, and the FWHM of the Stokes I LSD profile computed from lines with Landé factors larger than 1.5. As already discussed in Section 3.3.1, the chromospheric material might be differently probed in He I and Paβ, explaining that these twoo indicators are modulated at slightly different periods.

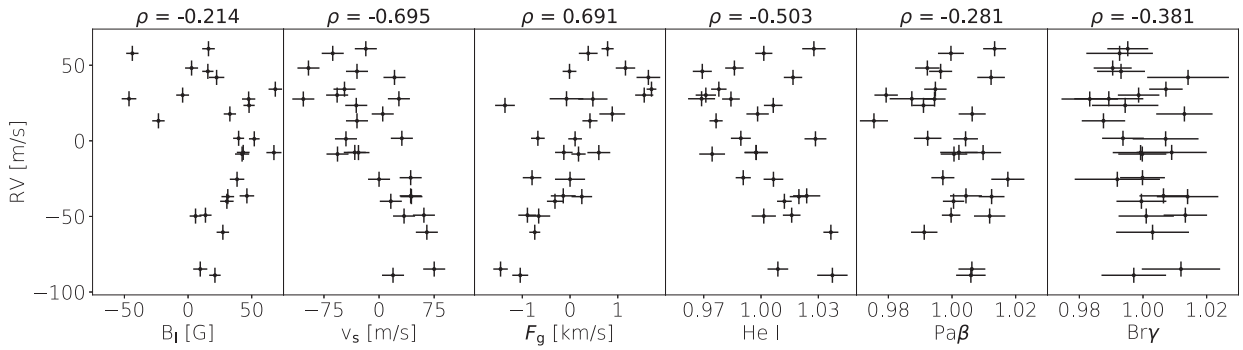

Figure 4.9 – Correlaton plots of each time series activity indicators with the planet-subtracted RV time-series. The Pearson correlation coefficient ρ are indicated atop each panel.

In order to compare the ability of each indicator to model stellar activity RV signals, we computed the Pearson correlation coefficient between each time series of indicators and the planet-subtracted RVs (see Figure 4.9). We find that V_s and FWHM correlate best with our reference RV time-series, with respective Pearson correlation coefficients of -0.7 and 0.7. The good correlation

between the small-scale magnetic field and the stellar activity RV signal was also observed for the Sun in Haywood et al. (2020). However, the origin of this correlation is likely different for AU Mic. In the case of the Sun, the inhibition of the convective blueshift due to active regions crossing the visible hemisphere of the star, which dominates the RV budget (e.g., Haywood et al., 2016; Collier Cameron et al., 2019; Haywood et al., 2020), is directly linked to the small scale magnetic field. As mentioned in Section 1.4, such phenomenon is expected to induce no more than a marginal contribution to the global stellar activity RV signal. It is thus likely that the observed stellar RV signal is mainly due to the Zeeman effect, which explains why the small-scale field correlates best with our observed RVs (see Klein et al., 2020). We also note that He I emission is found to be relatively well-correlated with our observed RVs. We independently fit the reference RV time-series with a linear model of V_s, F_g and He I, jointly coupled with a linear model of the planet RV signature given by Eq. 4.2. Modeling the stellar activity RV signal with the time series V_s, F_g and He I allows to reduce the RMS of RV variations by 32, 27 and 12%, respectively. However, the recovered planet signature is plagued by large errors and its detection remains inconclusive.

4.3 Unveiling planet signature using ZDI

4.3.1 3D paraboloid fit

In this section, we propose an independent method adapted from Petit et al. (2015) to simultaneously unveil the planet signature while inverting the Stokes I LSD profiles with ZDI (see the method described in Appendix A.1). The planet orbital period and phase are well-constrained from photometry, leaving K_s as the only unknown planet parameter. We simultaneously model the stellar DR (assumed solar-like) as described in Section A.1, adding thus two parameters, Ω_{eq} and $d\Omega$, to recover.

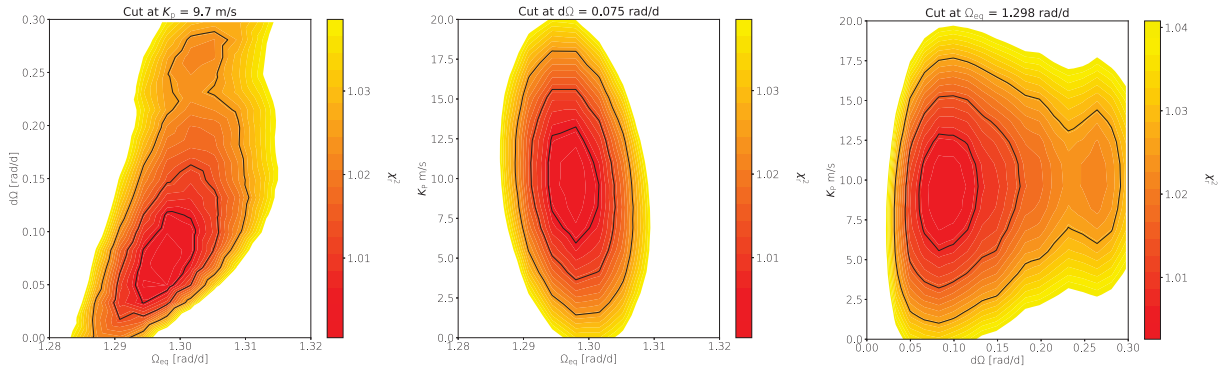

Figure 4.10 – 2D cuts of the 3D χ^2_r map obtained by simultaneously recovering the barycentric motion induced by AU Mic b while inverting the Stokes I LSD profiles with ZDI. From left to right: variations of χ^2_r in the (Ω_{eq},dΩ) space at K_s,$= 9.7\,m\,s^{-1}$, in the (K_s,dΩ) space at $\Omega_{eq} = 1.289$ rad/d and, in the (Ω_{eq},K_s) space at $d\Omega = 0.075$ rad/d. In each panel, the 1; 2 and 3σ levels of the χ^2_r distributions are indicated by the black solid lines.

We take the Stokes I LSD profiles $\boldsymbol{I_f}$ corrected for systematics in Section 3.3.1 as an input for the brightness reconstruction. To double-check that our procedure to correct for systematics (see Section 3.2.2) has no more than a marginal impact on RV estimates, we fitted a Gaussian function to each line profile of $\boldsymbol{I_f}$ and found that the resulting RVs differ by no more than $4.5\,m\,s^{-1}$ RMS from our reference RVs. Moreover, modeling this RV time-series using the process described in Section 4.2.2 yields similar planet and stellar activity parameters to those obtained from the RV modeling (see Table 4.2). For each value of the parameters in the grid (K_s,Ω_{eq},dΩ), the reduced

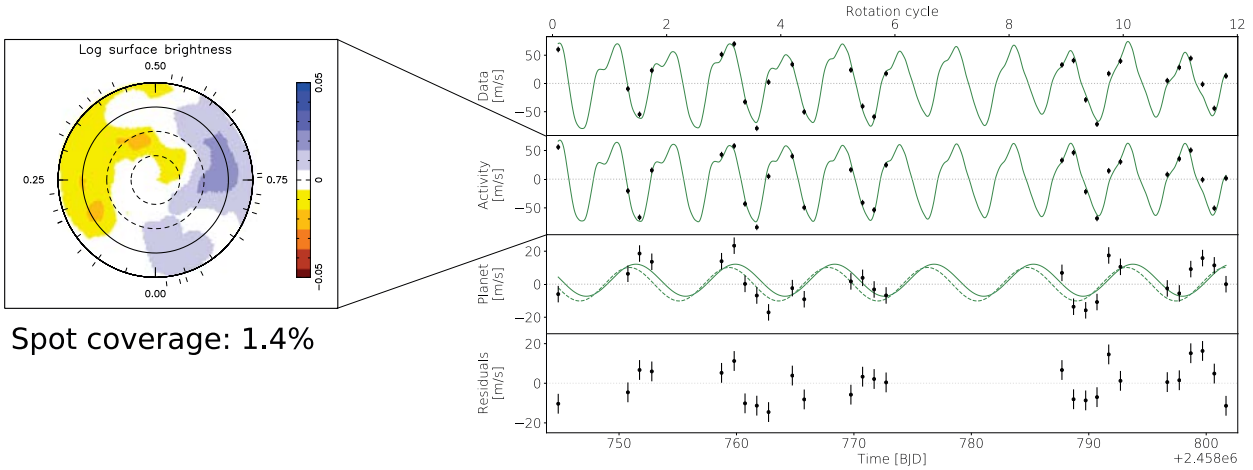

Figure 4.11 – *Left panel:* Flattened polar view of the surface brightness of AU Mic (same as Figure 3.9). *Right panel:* Same as Figure 4.4, but using the maximum entropy brightness distribution shown in the left panel to generate the stellar activity RV curve. In panel 3, the green solid and dashed lines show the prediction of the planet RV signature respectively when $\phi_{\rm p}$is assumed null and optimized by the model. The dispersion of the residuals is $9\,{\rm m\,s^{-1}}$ RMS.

Stokes I LSD profiles are corrected from the barycentric motion of the planet (given in Eq. 4.2), and inverted into a map of the surface brightness at the surface of the star for a given amount of spot coverage (1.4% here, see Section 3.3.1). The best parameters and 1σ error bars are obtained by fitting a 3D paraboloid around the minimum of the resulting map of $\chi^2_{\rm r}$ using the method described in Appendix A.1.

We find that $\Omega_{\rm eq} = 1.298 \pm 0.003\,{\rm rad/d}$, ${\rm d}\Omega = 0.075 \pm 0.031\,{\rm rad/d}$ and $K_{\rm s} = 9.7 \pm 2.5\,{\rm m\,s^{-1}}$ minimizes the $\chi^2_{\rm r}$ of the ZDI reconstruction (see the 2D cuts of the $\chi^2_{\rm r}$ map in Figure 4.10). The DR parameters are compared to those obtained from the Stokes V LSD profiles in Section 3.3.1. The semi-amplitude of AU Mic b's RV signature is remarkably consistent with the value recovered from the GP modeling of our reference RV time-series (see Table 4.2). We also note that the DR parameters do not appear correlated with $K_{\rm s}$ (see the two right panels of Figure 4.10), which reinforces the robustness of the planet detection.

4.3.2 Using ZDI brightness map to filter stellar activity RV signals

To ensure that the planet signature recovered from the 3D $\chi^2_{\rm r}$ map is reliable, we use the maximum entropy brightness map obtained in the process (see the left panel of Figure 4.11) to generate synthetic Stokes I profiles at the same epochs as our observations and measure their RVs through Gaussian fits. We subtract the resulting RVs from our reference RV time-series, and linearly model the residuals with a sine wave representing (see Eq. 4.2). The best fit to the RV time-series, shown in Figure 4.11, yields residuals whose dispersion is as high as $9\,{\rm m\,s^{-1}}$, $\sim 3\times$ larger than that obtained when modeling the stellar activity RV signal with GPs. This is due to the fact that GPs are intrinsically more flexible than ZDI, and thereby able to model the evolution of the stellar activity RV curve, whereas ZDI, in its current version, only models DR-induced variations. To account for the excess of dispersion in the RV residuals, the $K_{\rm s}$ uncertainties are empirically rescaled by $\sqrt{\chi^2_{\rm r}} = 1.8$, leading to $K_{\rm s} = 9.5 \pm 2.5\,{\rm m\,s^{-1}}$, consistent with the value obtained from the 3D $\chi^2_{\rm r}$ map.

4.4 Implications and perspectives

Mass-Radius diagram

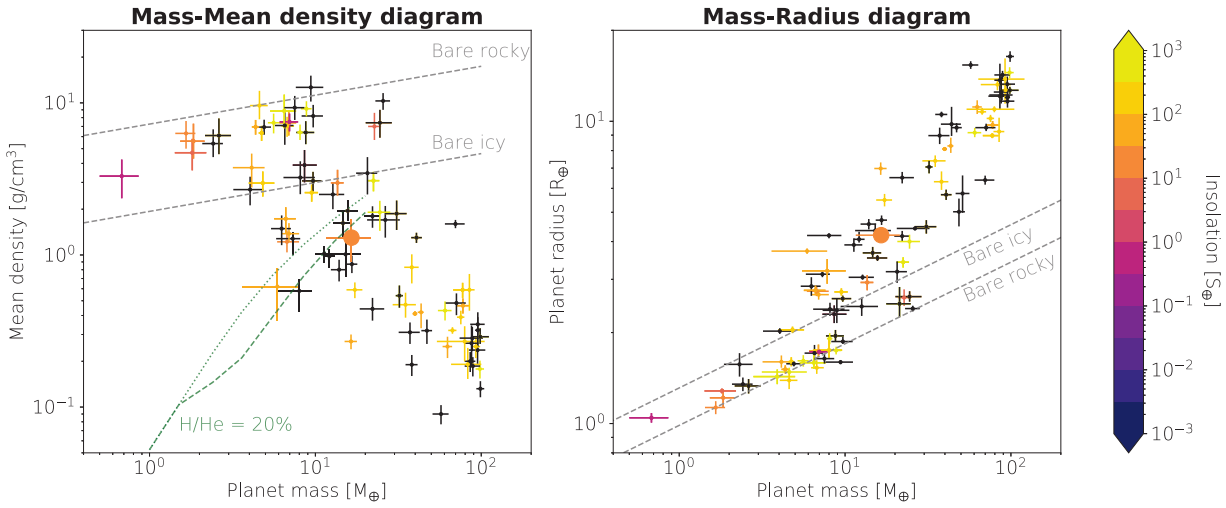

Figure 4.12 – Mass-mean density (left panel) and Mass-radius (right panel) diagrams of confirmed exoplanets of mass lower than 100 $M_\oplus$ and with relative uncertainties on the mass and the mean density (resp. the radius for the right-hand panel) lower than 33%. The data of the plot are extracted from the NASA Explanet Archive (https://exoplanetarchive.ipac.caltech.edu/index.html). The color scale depicts the insolation of the planet relative to the Earth (the planets are shown in black when their insolation is not known). AU Mic b is indicated by the large filled circle on both diagrams. We also indicate the theoretical limits of pure ice and rocky planet cores computed using Jin & Mordasini (2018)'s relations by the gray dashed lines in both plots (analytical expressions from equations 4 to 7). In the left-hand panel, the green dashed and dotted lines indicate the density of a 100 Myr old planet at AU Mic b's insolation hosting a 20% H/He envelope predicted by Lopez & Fortney (2014)'s theoretical models assuming respectively solar and 50× planet metallicities.

From the semi-amplitude of the RV signature induced by AU Mic b recovered from our reference RVs (see line 1 of Table 4.2), we derive a planet mass of $17.1^{4.7}_{-4.5}\,M_\oplus$. This implies a planet mean density of $1.1 \pm 0.3\,\mathrm{g\,cm^{-3}}$, consistent at 2σ with that of Neptune ($1.64\,\mathrm{g\,cm^{-3}}$)[2]. Since AU Mic b is the first close-in planet younger than 25 Myr to have its bulk density measured with a relative precision better than 30%, direct comparisons with the population of evolved planets is difficult. When compared to the predictions of the global planet formation and evolution models of Mordasini et al. (2012c), AU Mic b is found significantly denser that most of the planets of similar age and radius, which suggests that the planet features a high fraction of heavy elements ($\gtrsim$80% of elements heavier than He) or has already partly lost its H/He envelope under the impact of stellar X/UV fluxes. AU Mic b is placed in the mass-mean density and mass-radius diagrams of low-mass planets in Figure 4.12. On the one hand, the planet is expected to host a H/He envelope contributing to about 20% to the mass budget (Lopez & Fortney, 2014; Jin & Mordasini, 2018). On the other hand, the planet lies fairly close to the theoretical limit of the evaporation valley (Owen & Wu, 2013; Mordasini, 2020). Jin & Mordasini (2018) predicted that planets of masses, radii and insolations similar to AU Mic b are likely to be in the process of loosing their H/He envelope on time scales on a few tens of Myr. Moreover, AU Mic b features an equilibrium temperature $T_{\rm eq} \sim 600$ K, close to that the well-known evaporating planet of similar inner density Gj 436 b ($T_{\rm eq} = 650$ K; e.g., Salz

[2] Note that consistent uncertainties are obtained using the independent method of Southworth et al. (2007) to compute the planet inner density.

et al., 2015). The planet might therefore be a promising candidate for the detection of extended H/He exospheres.

Stellar accretion disk

Given its high density, AU Mic b likely formed at large distance of the star (typically a few au) and migrated inward to its present location as a consequence of interactions with the protoplanetary disk (see Section 1.1.3 and Baruteau et al., 2016). In particular, one may wonder whether the planet had enough time to reach the magnetospheric cavity induced by the host star's magnetic field. If this is the case, the distance between the star and the planet pinpoints the location of the inner accretion disk, i.e., corresponding to the corotation radius of the star at the time of the disk dissipation (Lin et al., 1996). Assuming that the angular momentum was conserved throughout the contraction of the star since the disk dissipation, we find that AU Mic should have had a radius of $\sim 1\,R_\odot$, at $P_{\rm rot} = P_{\rm orb} = 8.46$ d, implying that the disk dissipation occurred at an age of about $\sim$8 Myr (using the evolutionary tracks of Baraffe et al., 2015). This value is larger than the typical lifetime of the accretion disk surrounding cTTSs (of about 3-5 Myr; Richert et al., 2018) but remains plausible since disks have been observed around stars as old as 8-10 Myr (e.g., TW Hydrae; Rhee et al., 2007). This requires, on the other hand, that AU Mic hosts a dipolar magnetic field strong enough to disrupt the central regions of the accretion disk up to distances as large as 0.066 au. Using Bessolaz et al. (2008)'s relations and assuming that the young AU Mic accretes the disk material at a low rate of $10^{-10}\,M_\odot\,{\rm yr}^{-1}$ (compared to the typical rate of $\sim 10^{-8}\,M_\odot$/yr for cTTSs; Hartmann et al., 2016), we find that the star should have hosted a dipolar field stronger than 1.8 kG, significantly larger than the one it now hosts. This suggests that AU Mic b did likely not have enough time to reach to inner edge of the disk and may have been trapped by interactions with other planets of the system.

Perspectives for AU Mic b

AU Mic is now part of the SLS targets (in all 3 work packages) and was observed in 2020b, with about 100 spectropolarimetric visits collected. These observations will be useful to fine-tune the mass measurement of AU Mic b, following the study presented in this chapter. As shown in Section 2.3.2 for a similar system, these observations should allow to more precisely constrain the ellipticity of the planet orbit, which might help retracing the planet formation history and interactions with other planets in the system and the debris disk (e.g. Chatterjee et al., 2008; Plavchan et al., 2020b). Moreover, additional observations of AU Mic will allow to constrain the mass of the outer planet AU Mic c, identified in Plavchan et al. (2020b) and confirmed in Martioli et al. (2020b), whose past orbital evolution might help to explain the fast moving features identified in AU Mic's Debris disk (Boccaletti et al., 2015; Sezestre et al., 2017; Plavchan et al., 2020b).

AU Mic has been observed again by the TESS satellite (sector 27) from 2020 July 4 to 30. For this occasion, the P20 obtained simultaneous high-precision velocimetric measurements from visible and nIR spectrographs. Combining these observations with SPIRou is a great opportunity to achieve the goal mentioned in the above paragraph. We also noted that a few SPIRou observations were collected during giant flares of the star, which provides us with an additional opportunity to carry out a spectroscopic study of the frequent flares of the star as well as quantifying their impact on the measured RVs. Given the brightness of its host star, AU Mic b already appears as a primary candidate for the observation of its atmosphere with future space-based missions (e.g., JWST, ARIEL), and ground-based high-resolution spectrometers (the June 2019 transit of AU Mic b has been observed by EXPRESSO, see Palle et al., 2020, and SPIRou; see Chapter 5).

5 | Probing the atmosphere of transiting planets around low-mass stars with SPIRou

Contents

Planet atmospheres are the best laboratories to study the formation and evolution of exoplanetary systems as well as their surface conditions and interactions with the interplanetary medium. Over the past two decades, transmission and emission spectroscopy has emerged as a cornerstone of the characterization of exoplanet atmospheres (see the review of Madhusudhan, 2019). Future missions of planet atmosphere characterizations such as the JWST, ARIEL and the ELTs are expected to provide decisive information about the processes underlying the atmospheres of various types of exoplanets and probe the presence of biosignatures in the atmospheres of Earth-like planets (e.g., Snellen et al., 2015; Morley et al., 2017). Over the past few years, high-resolution infrared spectroscopy has emerged as a reliable method to characterize planetary atmospheres in

preparation for these missions (e.g., Snellen et al., 2010; Brogi et al., 2012; de Kok et al., 2013; Brogi et al., 2017). In particular, new-generation nIR high-resolution spectrometers like SPIRou seem particularly suited to revolutionize our knowledge of the atmosphere of exoplanets around low-mass stars. In this chapter, I present a preliminary analysis of how to use SPIRou to probe the atmosphere of transiting planets. After a brief introduction about the various mechanisms underlying planet atmospheres and the techniques to constrain them in Section 5.1, I present a method to carry out transmission spectroscopy of the hot Jupiter HD 189733 b with SPIRou in Section 5.2. The implications and prospects of the preliminary results presented in Section 5.2 are mentioned in Section 5.3. Note that the work presented in this chapter is in progress, and that the methods and results described here will be improved/simplified in the next few months.

5.1 Characterizing planet atmospheres

In this Section, I briefly review the various processes at work in planetary atmospheres and how they can be probed with current instruments. After briefly describing exoplanetary atmospheres in Section 5.1.1, I present the different techniques used to constrain the atmosphere of transiting planets in Section 5.1.2 before focusing on high-resolution spectroscopy in Section 5.1.3.

5.1.1 Structure and dynamics of exoplanetary atmospheres

At the interface between the interplanetary medium and the opaque planetary interior, planetary atmospheres are the stage where a number of important physio-chemical processes take place. These processes are the result of complex interactions between their constituent species and external sources of energy such as stellar irradiation or planet internal heating. Starting from the base of the atmosphere, i.e., at the rocky/liquid surface of terrestrial planets or at the point where radiative transfer is no longer dominated by radiation (but by conduction/convection) for gaseous giants, one can identify several atmospheric layers where different processes operate (see the illustration in Figure 5.1). In deep high-pressure layers (typically larger than 1 bar), the temperature of the atmosphere is large enough for chemical reactions to happen much faster than any other dynamical process. Between 1 and 10^{-3} bar, the system is no longer in thermochemical equilibrium and various dynamical processes start gaining importance with respect to chemical reactions. Most of the meteorological phenomena (e.g., formation of clouds or hazes, convection/advection processes, thermal inversion) occur in this layer, analogous to the Earth stratosphere. Higher-up in the atmosphere (up to pressures of $\sim 10^{-6}$ bar), stellar irradiation is strong enough to photo-dissociate molecular species into their atomic components. Above, in the exosphere, the mean free path of the particles exceeds the height scale of the atmosphere and can escape from the gravitational field of the planet (e.g., due to their interaction with incoming stellar particles). The presence of a planet magnetosphere interacting with the stellar wind and deviating most of incoming high-energy particles is thought to inhibit the atmospheric escape. Note however that the exact role of the magnetosphere in preventing atmospheric escape remains unclear as the Earth, Venus and Mars exhibit similar mass loss rates despite different sizes of magnetospheres.

Vertical structure

The conditions of pressure and temperature as a function of the altitude z in the atmosphere (a.k.a. the pressure-temperature or P-T profile) control the processes at work in regions out of chemical equilibrium (i.e., most of the regions we can observe from the Earth). In the simple assumption of an isothermal atmosphere at temperature T containing an ideal gas of mean density ρ and mean

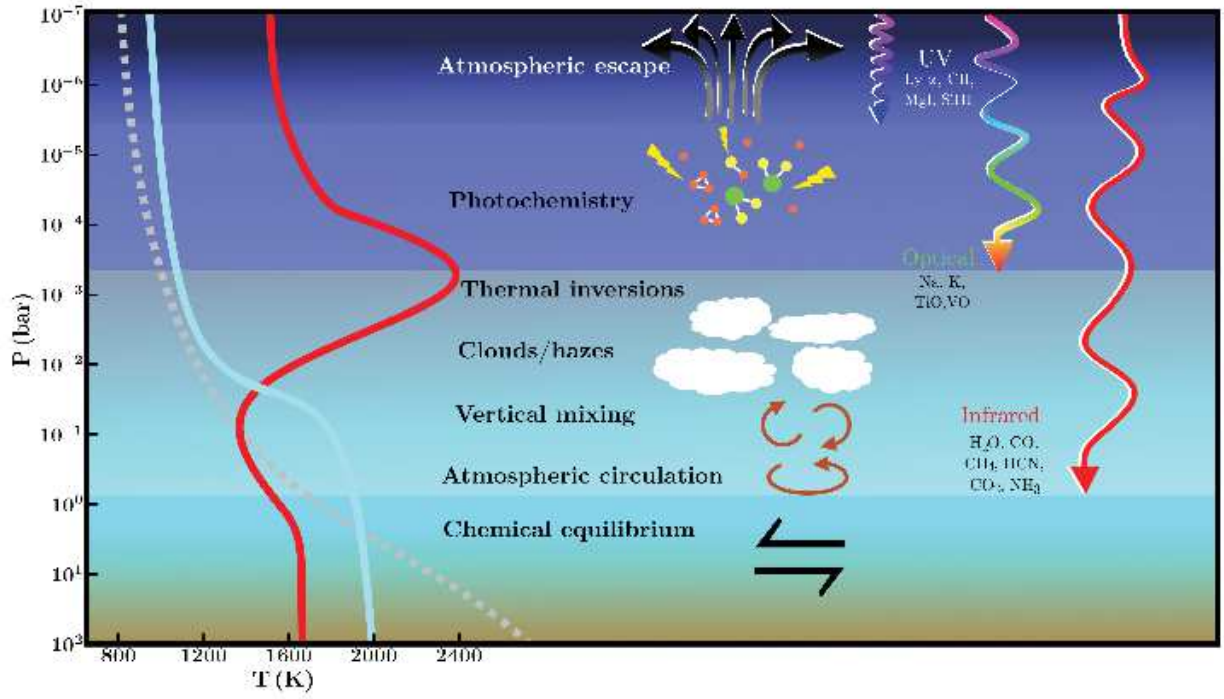

Figure 5.1 – Illustration of the main layers of planetary atmospheres with some of their underlying processes. The vertical arrows indicate how these layers are probed by different spectral domains. Typical pressure-temperature profiles corresponding to irradiated planets with and without thermal inversion, are respectively shown by the red and blue solid lines on the left side of the plot. The gray dotted line indicates the typical P-T profile of a weakly-irradiated close-in planet. Source of the figure: Madhusudhan (2019).

molecular mass μ[1], the planet atmosphere lies in the hydrostatic equilibrium and the pressure P in the atmosphere is simply given by

$$P(z) = P_0 e^{-\frac{z}{H}}, \tag{5.1}$$

where P_0 is the pressure at the surface of the planet and where

$$H = \frac{k_{\rm B} T}{\mu g} \tag{5.2}$$

is the so-called pressure height scale of the atmosphere (i.e., the vertical distance on which the pressure has evolved by e), g and $k_{\rm B}$ being respectively the surface gravity of the planet and the Boltzmann constant. H describes the typical extension of the planet atmosphere and will be larger for hotter low-density planet atmospheres (e.g., highly-irradiated planets like hot Jupiters), but also for small low-mass planets, which may have interesting prospects for the characterization of Earth-sized planets.

In practice, external sources of energy such as stellar irradiation or planet internal heating induce temperatures gradients that are compensated by radiation. However, in cases when the radiative temperature gradient is too strong (generally in the bottom layers of planet atmospheres), radiative energy transport is less efficient and convection start operating. In particular, the disequilibrium

[1] μ is defined by $\mu = \frac{1}{N_{\rm tot}} \sum_i n_i M_i$, where $N_{\rm tot}$, $n_{\rm i}$ and M_i are respectively the total number of molecules, the relative abundance and mass of component i.

processes induced by stellar irradiation (e.g., photochemical dissociation and modification of the kinetics of chemical reactions) modify the vertical distribution of opacity in planet atmospheres and thus affect their P-T profiles, resulting sometimes in thermal inversions for highly-irradiated planets (as illustrated in Figure 5.1; see Spiegel et al., 2009; Moses et al., 2011; Drummond et al., 2016).

Composition of the atmosphere

The chemical composition of an exoplanet atmosphere reflects that of the protoplanetary disk within which the planet was born. The relative abundances of the species in the planet atmosphere and more specifically the C/O ratio, can bring insights on the formation and migration of the planet (e.g., Öberg et al., 2011; Madhusudhan et al., 2014b, 2017). However, the vertical distribution of the relative abundances of the species is expected to be significantly affected by various dynamical processes (e.g., photodissociation, variations in the P-T profile; see Drummond et al., 2019), as evidenced by the large difference in the chemical composition of the solar system planets (reflecting the material accreted during their formation). Moreover, the P-T conditions can locally allow chemical species to condensate into clouds or hazes in the planet atmosphere, dramatically modifying its opacity. These clouds/hazes diffuse the incoming light through Rayleigh or Mie scattering (depending on the relative size of the aerosols relative to the wavelength of observation) that scramble most of the signatures induced by individual species and result in flat/slanted spectra difficult to interpret (Brown, 2001). Clouds/hazes have been detected on a wide range of exoplanets, from hot Jupiters (e.g., Sing et al., 2011; McCullough et al., 2014; Wakeford et al., 2017b) to warm Neptunes and super Earth (Kreidberg et al., 2014; Wakeford et al., 2017a; Benneke et al., 2019; Kreidberg et al., 2020), suggesting that they may be common in exoplanet atmospheres (as in the solar system planets).

Dynamics of planetary atmospheres

Atmospheric circulation plays an important role in redistributing the energy in the stratospheric layers of exoplanet atmospheres. In particular, as illustrated in Figure 5.2, tidally-locked exoplanets feature a significant temperature gradient between their hot day-side (facing the star) and their cold night-side (away from the star), inducing strong atmospheric winds and especially an eastward super-rotation and a shift in phase of the hottest region in the atmosphere (e.g., Showman & Guillot, 2002; Knutson et al., 2007; Zellem et al., 2014; Louden & Wheatley, 2015) with respect to the phase at which the planet day-side is best seen from the Earth. However, fully understanding the physical mechanisms controlling the dynamics of the winds and their effects on the transport of chemical species requires 3D self-consistent hydrodynamical simulations, called global climate models (GCM), highly demanding in term of computational cost, that have only recently been implemented for exoplanets (e.g., Leconte et al., 2013; Showman et al., 2015; Drummond et al., 2020; Sergeev et al., 2020).

Atmospheric escape

In the upper atmospheric regions of close-in exoplanets harbouring an envelope of molecular hydrogen and helium, the stellar UV fluxes are strong enough to dissociate the molecular hydrogen into volatile atomic hydrogen (Yelle, 2004). Under the effect of the stellar radiation pressure (e.g., Bourrier & Lecavelier des Etangs, 2013; Ehrenreich et al., 2015), and interactions between neutral hydrogen and stellar wind protons (Tremblin & Chiang, 2013), the atmospheric gas can acquire a velocity larger than the planet escape velocity and get away from the planet gravitational field. While atmospheric escape is not expected to have a major impact on hot Jupiters, it may affect

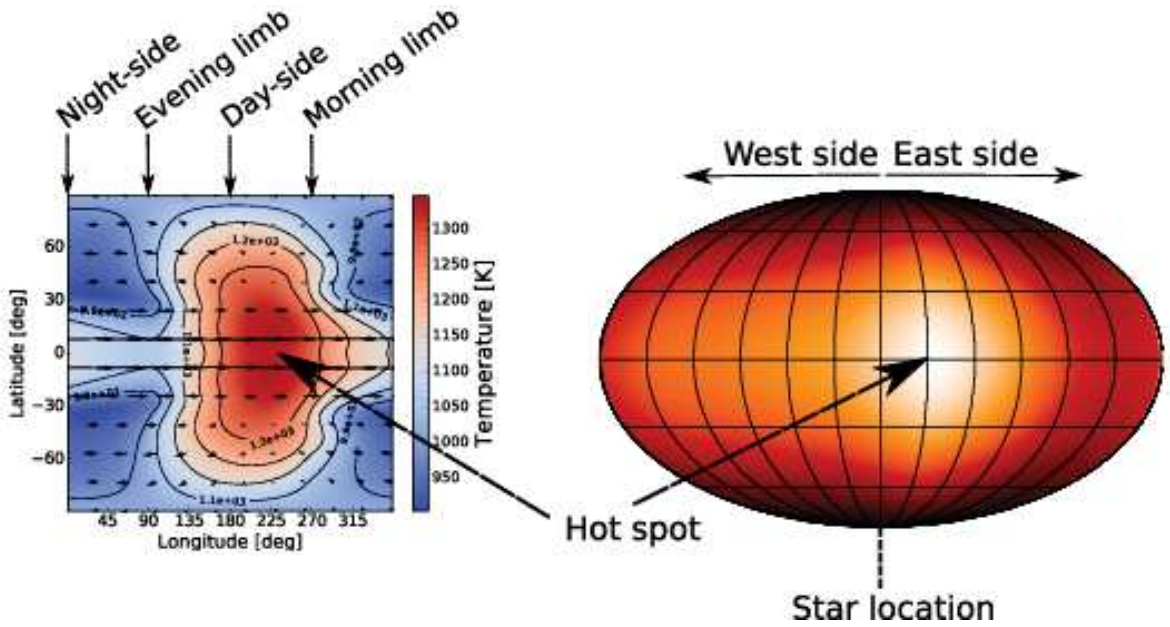

Figure 5.2 – Illustration of wind dynamics in the atmosphere of the hot Jupiter HD 189733 b. *Left panel:* temperature (color scale and isothermal contours) and winds (arrows) of the atmosphere of the planet at a pressure of 0.1 bar (source: Drummond et al., 2020). *Right panel:* thermal brightness distribution in the planet atmosphere reconstructed from Spitzer 8 μm IRAC band phase curve observations of HD 189733 b (see Knutson et al., 2007, from which the figure was taken).

the evolution of close-in Neptunes and has been invoked to potentially explain the origin of close-in super-Earths (see Owen, 2019, for a review of atmospheric escape in close-in planets).

5.1.2 Transit spectroscopy

Transiting planets are well-suited for atmospheric characterization. The favorable inclination of their orbits offers various ways to probe their atmosphere (see Figure 5.3). During the primary transit, some of the stellar flux passes through the optically thin part of the planet atmosphere. The variation of the absorption of the planet atmosphere as a function of wavelength is called the *transmission spectrum*. Just before the secondary eclipse, when the reflection of the stellar light on the planet atmosphere is maximum, one accesses the *emission spectrum* of the planet atmosphere. As the planet pursues its orbit, the amount of stellar light reflected on its atmosphere varies and so does the emergent spectrum of the planet. This offers the ability to obtain a phase-resolved emission spectrum for the planet.

Transmission spectroscopy

Transmission spectroscopy probes the fraction of the atmosphere, called day-night terminator region (and referred to as terminator region in the following), encircling the planet and separating the night-side and day-side hemispheres during the primary transit. The star light passing through the terminator is partly absorbed by the chemical species present in this region (Seager & Sasselov, 2000). As a result, the depth of the primary transit and thus the measured planetary radius varies as a function of the wavelength of observation. Let us consider a planet of radius R_p surrounded by a thin layer of atmosphere of characteristic height $z(\lambda) << R_\mathrm{p}$, λ being the wavelength of observation. The depth $D(\lambda)$ of the transit induced by transmission signal is given by (e.g., Ehrenreich et al., 2006):

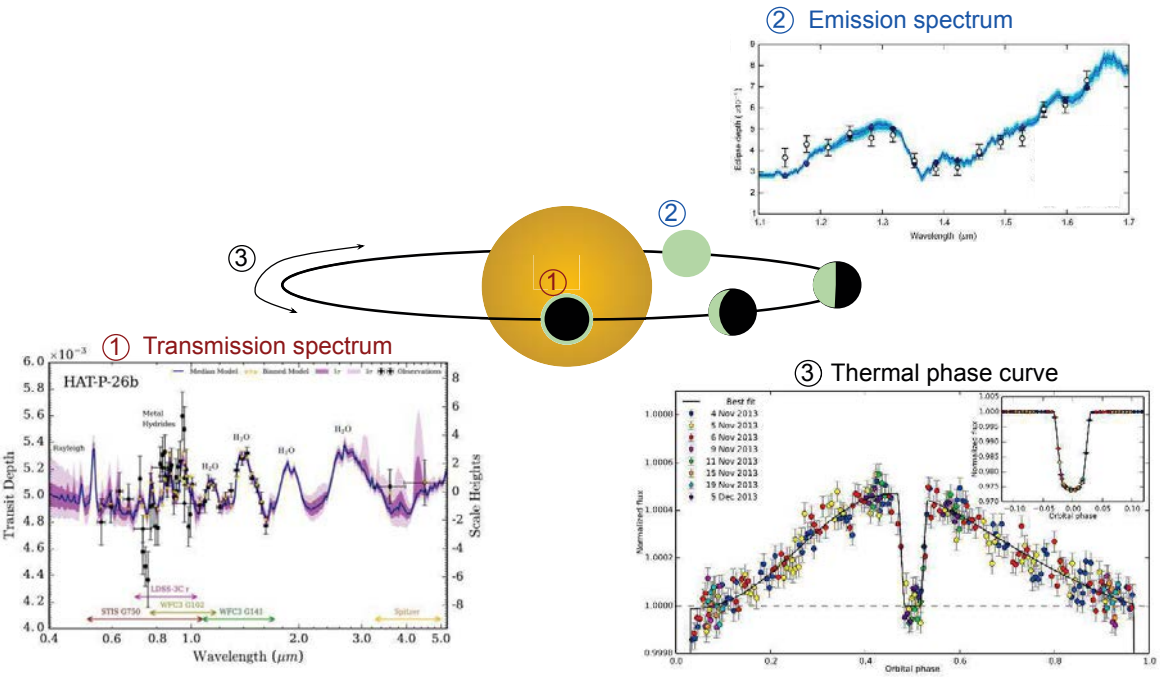

Figure 5.3 – Illustration of the different observational methods used to probe the atmosphere of transiting planets. The examples of transmission spectrum, emission spectrum and thermal phase curve were respectively those obtained on HAT-P-26b (MacDonald & Madhusudhan, 2019), WASP-43b (Kreidberg et al., 2014) and WASP-43b (Stevenson et al., 2014).

$$D(\lambda) = \frac{2R_\mathrm{p} z(\lambda) + z(\lambda)^2}{R_\mathrm{s}^2} \approx \frac{2R_\mathrm{p} z(\lambda)}{R_\mathrm{s}^2}, \tag{5.3}$$

where R_s is the stellar radius. The height of the atmosphere measured from the transit relies on the fundamental properties (e.g., temperature, pressure, chemical composition) of the terminator region. These properties can be recovered by comparing the observed transmission spectrum with synthetic spectra, generated by simulating the crossing of light rays through a modeled planetary atmosphere and solving the radiative transfer equation at the wavelengths of observation (in the so-called atmospheric retrieval process; e.g., Madhusudhan & Seager, 2009; Ehrenreich et al., 2014; Malik et al., 2017; Madhusudhan, 2019; Mollière et al., 2019; MacDonald & Madhusudhan, 2019). This however assumes that the stellar spectrum, generally observed shortly before and after the transit, is perfectly known at the time of the observations so the planet atmosphere transmission spectrum can be accurately recovered. In particular, the surface inhomogeneities exhibited by active stars can have a dramatic impact on the recovered parameters of the planet atmosphere (e.g., through the transit light source effect presented in Rackham et al., 2018).

The height of the planet atmosphere can be approximated as 5-10 pressure scale heights (Madhusudhan et al., 2014a), allowing us to compute a rough estimate of the transit depth induced by the planet atmosphere and assess its detectability. For example, a hot Jupiter like HD 189733 b (Bouchy et al., 2005) features a typical scale height of $H \sim 200$ km inducing excess of transit depth of the order of 1 mmag (for a transit depth of 25 mmag), detectable by space-based telescopes like Spitzer or HST. In contrast, the transmission signal induced by the Earth atmosphere is about 1 ppm ($H \sim 8.5$ km) which is far beyond reach of current and upcoming ground- and space-based spectrometers.

In practice, only a few atomic and molecular species induce strong enough absorption signatures to be probed by transmission spectroscopy. In the optical domain, sodium and potassium have been shown to be excellent probes of the atmosphere of hot Jupiters (e.g., Charbonneau et al., 2002; Sing et al., 2011; Wyttenbach et al., 2015). In the nIR, the most abundant asymmetric molecules of the planet atmosphere such as H_2O, CO, CH_4, HCN, FeH induce the strongest transmission signatures (Seager & Sasselov, 2000; Snellen et al., 2010; McCullough et al., 2014; Benneke et al., 2019). Low and medium resolution transmission spectroscopy has the additional potential to probe Rayleigh/Mie scattering induced by clouds and hazes (Seager & Sasselov, 2000; Brown, 2001; Wakeford & Sing, 2015), resulting in their detection in the atmosphere of hot Jupiters (Lecavelier Des Etangs et al., 2008; Pont et al., 2008), warm Neptunes (Kreidberg et al., 2014) and super-Earths (Benneke et al., 2019). Finally, UV transmission spectroscopy, and more specifically Lyman α emission associated to neutral hydrogen, has made it possible to detect evaporating atmospheres for a few hot Jupiters (Vidal-Madjar et al., 2003; Lecavelier Des Etangs et al., 2010), but also for the warm Neptune GJ 436 b (Ehrenreich et al., 2015).

Emission spectroscopy and thermal phase curve

Contrary to transmission spectroscopy that only accesses the temperature within the terminator region, emission spectroscopy probes the temperature and composition of the day-side of the planet atmosphere just before/after the secondary eclipse (e.g., Charbonneau et al., 2005; Deming et al., 2005; Kreidberg et al., 2014). By comparing the spectra obtained shortly before/after and during the secondary eclipse, we access the emission spectrum of the planet, which is a combination of a continuum (induced by intrinsic flux emitted by the planet) and absorption/emission features of its atmosphere. Assuming that the planet emits as a black body[2], the equilibrium temperature $T_{\rm eq}$ is given by

$$T_{\rm eq} = T_{\rm eff}\left(\frac{R_{\rm s}}{2a_{\rm p}}\right)^{1/2}(1-A_{\rm B})^{1/4}, \tag{5.4}$$

where $A_{\rm B}$ is the Bond albedo of the planet (i.e., the fraction of stellar flux reflected by the planet) and $a_{\rm p}$ is the semi-major axis of the planet orbit[3]. Moreover, the absorption/emission signatures of the emergent spectrum offers the ability to constrain the composition of the atmosphere and its T-P profile (as a result of the wavelength-dependent optical depths; see Madhusudhan, 2018, 2019). Over the past 2 decades, several planet emission spectra have been unveiled using mostly the Hubble Space Telescope wide-field camera 3 and Spitzer space telescope, whose wavelength range covers most of the planet emission spectrum (e.g., Charbonneau et al., 2008; Désert et al., 2011), but also from ground-based facilities (Sing & López-Morales, 2009; Mancini et al., 2013).

Thermal phase curves are obtained by monitoring the emergent flux of the planet throughout its orbit. The fraction of light reflected by the planet on the line-of-sight varies along its orbit (see Figure 5.3), allowing to constrain the longitudinal distribution of the temperature in the planet atmosphere (e.g., Knutson et al., 2007, 2009; Zellem et al., 2014). This is particularly interesting for

[2] Note that this ideal case assumes that the only source of energy heating the planet is absorption of stellar light and that the reradiation of their atmosphere is isotropic. While this crude approximation is relatively well respected for the Earth, deviations to blackbody emission are observed for planet atmospheres with strong greenhouse effects or intense dynamical processes (like hot-Jupiters; see Chapter 3 of Pierrehumbert, 2010, for more information). More generally, for planets with high albedos, starlight scattering could dominate over thermal emission at optical wavelengths, which is likely the case for solar-system planets. This approximation remains a first order guess allowing one to estimate the strength of an emission spectrum.

[3] Note that Eq. 5.4 assumes the that the thermal emission is homogeneous over the planet and thus that efficient mechanisms of energy redistribution of the incoming light operate in its atmosphere.

hot Jupiters whose hot spot is shifted eastward as a likely result of the superrotating atmosphere (see Figure 5.2 and Section 5.1.1). Note that an asymmetric phase curve of unclear origin has also been observed for the super-Earth planet 55 Cancri e (Demory et al., 2016). Spectrally-resolved curves present the additional advantage to provide the evolution of the emission spectrum of the planet atmosphere throughout the orbit. This allows one to constrain the longitudinal distribution of the P-T profile and chemical abundances in the planet atmosphere and thereby constrain the dynamical processes at work in the atmosphere (Stevenson et al., 2014).

5.1.3 Probing planet atmospheres with high-resolution spectroscopy

Over the past decade, high-resolution spectroscopy (HRS; $\mathscr{R} \geq 25\,000$) has emerged as an essential technique in the characterization of exoplanet atmospheres (see the review of Birkby, 2018). In the nIR, high-resolution cross-correlation échelle spectroscopy leverages the multitude of resolved molecular absorption lines to extract prominent chemical species in the planet atmosphere and constrain the Doppler motion of the planet around the star. This technique quickly proved to be particularly effective to unambiguously detect carbon monoxide and water in the terminator and dayside regions of transiting planets (e.g., Snellen et al., 2010; Birkby et al., 2013; de Kok et al., 2013; Brogi et al., 2016; Webb et al., 2020), but also in the atmosphere of non-transiting planets (e.g., Brogi et al., 2012; Lockwood et al., 2014; Brogi et al., 2014; Birkby et al., 2017). The recent fair detections of HCN and CH_4 in exoplanet atmospheres (Hawker et al., 2018; Cabot et al., 2019; Guilluy et al., 2019), confirms that HRS is a reliable alternative to low-resolution spectroscopy to unveil the composition of planet atmospheres. A few atomic (e.g., Na, Fe, Ti) and molecular (e.g., TiO, VO, FeH) species induce strong spectrally-resolved absorption signatures in the visible domain, from which the thermal structure and dynamics of the atmosphere can be inferred (e.g., Wyttenbach et al., 2015; Louden & Wheatley, 2015; Seidel et al., 2020; Ehrenreich et al., 2020).

High-resolution cross-correlation spectroscopy

The semi-amplitude K_p of the RV signal of the planet scales as the ratio q between the stellar and planet masses, M_s and M_p, such that

$$K_\mathrm{p} = K_\mathrm{s} q \tag{5.5}$$

where K_s is the semi-amplitude of the RV signature induced by the planet on the host star. As a result, spectral lines in the atmosphere of close-in planets undergo Doppler-shifts of amplitudes significantly larger than those of the stellar or Earth atmosphere lines. For example, the semi-amplitude of the RV signal of the hot Jupiter HD 189733 b ($q \approx 758$) is about $150\,\mathrm{km\,s^{-1}}$, whereas the amplitude of the stellar RV variations (e.g., due to Doppler motion induced by the planet and stellar activity) is typically of the order of a few hundreds of $\mathrm{m\,s^{-1}}$. The barycentric Earth RV (BERV) exhibits larger variations of $\pm 30\,\mathrm{km\,s^{-1}}$, but on significantly longer time scales than the orbital period of the system. As a result, both stellar and Earth atmosphere spectra appear more or less motionless in sequences of spectra obtained on a timescale of a night (e.g., for the observations of primary and secondary transits of the planet), whereas the planetary signal is shifted by a few $\mathrm{km\,s^{-1}}$ to a few $10\,\mathrm{km\,s^{-1}}$ (see the illustration in Figure 5.4). This allows to remove most stellar and Earth atmosphere contributions while keeping the planet signatures almost unchanged in the sequence of spectra (see the description of the data reduction process in Section 5.2).

The resulting sequence of spectra ideally contains the planet atmospheric signature drowned into random noise (e.g., photon and instrumental noise). Nevertheless, the typical depth of H_2O or CO individual absorption lines generally lies more than one order of magnitude below the noise level (e.g., the relative depth of H_2O absorption lines of HD 189733 b in the K band is typically

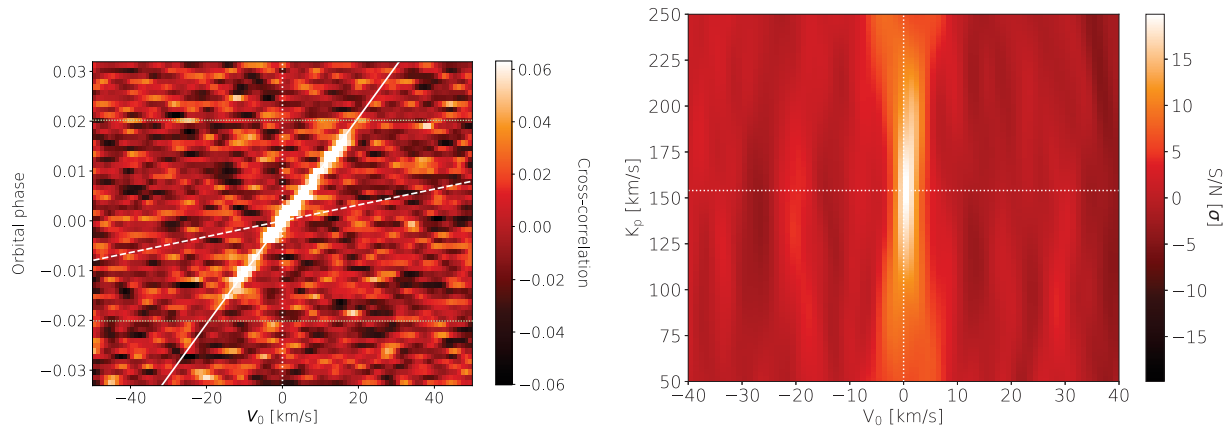

Figure 5.4 – Illustration of the typical Doppler shift of the close-in planet during its primary transit. The cross-correlation map (left panel) is obtained by cross-correlating a template of water absorption spectrum of HD 189733 b's atmosphere, generated using the PETITRADTRANS python module (Mollière et al., 2019), to a sequence of reduced SPIRou spectra of the SPIRou standard star Gl 514. We generated a synthetic water absorption signature 5× stronger than that expected for HD 189733 b and Doppler-shifted it at HD 189733 b's RV signature (assuming $K_p = 154\,km\,s^{-1}$ and $V_0 = 0\,km\,s^{-1}$, see Eq. 5.10) before adding it to the observed sequence of spectra. The white dotted, solid and dashed lines indicate the expected planet Doppler motions at K_p of 0, 154 and $1000\,km\,s^{-1}$, respectively. The start and end of the synthetic transit event are indicated by the two horizontal green dashed lines. The right-handed panel show the corresponding detection of water in the (K_p,V_0) using the method described in Section 5.1.3. The orbital parameters of the injected planet signature are indicated by the white dotted lines.

$\lesssim 10^{-3}$ whereas the peak S/Ns of the observation is generally about 100 for the brightest targets). We thus need to combine all the lines expected for the planet atmosphere in order to unveil the planet contribution in the sequence of spectra. To do so, a template spectrum of the planet atmosphere is generated by modeling the planet atmosphere and solving the associated radiative transfer equation from a list of line opacities (see Section 5.2.3). From a given set of planet RV orbital parameters (typically K_p and V_0, the planet RV offset at phase 0), a synthetic sequence of spectra is built by shifting the template according to the RV signature of the planet at K_p and V_0, and the correlation coefficient between the synthetic and observed sequences of spectra is computed. By repeating the process for a range of K_p and V_0, one obtains a map of correlation that is converted into a map of significance (e.g., by estimating the level of noise associated to the correlation between the template and the white noise alone, see Section 5.2.4), from which we compute the best set of orbital parameters and their error bars (see Figures 5.4 and 5.5). In the case when K_s is known from RV analyses (which is the case for the planets whose atmosphere is probeable by HRS), the estimation of K_p allows one to determine the planet mass (using Eq. 5.5) and thereby access the orbital inclination of the planet[4]. The evolution of the significance of the detection with the parameters of the modeled planetary atmosphere allows one to constrain the abundances in the planet atmosphere and its P-T profile, to a lesser extent. Note however that these constraints are highly model-dependent and remain rough in general. Nonetheless, promising efforts have recently been made to allow for a more robust exploration of the parameter space through a Bayesian framework (Brogi et al., 2017; Brogi & Line, 2019).

[4] In practice, other orbital parameters such as its eccentricity could be constrained with high-resolution cross-correlation spectroscopy, provided that the observational coverage of the planet orbit is dense enough.

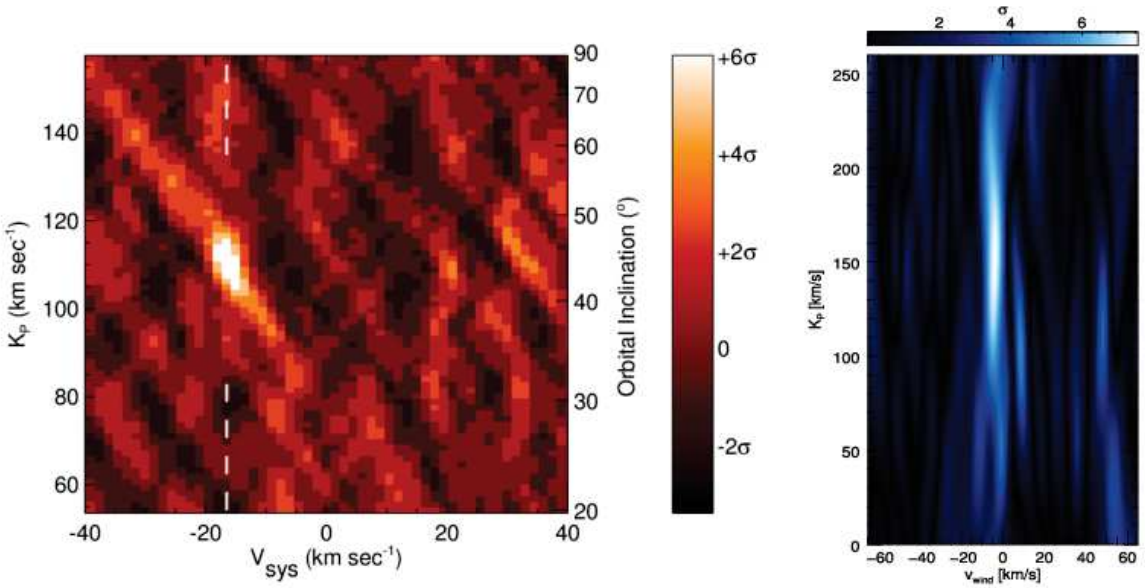

Figure 5.5 – Detections of CO (left panel) and H_2O (right panel) in the dayside spectrum of τ Bo otis b (Brogi et al., 2012) and in the terminator region of the atmosphere of HD 189733 b (Alonso-Floriano et al., 2019).

Interest of nIR high-resolution spectroscopy

Until recently, most of the nIR detections of planetary atmospheres in HRS were obtained using K-band observations mostly collected with CRIRES at the VLT (Kaeufl et al., 2004). Despite its large resolving power of 100 000 and its wide spectral range over the $YJHKLM$ bands (0.95-5.38 μm), CRIRES's wavelength coverage in a single exposure is interspersed by many gaps, limiting thereby the number of accessible lines in the planet atmosphere[5]. The emergence of high-resolution spectrographs featuring a continuous coverage of nIR spectral bands (e.g., GIANO, CARMENES, IRD, SPIRou and soon NIRPS) is a milestone in HRS. With the continuous spectral domain that can be collected in a single exposure (YJH bands for CARMENES, NIRPS and IRD, and $YJHK$ bands for SPIRou and GIANO), they access a profusion of absorption signatures from the planet atmosphere which should in principle provide more robust constraints on the elemental abundances in the planet atmospheres (e.g., by detecting new species like in Hawker et al., 2018; Guilluy et al., 2019) and on their P-T profiles (e.g., by analysing each diffraction order independently as tentatively done in Alonso-Floriano et al., 2019). Thanks to their coverage of the K band, SPIRou and GIANO have the additional potential to detect molecules on cloudy atmospheres whose low-resolution spectra appear featureless (Gandhi et al., 2020; Hood et al., 2020). Moreover, the recent detection of a $\sim -3\,\mathrm{km\,s^{-1}}$ shift in the water detection in the atmosphere of HD 189733 b (see the right-handed panel of 5.5 and Brogi et al., 2016, 2018; Alonso-Floriano et al., 2019), indicates that nIR HRS have also the additional ability to bring insights on the wind dynamics in the atmosphere, even though further investigations are needed on the modeling side to determine the physical mechanisms underlying the wind dynamics (e.g., Koll & Komacek, 2018; Caldas et al., 2019; Flowers et al., 2019). Finally, nIR HRS allows to monitor the He I triplet (1083 nm) which has recently been shown to be a reliable alternative to Ly-α for probing upper atmospheres of exoplanets (e.g., Spake et al., 2018; Nortmann et al., 2018; Salz et al., 2018; Allart et al., 2018; Oklopčić & Hirata, 2018; Mansfield et al., 2018; Alonso-Floriano et al., 2019). Thanks to these

[5] Note that despite larger spectral bands, CRIRES+ is expected to face similar limitations.

opportunities, nIR HRS is well suited to provide a robust basis to understand the physics of exoplanetary atmospheres in preparation for future missions such as JWST, ARIEL and the ELTs.

Despite these promising opportunities, nIR HRS is still in its infancy. As illustrated in Figure 1.17, nIR spectra are plagued by a forest of telluric lines whose temporal variation is not fully understood yet (notably for water). The stellar spectrum itself varies from one observation to the next under the effect of stellar activity and of the RM effect induced by transiting planets on stellar lines, which, if not corrected, can lead to false positives (e.g., Brogi et al., 2016; Casasayas-Barris et al., 2020; Flowers et al., 2019; Chiavassa & Brogi, 2019). Moreover, high-resolution cross-correlation spectroscopy remains highly model-dependant and errors on the line list or on the planet model can also have dramatic impacts on the recovered planet parameters (e.g., Caldas et al., 2019; Pluriel et al., 2020). Hence the need for dedicated benchmark analyses in order to quantify the various sources of errors affecting atmosphere characterization with HRS and implement a robust framework for planet atmospheric analyses.

5.2 Unveiling planet atmospheres with SPIRou

A few planetary transits were already observed with SPIRou as part of the SLS-TF. In this section, we use the well-known transiting hot Jupiter HD 189733 b as a benchmark to assess the ability of SPIRou to detect and constrain the atmosphere of close-in transiting planets. Although SPIRou is not fully optimized to observe as hot a star as HD 189733 (K2), the star is bright in the nIR and its close-in planet has been shown to be an excellent target for atmospheric characterizations (see the stellar and planet parameters in Table 5.1 and Section 5.2.1). The two planet transits observed with SPIRou in September 2018 and June 2019 are thus perfect test cases to develop and validate a procedure to correct sequences of spectra from stellar and telluric contributions, and carry out a search for planet atmosphere contributions using high-resolution cross-correlation spectroscopy. The application of this procedure to the standard SPIRou target Gl 514 is presented as a tutorial in a notebook[6] developed for conference *EXOSYSTÈMES I, Evolution* which took place in Paris in January 2020 [7].

5.2.1 Observations and description of the target

HD 189733 b

HD 189733 b is a transiting hot Jupiter that has been widely used as a benchmark for atmospheric characterization (e.g., Tinetti et al., 2007; Redfield et al., 2008; Madhusudhan & Seager, 2009; de Kok et al., 2013; Wyttenbach et al., 2015; Brogi et al., 2016, 2018; Alonso-Floriano et al., 2019). This planet has been one of the bedrocks of our knowledge of the atmosphere of hot Jupiters (together with HD 209458 b; Charbonneau et al., 2000). Low-resolution spectroscopic observations of the planet atmosphere have revealed that its transmission spectrum was dominated by a featureless slanted continuum suggesting the presence of low-altitude clouds and high-altitude hazes in the planet atmosphere (Pont et al., 2008; Lecavelier Des Etangs et al., 2008; Sing et al., 2011; Helling et al., 2016). Despite the Rayleigh scattering, atomic and molecular species such as Na D, K, He I, H_2O, CO, CH_4 have still been detected in the planet atmosphere with low- and high-resolution spectroscopy[8]. In particular, recent high-resolution transmission spectroscopy of HD 189733 b has revealed that the water signature of the terminator region of the planet was blueshifted by

[6] The notebook can be found on my github webpage: https://github.com/baptklein/Transmission-Spectroscopy-with-SPIRou.

[7] https://exosystemes1.sciencesconf.org/

[8] See the list of the molecular and atomic species detected in the atmosphere of HD 189733 b and the associated references in http://exoplanet.eu/catalog/hd_189733_b/.

Table 5.1 – Stellar and planet parameters of the HD 189733 b system.

Parameter	Value	Reference
Stellar parameters		
Distance d [pc]	19.7752 ± 0.0126	Gaia Collaboration et al. (2018)
Magnitude H	5.59 ± 0.03	Cutri et al. (2003)
Effective Temp. $T_{\rm eff}$ [K]	$\sim$5000	e.g., Sousa et al. (2018)
Radius $R_{\rm s}$ $[R_\odot]$	0.756 ± 0.018	Torres et al. (2008)
Mass $M_{\rm s}$ $[M_\odot]$	$0.823^{+0.023}_{-0.029}$	Triaud et al. (2009)
Systemic velocity $V_{\rm sys}$ [km s^{-1}]	-2.361 ± 0.003	Bouchy et al. (2005)
Rotation period $P_{\rm rot}$ [d]	11.953 ± 0.009	Henry & Winn (2008)
Non-linear limb darkening coefficients - H band		
c_1	0.9488	Hayek et al. (2012)
c_2	-0.5850	Hayek et al. (2012)
c_3	0.3856	Hayek et al. (2012)
c_4	-0.1318	Hayek et al. (2012)
Planet parameters		
Radius $R_{\rm p}$ [R$_{\rm jup}$]	1.138 ± 0.027	Torres et al. (2008)
$K_{\rm s}$ [m s^{-1}]	$201.96^{+1.07}_{-0.63}$	Triaud et al. (2009)
Mass $M_{\rm p}$ [M$_{\rm jup}$]	$1.138^{+0.022}_{-0.025}$	Triaud et al. (2009)
Orbital period $P_{\rm orb}$ [d]	$2.21857567 \pm 0.00000015$	Agol et al. (2009)
Orbital inclination $i_{\rm orb}$ [°]	85.71 ± 0.02	Agol et al. (2009)
Eccentricity $e_{\rm p}$	$0.0041^{+0.0025}_{-0.0020}$	Triaud et al. (2009)
Spin-orbit obliquity $\lambda_{\rm p}$ [°]	$0.85^{+0.32}_{-0.28}$	Triaud et al. (2009)
Atmospheric winds V_0 [km s^{-1}]	-3.9 ± 1.3	Alonso-Floriano et al. (2019)
SPIRou observations		
Number of transits	2	–
Observation dates	21/09/2018 - 14/06/2019	–
Number of spectra	36 - 50	–
Median SNR in H band	263 - 235	–
Observing time [h]	2.7 - 3.8	–

$\sim -3\,{\rm km\,s^{-1}}$, suggesting the presence of strong winds therein (Brogi et al., 2016, 2018; Alonso-Floriano et al., 2019; Flowers et al., 2019) compatible with the eastward super-rotation of the atmosphere shifting the position of the hot spot eastwards and thus implying different atmospheric composition in east and west limbs (see Knutson et al., 2007; Louden & Wheatley, 2015; Koll & Komacek, 2018; Caldas et al., 2019). Finally, the He I triplet at 1083 nm might be used to probe the upper escaping atmosphere of HD 189733 b (Lecavelier Des Etangs et al., 2010; Lecavelier des Etangs et al., 2012), although no secure measurements of the planet escape have been carried out so far using nIR HRS (Salz et al., 2018).

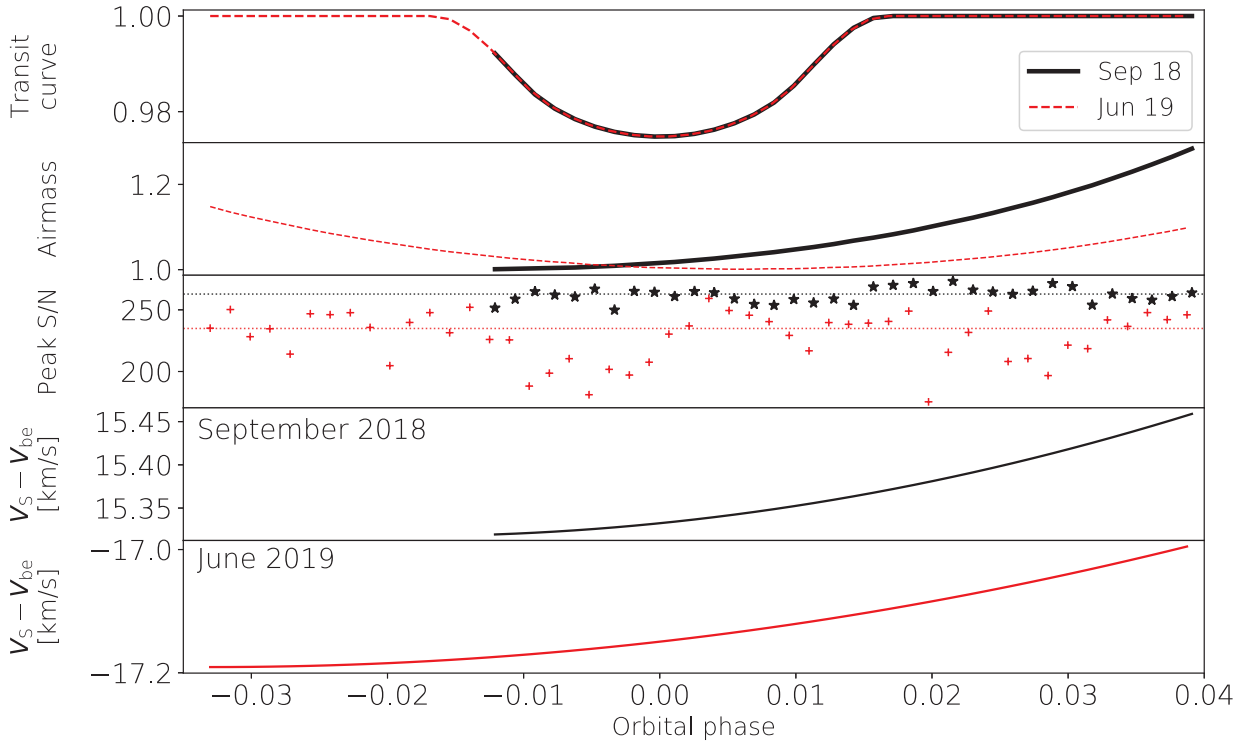

Figure 5.6 – Transit light curves (top panel), airmass (panel 2) and peaks S/N per pixel (panel 3) during the transits of HD 189733 b observed in September 2018 (black solid lines and stars) and June 2019 (red dashed lines and crosses). The black/red horizontal dotted lines in the third panel indicate the median peak S/N per pixel of the observations of the first and second transit, respectively. In the last two panels, we plot the RV shift to apply to move the spectra from Geocentric to stellar rest frames in September 2018 (panel 4) and June 2019 (panel 5).

SPIRou observations of HD 189733 b

Early science observations of HD 189733 have already been carried out with SPIRou in order to evaluate the performances of the instrument (see the summary of 2018-2019 observations in Moutou et al., 2020). In particular, sequences of $N_{obs} = 36$ and $N_{obs} = 50$ intensity spectra were respectively collected during the transits of September 21, 2018 and June 15, 2019 (resp. September 18 and June 19 in what follows). As shown in Figure 5.6, while the second transit is entirely covered by our observations, the ingress part of the September 2018 transit is only partly covered by the observations. Both data sets were collected at low airmass of ∼1 and feature S/Ns of 200-250 in the H band, about twice as large as the S/Ns of the GIANO spectra of HD 189733 b from which Brogi et al. (2018) reported a $\sim 5\sigma$ detection of water in the planet atmosphere. The spectra are reduced using version 0.5.0 of the SPIRou DRS (called APERO; Cook et al., in prep.) as described in Moutou et al. (2020). The DRS output is a 2-dimensional spectrum consisting of $N_o = 49$ orders (orders 79 to 31) of $N_{pt} = 4088$ data points (hence ∼200 000 data points in total). The spectrum of each order is to be divided by the blaze function of the grating, estimated from flat field exposures prior to the observations. A typical example of the resulting spectrum is shown in Figure 1.17. In addition to the reduced spectrum, the DRS also provides a spectrum corrected from tellurics using the method described in Artigau et al. (2014) (see Figure 1.17). The telluric-corrected spectra will be used to carry out the search for chemical species that are not present in the Earth atmosphere (e.g., CO, He). In contrast, the search for H_2O and CH_4 will be carried out from spectra uncorrected for tellurics, to ensure that the correction process does not affect

signatures from the planet atmosphere[9].

5.2.2 Pre-processing the sequences of spectra

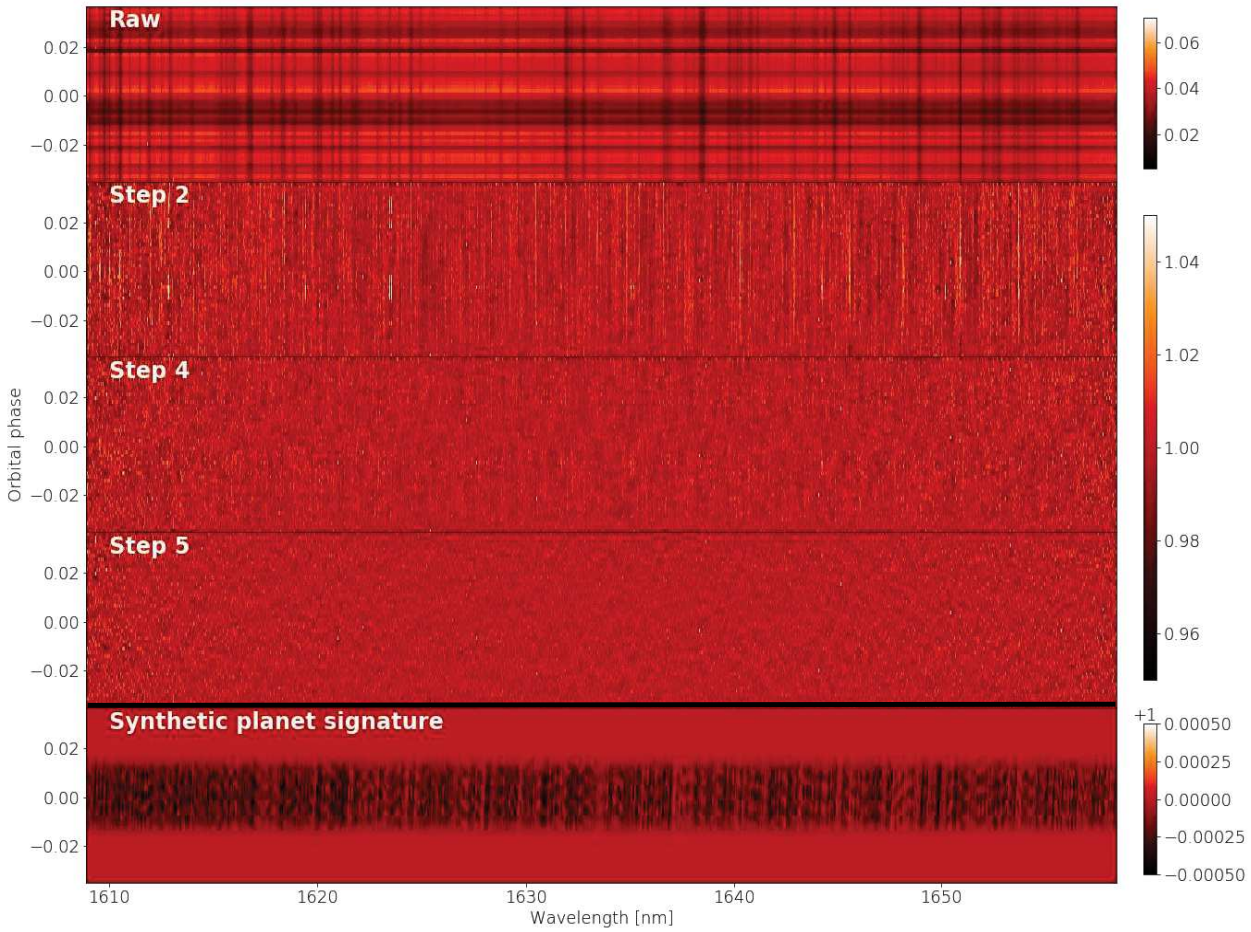

Figure 5.7 – Dynamical spectra (non-corrected for tellurics) of the order 47 of the June 19 sequence of spectra of HD 189733 b after different pre-processing steps (see Section 5.2.2). From top to bottom: spectra normalized by the blaze function uncorrected from Earth atmosphere and stellar contributions; median-divided normalized spectra obtained at step 2; spectra obtained at step 4 (after airmass detrending and outlier removal); sequence of spectra obtained after removing the first 4 PCA components of the sequence. For comparison, we show in the last panel a synthetic sequence of spectra containing only the water absorption signature of HD 189733 b's atmosphere (generated using petitRADTRANS) and shifted according to the planet RV signature (note the change in the color scale compared to the upper panels).

The reduced SPIRou spectra contains the contributions of the star and the Earth atmosphere polluted by a random noise (e.g., of photon and instrumental origins), and the weak signature of HD 189733 b's atmosphere that we want to unveil. Accurately filtering stellar and Earth atmosphere contributions from each sequence of spectra is a fundamental prerequisite to bring out the planet signature in the cross-correlation process, as any correlated residuals in the sequence of spectra may produce spurious signals in the correlation map. In this section, we describe the procedure that we implemented to clean most of the correlated noise from the observed sequences of spectra while leaving the planetary signal almost untouched. This method is inspired by previous developments

[9] Note however that a recent study of SPIRou spectroscopic observations of τ Bo otis b have shown that the method of Artigau et al. (2014) only marginally impacts the atmosphere of the planetary spectrum

carried out for HRS (e.g., de Kok et al., 2013; Brogi et al., 2016, 2018). In order to avoid any issue related to the overlap between diffraction orders, the steps detailed below are independently applied to each order of the sequence of spectra. Orders 37 to 44, 51 to 58, and 66 to 69, which are located within water absorption bands of the Earth atmosphere (see Figure 1.17), are discarded for the present analysis. The sequence of spectra of the reddest order (i.e., order 31) exhibits a significantly larger level of noise than its bluer counterparts and is also removed from the analysis.

5.2.2.1 Step 1: Preliminary cleaning

The SPIRou spectra are reduced in the Geocentric frame and, as a consequence, the Earth atmosphere signatures are aligned in the sequence of spectra (see the top panel of Figure 5.7). Due to stellar variability and HD 189733 b's Doppler motion, the stellar RV (directly measured from the SPIRou spectra) varies by respectively $\sim$100 m s^{-1} and $\sim$50 m s^{-1} throughout each of the two sequences of spectra. As this variation is significantly lower than the pixel size (2.28 km s^{-1}), we consider at first that all stellar spectra are aligned in the Geocentric frame and correct potential residuals of the stellar spectra in a subsequent step. We built a median observed spectrum $\bar{\boldsymbol{I}}$ for the night by taking the temporal median of the sequence of spectra (in each order). We then carry out a linear fit between each observed spectrum $\boldsymbol{I}$ and $\bar{\boldsymbol{I}}$, and divide $\boldsymbol{I}$ by the best-fitted median spectrum. The planet atmosphere transmission spectrum is shifted by a few 10 km s^{-1} during the transit and is thus no more than marginally impacted by this process.

5.2.2.2 Step 2: Normalizing the spectra

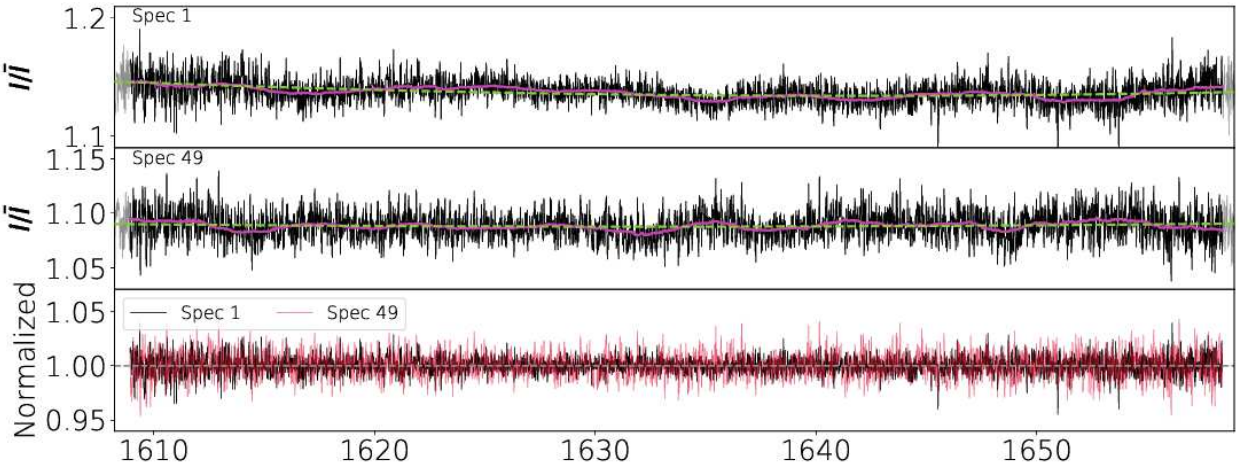

Figure 5.8 – *Panels 1 and 2:* example of two spectra (black line; resp. spectrum 1 and 49 of the June 2019 sequence) and moving average based of 120 points (magenta solid line). The best-fitted second order polynomials are shown by the green dashed lines. The last 50 points located at both ends of the spectra, not included in the computation of the moving average, are shown in gray. *Bottom panel:* normalized spectra (black and red for spectrum 1 and 49) after dividing them by the moving average.

Differences of fluxes are observed between the different exposures of the sequence (e.g., the different lines in the first panel of Figure 5.7). A simple low-order polynomial fit to each spectrum is often carried out to correct these differences and normalize the spectra. The choice of this model is justified by the fact that the flux at both ends of each order is slightly lower than that in the center of the order. If this normalizing process works well for the bluest orders (typically, orders 80 to 50), some uncorrected higher frequency structures are observed for redder orders. To correct them in the normalization process, we generate a smoothed version $\boldsymbol{I_s}$ of the each spectrum by taking

its moving average on $\pm N_{\rm a}$ points, and normalize the spectrum by $\boldsymbol{I_{\rm s}}$ (see the example shown in Figure 5.8. In order to get rid of potential boundary effects, we remove the last 50 points at each end of the spectrum, which are anyway much noisier than the central regions of the spectrum. The process is similar to applying a high-pass filter to each spectrum with a cut-off frequency of $1./N_{\rm a}$ (small values of $N_{\rm a}$ results in higher frequencies structures in the spectrum). We tune the value of $N_{\rm a}$ so that the correlated noise is filtered on a scale of a few tens pixels. In practice, $N_{\rm a} = 60$ has been shown to remove most of the visible low-frequency fluctuations in the observed spectra without significantly impacting their dispersion (contrary to values of $N_{\rm a}$ lower 10 for which the moving average start including uncorrelated noise in the process).

5.2.2.3 Step 3: Detrending with airmass

As shown in the second panel of Figure 5.7, steps 1 and 2 remove a large fraction of the stellar and Earth atmosphere contributions and homogenize the flux level in the sequence spectra. However, clear temporal variations are observed at the locations of the most prominent telluric lines. The variation of the column density of the Earth atmosphere along the line-of-sight produces fluctuations in the depth of telluric absorption lines which are not corrected by the previous steps.

The depth of a telluric line is correlated with the airmass along the line-of-sight. Therefore, a detrending of the sequence of spectra with airmass is frequently done in the literature to remove uncorrected telluric lines (e.g., Brogi et al., 2016, 2018). The time-variation of the flux in the telluric lines by a polynomial of order $N_{\rm d}+1$ in the airmass whose coefficients are linearly adjusted to match the observations. In practice, we estimate the $N_{\rm d}+1$ mono-dimensional spectra $\left(\boldsymbol{I_{(0)}}, ..., \boldsymbol{I_{(N_{\rm d})}}\right)$ such that

$$\boldsymbol{I_{\rm nor}} = \sum_{i=0}^{N_{\rm d}} \boldsymbol{I_{(i)}} \boldsymbol{A}^i + \boldsymbol{I_{\rm res}}, \tag{5.6}$$

where $\boldsymbol{A}$ is a $(1, N_{\rm obs})$ vector containing the values of airmass measured at each visit[10]. The residual sequence of spectra $\boldsymbol{I_{\rm res}}$ is assumed dominated by the white noise (which is more or less the case in practice, as the Fourrier transform of $\boldsymbol{I_{\rm res}}$ does not exhibit any prominent peak in the frequency space). Using a linear Least-squares estimator, we compute the spectra that minimize the χ^2 between the observations and the model, and subtract the best prediction from $\boldsymbol{I_{\rm nor}}$. In practice, we found that $N_{\rm d} = 2$ was enough to remove most of airmass-dependent contributions from the sequence of spectra. Note that this procedure is quite ad hoc, as the variation of the telluric contribution (especially water) depends on much more parameters than airmass, but has been shown not to significantly impact the signature of the planet atmosphere (Brogi et al., 2016). Brogi et al. (2018) suggested to carry out this detrending in logarithmic space (i.e., work with $\log \boldsymbol{I_{\rm nor}}$ instead of $\boldsymbol{I_{\rm nor}}$), as it allows for a more realistic description of the absorption processes in the Earth atmosphere. In our case, working in the logarithmic space only marginally impacts the dispersion in $\boldsymbol{I_{\rm res}}$ and we decided to keep using the linear detrending process for now.

5.2.2.4 Step 4: Outlier removal

To correct for bad pixels in the resulting sequence of spectra $\boldsymbol{I_{\rm res}}$, we computed the temporal dispersion of the flux in each pixel in the sequence (i.e., the dispersion along the time axis). As the sequence of spectra now contains mainly white noise, the resulting distribution of dispersion as a function of wavelength should have a parabola shape (see the right panel of Figure 5.9), with the ends of each order being more dispersed than the central part as a consequence of the blaze function

[10] Note that in Eq. 5.6, "^{i}" refers to the Hadamard product and thus that $\boldsymbol{A}^i_m = A^i_m$.

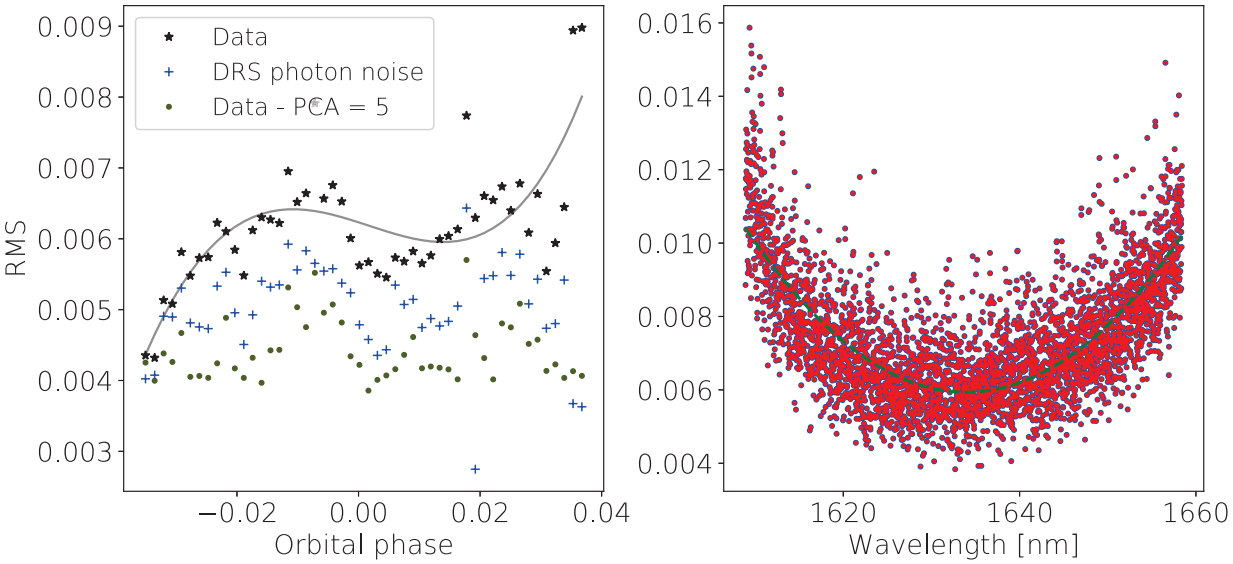

Figure 5.9 – *Left panel:* RMS of each spectrum of $\boldsymbol{I}_{\mathbf{res}}$ (order 47), computed on 800 points centered on the mean wavelength of the order (black stars). Green dots indicate the RMS of each spectrum after removing the largest 5 PCA components. The photon noise reported by the SPIRou DRS is shown in blue crosses. We fit the distribution of spectrum RMSs (before applying PCA) by a fourth order polynomial (shown to match relatively well the distribution), whose best-fitting model is shown by the gray solid line. *Right panel:* RMS of each pixel of the sequence of spectra obtained at step 4 (red dots) and best paraboloid fit $P_{\rm px}$ to the distribution of pixels (green dashed line).

of the grating. We fit a second order polynomial $P_{\rm px}$ to the distribution of RMS and remove all the pixels whose dispersion deviates by more than 5σ from the prediction. We then repeat steps 1 to 4 until no more pixel is rejected in the process (typically no more than 2 iterations).

The RMS in the center of each spectrum of $\boldsymbol{I}_{\mathbf{res}}$ is shown in the left panel of Figure 5.9. The dispersion of the reduced spectra appears significantly larger (by 38% in average) than the dispersion computed by the DRS. This suggests that our reduced sequence of spectra is still plagued by systematics (e.g., due to uncorrected telluric or stellar contributions). We thus need an additional step to correct for residuals of correlated noise in the sequence of spectra. The median dispersion at the center of the sequence of spectra in each order is shown in Figure 5.10. We note that, except in regions highly contaminated by tellurics, our reduced sequences of spectra agree well with the dispersion measured by SPIRou DRS for the bluest orders (i.e., 59 to 80). As a result of the stronger thermal noise not included in the DRS estimation, the sequence of spectra are increasingly more dispersed than the DRS estimate as the wavelength increases. Finally, we mask the points deviating by more than 7σ from the mean value in each spectrum for the following analysis.

5.2.2.5 Step 5: Correcting residuals with principal component analysis

After step 4, the sequence of spectra $\boldsymbol{I}_{\mathbf{r}}$ of each order is a 2-dimensional matrix of dimensions $(N_{\rm w}, N_{\rm obs})$, where $N_{\rm w}$ is the number of pixels after removing bad pixels in step 4. We use principal component analysis (PCA) to clean the residuals of correlated noise in the sequences of spectra. In the PCA framework, the sequence of spectra is regarded as a set of $N_{\rm w}$ random variables (the pixels of the order) for each of which we have $N_{\rm obs}$ realizations (i.e., each observation). After centering all the random variables, we use the SKLEARN python module[11] to project the sequence of spectra onto an orthonormal basis $\mathscr{B}_{\rm pca}$ whose components are the eigenvectors of the covariance

[11] https://scikit-learn.org/stable/modules/generated/sklearn.decomposition.PCA.html

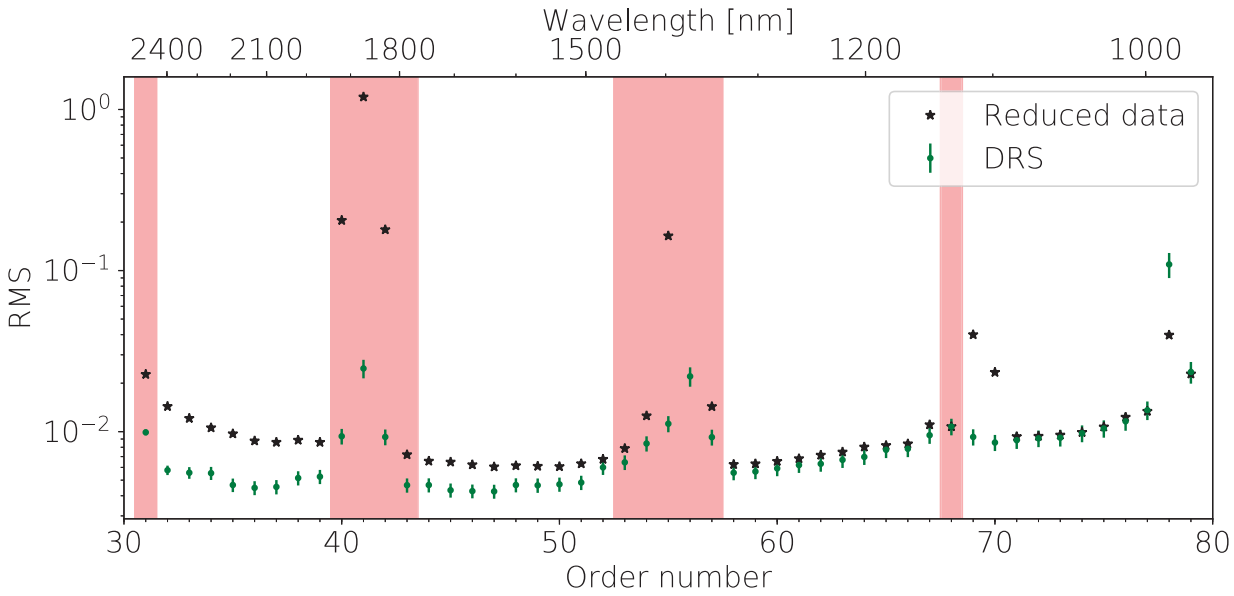

Figure 5.10 – Median dispersion of ∼800 pixels at the center of the June 2019 sequence of spectra in each order after step 4 (black stars). The values are missing for order 57 as no parabola fit to the distribution of RMS could be carried out given the high pollution of the spectra by telluric lines. The dispersion provided by SPIRou DRS is shown in green dots (with error bars indicating the standard deviation in the sequence of spectra). The orders located in the red vertical bands, visually contaminated by telluric lines or too noisy, are discarded for the analysis.

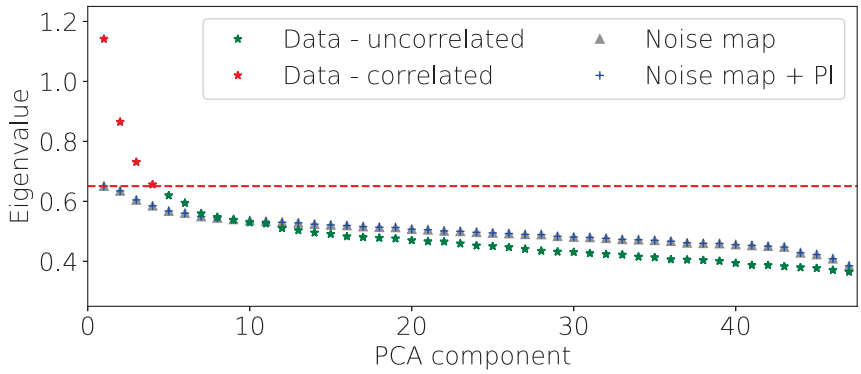

Figure 5.11 – Distribution of the eigenvalues of the covariance matrix of the June 2019 sequence of spectra of order 47 (red/green stars for removed/kept components). For comparison, the eigenvalues associated to the white noise map shown in the bottom panel of Figure 5.13 alone and with an injected planet signature (shown in the bottom panel of Figure 5.7) are respectively shown in gray triangles and blue crosses. The horizontal red dashed line indicates the limit above which the PCA components are removed from the sequence of spectra.

matrix $\boldsymbol{C}$ of the sequence of spectra defined as $\boldsymbol{C} = \boldsymbol{I_r}^{\mathrm{T}} \boldsymbol{I_r}$ (hence a total of N_{obs} eigenvectors of size N_{w}). The eigenvalues associated to the vectors of $\mathscr{B}_{\mathrm{pca}}$ scale with the variance in the data (which can be easily demonstrated by searching for the vector $\boldsymbol{u}$ such that the projection of $\boldsymbol{C}$ on $\boldsymbol{u}$ yield the maximum variance in $\boldsymbol{I_r}$). As a consequence, the larger the eigenvalue, the more the associated eigenvector (a.k.a. PCA component) contributes to the variance in the sequence of spectra. In practice, if $\boldsymbol{I_r}$ only contains uncorrelated noise, the distribution of eigenvalues sorted in descending order will be flat or slowly decreasing. In contrast, if correlated structures are the

present in $\boldsymbol{I}_\mathbf{r}$, the largest eigenvalues will contribute significantly more to the variance than their counterparts associated to white noise. For example, the eigenvalues associated to the covariance matrix of the June 2019 sequence of spectra of the order 47 are shown in Figure 5.11. The first 3 PCA components contribute significantly more to the variance budget of the data than the others and are therefore likely associated to correlated structures in $\boldsymbol{I}_\mathbf{r}$. This is confirmed in Figure 5.12 by the fact that the sequence of spectra reconstructed using only components 1 and 2 (and 3 also) are dominated by vertical structures associated to residuals of the Earth atmosphere contribution. The components associated to correlated noise are removed from $\mathscr{B}_{\rm pca}$ and the data are projected back to the original space.

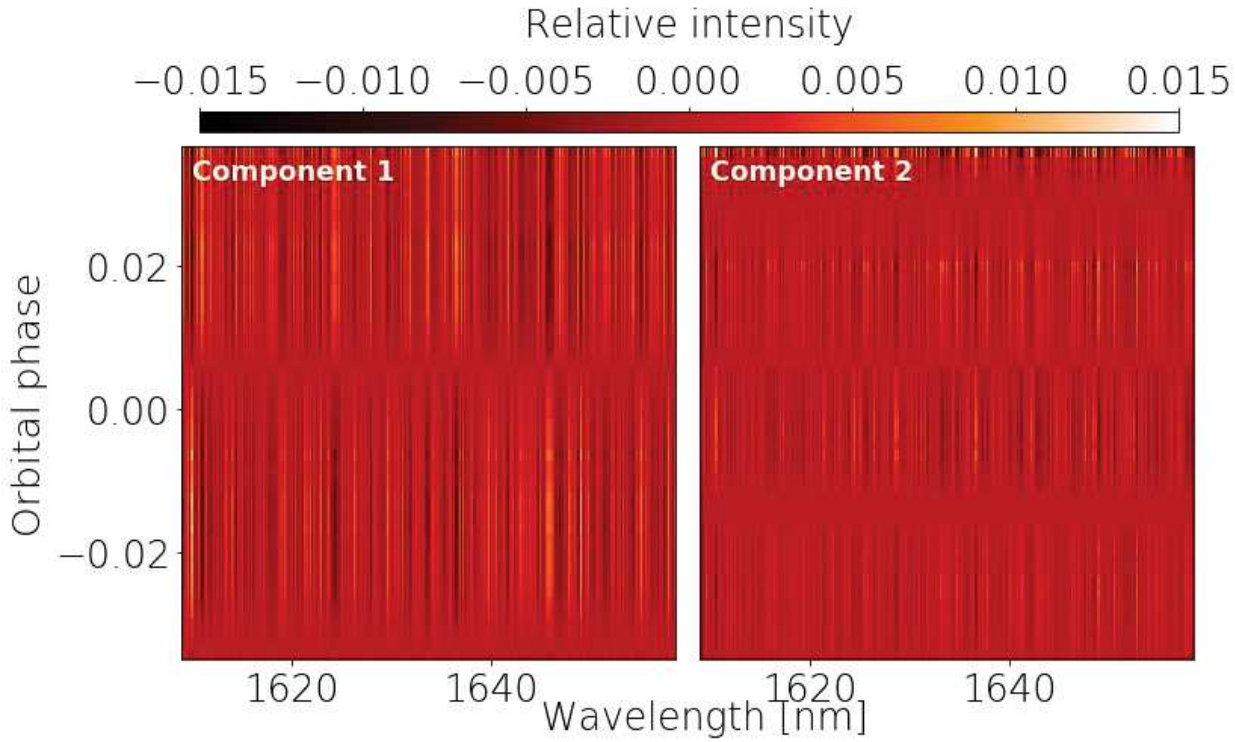

Figure 5.12 – Dynamical spectra of the first 2 PCA components (resp. left- and right-handed panels) of the June 2019 sequence of spectra of HD 189733 b transit.

The number of PCA components to be removed from the sequence of spectra must be carefully chosen in order not to affect the planet atmosphere signature. We propose to estimate this number from a sequence of synthetic spectra $\boldsymbol{N}_\mathbf{r}$ with the same dimension as $\boldsymbol{I}_\mathbf{r}$, but containing only white noise. Let us call $\boldsymbol{E}$ the vector containing the eigenvalues of the covariance matrix of $\boldsymbol{I}_\mathbf{r}$. The goal is to use $\boldsymbol{N}_\mathbf{r}$ to determine the threshold $e_{\rm max}$ such that PCA components associated with eigenvalues larger than $e_{\rm max}$ are removed from $\boldsymbol{I}_\mathbf{r}$ (as they are dominated by correlated noise). $\boldsymbol{N}_\mathbf{r}$ is drawn from a centered uncorrelated normal distribution of standard deviation equal to the mean temporal dispersion in the central region of $\boldsymbol{I}_\mathbf{r}$. $\boldsymbol{N}_\mathbf{r}$ is then amplified to tentatively account for the distribution of noise in wavelength and temporal spaces. Each column of wavelength λ is multiplied $P_{\rm px}(\lambda)$ (where $P_{\rm px}$ is the second order polynomial introduced in step 4 and shown by the green dashed line in the right-hand panel of Figure 5.9). To account for the different S/Ns of the reduced spectra, we fit a fourth order polynomial $P_{\rm sp}$ to the temporal distribution of the spectrum dispersion (see the gray solid line in the left-hand panel of Figure 5.9). The line of $\boldsymbol{N}_\mathbf{r}$ associated to time t is then multiplied by $P_{\rm sp}(t)$. An example of noise map built using this procedure is shown in Figure 5.13. We generate a set of $\sim$10 noise maps with different noise realizations that we amplify

using the procedure described above. The largest eigenvalue $e_{\rm m}$ of the covariance matrix of each of these maps is stored and we choose the 95$^{\rm th}$ of the distribution of $e_{\rm m}$ as the threshold $e_{\rm max}$ for tuning the number of PCA components to be removed from $\boldsymbol{I_r}$. By injecting a synthetic planet signature (modeled using the process described in Section 5.2.3) to $\boldsymbol{N_r}$, we double-checked that this procedure affects no more than marginally the planet atmosphere contribution (see Figure 5.11).

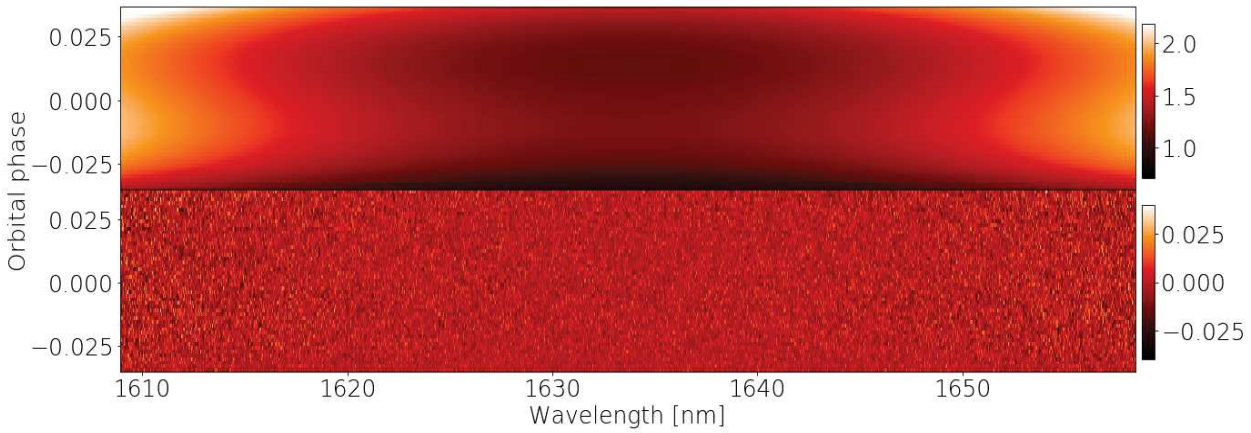

Figure 5.13 – Example of a realistic white noise map (bottom panel) obtained by (i) generating a sequence of spectra containing only Gaussian white noise of standard deviation equal to the average dispersion (here 0.0062) in the ∼400 pixels in the center of order 47 and (ii) multiplying the resulting noise map by the amplification map shown in the top panel. The noise amplification factor is obtained as described in Section 5.2.2.5, i.e., by multiplying the parabola $P_{\rm px}$ fitted to the distribution of dispersion in wavelength space (see the right panel of Figure 5.9) by the fourth order polynomial $P_{\rm sp}$ fitted to the distribution of the RMS of each spectrum (see the left panel of Figure 5.9).

Finally, we shift the wavelengths $\lambda_{\rm geo}$ of the observed spectra in the wavelengths $\lambda_{\rm rest}$ in the stellar rest frame by applying

$$\lambda_{\rm rest} = \frac{\lambda_{\rm geo}}{1 + \frac{\Delta v}{c_0}}, \tag{5.7}$$

where $\Delta v = V_{\rm S} - V_{\rm be}$, $V_{\rm S}$ being the stellar RV measured with SPIRou and $V_{\rm be}$ the BERV (see the values of Δv for the two sequences of spectra in Figure 5.6). The resulting sequence of spectra in the stellar rest frame is called $\boldsymbol{I_f}$ in the following.

5.2.3 Modeling the transmission spectrum of an exoplanet's atmosphere

In order to extract the signature of HD 189733 b's atmosphere from the noise in our sequence of spectra, we generate a model transmission spectrum for the planet atmosphere. In HRS, this is done by carrying out a line-by-line solving of the radiative transfer equation (RTE) for each wavelength λ (Mihalas, 1970, 1978):

$$\mu_\theta \frac{\partial I_\lambda}{\partial \tau_\lambda} = I_\lambda - S_\lambda, \tag{5.8}$$

where I is the specific intensity and S the source function, which describes the emission and scattering of the light (and where most of the complexity of Eq. 5.8 lies), and where $\mu_\theta = \cos\theta$, θ being the colatitude. τ_λ is the optical depth which describes the thickness of the medium and can be expressed as a function of the opacity κ_λ and the column mass density m along the line-of-sight, such

that $\tau_\lambda = \int \kappa_\lambda \mathrm{dm}$. To solve Eq. 5.8, we need a list of opacities for each atomic/molecular species in the atmosphere to model, which are computed at given pressure and temperature conditions using quantum mechanics and stored in data bases like HITRAN (Rothman et al., 1992), HITEMP (Rothman et al., 2010) or EXOMOL (Tennyson et al., 2016). In particular, the interested reader is invited a look to the HITRAN webpage[12] that contains pedagogical explanations on the opacity computation as well as many links towards easy-to-use publicly available tools to generate atomic and molecular opacity lists. Once the opacities and their dependencies on pressure and temperature conditions are known, we need to model the planet atmosphere in order to compute the optical depth and the source function and solve the RTE at the wavelengths of interest. Various forward modeling approaches exist in the literature[13] (see the review of Heng & Marley, 2018), ranging from fast mono-dimensional descriptions of the planet atmospheres at chemical equilibrium (e.g., Baudino et al., 2015; Waldmann et al., 2015a,b; Zhang et al., 2019; Mollière et al., 2019), to fully-consistent state of the art 3-dimensional models able to describe atmospheric circulation and non-equilibrium chemistry in planet atmospheres (see Showman et al., 2015; Drummond et al., 2020, and the references therein).

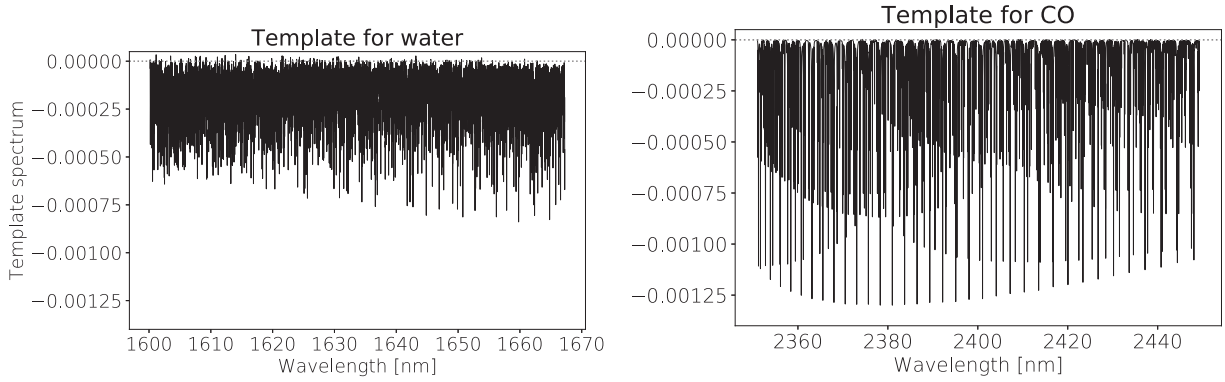

Figure 5.14 – Examples of modeled signatures of HD 189733 b assuming an atmosphere containing respectively only H_2, He and H_2O (left panel; order 47) and only H_2, He and CO (right panel).

For our analysis, we use the fast mono-dimensional self-consistent python package petitRADTRANS (Mollière et al., 2019), to generate a high-resolution absorption template for the planet atmosphere. We assume an homogeneous isothermal planet atmosphere at a temperature of $T_{eq} = 1200$ K for HD 189733 b (Guillot, 2010). The planet atmosphere is dominated by molecular hydrogen and helium and contains traces of two heavier species such as water and carbon monoxide, whose volume mixing ratios (VMR; i.e., relative abundances) are those reported in Brogi et al. (2016) (i.e., 10^{-3} for H_2O and CO). The relative abundances of H_2 and He are computed assuming solar system abundances (Anders & Grevesse, 1989). For our study, we want to assess our capability to detect each of the two species in the atmosphere. We thus consider two independent atmospheres A_{H2O} and A_{CO} containing respectively only H_2O and CO as heavy elements. The model also includes H_2-H_2 and H_2-He collision-induced absorptions as well as Rayleigh scattering from H_2 and He (see Table 3 of Mollière et al., 2019). We use the HITEMP water and carbon monoxide line list (Rothman et al., 2010) as an input for petitRADTRANS and compute an ultra high-resolution ($\mathscr{R} = 10^6$) transmission spectrum for the planet atmosphere in each order. We finally correct for potential slanted continuums (e.g., induced Rayleigh scattering), by fitting a straight line on the 1% points with the strongest flux. Examples of water and CO absorption

[12] https://hitran.org/links/

[13] A few easy-to-use publicly available tools are available in the Exoplanet Modeling and Data Analysis center: https://emac.gsfc.nasa.gov/.

templates respectively generated using models A_{H2O} and A_{CO} are shown in Figure 5.14.

5.2.4 Correlation analysis

Principle

We now compare the 1D-template $\boldsymbol{I_{mod}}$ to each spectrum in $\boldsymbol{I_f}$ using the cross-correlation process introduced in Section 5.1.3. For given values of K_p and V_0, we build a synthetic sequence of spectra $\boldsymbol{I_{syn}}$ by Doppler-shifting $\boldsymbol{I_{mod}}$ to its expected location at each observing epoch given K_p and V_0. To do so, we linearly interpolate $\boldsymbol{I_{mod}}$ such that, at a given time t:

$$\boldsymbol{I_{syn}}(t; K_p, V_0) = W(t)\frac{1}{2\delta v}\int_{-\delta v}^{\delta v} \boldsymbol{I_{mod}}[V_d(t) + V_p(t; K_p, V_0) + v]\,dv, \tag{5.9}$$

where $V_d(t)$ is the velocity vector of the observed spectrum at time t and $V_p(t; K_p, V_0)$ the expected planet signature, given by

$$V_p = V_0 + K_p \sin 2\pi\phi(t), \tag{5.10}$$

where $\phi(t)$ is defined from the mid-transit time and orbital period of the planet given in Table 5.1. The term δv is chosen to be half the SPIRou velocity bin (i.e, $1.14\,km\,s^{-1}$). Integrating over one pixel allows to minimize most of the errors introduced by linearly interpolating the template (it roughly amounts to convolve the spectrum by an instrumental profile). The measured planetary signal depends on the position of the planet on its transit curve. To account for this when computing the synthetic sequence of spectra, we generate the expected transit light curve Z for HD 189733 b using the BATMAN python package (Kreidberg, 2015) for the planet and limb darkening parameters listed in Table 5.1 (see the transit curves in the top panel of Figure 5.3). We then define a transit window (i.e., the term $W(t)$ in Eq. 5.9) using $W(t) = (1 - Z(t))/max(Z)$. We then compute the correlation coefficient $R(K_p, V_0)$ between $\boldsymbol{I_{syn}}(t; K_p, V_0)$ and $\boldsymbol{I_f}$ and repeat the process for a range of K_p and V_0 values (in our case, K_p and V_0 vary respectively between 50 and $250\,km\,s^{-1}$ and -40 and $40\,km\,s^{-1}$ with a step of $1\,km\,s^{-1}$). This process yields a map of correlation coefficients $\boldsymbol{R}$.

Significance of the detection

To estimate the probability that a given recovered signal is not just the effect of the noise realization, we must estimate the typical dispersion induced by cross-correlating the template to sequences of spectra containing only uncorrelated random noise. To do so, we apply the cross-correlation procedure presented above but replacing $\boldsymbol{I_f}$ by the amplified white noise maps computed in Step 5 of Section 5.2.2 (see also the example shown in Figure 5.13). The average dispersion $\bar{\sigma}$ of the resulting correlation maps is chosen as a reference for the noise level for $\boldsymbol{R}$. We then convert the correlation map into a S/N map $\boldsymbol{S} = \boldsymbol{R}/\bar{\sigma}$ and determine the best parameters and their error bars from the maximum and associated 1σ contour. This simple procedure relies on the fact that the distribution of the correlation values is Gaussian (Brogi et al., 2012, 2013). More robust approaches consist in estimating the significance of the signal through a set of statistical tests (e.g., Welsh T-Test Brogi et al., 2016; Birkby, 2018), computing a likelihood function instead of the cross-correlation (Brogi et al., 2017; Brogi & Line, 2019), or even use Doppler tomography instead of the cross-correlation process (Watson et al., 2019).

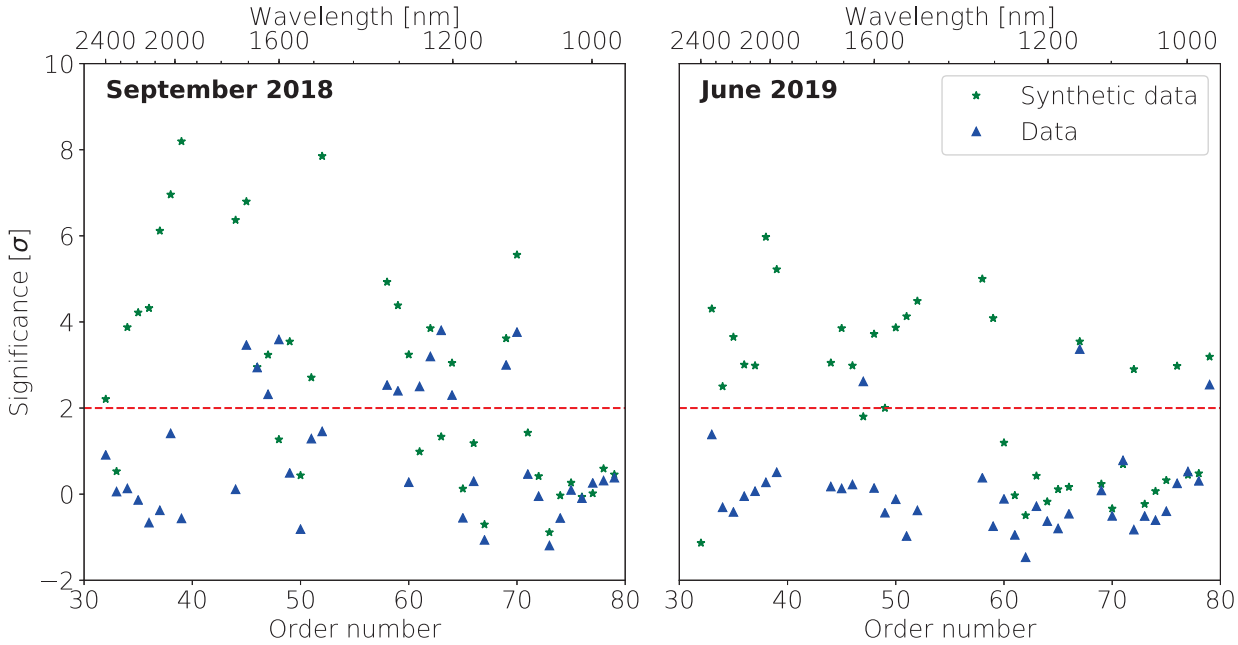

Figure 5.15 – Significance of the detection of water for each order in September 2018 (left panel) and June 2019 (right panel) sequences of spectra. In each panel, the peaks of S/N of the (K_p,V_0) map is shown for the synthetic (green stars) and observed (blue triangles) data. The red dashed line indicates a significance of 2σ.

5.2.5 Validation on synthetic data

Detection of water from sequences of synthetic spectra

In order to quantify the detectability of water in the data sets, we built sequences of synthetic spectra $\boldsymbol{I_{syn}}$ by adding the synthetic water absorption template, Doppler-shifted at the planet RV signature assuming $K_P = 154\,\mathrm{km\,s^{-1}}$ and $V_0 = 0.0\,\mathrm{km\,s^{-1}}$, to the reduced sequence of spectra $\boldsymbol{I_f}$. These new sequences of spectra are referred to as sequences of synthetic spectra in the following. We then compute the S/N map associated to each diffraction order using the method described in Section 5.2.4. The resulting detection significance as a function of the diffraction order is shown for the two transits in Figure 5.15. In Figure 5.16, we show the resulting S/N maps obtained by simultaneously searching for water in all orders of interest. The synthetic planet signature is detected at 9.6 and 5.8σ in September 2018 and June 2019 observations, respectively. This difference in the detection significance is surprising as the second transit is entirely covered by the observations whereas a significant part of the ingress of the first transit is missing. We found that the June 2019 set of reduced spectra exhibits a significantly higher dispersion relative to that provided by the SPIRou DRS than September 2018 observations. The origin of this dispersion remains unclear and is tentatively investigated in the next paragraph.

Tentative definition of a merit function

SPIRou, with its large continuous domain, offers the ability to search for planet atmosphere signatures in several orders simultaneously. This is particularly interesting for water whose numerous relatively deep absorption lines are spread over the whole nIR domain (compared to CO which is almost only present in the K band). However, the selected orders must be carefully chosen in order not to significantly lower the significance of the planetary signal nor introduce spurious signatures

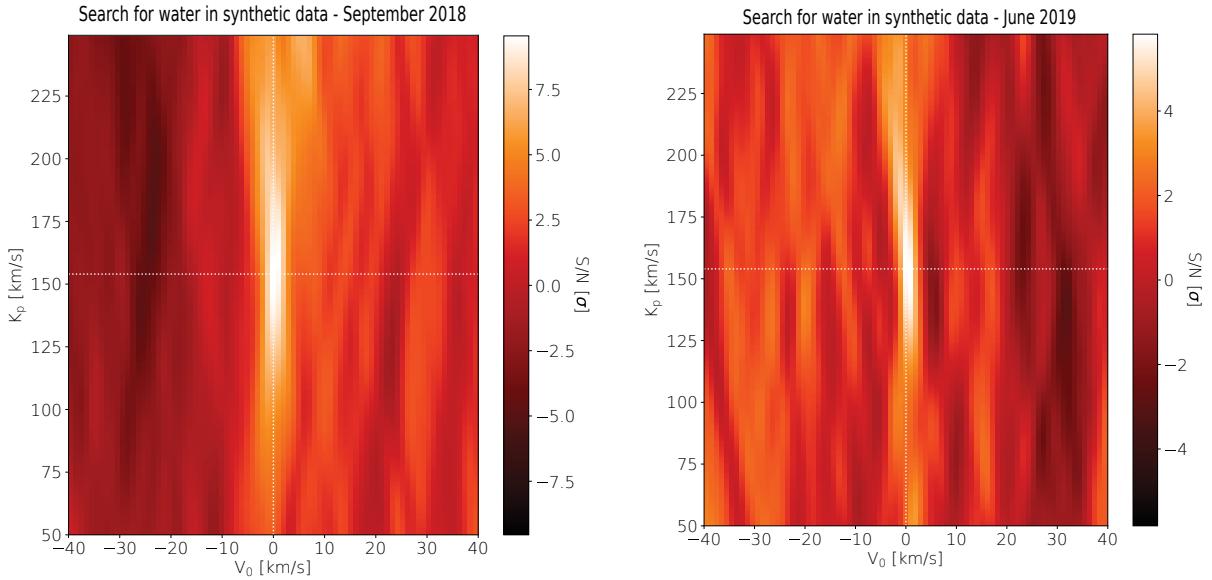

Figure 5.16 – S/N maps obtained by searching for water absorption signatures in September 2018 (left panel) and June 2019 (right panel) sequences of spectra after adding a synthetic water absorption template of HD 189733 b's atmosphere. The correlation process is jointly applied to all orders (except those rejected in the introduction of Section 5.2.2). The maximum S/Ns are respectively 9.6σ and 5.8σ for the left and right panels, respectively.

in the correlation maps. We thus propose to define a merit function $\mathscr{G}_C$ that would quantify how favourable a given order $\mathbf{O}$ is to the detection of a given chemical species C (here water). We first note that the more numerous and the deeper the expected water absorption lines are, the larger the significance of the detection. To quantify this effect, we integrate the autocorrelation function A_C of the template of C signatures generated for order $\mathbf{O}$. In contrast, the significance of the detection will decrease with decreasing S/Ns in order $\mathbf{O}$. Moreover, an order highly-polluted by telluric lines is more likely to introduce spurious signatures in the correlation map due to significant correlated residuals in the reduced sequence of spectra. We thus define the merit function as follows:

$$\mathscr{G}_C(\mathbf{O}) = \mathrm{S_N}(\mathbf{O})\frac{\mathrm{A_C}(\mathbf{O})}{\mathrm{A_T}(\mathbf{O})}, \tag{5.11}$$

where A_T is the autocorrelation function of the mean telluric spectrum provided by SPIRou DRS, and S_N is the S/N of the reduced sequence of spectra. We computed the merit function $\mathscr{G}_{H_2O}$ for each order of the two sequences of spectra of HD 189733 b and compare it to the S/N of the significance of water detection from the sequences of synthetic data shown in Figure 5.16. We find that the merit function is correlated with the water detection significances of the synthetic data (Pearson correlation coefficients of 0.6 for both transits). Interestingly, $\mathscr{G}_{H_2O}$ decreases by 25% in average between September 2018 and June 2019 (whereas the S_N decreases by no more than 10%). Therefore, one may speculate that the drop in water detection significance is possibly attributable to a stronger telluric absorption spectrum between September 2018 and June 2019. However, the merit function as presented in Eq. 5.11 does not account for temporal fluctuations in the telluric spectra which might have contributed to the observed decrease in water detection significance between September 2018 and June 2019. Further investigations are needed on this point to investigate how the water detection significance might be affected by the telluric spectrum and the pre-processing steps to filter it.

5.2.6 Preliminary results

Search for water

We now carry out the search for water from the observed reduced sequence of spectra $\boldsymbol{I_f}$. As a first step, we run the correlation analysis independently on each diffraction order. The resulting distribution of water detection significances is shown in Figure 5.15 (blue triangles). We find that 12 and 3 orders exhibit a $>2\sigma$-water detection in September 2018 and June 2019 sequences, respectively. However, the significance maps associated to the best 3 orders of the June 2019 sequence of spectra are plagued by strong signatures at the position of the telluric lines in the stellar rest frame, probably induced by uncorrected tellurics. The detection appears more reliable for the September 2018 data set, especially in orders 70 ($\sim$1100 nm) and 47 (1630 nm). However, we note that significance of the detection is poorly correlated with the merit function, suggesting that more work is needed to accurately quantify the ability to detect water from a given data set in the definition of $\mathscr{G}_{H_2O}$.

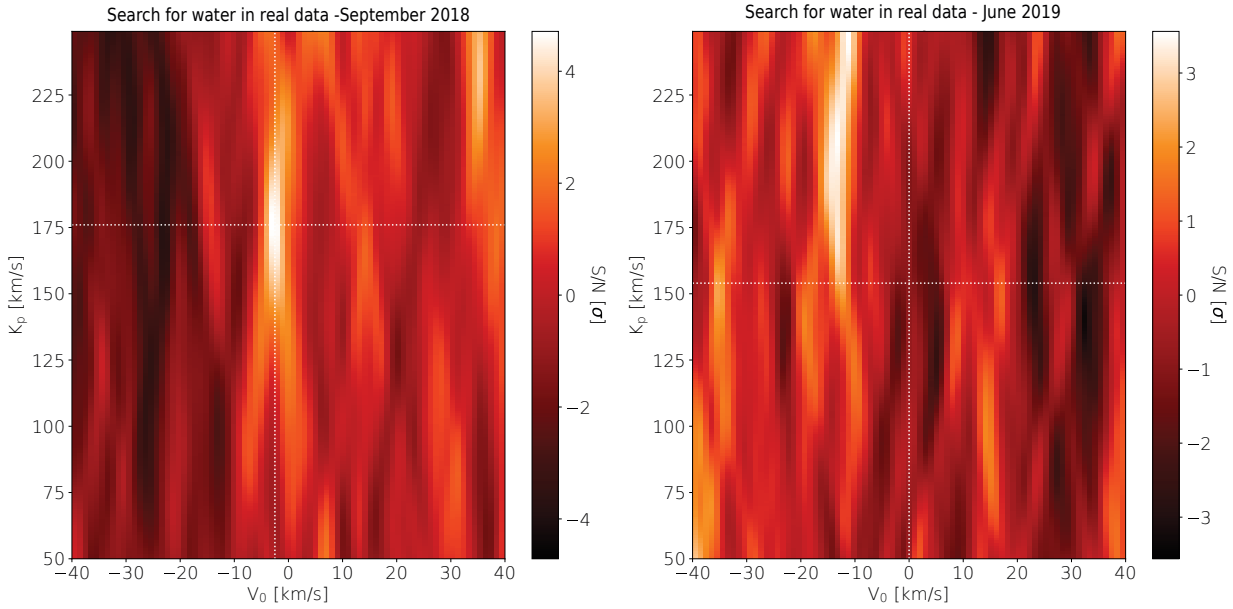

Figure 5.17 – S/N map obtained by jointly searching for water signatures in HD 189733 b's atmosphere in the orders for which we obtained an individual detection higher than 2σ in September 2018 (left panel) and June 2019 (right panel) data sets. In September 2018, we report a 4.7σ detection of water at $K_\mathrm{p} = 176 \pm 22\,\mathrm{km\,s^{-1}}$ and $V_0 = \text{-}3.5 \pm 1.0\,\mathrm{km\,s^{-1}}$. No water signature is detected in the June 2019 data set yet.

In order to enhance the water detection from the September 2018 sequence of spectra, we ran our correlation analysis simultaneously on all orders for which water is detected at more than 2σ (except order 58 which is highly polluted by telluric signals). The resulting S/N map is shown in Figure 5.17. We report a 4.7σ detection of water at $K_\mathrm{p} = 176 \pm 22\,\mathrm{km\,s^{-1}}$ and $V_0 = \text{-}3.5 \pm 1.0\,\mathrm{km\,s^{-1}}$, consistent with the literature values, within the error bars. In particular, the net blueshift of water absorption signatures in HD 189733 b's atmosphere is consistent with the values recently published (e.g., Brogi et al., 2016, 2018; Alonso-Floriano et al., 2019; Flowers et al., 2019).

Search for CO

In the same way as for the search for water, we build sequences of synthetic spectra by adding a synthetic planet signature computed using petitRADTRANS (with model A_{CO}) to $\boldsymbol{I_f}$. The search for CO absorption signatures in the atmosphere of HD 189733 b is not yet conclusive. CO remains

undetected in both synthetic and real data and, instead, both significance maps are dominated by a $\sim$7.5σ signature around $K_p = 80\,km\,s^{-1}$ and $V_0 = -7\,km\,s^{-1}$. A similar signature was also obtained in CO search carried out by Brogi et al. (2016) in the atmosphere HD 189733 b, and is attributed to the distortion of the stellar CO lines through the RM effect. This point is discussed in Section 5.2.7.

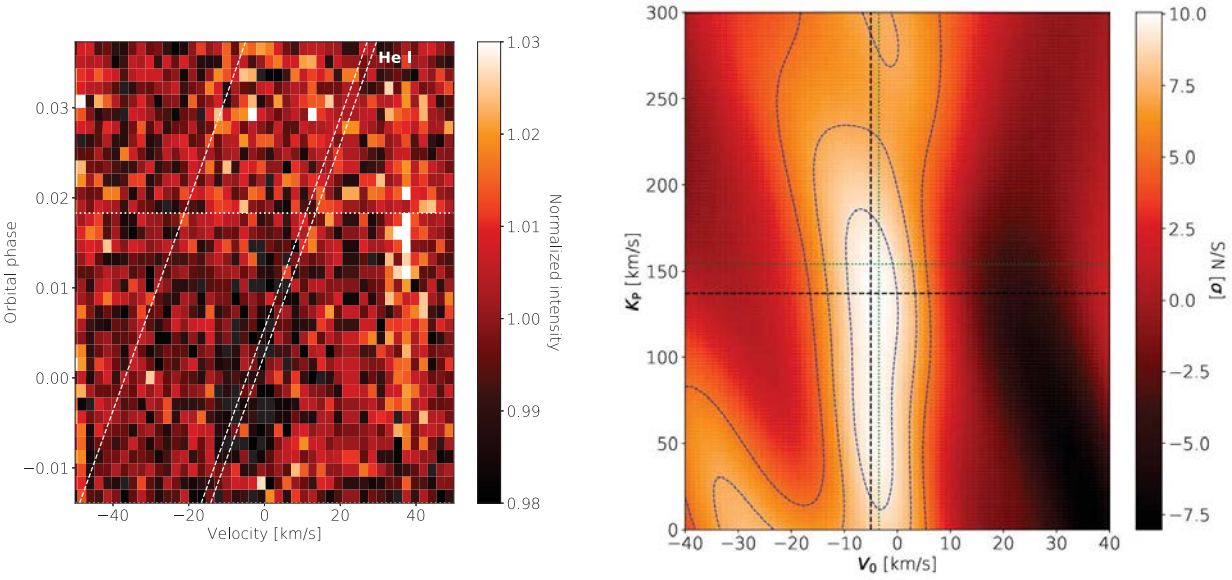

Figure 5.18 – *Left panel:* Reduced sequence of spectra (September 2018) centered on the He I triplet. The end of the transit is indicated by the horizontal dotted line. The expected position of the He I signatures of the planet atmosphere are indicated by the white dashed lines. *Right panel:* Significance map of the search for He I in the September 2018 reduced sequence of spectra in order 72. The blue contours indicate the 1, 3 and 5σ levels starting from the maximum significance (of 11.7σ). We find $K_p = 137^{+44}_{-121}\,km\,s^{-1}$ and $V_0 = -5 \pm 4\,km\,s^{-1}$ (indicated by the black dashed lines). The expected position from the literature is indicated by the green dotted lines (taking the values of Salz et al., 2018).

Search for He I

We also carried out a preliminary search for He I (1083 nm) signatures from the planet atmosphere in order 72 ($\sim$1080 nm) of the reduced September 2018 data set. The nIR He I triplet is a prominent stellar line that we filter using the pre-processing steps detailed in Section 5.2.2. As a first guess, we model the He I transmission signature of the planet atmosphere by simply fitting a double Gaussian function to the median He I stellar lines. We then compute a S/N map in the (K_p,V_0) space using the process described in Section 5.2.4 and report a 11.7σ detection of He I at $K_p = 137^{+44}_{-121}\,km\,s^{-1}$ and $V_0 = -5 \pm 4\,km\,s^{-1}$ (see the right panel of Figure 5.18), consistent with the literature (Salz et al., 2018). By averaging the spectra observed during the mid-transit in the planet rest frame, we isolate the most prominent lines of the He I triplet (see the right-handed panel of Figure 5.18) and find a relative absorption of $\sim$0.5% slightly stronger but still compatible within 3σ with that measured in Salz et al. (2018).

The origin of the long tail towards lower K_p values in the left-handed panel of Figure 5.18 is likely stellar. The prominent stellar He I triplet is partly occulted during the planetary transit, leaving a non-planetary signature at values of K_p comparable to that of the planet orbit (see point 3 of Section 5.2.7). As a consequence, the observed He I signature is probably the combination of stellar and planet atmospheric contributions that must be disentangled to secure the detection of the planet atmosphere. Another specific issues of the He I triplet is that these lines are proxies of

magnetic regions at the stellar surface. As a result, the occultation of active stellar surface regions by the planet may trigger variations in stellar He I fluxes yielding additional signatures in the S/N map. Proper simulations of the stellar surface with ZDI are needed to quantify the impact of this signal and come up with a solution to filter it (in a way similar to Section 4.1 of Salz et al., 2018). Once the stellar contribution has been accurately-filtered from the observed spectra, the analysis will be carried out again using more realistic models. In particular, studying the evolution of He I absorption levels throughout the transit could allow to probe the escape signatures of the planet atmosphere (despite no secure measurement of HD 189733 b's atmospheric escape has been reported from the observation of He I yet; Salz et al., 2018).

5.2.7 Next steps for HD 189733 b and perspectives of improvement

The preliminary results obtained in Section 5.2.5 and 5.2.6 confirm that SPIRou is able to constrain the atmospheres of close-in exoplanets. They also allow us to identify potential directions for improving the sensing of planetary atmospheres. We give below a non-exhaustive list of points that will be investigated in a near future. The analysis presented above will result in a benchmark paper presenting the ability of SPIRou to carry out a robust search of hot Jupiters' atmospheric constituents.

1. **Realistic simulations:** Up to now, our procedure to constrain planetary atmospheres with SPIRou was mostly data-driven. The atmospheric properties of our benchmark planet are indeed well-constrained from the literature, which offers the ability to empirically validate our results. We now propose to investigate the effect of the pre-processing steps presented in Section 5.2.2 on the planetary signature by conducting realistic simulations of the sequence of spectra. We will build a sequence of spectra $\boldsymbol{I}_{\mathbf{syn}}$ containing (i) a synthetic stellar spectrum (e.g., from the observed telluric-corrected spectra of the sequence or using radiative hydrodynamical simulations, e.g., Husser et al., 2013), (ii) the Earth atmosphere spectra provided by the DRS during the sequence, (iii) the planet atmospheric signature (e.g., computed with model A_{h2o}) and (iv) realistic white noise (i.e., DRS-estimate of the photon noise amplified by the blaze function). By applying our data reduction procedure to $\boldsymbol{I}_{\mathbf{syn}}$, we will be able to finely tune each pre-processing step so that it only marginally affects the injected planet signature. Working on synthetic data will also enable us to improve the definition of the merit function that could then be tuned using either a backward engineering approach or even machine-learning algorithms. Another less expensive way to improve our data reduction procedure would be to directly apply PCA to the normalized spectra obtained in step 2. The detrending with airmass carried out in step 3 does not filter well the temporal variations of water absorption signatures from the Earth atmosphere. This method is to be applied to the search for water in the 2019 spectral sequence in which the detection of the planet atmosphere is possibly limited by the Earth's atmosphere contribution.
2. **On the modeling side:** The modeling of the planetary signature presented in this manuscript remains very simplistic and changes in the process are expected to affect the resulting detections. Errors in the line list can result in a strong bias in the retrieved parameter signal (see Brogi & Line, 2019). Hence the need to validate them on a different line list like EXOMOL (Tennyson et al., 2016), which is being installed on the IRAP computer cluster. Moreover, 2D and 3D effects as well as non equilibrium chemistry can have dramatic effects on the recovered atmospheric parameters for hot Jupiters (Debras et al., 2020; Pluriel et al., 2020). Thanks to our access to state of the art GCMs (via Florian Debras), we are able to assess the impact of more complex modelling of the planet atmosphere. However, premiminary results[14]

[14] These results were obtained during two undergraduate interships (resp. Léa COSTES and Orianne SOHIER) supervized by Florian Debras and myself in 2020.

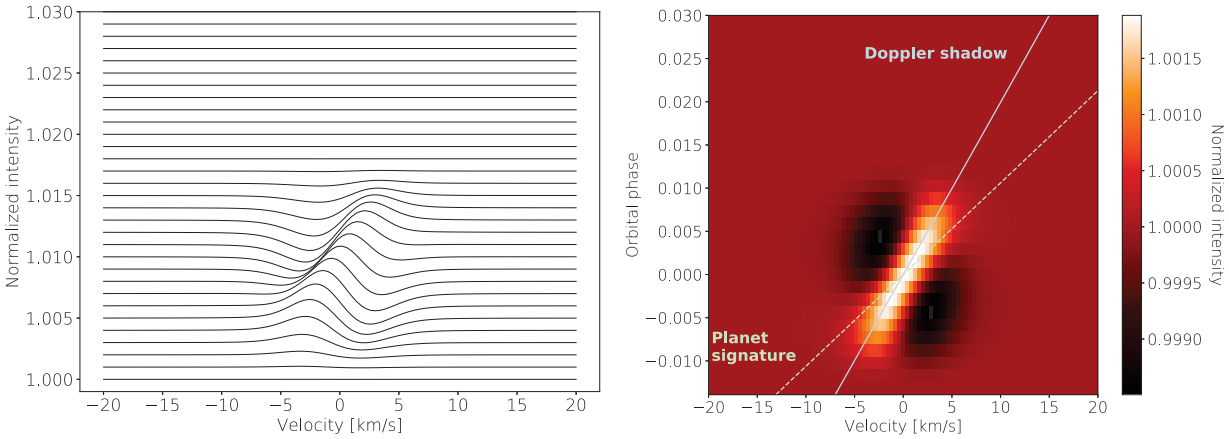

Figure 5.19 – Illustration of the RM effect induced by HD 189733 b on synthetic line profiles generated with ZDI (in the forward approach; see Appendix A.1). The synthetic line profiles are scaled on those of HD 189733 and we occult part of the modeled stellar disk using a circular structure moving like the transiting planet (based on the parameters reported in Table 5.1). *Left panel:* Individual line profiles normalized by the median profile and shifted vertically for clarity purposes. *Right panel:* dynamical spectrum of median-divided line profiles. The expected planet signature is shown by the green dashed line ($K_p = 154\,km\,s^{-1}$) while the evolution of the RM effect is shown by the blue solid line ($K_p = 80\,km\,s^{-1}$) .

based on orders 70 and 47 in the September 2018 sequence of spectra have shown that the detection of water was marginally impacted by the change in the model. Finally, the transit curve used to produce synthetic sequence of spectra in the correlation analysis presented in Section 5.2.4 is assumed unchanged from one order to the other. However, the latter strongly depends on the assumed wavelength-dependent limb-darkening coefficients which may affect the recovered planetary signal.

3. **Variability of the stellar spectrum:** Our data reduction process assumes that the stellar spectrum does not vary during the observations. In this rough assumption, we neglect some processes that vary on the time scale of the observations, yielding thus correlated leftovers that could affect our recovered planetary estimates. The first of these effects, pointed out by Brogi et al. (2016), is linked to the RM effect of the transiting planet. During its transit, the shadow of the planet on the stellar disk distorts the average stellar lines. As illustrated on synthetic profiles in Figure 5.19, as the planet moves along its transit chord, this distortion (a.k.a. the Doppler shadow; Collier Cameron et al., 2010) moves over the stellar lines. The speed K_D at which the Doppler shadow moves over each line roughly scales as $\Delta v/[2\pi(\phi_f - \phi_i)]$, where Δv is the line width (in velocity unit), and ϕ_i and ϕ_f are the orbital phases at the beginning and end of the transit, respectively. For HD 189733 b, K_D is about $100\,km\,s^{-1}$, i.e., of the same order of magnitude as the velocity of the planet signature (as shown in the right panel of Figure 5.19). This effect is expected to significantly affect the search for species like CO or He I whose signatures are present in both stellar and planetary atmosphere spectra (Brogi et al., 2016; Flowers et al., 2019). In particular, this could explain the peak S/N at $K_p \sim 80\,km\,s^{-1}$, obtained in the search for CO in the HD 189733 b atmosphere, as well as the local minimum obtained in the search for He I (see Figure 5.18). Several methods have been proposed in the literature to model the RM effect of the lines of interest (e.g., Cegla et al., 2016; Brogi et al., 2016; Flowers et al., 2019; Chiavassa & Brogi, 2019). Our project is to use the forward modeling approach of ZDI to generate synthetic line profiles for the stellar CO and He I lines, to simulate the transit of the planet in front of the modeled stellar disk and correct the modeled RM effect from the sequences of spectra at the position of the lines

of interest (see the preliminary example in Figure 5.19). Other more complex effects such as the wavelength-dependent shift of CO lines induced by stellar granulation would require to couple our cross-correlation process to 3D hydrodynamical simulations of the stellar surface, for example in the framework described in Chiavassa & Brogi (2019).

4. **Cross-correlation framework and model comparison:** The cross-correlation framework used in our analysis relies on a simple forward model, which makes it difficult to compare planet atmosphere models with each others and, thereby, to retrieve robust estimates for the parameters of the planet atmosphere. Recent efforts to move the standard high-resolution cross-correlation procedure into a Bayesian atmospheric retrieval framework have shown promising results for HD 189733 b (on a single CRIRES order; Brogi & Line, 2019). Once the pre-processing steps have been validated on simulations, we plan to implement this retrieval framework to SPIRou data. In particular, this framework may allow to optimally invert the wealth of information about the planet atmosphere present in the whole SPIRou spectra into precise constraints on the abundances, P-T profiles and atmospheric circulation of the atmospheres of hot Jupiters, and maybe of lower mass planets. This long-term project will be demanding in term of computational facilities and thereby require the use of dedicated computer clusters. In this purpose, 350 kh were attributed to this project by the CALMIP computer cluster in Toulouse[15] (PI: Debras & Klein).
5. **Combining transits:** As other transits of HD 189733 b will be observed with SPIRou as part of the SLS-TF, it will become interesting to combine the sequences of spectra into a master densely-sampled data set. In particular, this would allow one to isolate the ingress and egress in the correlation analysis, and probe the evolution of the wind in the two limbs of the planet atmosphere. When combined with 3D-atmospheric models as in Flowers et al. (2019), this offers a way to better understand the complex circulation patterns within the atmosphere of hot Jupiters.

5.3 Future prospects

5.3.1 The ATMOSPHERIX observation program

The ability of SPIRou to constrain the atmospheres of close-in giant planets motivated the creation of a large French consortium involving complementary expertises (Debras, Moutou, Klein and 16 others french collaborators). The goal of this collaboration is to carry out a global atmospheric characterization of multiple transiting planetary systems with SPIRou in order to provide a robust basis for upcoming missions such as the JWST, ARIEL, and the ELTs. Such observations will allow (i) to confirm the ability of SPIRou to measure elemental abundances and more specifically the C/O ratio in planetary atmospheres (including cloudy atmospheres; Gandhi et al., 2020), (ii) constrain the P-T profile and wind circulation in the planet atmospheres using state of the art 3D hydrodynamical models, and (iii) probe the planets' exospheres and investigate their escaping processes through the He I triplet.

We have built a list of versatile targets accessible from the CFHT including hot Jupiters (e.g., HD 209458 b, WASP 127 b) and colder less massive planets (e.g., HAT-P-11 b, 55 Cancri e). The expected significance $\sigma_{\rm exp}$ of molecular detection in the atmosphere of each planet is quantified through a metric empirically built on the detection of water obtained for HD 189733 b (from September 2018 sequence of spectra; see Figure 5.17). This significance depends on the transit depth of the transmission signal (see Eq. 5.3), but also on the magnitude m_H of the host star in the H band (the number of exposures reachable per sequence increasingly depends on how bright the star is), and on the transit duration τ, such that

[15] https://www.calmip.univ-toulouse.fr/

$$\sigma_{\rm exp} = \sigma_{\rm ref} \frac{(HR_{\rm p}/R_{\rm s}^2)}{(HR_{\rm p}/R_{\rm s}^2)_{\rm ref}} 10^{0.2(m_{H_{\rm ref}} - m_H)} \left(\frac{\tau}{\tau_{\rm ref}}\right)^{0.5}, \tag{5.12}$$

where H is the pressure scale height defined in Eq. 5.2. Quantities indexed by ref refer to HD 189733 b values. In particular, we take $\sigma_{\rm ref} = 4.7$. Note that $\sigma_{\rm exp}$ is conservative as the detection of water in HD 189733 b's atmosphere remains preliminary (see Section 5.2.7). Moreover, our metric does not account for changes in the planet metallicity and is likely under-estimated for Neptune mass planets whose atmospheres are expected to be enriched in heavy elements. The ability to detect He I was quantified using the recommendations of Kirk et al. (2020). Using the metric, we computed the number of transits required to obtained a significance larger than 4σ on each system. Observations of the transits of 6 systems were requested to the french time allocation committee in 2021A. The goal is now to pursue request the observation of additional transits in each semester. On the analysis size, we plan to develop joint modelling and simulation tools in order to make efficient and robust comparisons between all the observed targets of the list.

5.3.2 Transmission spectroscopy of AU Microscopii with SPIRou

As mentioned in Chapter 4, the close-in planet AU Mic b appears well suited for an atmospheric characterization given how bright the star is in the H band. With Eq. 5.12, we obtain a score of $\sigma_{\rm exp} = 3.27$ for the detection of water in the planet atmosphere. AU Mic b likely formed at a few au from its host star and likely features a significantly enriched atmosphere (as expected for hot Neptunes Fortney et al., 2013; Moses et al., 2013, and from the relatively high bulk density measured in Section 4.4). Moreover, AU Mic b has an equilibrium temperature of ∼600 K and a large stellar irradiation (20× larger than the Earth insolation) that could drive the photo-dissociation of low-mass species like H_2O or CH_4, resulting in upper atmospheres dominated by CO_2 and deeper layer (probed by nIR transmission spectroscopy) dominated by CO (over methan, as observed for the atmosphere of the Neptune-sized planet GJ 436 b, see Stevenson et al., 2010; Madhusudhan & Seager, 2011; Moses et al., 2013; MacDonald & Madhusudhan, 2019). On the other hand, the planet is still in its youth and the evolution of its atmosphere composition since its formation remains unclear. The atmosphere enrichment could also favours the detection of helium, especially if AU Mic b hosts an extended exosphere, which is possible given its insolation (as mention in Section 4.4).

A transit of AU Mic was observed with SPIRou in 2019 June 17 as part of the SLS-TF. A total of 29 spectropolarimetric sequences of spectra (i.e., 116 spectroscopic observations) were collected during the planet transit. As shown in the left panel of Figure 5.20, the transit ingress could not be observed because the star was not visible from CFHT. Moreover, the airmass remains higher than 2.5 during the transit ingress, implying that the spectra obtained during this period are likely strongly contaminated by tellurics. Martioli et al. (2020a) detected the RM effect induced by the planet during the transit and measured a projected spin-obliquity compatible with 0° for the planet, which was confirmed by simultaneous observations of the transit (Palle et al., 2020; Hirano et al., 2020).

As a preliminary analysis, we used the method described in Section 5.2 to clean stellar and Earth atmosphere contribution from the observed sequence of spectra. Using petitRADTRANS, we generated two absorption templates containing respectively water and CO, assuming a 50× solar metallicity (compatible with that of Uranus and Neptune; Fletcher et al., 2010; Nettelmann et al., 2013). Using the cross-correlation process described in Section 5.2.4, we do not find any conclusive detection of water from the data. In contrast, the search for CO in orders 31-33 yields a positive correlation close at $K_{\rm p}$ and V_0 relatively close to the expected values for AU Mic b, as

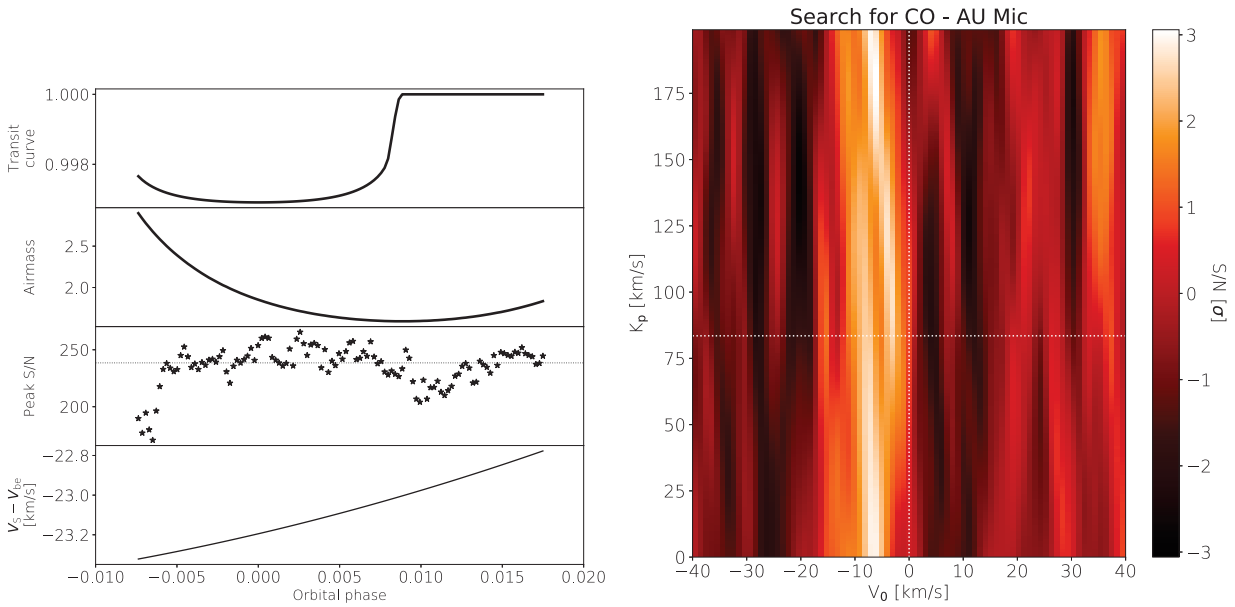

Figure 5.20 – *Left panel:* Transit light curve, airmass, peak S/N per pixel and RV shift from Geocentric to stellar rest frames during the June 2019 transit of AU Mic b. The figure properties are the same as in Figure 5.6. *Right panel:* S/N map obtained by jointly searching for CO in the atmosphere of AU Mic b in the 3 reddest SPIRou orders. The dotted lines indicate the orbital parameters expected for the planet from the RV analysis presented in Chapter 4 (i.e., $K_p = 83.5\,\mathrm{km\,s^{-1}}$ and $V_0 = 0\,\mathrm{km\,s^{-1}}$).

shown in the right panel of Figure 5.20. This signature is however polluted by strong correlations at $K_p \sim 200\,\mathrm{km\,s^{-1}}$, consistent with the signature produced by the RM effect (assuming a line profile of width $30\,\mathrm{km\,s^{-1}}$ see Section 3.3.1), and at $K_p \sim 0\,\mathrm{km\,s^{-1}}$, whose origin is unclear for now. Further investigations are need to correct for the RM effect and observe the CO signature of AU Mic b's atmosphere. Finally, we did not find any signature of He I in our reduced sequence of spectra yet.

6 | Conclusions and perspectives

This thesis was focused on providing constraints on the magnetic activity of low-mass stars in preparation for SPIRou observations and searches for planets. After conducting simulations to assess the ability of SPIRou to detect planets under nIR stellar activity RV signals, I investigated how spectropolarimetry could be used to constrain the distribution of bright/dark features and magnetic fields at the surface of the young M1 dwarf AU Mic and the low-mass stars Proxima Centauri, EPIC 211889233 and V471 Tau. By carrying out a spectropolarimetric and velocimetric analysis of AU Mic, we confirmed the ability of SPIRou to detect planets around active stars while simultaneously constraining their surface magnetic fields and associated activity. At the same time, I showed that SPIRou has the ability to constrain the atmosphere of close-in transiting giants which suggests that it could play a key role in paving the way for next-generation missions aiming at characterizing exoplanet atmospheres. All these studies allow us to identify challenges to overcome in the short and long term as well as promising prospects that will be investigated in the years to come.

Understanding the magnetic activity of M dwarfs

Although our knowledge of the magnetic fields of M dwarfs has kept growing up over the past 2 decades, the processes driving their generation and evolution remain unclear, especially for late fully-convective M dwarfs and PMS stars. Spectropolarimetric monitoring of these stars has the ability to probe the surface distribution of the large-scale magnetic field as well as the differential rotation shearing it. Our spectropolarimetric analysis of Proxima Centauri confirms that the large-scale magnetic topology of FC M dwarfs can be retrieved with ZDI. The long-term variations of the stellar magnetic properties constrained with ZDI (especially the degree of axisymmetry, fraction of poloidal energy, and field strength) are expected to yield key information about potential stellar magnetic cycles reflecting the dynamo processes at work in stellar interiors (see Lehmann et al., 2021). The recent commissioning of SPIRou and the forthcoming installation of state-of-the-art spectropolarimeters like SPIP (at Pic du Midi observatory) or CRIRES+ (at the VLT; Follert et al., 2014), offers the opportunity to monitor the magnetic properties of a sample of M dwarfs (from early to late types) over a few years (similarly to what was done in Donati et al., 2008b; Morin et al., 2008b, 2010, but on longer time scales). Such large program will allow to constrain how the evolution of the large-scale magnetic field depends on the spectral type and in particular whether FC M dwarfs exhibit similar dynamo processes than their partly convective counterparts.

Another way to investigate the magnetic properties of low-mass stars is to study specific magnetic-sensitive molecular lines. The decrease in temperature within spots allows for a few diatomic molecular lines to form therein, inducing signatures at optical and nIR wavelengths (see Afram & Berdyugina, 2015, and the references therein). Some of these lines, particularly sensitive to the magnetic field, have been shown to be excellent probes of the relative area, temperature and

magnetic field of stellar spots at the surface of M stars (especially TiO, for slow rotators, and FeH; e.g., Afram & Berdyugina, 2015, 2019). As star spots might reflect the surface magnetic field of the star (at least at the statistical level), this method stands out as a good complement to ZDI to constrain the magnetic activity of M dwarfs. The nIR domain offers a wealth of molecular lines whose formation processes and dependency to the magnetic field are yet unclear. Identifying the best nIR probes of star spots stands as one of the main challenge for future stellar characterizations with nIR high-resolution spectrographs. SPIRou, in particular, has the additional ability to detect linearly or circularly polarized Zeeman signatures at the spectral location of the most magnetically-sensitive molecular lines, once these have been identified. These signatures could be used to locally constrain the magnetic geometry and thereby complement ZDI reconstructions.

Finally, nIR high-resolution spectroscopy has the potential to access the surface distribution of the small-scale magnetic field (similarly to what was done on M dwarfs and T Tauri stars; e.g., Saar & Linsky, 1985; Valenti et al., 1995; Johns-Krull et al., 1999b). The increase in the Zeeman broadening from optical to nIR wavelengths makes it possible to monitor how the broadening of spectral lines with different Landé factors evolve with the rotation of the star. For example, by reconstructing the surface distributions of the relative brightness and small-scale field for lines with different Landé factors, one should in principle be able to disentangle between magnetically- and spot-induced distortions on the line profiles. This is particularly exciting as small-scale magnetic fields have been shown to be highly correlated to stellar activity RV signals (Haywood et al., 2020), and especially in the nIR as evidenced by our spectropolarimetric analysis of AU Mic. As this approach requires a full-size study in itself, we postpone it to a forthcoming analysis.

Improving the filtering of stellar activity RV jitter

Detecting the Doppler shifts induced by Earth twins on the spectra of their stellar host is now within reach of the new generation of high-precision velocimeters. In the optical, instruments like ESPRESSO (Pepe et al., 2010, 2020), EXPRES (Jurgenson et al., 2016) or the 3 HARPS spectrographs (Thompson et al., 2016) should soon have the precision required to detect Earth-like planets in the HZ of solar-like stars. In the nIR, SPIRou/SPIP (Donati et al., 2020a), GIANO (Claudi et al., 2017) or NIRPS (Wildi et al., 2017) will soon be able to unveil the potentially habitable planets orbiting the M dwarf population in the solar neighborhood. In both domains, the current main limitations arise from stellar activity and telluric contaminations on stellar lines. With the upcoming PLATO 2.0 mission (Rauer et al., 2014), it becomes crucial to come up with an efficient solution to accurately correct these signals in order to unveil the RV signatures of temperate Earth-like planets. Promising ideas have been recently proposed to achieve an unprecedented level of filtering of stellar activity and telluric RV contributions.

First of all, the Sun remains an excellent laboratory to better understand (i) the origin of stellar activity RV signals and (ii) the sensitivity of the activity indicators to stellar activity. Over the past 25 years, continuous monitorings of the Sun with the SOHO mission (Domingo et al., 1995) and its magnetograms (see Scherrer et al., 1995) allowed to precisely investigate the effects of different activity phenomena on the velocimetric detection of Earth like planets (Lagrange et al., 2010; Meunier et al., 2010; Meunier & Lagrange, 2013; Borgniet et al., 2015; Meunier et al., 2015). Over the past few years, high-precision velocimetric observations of the Sun, either from the reflection of the sunlight on asteroids (Haywood et al., 2016; Lanza et al., 2016), or in a more direct way using HARPS-N (Dumusque et al., 2015; Collier Cameron et al., 2019; Dumusque et al., 2020) and soon HARPS (through the HELIOS project, PI: Dumusque) allowed for an unprecedented understanding on the origin of the various stellar RV contributions. When coupled with the high-

resolution imagers and magnetograms of the Solar Dynamics Observatory (SDO; Pesnell et al., 2012), these RV observations offer the ability to identify the best indicators to filter stellar activity RV signals (e.g., the small-scale magnetic field; see Haywood et al., 2016, 2020). The huge amount of data that long-term solar observations will provide are expected to play a crucial role in reaching the extreme RV precision required by the search for HZ Earth-like planets around Sun-like stars (or at least in validating new RV extraction methods as proposed in Collier Cameron et al., 2020). Applying these results to other stars is not trivial though as the latter might exhibit activity phenomena driven by different dynamics (especially for late-type stars).

Hence the need to extensively monitor stars of various spectral types using different techniques in order to improve the modeling of their activity RV signals. As shown in Hébrard et al. (2016) and on EPIC 211889233 (Lopez, Klein et al., in prep.), obtaining simultaneously densely-sampled photometric, velocimetric and spectropolarimetric time-series of a given star is undoubtedly an encouraging way to constrain quasi-periodic RV signals. In particular, combining optical and nIR spectroscopic observations will yield a branch of activity indicators including the small-scale magnetic field, that could be compared to the surface distribution of bright/dark features and large-scale field provided by ZDI, offering the opportunity to implement physically-driven procedures to model stellar activity RV signals. The implementation of the technique applied to EPIC 211889233 to different types of stars should provide a solid basis to apply the results obtained from solar observations to other stars.

Finally, the very process of RV measurement, barely questioned until recently, can be advantageously rethought to include the filtering of tellurics and stellar activity. The RV value contains far less information that the average LSD line (or CCF), which itself contains less information that the whole spectrum itself. The detection of AU Mic b directly from the time series of Stokes I LSD profiles obtained in Chapter 4 provides a planet mass estimate consistent with that obtained from the RV modeling, but with a more physically-motivated approach. This result is promising as it suggests that planets could be directly unveiled from the average spectral line, even for slow rotators like EPIC 211889233. In particular, accounting for the evolution of surface features (and small-scale magnetic field) in the ZDI modeling process could provide a robust basis to unveil planetary signatures while correcting stellar activity contributions directly from the Stokes I LSD profiles. Exploratory data-driven methods to separate shift- (e.g., planet-induced) and shape-driven (i.e., activity-induced) variations of stellar line profiles yielded extreme precision RVs well-filtered from the activity contribution and is surely a promising way to (i) leverage the information present in the line profiles to filter stellar activity and (ii) come up with time series of optimal activity indicators to model RV time-series (e.g., using the GP framework of Rajpaul et al., 2015). Beyond that, tentative analyses of the sensitivity of each individual spectral line to stellar activity in order to identify the lines that are the most likely to unveil the planet signature give promising results (Dumusque, 2018; Cretignier et al., 2020). On the other hand, data-driven template-free methods have recently demonstrated their ability to accurately filter stellar activity and telluric contributions while extracting RVs from high-precision spectra of Sun-like stars (Rajpaul et al., 2020). Applying this technique to nIR SPIRou spectra could be interesting although the profusion of telluric lines will probably be more difficult to filter than at optical wavelengths.

Characterizing planetary systems of M dwarfs and PMS stars with SPIRou

The study of AU Mic described in Section 3.3.1 and Chapter 4 confirms the ability of SPIRou to carry out precise spectropolarimetric and velocimetric measurements of bright nearby active M dwarfs. In the specific case of low-mass PMS stars like AU Mic, observing in the nIR turns

out to a powerful advantage to disentangle planet and stellar activity RV contributions. As a consequence, the observations of K2-33 (Mann et al., 2016) and V1298 Tau (David et al., 2019a,b) conducted as part of the SLS WP2/WP3 are expected to yield mass measurements of the most massive close-in transiting planets (especially K2-33 b and V1298 Tau b), allowing to populate the MR diagram of close-in planets orbiting PMS stars. These stars exhibit long-lived spots inducing slowly-evolving stellar activity RV curves that might be particularly suited to be modeled, provided that the rotation curve of the stars is densely sampled over one observing season. On the other hand, obtaining precise RV measurement for these stars remain challenging as both targets remain faint in the nIR and require (i) long exposure times (typically several tens of minutes), quite difficult to obtain given the large amount of targets to be observed with SPIRou and (ii) to address the persistence on the detector which was also observed for targets like TRAPPIST-1. In addition, 1298 Tau features a relatively large $v \sin i$ of 23 km s^{-1} implying RV uncertainties of a few tens of m s^{-1} that will likely harm the planet mass measurement.

As SPIRou RV precision will be increased as a result of the continuous upgrades of the instrument, DRS and telluric correction process (see Donati et al., 2020a), increasingly fainter stars will be precisely monitored as parts of the WP1 and WP2. As demonstrated in the simulations presented in Chapter 2, both the planet orbital periods and the stellar rotation cycles must be densely sampled on the time scales on which stellar activity changes in order for the planet mass to be accurately measured. This is very costly in terms of telescope time, which is currently the main limitation for SPIRou RV follow-ups of stars like TRAPPIST-1 (in addition to persistence on the detector). Given that SPIRou cannot observe continuously (due to several instruments that do not operate simultaneously) and faces an important observing pressure, velocimetric follow-up of faint late-type stars harbouring a fast-evolving magnetic activity remain challenging for now. The forthcoming commissioning of SPIP at the Telescope Bernard Lyot at Pic du Midi Observatory is expected to provide a crucial back-up for SPIRou follow-up campaigns. SPIP will benefits from the experience acquired on SPIRou conception and implementation, allowing it to be quickly operational after its installation in 2021/2022. In a near future, the launch of the cubesat MARSU[1] (and potentially of other twins on the longer term) will provide continuous nIR photometric follow-up for some SLS targets, allowing to bring independent measurements of the stellar activity curve and to search for new transiting planets. Ideally, on a longer term, having a set of nIR and optical high-precision velocimeters and photometers longitudinally-distributed in both northern and southern hemispheres would definitely ensure a precise velocimetric and spectroscopic characterization of the most exciting planetary systems unveiled so far. On the longer term, one could even imagine precise RV measurements to be carried out from space as evidenced by recently proposed space-based missions (Plavchan et al., 2020a). However, this remains highly-speculative and ground-based velocimetry still has a very bright future in store.

As evidenced by the results obtained for HD 189733 b and AU Mic b (Moutou et al., 2020; Martioli et al., 2020a, and the atmospheric characterization presented in Chapter 5), SPIRou already appears as a key instrument to achieve a velocimetric and spectroscopic characterization of planets during their transit. Numerous planetary transits are to be observed as part of the SLS WP2, but also of other independent PI programs like ATMOSPHERIX. As our data reduction and modeling process improve, more accurate atmospheric characterizations will be carried out, enabling to yield priors on the best JWST, ARIEL and ELTs targets. SPIRou, thanks to its spectropolarimetric capabilities, has the additional potential to detect the polarization variability induced by the scattering of the star light in the atmosphere of transiting planets throughout their orbit (Berdyugina et al., 2008, 2011), allowing not only to constrain their orbital and atmospheric properties (Fluri & Berdyugina, 2010; Berdyugina et al., 2011), but also to constrain the position and size of features at the stellar surface (Kostogryz et al., 2015). This capability could be ingeniously exploited by

[1] https://www.csut.eu/marsu/

carrying out the SPIRou observations systematically in spectropolarimetric mode.

The future landscape of the search for exoplanets

Over the last few decades, exoplanetology has never stopped surprising us, with new exciting discoveries every year made possible by continuous improvements of instruments and post-analysis techniques. This trend is not expected to fade any time soon. We currently dispose of state-of-the-art photometers such as TESS, CHEOPS, SAINT-EX, MASCARA, ExTrA, SPECULOOS, NGTS, MEarth, and soon PLATO 2.0, that are able to search for transiting planets around nearby stars with an unrivalled precision. On the velocimetry side, extreme precision RV projects at visible wavelengths such as ESPRESSO, the three HARPS velocimeters (and their polarimetric modules) or EXPRES (see the state of the field of Fischer et al., 2016) will ensure robust ground-based detections of temperate Earth-mass planets around increasingly hotter stars. In the nIR, high-precision velocimeters like GIARPS, CARMENES, NIRPS, HPF, IRD, SPIRou and SPIP will soon acquire the required precision to detect and characterize the planet population in the solar neighborhood. Other exoplanet detection techniques like microgravitational lensing with WFIRST, astrometry with GAIA, and interferometry with GRAVITY are expected to detect a versatile range of exoplants, supplementing the exoplanet population unveiled from transit photometry and Doppler spectroscopy. In the years to come the characterization of exoplanet atmospheres will be governed from space by the JWST and ARIEL missions, and from the ground, with the advent of giant telescopes such as the ELTs, GMT and TMT.

Direct imaging is probably the domain which will experience the most phenomenal boom in the coming years. Over the past decade, direct imaging has proven to be a key technique to detect giant planets at large orbital distances from their host star (e.g., Marois et al., 2010; Lagrange et al., 2010). Currently operating state-of-the-art instruments such as SPHERE, GPI, Project 1640 and LBTI are expected to largely improve our knowledge of the formation and evolution of increasingly less massive and closer-in planets. Upcoming ambitious projects to combine the high-resolution spectroscopy of new generation giant telescopes like the HIRES spectrographs at the ELTs, and high-contrast imaging or interferometetry are expected to probe the presence of biosignatures in the atmospheres of Earth-like planets like Proxima-b (Snellen et al., 2015; Wang et al., 2017; Lovis et al., 2017; Hawker & Parry, 2019; Snellen et al., 2019) and even to potentially map their surface (Berdyugina & Kuhn, 2019). With all these efforts, it will not be surprising to detect biosignatures in the atmosphere of HZ planets in the decade to come. Confirming their biological origins will probably be an extremely difficult process requiring ambitious dedicated missions whose concepts lie beyond what we can conceive for now. To be continued...

> "We know they're extremely advanced technologically, which suggests - very rightfully so - that they're peaceful. An advanced civilization, by definition, is not barbaric."
>
> *Professor Donald Kessler, Mars Attacks!, 1996, Tim Burton*

Conclusions et perspectives

Cette thèse de doctorat visait à explorer l'activité magnétique des étoiles de faible masse en préparation des premières observations de SPIRou. Après avoir effectué des simulations pour évaluer la capacité de l'instrument à détecter des planètes en présence de signaux VR d'activité stellaire dans le nIR, j'ai étudié comment la spectropolarimétrie pouvait être mise à profit pour contraindre la distribution des taches et du champ magnétique à la surface des étoiles PSP de faibles masses (comme AU Microscopii) et des naines de faibles masses (Proxima Centauri, EPIC 211889233, V471 Tau). En effectuant une analyse spectropolarimétrique et vélocimétrique de la jeune étoile M1 AU Mic, nous avons confirmé la capacité de SPIRou à détecter des planètes autour d'étoiles actives tout en investiguant leurs champs magnétiques de surface. En parallèle, nous avons démontré que SPIRou avait la capacité de sonder l'atmosphère de planètes géantes en transit devant leur étoile hôte, suggérant ainsi que cet instrument pourrait jouer un rôle clé dans la préparation de la nouvelle génération de missions visant à caractériser les atmosphères des exoplanètes. Toutes ces différentes études nous permettent d'identifier des perspectives prometteuses pour SPIRou qui seront explorées dans les années à venir.

Comprendre l'activité magnétique des naines M

Bien que notre connaissance des champs magnétiques des étoiles PSP et des naines M n'ait cessé de s'améliorer au cours des dernières décennies, les processus à l'origine de leur génération et de leur évolution restent mystérieux, en particulier pour les étoiles dont l'intérieur est entièrement convectif. Le suivi spectropolarimétrique de ces étoiles permet d'investiguer la distribution surfacique du champ magnétique à grande échelle, ainsi que son cisaillement sous l'effet de la rotation différentielle. L'analyse spectropolarimétrique de Proxima Centauri que nous présentons dans ce manuscrit confirme que la topologie magnétique à grande échelle des naines M entièrement convectives en rotation lente peut être retrouvée en utilisant ZDI. Les variations à long terme des propriétés magnétiques stellaires prédites par ZDI (en particulier le degré de d'axisymétrie, la fraction d'énergie poloïdale et l'intensité du champ magnétique) devraient fournir des informations sur les cycles magnétiques stellaires potentiels et les processus de dynamo les alimentant (cf. Lehmann et al., en préparation). La mise en service récente de SPIRou ainsi que l'arrivée prochaine de spectropolarimètres de pointe comme SPIP (à l'observatoire du Pic du Midi de Bigorre) et CRIRES+ (au VLT ; Follert et al., 2014), offre la possibilité de monitorer les propriétés magnétiques d'un échantillon de naines M sur plusieurs années (de façon similaire aux travaux menés par Donati et al., 2008b; Morin et al., 2008b, 2010, mais sur des échelles de temps plus longues). Un programme aussi vaste permettra de mieux comprendre l'évolution du champ magnétique à grande échelle en fonction du type spectral et, en particulier, de savoir si le champ magnétique des étoiles de faible masse entièrement convectives est effectivement contrôlé par des processus de dynamo similaires à ceux de leurs homologues partiellement convectifs.

Une autre façon d'étudier les propriétés magnétiques des étoiles de faible masse consiste à analyser certaines raies moléculaires particulièrement sensibles au champ magnétique. La baisse de température à l'intérieur des taches stellaires conduit à l'apparition de certaines raies moléculaires diatomiques dans les domaines optique et proche infrarouge (voir Afram & Berdyugina, 2015, et les références qui y figurent). Certaines de ces raies, particulièrement sensibles au champ magnétique, se sont révélées être d'excellents indicateurs des propriétés des taches stellaires (e.g., surface relative, température, champ magnétique) à la surface des naines M et des étoiles jeunes de faibles masses (en particulier TiO, pour les étoiles en rotation lente, et FeH ; e.g., Afram & Berdyugina, 2015, 2019). Étant donné que les taches stellaires sont étroitement liées au champ magnétique de surface de l'étoile, cette méthode pourrait bien être un complément à ZDI pour mieux comprendre l'activité magnétique des étoiles PSP et des naines M. Le domaine du proche infrarouge offre une richesse de raies moléculaires dont les processus de formation et la dépendance au champ magnétique sont encore mal connus. L'identification des raies les plus propices à la caractérisation des taches stellaires est l'un des principaux défis à relever pour les spectrographes nIR à haute résolution. SPIRou, en particulier, a la capacité supplémentaire de détecter des signatures Zeeman polarisées linéairement ou circulairement à l'emplacement spectral des raies moléculaires les plus sensibles au champ magnétique, lorsque celles-ci auront étét identifiées. Ces signatures pourraient être utilisées pour contraindre localement la géométrie du champ magnétique, complétant ainsi les reconstructions ZDI.

Enfin, la spectroscopie nIR à haute résolution permet d'accéder à la distribution de surface du champ magnétique à petite échelle (à la manière de Saar & Linsky, 1985; Valenti et al., 1995; Johns-Krull, 1996). L'intensification de l'effet Zeeman dans le nIR permet d'explorer le lien entre l'élargissement des raies spectrales et le facteur de Landé. Par exemple, en reconstruisant les distributions de brillance relative et de champ magnétique à petite échelle à la surface de l'étoile à partir de raies de facteurs de Landé effectifs différents, nous devrions en principe être capable de séparer les contributions du champ magnétique de celles des taches stellaires sur les raies spectrales. Ceci est d'autant plus intéressant qu'il a été démontré que les champs magnétiques à petite échelle étaient fortement corrélés aux signaux VR de l'activité stellaire (Haywood et al., 2020), notamment dans le proche infrarouge comme démontré dans notre analyse spectropolarimétrique d'AU Mic. Comme cette approche nécessite une étude de grande envergure en soi, nous la reportons à une analyse ultérieure à court/moyen terme.

Améliorer le filtrage des signaux VR de l'activité stellaire

La détection des décalages Doppler induits par des planètes telluriques en orbite dans la ZH sur leur étoile hôte est désormais à la portée de la nouvelle génération de vélocimètres à haute précision. Dans le domaine optique, des instruments comme ESPRESSO (Pepe et al., 2010, 2020), EXPRES (Jurgenson et al., 2016) ou les 3 spectrographes HARPS (Thompson et al., 2016) devraient bientôt avoir la précision requise pour détecter des jumelles de la Terre autour d'analogues solaires. Dans le proche infrarouge, SPIRou/SPIP (Donati et al., 2020a), GIANO (Claudi et al., 2017) ou NIRPS (Wildi et al., 2017) pourront bientôt dévoiler les planètes potentiellement habitables en orbite autour des naines M du voisinage solaire. Dans les deux cas, les principales limitations actuelles proviennent de l'activité stellaire et des contaminations telluriques sur les lignes stellaires. Des idées prometteuses ont été récemment proposées pour atteindre un niveau de filtrage sans précédent de l'activité stellaire et des contributions telluriques en VR.

Tout d'abord, le Soleil est un excellent laboratoire pour mieux comprendre l'origine des signaux VR induits par l'activité stellaire et la sensibilité des indicateurs d'activité à cette dernière. Au

cours des 25 dernières années, l'observation continue du Soleil avec le satellite SOHO (Domingo et al., 1995) et ses magnétogrammes (see Scherrer et al., 1995) a permis de mener une étude approfondie des effets de différentes manifestations de l'activité stellaire sur la détection vélocimétrique de planètes semblables à la Terre (Lagrange et al., 2010; Meunier et al., 2010; Meunier & Lagrange, 2013; Borgniet et al., 2015; Meunier et al., 2015). Plus récemment, des études visant à mesurer précisément la VR du soleil, soit à partir de la réflexion de la lumière solaire sur des astéroïdes (Haywood et al., 2016; Lanza et al., 2016), soit de manière plus directe en utilisant le spectrographe HARPS-N (Dumusque et al., 2015; Collier Cameron et al., 2019; Dumusque et al., 2020) et bientôt HARPS (par le biais du projet HELIOS) permettent une compréhension accrue de l'origine des différentes contributions stellaires en VR. Ces observations, associées aux imageurs et magnétogrammes à haute résolution du télescope SDO (Pesnell et al., 2012), permettent d'identifier les meilleurs indicateurs pour filtrer les signaux VR induits par l'activité stellaire (e.g., le champ magnétique à petite échelle ; Haywood et al., 2016, 2020). L'énorme quantité de données que ces observations solaires fourniront sur le long terme devrait jouer un rôle décisif dans l'obtention de données VR d'extrême précision (i.e., $\sim 0.1\,\mathrm{m\,s^{-1}}$) requises par la recherche de planètes HZ semblables à la Terre autour d'étoiles solaires. L'application de ces résultats à d'autres étoiles n'est cependant pas triviale, ces dernières pouvant présenter des phénomènes d'activité gouvernées par des processus dynamiques différents (en particulier pour les étoiles entièrement convectives).

Il apparaît nécessaire d'observer abondamment des étoiles de types spectraux variés au moyen de techniques instrumentales complémentaires, afin d'améliorer la modélisation des signaux VR induits par leur activité magnétique. Comme démontré dans Hébrard et al. (2016) ainsi que dans l'analyse de l'étoile EPIC 211889233 présentée dans ce manuscrit (Lopez, Klein et al., en préparation), l'obtention simultanée de séries temporelles photométriques, vélocimétriques et spectropolarimétriques d'étoiles est sans aucun doute un moyen encourageant pour mieux modéliser les signaux VR quelles émettent. En particulier, la combinaison d'observations spectroscopiques/spectropolarimétrique dans les domaines optiques et nIR fournira un panel varié d'indicateurs d'activité pouvant être comparé aux distributions de taches et de champ magnétique à la surface de l'étoile prédites par ZDI, offrant ainsi la possibilité de mettre en œuvre de nouvelles techniques pour modéliser les signaux VR induits par l'activité stellaire.

Enfin, le processus même de mesure de la VR, à peine remis en question jusqu'à récemment, peut être avantageusement repensé pour y inclure le filtrage des contaminations de l'atmosphère terrestre et de l'activité stellaire. La mesure de VR contient beaucoup moins d'information que la raie LSD (ou CCF) moyenne, qui elle-même contient moins d'information que l'ensemble des raies du spectre. La détection de AU Mic b à partir de la modélisation des profils LSD en intensité présentée dans le chapitre 4 fournit une estimation de la masse de la planète conforme à celle obtenue à partir de la modélisation des séries temporelles de VR, mais avec une approche plus axée sur les processus physiques induisant des déformations sur la raie. Ce résultat est prometteur car il suggère que les planètes pourraient être directement détectées à partir des raies spectrales moyennes, et ce même pour des rotateurs lents comme EPIC 211889233. En particulier, la prise en compte de l'évolution des caractéristiques de surface (et du champ magnétique à petite échelle) dans le processus de modélisation ZDI pourrait fournir une base solide pour dévoiler les signatures planétaires tout en corrigeant les contributions de l'activité stellaire directement dans les profils LSD en intensité. Dans une optique encore plus ambitieuse, des analyses préliminaires visant à étudier la sensibilité de chaque raie spectrale individuelle à l'activité stellaire afin d'identifier les raies les plus adaptées pour dévoiler des signaux planétaires donnent des résultats prometteurs (Dumusque, 2018; Cretignier et al., 2020). D'autre part, des méthodes de calcul de VR sans catalogue de raies spectrales ont récemment démontré leur capacité à filtrer avec précision l'activité stellaire et les contributions telluriques sur des étoiles de type solaire (Rajpaul et al., 2020). L'application de cette technique aux spectres SPIRou dans le proche infrarouge pourrait être intéressante, bien que

le grand nombre de raies telluriques y sera probablement plus difficile à filtrer.

Caractériser les systèmes planétaires des naines M et des étoiles jeunes avec SPIRou

L'étude de l'étoile AU Mic que nous présentons dans ce manuscrit (dans les chapitres 3 et 4) confirme que SPIRou est en capacité d'effectuer des mesures spectropolarimétriques et vélocimétriques précises de naines M brillantes actives du voisinage solaire. Dans le cas spécifique des étoiles PSP de faible masse comme AU Mic, l'observation dans le proche infrarouge s'avère être un avantage décisif pour séparer les contributions VR des planètes et de l'activité stellaire. Par conséquent, les observations de K2-33 (Mann et al., 2016) et V1298 Tau (David et al., 2019a,b) menées dans le cadre du SLS WP2/WP3 devraient fournir des mesures de masse pour les planètes les plus massives de ces systèmes (en particulier K2-33 b et V1298 Tau b), permettant de remplir le diagramme masse-rayon des planètes en orbite autour d'étoiles PSP. Ces étoiles présentent en effet des taches à longue durée de vie induisant des courbes VR dont la modélisation semble relativement abordable, à condition que la courbe de rotation des étoiles soit échantillonnée de manière dense sur une saison d'observation. Toutefois, l'obtention d'une mesure précise de la VR de ces étoiles reste difficile, V1298 Tau, à cause de son grand $v \sin i$ de $23\,\mathrm{km\,s^{-1}}$ et, K2-33, à cause de sa faible luminosité dans la bande H et des problèmes de persistance sur le détecteur qui y sont associés (Donati et al., 2020a).

À mesure que la précision en VR de SPIRou augmentera sous l'effet des mises à jour continues de l'instrument, de l'algorithme de réduction de données, et du processus de correction des raies telluriques, des étoiles de moins en moins brillantes pourront être observées avec précision dans le cadre des WP1 et WP2 du large programme d'observation de SPIRou. Comme le démontrent les simulations présentées au chapitre 2, le cicle de rotation stellaire ainsi que la période orbitale des planètes doivent être échantillonnés de manière dense sur les échelles de temps sur lesquelles l'activité stellaire évolue afin que les masses des planètes puissent être mesurées avec précision. Cela est cependant très coûteux en terme de temps de télescope, ce qui représente la principale limitation des suivis en VR d'étoiles comme TRAPPIST-1 avec SPIRou. La mise en service de SPIP au télescope Bernard Lyot de l'observatoire du Pic du Midi devrait fournir un soutien crucial pour les campagnes de suivi vélocimétriques de SPIRou. SPIP bénéficiera de l'expérience acquise lors de la conception et de la mise en œuvre de SPIRou, ce qui lui permettra d'être rapidement opérationnel après son installation en 2021.

Dans les années à venir, le lancement du cubesat MARSU[2] (et potentiellement d'autres jumeaux à plus long terme) permettra de réaliser un suivi photométrique nIR continu de cibles du large programme d'observation de SPIRou, apportant ainsi des contraintes indépendantes de la VR sur la courbe d'activité stellaire et la recherche de potentiels transits planétaires devant les étoiles observées. Idéalement, à plus long terme, un ensemble de vélocimètres et de photomètres nIR et optiques à haute précision, distribué longitudinalement dans les hémisphères nord et sud, permettrait certainement d'assurer une caractérisation vélocimétrique et spectroscopique précise des systèmes planétaires les plus intéressants dévoilés à ce jour. À beaucoup plus long terme, il pourrait même être envisagé d'effectuer des mesures précises de VR depuis l'espace, comme en témoignent les projets de missions spatiales récemment proposées (Plavchan et al., 2020a). Cependant, cela reste très spéculatif et la vélocimétrie au sol a encore un bel avenir devant elle.

Fort des résultats obtenus pour HD 189733 b et AU Mic b (cf. Moutou et al., 2020; Martioli et al., 2020a, et la caractérisation atmosphérique présentée au chapitre 5), SPIRou apparaît comme un instrument prometteur pour assurer une caractérisation vélocimétrique et spectroscopique des

[2] https://www.csut.eu/marsu/

planètes pendant leur transit. De nombreux transits planétaires vont être observés dans le cadre du SLS WP2, mais aussi dans le cadre de programmes PI indépendants comme ATMOSPHERIX. À mesure que notre procédure de réduction de données et de modélisation atmosphérique s'etoffera, des caractérisations atmosphériques plus précises pourront être effectuées, permettant ainsi d'obtenir des informations cruciales sur les futures cibles du JWST, d'ARIEL et des ELTs. SPIRou, fort de ses capacités spectropolarimétriques, a le potentiel supplémentaire de détecter la variabilité de la polarisation induite par la diffusion de la lumière stellaire dans l'atmosphère des planètes lors de leur transit et sur l'ensemble de leur orbite (Berdyugina et al., 2008, 2011), permettant non seulement de contraindre leurs propriétés orbitales et atmosphériques (Fluri & Berdyugina, 2010; Berdyugina et al., 2011), mais aussi de sonder la distribution de taches à la surface stellaire (Kostogryz et al., 2015).

Le future paysage de la recherche exoplanétaire

Au cours des dernières décennies, l'exoplanétologie n'a cessé de nous surprendre, avec de nouvelles découvertes passionnantes chaque année, rendues possibles par l'amélioration continue des instruments et des techniques de post-analyse. Cette tendance ne devrait pas s'atténuer de sitôt. Nous disposons actuellement de photomètres de pointe tels que TESS, CHEOPS, SAINT-EX, MASCARA, ExTrA, SPECULOOS, NGTS, MEarth, et bientôt PLATO 2.0, qui sont capables de rechercher des planètes en transit autour d'étoiles proches avec une précision inégalée. Du côté de la vélocimétrie dans le domaine optique, l'extrême précision en VR convoitées par des spectrographes comme ESPRESSO, les trois vélocimètres HARPS (et leurs modules polarimétriques) ou EXPRES (see the state of the field of Fischer et al., 2016) permettra d'assurer une détection robuste de planètes de masse terrestre en orbite dans la zone habitable d'étoiles de plus en plus chaudes. Dans le proche infrarouge, des vélocimètres de haute précision comme GIARPS, CARMENES, NIRPS, HPF, IRD, SPIRou et SPIP acquerront bientôt la précision requise pour détecter et caractériser la population de planètes autour des naines M dans le voisinage du soleil. D'autres techniques de détection d'exoplanètes, comme les micro-lentilles gravitationelles (avec WFIRST), l'astrométrie (avec GAIA) et l'interférométrie (avec GRAVITY), devraient permettre de détecter une gamme variée d'exoplanètes, complétant ainsi la population d'exoplanètes révélée par la photométrie de transit, la spectroscopie Doppler et l'imagerie directe. Dans les années à venir, la caractérisation des atmosphères des exoplanètes sera régie depuis l'espace par les missions JWST et ARIEL, et depuis le sol, avec l'avènement de télescopes géants tels que les ELTs, GMT et TMT.

L'imagerie directe est probablement le domaine qui connaîtra l'essor le plus phénoménal dans les années à venir. Au cours de la dernière décennie, cette technique de détection s'est avérée efficace pour détecter des planètes géantes à de larges distances orbitales de leur étoile hôte (e.g., Marois et al., 2010; Lagrange et al., 2010). Les instruments de pointe actuellement en service, tels que SPHERE, GPI, le projet 1640 et LBTI, devraient améliorer considérablement nos connaissances sur la formation et l'évolution de planètes de moins en moins massives et de plus en plus proches de leur étoile hôte. Des projets ambitieux, visant à combiner la spectroscopie à haute résolution des télescopes géants de nouvelle génération comme les spectrographes HIRES des ELTs, et l'imagerie à fort contraste ou l'interférométrie, devraient permettre de sonder la présence de biosignatures dans l'atmosphère de planètes proches semblables à la Terre comme Proxima-b (Snellen et al., 2015; Wang et al., 2017; Lovis et al., 2017; Hawker & Parry, 2019; Snellen et al., 2019) voire même de cartographier leur surface (Berdyugina & Kuhn, 2019). Avec tous ces efforts, il ne sera pas surprenant de détecter des biosignatures dans l'atmosphère des planètes HZ dans la décennie à venir. Confirmer leur origine biologique sera probablement un processus extrêmement difficile qui

nécessitera des missions ambitieuses dont les concepts dépassent ce que nous pouvons concevoir pour l'instant. A suivre dans le prochain épisode.

Bibliography

ALMA Partnership et al., 2015, ApJ, 808, L3
Abreu J. A., Beer J., Ferriz-Mas A., McCracken K. G., Steinhilber F., 2012, A&A, 548, A88
Addison B. C., et al., 2020, arXiv e-prints, p. arXiv:2006.13675
Aerts C., Christensen-Dalsgaard J., Kurtz D. W., 2010, Asteroseismology
Afram N., Berdyugina S. V., 2015, A&A, 576, A34
Afram N., Berdyugina S. V., 2019, A&A, 629, A83
Afram N., Berdyugina S. V., Fluri D. M., Solanki S. K., Lagg A., 2008, A&A, 482, 387
Agol E., Steffen J., Sari R., Clarkson W., 2005, MNRAS, 359, 567
Agol E., Cowan N. B., Bushong J., Knutson H., Charbonneau D., Deming D., Steffen J. H., 2009, in Pont F., Sasselov D., Holman M. J., eds, IAU Symposium Vol. 253, Transiting Planets. pp 209–215 (arXiv:0807.2434), doi:10.1017/S1743921308026422
Agol E., et al., 2020, arXiv e-prints, p. arXiv:2010.01074
Aigrain S., Pont F., Zucker S., 2012, MNRAS, 419, 3147
Albrecht S., et al., 2012, ApJ, 757, 18
Alibert Y., Mordasini C., Benz W., Winisdoerffer C., 2005, A&A, 434, 343
Alibert Y., Mordasini C., Benz W., 2011, A&A, 526, A63
Allart R., et al., 2018, Science, 362, 1384
Alonso-Floriano F. J., et al., 2019, A&A, 621, A74
Anders E., Grevesse N., 1989, Geochimica Cosmochimica Acta, 53, 197
André P., et al., 2010, A&A, 518, L102
André P., Di Francesco J., Ward-Thompson D., Inutsuka S. I., Pudritz R. E., Pineda J. E., 2014, in Beuther H., Klessen R. S., Dullemond C. P., Henning T., eds, Protostars and Planets VI. p. 27 (arXiv:1312.6232), doi:10.2458/azu_uapress_9780816531240-ch002
Andrews S. M., Wilner D. J., Hughes A. M., Qi C., Dullemond C. P., 2010, ApJ, 723, 1241
Andrews S. M., et al., 2016, ApJ, 820, L40
Anglada-Escudé G., Butler R. P., 2012, ApJS, 200, 15
Anglada-Escudé G., et al., 2016, Nature, 536, 437
Applegate J. H., 1992, ApJ, 385, 621
Armitage P. J., 2011, ARA&A, 49, 195
Armitage P. J., 2015, arXiv e-prints, p. arXiv:1509.06382
Armitage P. J., 2018, A Brief Overview of Planet Formation. p. 135, doi:10.1007/978-3-319-55333-7_135
Artigau É., et al., 2014, in Proc. SPIE. p. 914905 (arXiv:1406.6927), doi:10.1117/12.2056385
Artigau É., Saint-Antoine J., Lévesque P.-L., Vallée P., Doyon R., Hernandez O., Moutou C., 2018, in High Energy, Optical, and Infrared Detectors for Astronomy VIII. p. 107091P, doi:10.1117/12.2314475
Arzoumanian D., et al., 2011, A&A, 529, L6
Arzoumanian D., André P., Peretto N., Könyves V., 2013, A&A, 553, A119
Arzoumanian D., Shimajiri Y., Inutsuka S.-i., Inoue T., Tachihara K., 2018, PASJ, 70, 96

Astudillo-Defru N., et al., 2015, A&A, 575, A119
Astudillo-Defru N., Delfosse X., Bonfils X., Forveille T., Lovis C., Rameau J., 2017a, A&A, 600, A13
Astudillo-Defru N., et al., 2017b, A&A, 602, A88
Auvergne M., et al., 2009, A&A, 506, 411
Babcock H. W., 1961, ApJ, 133, 572
Bae J., Nelson R. P., Hartmann L., 2016, ApJ, 833, 126
Bagnulo S., Landolfi M., Landstreet J. D., Land i Degl'Innocenti E., Fossati L., Sterzik M., 2009, PASP, 121, 993
Bakos G., Noyes R. W., Kovács G., Stanek K. Z., Sasselov D. D., Domsa I., 2004, PASP, 116, 266
Bakos G. Á., et al., 2010, ApJ, 710, 1724
Bally J., 2016, ARA&A, 54, 491
Baluev R. V., 2008, MNRAS, 385, 1279
Baluev R. V., 2015, MNRAS, 446, 1478
Baraffe I., Chabrier G., Allard F., Hauschildt P. H., 1998, A&A, 337, 403
Baraffe I., Chabrier G., Fortney J., Sotin C., 2014, in Beuther H., Klessen R. S., Dullemond C. P., Henning T., eds, Protostars and Planets VI. p. 763 (arXiv:1401.4738), doi:10.2458/azu_uapress_9780816531240-ch033
Baraffe I., Homeier D., Allard F., Chabrier G., 2015, A&A, 577, A42
Baranne A., et al., 1996, A&AS, 119, 373
Barnes J. R., Collier Cameron A., Donati J. F., James D. J., Marsden S. C., Petit P., 2005, MNRAS, 357, L1
Barnes J. R., Jeffers S. V., Jones H. R. A., Pavlenko Y. V., Jenkins J. S., Haswell C. A., Lohr M. E., 2015, ApJ, 812, 42
Barnes R., et al., 2016, arXiv e-prints, p. arXiv:1608.06919
Baroch D., et al., 2020, arXiv e-prints, p. arXiv:2006.16608
Barstow J. K., Irwin P. G. J., 2016, MNRAS, 461, L92
Baruteau C., et al., 2014, in Beuther H., Klessen R. S., Dullemond C. P., Henning T., eds, Protostars and Planets VI. p. 667 (arXiv:1312.4293), doi:10.2458/azu_uapress_9780816531240-ch029
Baruteau C., Bai X., Mordasini C., Mollière P., 2016, Space Sci. Rev., 205, 77
Basri G., et al., 2010, ApJ, 713, L155
Batalha N. E., Lewis T., Fortney J. J., Batalha N. M., Kempton E., Lewis N. K., Line M. R., 2019, ApJ, 885, L25
Baudino J. L., Bézard B., Boccaletti A., Bonnefoy M., Lagrange A. M., Galicher R., 2015, A&A, 582, A83
Bazot M., Christensen-Dalsgaard J., Gizon L., Benomar O., 2016, MNRAS, 460, 1254
Beech M., 2019, Introducing the Stars
Beeck B., Schüssler M., Cameron R. H., Reiners A., 2015, A&A, 581, A42
Bell C. P. M., Naylor T., Mayne N. J., Jeffries R. D., Littlefair S. P., 2013, MNRAS, 434, 806
Bell C. P. M., Mamajek E. E., Naylor T., 2015, MNRAS, 454, 593
Benisty M., et al., 2015, A&A, 578, L6
Benneke B., et al., 2019, ApJ, 887, L14
Benz A. O., 2017, Living Reviews in Solar Physics, 14, 2
Berdyugina S. V., 2005, Living Reviews in Solar Physics, 2, 8
Berdyugina S. V., Kuhn J. R., 2019, AJ, 158, 246
Berdyugina S. V., Solanki S. K., 2002, A&A, 385, 701
Berdyugina S. V., Solanki S. K., Frutiger C., 2003, A&A, 412, 513

Berdyugina S. V., Petit P., Fluri D. M., Afram N., Arnaud J., 2006, in Casini R., Lites B. W., eds, Astronomical Society of the Pacific Conference Series Vol. 358, Solar Polarization 4. p. 381 (arXiv:astro-ph/0703560)
Berdyugina S. V., Berdyugin A. V., Fluri D. M., Piirola V., 2008, ApJ, 673, L83
Berdyugina S. V., Berdyugin A. V., Fluri D. M., Piirola V., 2011, ApJ, 728, L6
Berta-Thompson Z. K., et al., 2015, Nature, 527, 204
Bessell M. S., 1991, AJ, 101, 662
Bessolaz N., Zanni C., Ferreira J., Keppens R., Bouvier J., 2008, A&A, 478, 155
Beuzit J.-L., et al., 2008, in Ground-based and Airborne Instrumentation for Astronomy II. p. 701418, doi:10.1117/12.790120
Biddle L. I., Llama J., Cameron A., Prato L., Jardine M., Johns-Krull C. M., 2021, ApJ, 906, 113
Birkby J. L., 2018, arXiv e-prints, p. arXiv:1806.04617
Birkby J. L., de Kok R. J., Brogi M., de Mooij E. J. W., Schwarz H., Albrecht S., Snellen I. A. G., 2013, MNRAS, 436, L35
Birkby J. L., de Kok R. J., Brogi M., Schwarz H., Snellen I. A. G., 2017, AJ, 153, 138
Bitsch B., Morbidelli A., Lega E., Kretke K., Crida A., 2014, A&A, 570, A75
Bitsch B., Izidoro A., Johansen A., Raymond S. N., Morbidelli A., Lambrechts M., Jacobson S. A., 2019, A&A, 623, A88
Boccaletti A., et al., 2015, Nature, 526, 230
Boccaletti A., et al., 2018, A&A, 614, A52
Bodenheimer P. H., 2011, Principles of Star Formation, doi:10.1007/978-3-642-15063-0.
Bohn A. J., et al., 2020, MNRAS, 492, 431
Boisse I., et al., 2009, A&A, 495, 959
Boisse I., Bonfils X., Santos N. C., 2012, A&A, 545, A109
Bolmont E., 2018, Habitability in Brown Dwarf Systems. p. 62, doi:10.1007/978-3-319-55333-7_62
Bolmont E., Mathis S., 2016, Celestial Mechanics and Dynamical Astronomy, 126, 275
Bolmont E., Selsis F., Owen J. E., Ribas I., Raymond S. N., Leconte J., Gillon M., 2017, MNRAS, 464, 3728
Bonfils X., et al., 2007, A&A, 474, 293
Bonfils X., et al., 2013, A&A, 549, A109
Bonfils X., et al., 2015, in Techniques and Instrumentation for Detection of Exoplanets VII. p. 96051L (arXiv:1508.06601), doi:10.1117/12.2186999
Borgniet S., Meunier N., Lagrange A. M., 2015, A&A, 581, A133
Borucki W. J., et al., 2010, Science, 327, 977
Bouchy F., Carrier F., 2002, A&A, 390, 205
Bouchy F., Pepe F., Queloz D., 2001, A&A, 374, 733
Bouchy F., et al., 2005, A&A, 444, L15
Bouchy F., et al., 2017, The Messenger, 169, 21
Bourrier V., Lecavelier des Etangs A., 2013, A&A, 557, A124
Bourrier V., Lecavelier des Etangs A., Ehrenreich D., Tanaka Y. A., Vidotto A. A., 2016, A&A, 591, A121
Bourrier V., et al., 2017, AJ, 154, 121
Bouvier J., Bertout C., 1989, A&A, 211, 99
Bouvier J., Forestini M., Allain S., 1997, A&A, 326, 1023
Bouvier J., Alencar S. H. P., Harries T. J., Johns-Krull C. M., Romanova M. M., 2007, in Reipurth B., Jewitt D., Keil K., eds, Protostars and Planets V. p. 479 (arXiv:astro-ph/0603498)
Bouvier J., Matt S. P., Mohanty S., Scholz A., Stassun K. G., Zanni C., 2014, in Beuther H., Klessen R. S., Dullemond C. P., Henning T., eds, Protostars and Planets VI. p. 433 (arXiv:1309.7851), doi:10.2458/azu_uapress_9780816531240-ch019

Bowler B. P., 2016, PASP, 128, 102001
Brewer B. J., 2014, arXiv e-prints, p. arXiv:1411.3921
Brewer B. J., Pártay L. B., Csányi G., 2009, arXiv e-prints, p. arXiv:0912.2380
Brogi M., Line M. R., 2019, AJ, 157, 114
Brogi M., Snellen I. A. G., de Kok R. J., Albrecht S., Birkby J., de Mooij E. J. W., 2012, Nature, 486, 502
Brogi M., Snellen I. A. G., de Kok R. J., Albrecht S., Birkby J. L., de Mooij E. J. W., 2013, ApJ, 767, 27
Brogi M., de Kok R. J., Birkby J. L., Schwarz H., Snellen I. A. G., 2014, A&A, 565, A124
Brogi M., de Kok R. J., Albrecht S., Snellen I. A. G., Birkby J. L., Schwarz H., 2016, ApJ, 817, 106
Brogi M., Line M., Bean J., Désert J. M., Schwarz H., 2017, ApJ, 839, L2
Brogi M., Giacobbe P., Guilluy G., de Kok R. J., Sozzetti A., Mancini L., Bonomo A. S., 2018, A&A, 615, A16
Brown T. M., 2001, ApJ, 553, 1006
Brown S. F., Donati J. F., Rees D. E., Semel M., 1991, A&A, 250, 463
Brown B. P., Browning M. K., Brun A. S., Miesch M. S., Toomre J., 2010, ApJ, 711, 424
Browning M. K., 2008, ApJ, 676, 1262
Browning M. K., Miesch M. S., Brun A. S., Toomre J., 2006, ApJ, 648, L157
Brun A. S., Miesch M. S., Toomre J., 2004, ApJ, 614, 1073
Bryan M. L., et al., 2016, ApJ, 821, 89
Burgasser A. J., Mamajek E. E., 2017, ApJ, 845, 110
Burrows A., et al., 1997, ApJ, 491, 856
Burt J., Holden B., Wolfgang A., Bouma L. G., 2018, AJ, 156, 255
Butler R. P., Marcy G. W., Williams E., McCarthy C., Dosanjh P., Vogt S. S., 1996, PASP, 108, 500
Cabot S. H. C., Madhusudhan N., Hawker G. A., Gandhi S., 2019, MNRAS, 482, 4422
Caldas A., Leconte J., Selsis F., Waldmann I. P., Bordé P., Rocchetto M., Charnay B., 2019, A&A, 623, A161
Campbell B., Walker G. A. H., 1979, PASP, 91, 540
Carmona A., 2010, Earth Moon and Planets, 106, 71
Carolan S., Vidotto A. A., Plavchan P., D'Angelo C. V., Hazra G., 2020, MNRAS,
Casasayas-Barris N., et al., 2020, A&A, 635, A206
Cegla H. M., Lovis C., Bourrier V., Beeck B., Watson C. A., Pepe F., 2016, A&A, 588, A127
Chabrier G., Küker M., 2006, A&A, 446, 1027
Chandrasekhar S., 1961, Hydrodynamic and hydromagnetic stability
Charbonneau D., Brown T. M., Latham D. W., Mayor M., 2000, ApJ, 529, L45
Charbonneau D., Brown T. M., Noyes R. W., Gilliland R. L., 2002, ApJ, 568, 377
Charbonneau D., et al., 2005, ApJ, 626, 523
Charbonneau D., Knutson H. A., Barman T., Allen L. E., Mayor M., Megeath S. T., Queloz D., Udry S., 2008, ApJ, 686, 1341
Charbonneau D., et al., 2009, Nature, 462, 891
Chatterjee S., Ford E. B., Matsumura S., Rasio F. A., 2008, ApJ, 686, 580
Chauvin G., Lagrange A. M., Dumas C., Zuckerman B., Mouillet D., Song I., Beuzit J. L., Lowrance P., 2004, A&A, 425, L29
Chiang E., Fung J., 2017, ApJ, 848, 4
Chiavassa A., Brogi M., 2019, A&A, 631, A100
Chib S., Jeliazkov I., 2001, J. Amer. Statist. Assoc., 96, 270
Christensen-Dalsgaard J., 2004, Sol. Phys., 220, 137

Claret A., 2018, A&A, 618, A20
Claret A., Hauschildt P. H., Witte S., 2012, A&A, 546, A14
Claudi R., et al., 2017, European Physical Journal Plus, 132, 364
Cloutier R., et al., 2018, AJ, 155, 93
Cockell C. S., et al., 2016, Astrobiology, 16, 89
Coleman G. A. L., Papaloizou J. C. B., Nelson R. P., 2017, MNRAS, 470, 3206
Coleman G. A. L., Leleu A., Alibert Y., Benz W., 2019, A&A, 631, A7
Collier Cameron A., Robinson R. D., 1989, MNRAS, 236, 57
Collier Cameron A., Bruce V. A., Miller G. R. M., Triaud A. H. M. J., Queloz D., 2010, MNRAS, 403, 151
Collier Cameron A., et al., 2019, MNRAS, 487, 1082
Collier Cameron A., et al., 2020, arXiv e-prints, p. arXiv:2011.00018
Cosentino R., et al., 2012, in Proc. SPIE. p. 84461V, doi:10.1117/12.925738
Cotera A. S., et al., 2001, ApJ, 556, 958
Cretignier M., Dumusque X., Allart R., Pepe F., Lovis C., 2020, A&A, 633, A76
Crida A., Morbidelli A., Masset F., 2006, Icarus, 181, 587
Crockett C. J., Mahmud N. I., Prato L., Johns-Krull C. M., Jaffe D. T., Hartigan P. M., Beichman C. A., 2012, ApJ, 761, 164
Crutcher R. M., 2012, ARA&A, 50, 29
Cumming A., 2004, MNRAS, 354, 1165
Cuntz M., Saar S. H., Musielak Z. E., 2000, ApJ, 533, L151
Currie T., Daemgen S., Debes J., Lafreniere D., Itoh Y., Jayawardhana R., Ratzka T., Correia S., 2014, ApJ, 780, L30
Cutri R. M., et al., 2003, 2MASS All Sky Catalog of point sources.
Czesla S., Schröter S., Schneider C. P., Huber K. F., Pfeifer F., Andreasen D. T., Zechmeister M., 2019, PyA: Python astronomy-related packages (ascl:1906.010)
Daley C., et al., 2019, ApJ, 875, 87
Damasso M., Del Sordo F., 2020, MNRAS, 494, 1387
Damasso M., Pinamonti M., Scandariato G., Sozzetti A., 2019, MNRAS, 489, 2555
Damasso M., et al., 2020, Science Advances, 6, eaax7467
Davenport J. R. A., Kipping D. M., Sasselov D., Matthews J. M., Cameron C., 2016, ApJ, 829, L31
David T. J., Hillenbrand L. A., Cody A. M., Carpenter J. M., Howard A. W., 2016, ApJ, 816, 21
David T. J., et al., 2019a, AJ, 158, 79
David T. J., Petigura E. A., Luger R., Foreman-Mackey D., Livingston J. H., Mamajek E. E., Hillenbrand L. A., 2019b, ApJ, 885, L12
Dawson R. I., Johnson J. A., 2018, ARA&A, 56, 175
Debras F., Mayne N., Baraffe I., Jaupart E., Mourier P., Laibe G., Goffrey T., Thuburn J., 2020, A&A, 633, A2
Delfosse X., Forveille T., Ségransan D., Beuzit J. L., Udry S., Perrier C., Mayor M., 2000, A&A, 364, 217
Delisle J. B., et al., 2018, A&A, 614, A133
Delrez L., et al., 2018, MNRAS, 475, 3577
Deming D., Seager S., Richardson L. J., Harrington J., 2005, Nature, 434, 740
Deming D., et al., 2009, PASP, 121, 952
Demory B.-O., et al., 2016, Nature, 532, 207
Des Marais D. J., et al., 2002, Astrobiology, 2, 153
Désert J.-M., et al., 2011, ApJS, 197, 11
Desort M., Lagrange A. M., Galland F., Udry S., Mayor M., 2007, A&A, 473, 983

Deupree R. G., 1996, ApJ, 471, 377
Díaz R. F., Almenara J. M., Santerne A., Moutou C., Lethuillier A., Deleuil M., 2014, MNRAS, 441, 983
Dittmann J. A., et al., 2017, Nature, 544, 333
Dobler W., Stix M., Brandenburg A., 2006, ApJ, 638, 336
Domingo V., Fleck B., Poland A. I., 1995, Sol. Phys., 162, 1
Donati J. F., 2001, Imaging the Magnetic Topologies of Cool Active Stars. p. 207
Donati J. F., Brown S. F., 1997, A&A, 326, 1135
Donati J. F., Landstreet J. D., 2009, ARA&A, 47, 333
Donati J. F., Semel M., Praderie F., 1989, A&A, 225, 467
Donati J. F., Brown S. F., Semel M., Rees D. E., Dempsey R. C., Matthews J. M., Henry G. W., Hall D. S., 1992, A&A, 265, 682
Donati J. F., Semel M., Carter B. D., Rees D. E., Collier Cameron A., 1997, MNRAS, 291, 658
Donati J. F., Mengel M., Carter B. D., Marsden S., Collier Cameron A., Wichmann R., 2000, MNRAS, 316, 699
Donati J. F., Collier Cameron A., Petit P., 2003, MNRAS, 345, 1187
Donati J.-F., Forveille T., Collier Cameron A., Barnes J. R., Delfosse X., Jardine M. M., Valenti J. A., 2006a, Science, 311, 633
Donati J. F., Catala C., Landstreet J. D., Petit P., 2006b, in Casini R., Lites B. W., eds, Astronomical Society of the Pacific Conference Series Vol. 358, Solar Polarization 4. p. 362
Donati J. F., et al., 2006c, MNRAS, 370, 629
Donati J. F., et al., 2007, MNRAS, 380, 1297
Donati J. F., et al., 2008a, MNRAS, 386, 1234
Donati J. F., et al., 2008b, MNRAS, 390, 545
Donati J. F., et al., 2010, MNRAS, 409, 1347
Donati J. F., et al., 2011a, MNRAS, 417, 472
Donati J. F., et al., 2011b, MNRAS, 417, 1747
Donati J. F., et al., 2012, MNRAS, 425, 2948
Donati J. F., et al., 2014, MNRAS, 444, 3220
Donati J. F., et al., 2015, MNRAS, 453, 3706
Donati J. F., et al., 2016, Nature, 534, 662
Donati J.-F., et al., 2018, SPIRou: A NIR Spectropolarimeter/High-Precision Velocimeter for the CFHT. p. 107, doi:10.1007/978-3-319-55333-7_107
Donati J. F., et al., 2020a, arXiv e-prints, p. arXiv:2008.08949
Donati J. F., et al., 2020b, MNRAS, 491, 5660
Dong S., Xie J.-W., Zhou J.-L., Zheng Z., Luo A., 2018, Proceedings of the National Academy of Science, 115, 266
Dorn C., Khan A., Heng K., Connolly J. A. D., Alibert Y., Benz W., Tackley P., 2015, A&A, 577, A83
Dorn C., Mosegaard K., Grimm S. L., Alibert Y., 2018, ApJ, 865, 20
Dressing C. D., Charbonneau D., 2015, ApJ, 807, 45
Drummond B., Tremblin P., Baraffe I., Amundsen D. S., Mayne N. J., Venot O., Goyal J., 2016, A&A, 594, A69
Drummond B., Carter A. L., Hébrard E., Mayne N. J., Sing D. K., Evans T. M., Goyal J., 2019, MNRAS, 486, 1123
Drummond B., et al., 2020, A&A, 636, A68
Ducrot E., et al., 2018, AJ, 156, 218
Ducrot E., et al., 2020, arXiv e-prints, p. arXiv:2006.13826
Dumusque X., 2018, A&A, 620, A47

Dumusque X., Lovis C., Udry S., Santos N. C., 2011a, in Sozzetti A., Lattanzi M. G., Boss A. P., eds, IAU Symposium Vol. 276, The Astrophysics of Planetary Systems: Formation, Structure, and Dynamical Evolution. pp 530–532 (arXiv:1011.5581), doi:10.1017/S1743921311021090
Dumusque X., Udry S., Lovis C., Santos N. C., Monteiro M. J. P. F. G., 2011b, A&A, 525, A140
Dumusque X., Santos N. C., Udry S., Lovis C., Bonfils X., 2011c, A&A, 527, A82
Dumusque X., Boisse I., Santos N. C., 2014, ApJ, 796, 132
Dumusque X., et al., 2015, ApJ, 814, L21
Dumusque X., et al., 2017, A&A, 598, A133
Dumusque X., et al., 2020, arXiv e-prints, p. arXiv:2009.01945
Edelson R. A., Krolik J. H., 1988, ApJ, 333, 646
Ehrenreich D., Tinetti G., Lecavelier Des Etangs A., Vidal-Madjar A., Selsis F., 2006, A&A, 448, 379
Ehrenreich D., et al., 2014, A&A, 570, A89
Ehrenreich D., et al., 2015, Nature, 522, 459
Ehrenreich D., et al., 2020, Nature, 580, 597
Evans Neal J. I., et al., 2009, ApJS, 181, 321
Fabrycky D., Tremaine S., 2007, ApJ, 669, 1298
Fabrycky D. C., Winn J. N., 2009, ApJ, 696, 1230
Faria J. P., Haywood R. D., Brewer B. J., Figueira P., Oshagh M., Santerne A., Santos N. C., 2016, A&A, 588, A31
Fauchez T. J., et al., 2019, ApJ, 887, 194
Feroz F., Hobson M. P., 2014, MNRAS, 437, 3540
Ferraz-Mello S., 1981, AJ, 86, 619
Figueira P., et al., 2016, A&A, 586, A101
Fischer D. A., Valenti J., 2005, ApJ, 622, 1102
Fischer D. A., et al., 2016, PASP, 128, 066001
Fleming D. P., Barnes R., Luger R., Vand erPlas J. T., 2020, ApJ, 891, 155
Fletcher L. N., Drossart P., Burgdorf M., Orton G. S., Encrenaz T., 2010, A&A, 514, A17
Flock M., Ruge J. P., Dzyurkevich N., Henning T., Klahr H., Wolf S., 2015, A&A, 574, A68
Flowers E., Brogi M., Rauscher E., Kempton E. M. R., Chiavassa A., 2019, AJ, 157, 209
Fluri D. M., Berdyugina S. V., 2010, A&A, 512, A59
Follert R., et al., 2014, in Ramsay S. K., McLean I. S., Takami H., eds, Society of Photo-Optical Instrumentation Engineers (SPIE) Conference Series Vol. 9147, Ground-based and Airborne Instrumentation for Astronomy V. p. 914719, doi:10.1117/12.2054197
Folsom C. P., et al., 2016, MNRAS, 457, 580
Folsom C. P., et al., 2018, MNRAS, 481, 5286
Folsom C. P., Fionnagáin D. Ó., Fossati L., Vidotto A. A., Moutou C., Petit P., Dragomir D., Donati J. F., 2020, A&A, 633, A48
Ford E. B., 2008, AJ, 135, 1008
Foreman-Mackey D., Hogg D. W., Lang D., Goodman J., 2013, PASP, 125, 306
Fortney J. J., Nettelmann N., 2010, Space Sci. Rev., 152, 423
Fortney J. J., Mordasini C., Nettelmann N., Kempton E. M. R., Greene T. P., Zahnle K., 2013, ApJ, 775, 80
Fouqué P., et al., 2018, MNRAS, 475, 1960
Fulton B. J., et al., 2017, AJ, 154, 109
Gagné J., et al., 2016, ApJ, 822, 40
Gaia Collaboration et al., 2018, A&A, 616, A1
Gaidos E., Mann A. W., Kraus A. L., Ireland M., 2016, MNRAS, 457, 2877
Gallet F., Bouvier J., 2015, A&A, 577, A98

Gandhi S., Brogi M., Webb R. K., 2020, MNRAS, 498, 194
Garcia-Sage K., Glocer A., Drake J. J., Gronoff G., Cohen O., 2017, ApJ, 844, L13
Gardner J. P., et al., 2006, Space Sci. Rev., 123, 485
Garraffo C., Drake J. J., Cohen O., 2016, ApJ, 833, L4
Gastine T., Duarte L., Wicht J., 2012, A&A, 546, A19
Gastine T., Morin J., Duarte L., Reiners A., Christensen U. R., Wicht J., 2013, A&A, 549, L5
Gelman A., Roberts G. O., Gilks W. R., 1996, Bayesian Statistics 5, pp 599–607
Ghosh P., Lamb F. K., 1979, ApJ, 234, 296
Gilbert E. A., et al., 2020, AJ, 160, 116
Gillon M., et al., 2007, A&A, 472, L13
Gillon M., Jehin E., Fumel A., Magain P., Queloz D., 2013, in European Physical Journal Web of Conferences. p. 03001, doi:10.1051/epjconf/20134703001
Gillon M., et al., 2016, Nature, 533, 221
Gillon M., et al., 2017, Nature, 542, 456
Gillon M., et al., 2020, arXiv e-prints, p. arXiv:2002.04798
Gomes da Silva J., Santos N. C., Bonfils X., Delfosse X., Forveille T., Udry S., 2011, A&A, 534, A30
Gomes da Silva J., Santos N. C., Bonfils X., Delfosse X., Forveille T., Udry S., Dumusque X., Lovis C., 2012, A&A, 541, A9
Goodman J., Weare J., 2010, Commun. Appl. Math. Comput. Sci., 5, 65
Grankin K. N., Melnikov S. Y., Bouvier J., Herbst W., Shevchenko V. S., 2007, A&A, 461, 183
Grankin K. N., Bouvier J., Herbst W., Melnikov S. Y., 2008, A&A, 479, 827
Gravity Collaboration et al., 2019, A&A, 623, L11
Gray D. F., 1982, ApJ, 255, 200
Gray D. F., 1989, PASP, 101, 832
Gray D. F., 1997, Nature, 385, 795
Gray D. F., Desikachary K., 1973, ApJ, 181, 523
Greene T., 2001, American Scientist, 89, 316
Gregory P. C., 2005a, ApJ, 631, 1198
Gregory P. C., 2005b, ApJ, 631, 1198
Gregory P. C., 2007, MNRAS, 381, 1607
Gregory S. G., Donati J. F., Morin J., Hussain G. A. J., Mayne N. J., Hillenbrand L. A., Jardine M., 2012, ApJ, 755, 97
Grimm S. L., et al., 2018, A&A, 613, A68
Guillot T., 2010, A&A, 520, A27
Guilluy G., Sozzetti A., Brogi M., Bonomo A. S., Giacobbe P., Claudi R., Benatti S., 2019, A&A, 625, A107
Günther M. N., et al., 2020, AJ, 159, 60
Gustafsson B., Edvardsson B., Eriksson K., Jørgensen U. G., Nordlund Å., Plez B., 2008, A&A, 486, 951
Güttler C., Blum J., Zsom A., Ormel C. W., Dullemond C. P., 2010, A&A, 513, A56
Haario H., Saksman E., Tamminen J., 2001, Bernoulli, 7, 223
Haffert S. Y., Bohn A. J., de Boer J., Snellen I. A. G., Brinchmann J., Girard J. H., Keller C. U., Bacon R., 2019, Nature Astronomy, 3, 749
Haisch Karl E. J., Lada E. A., Lada C. J., 2001, ApJ, 553, L153
Hale G. E., 1908, ApJ, 28, 315
Hall J. C., 2008, Living Reviews in Solar Physics, 5, 2
Hall D. S., Henry G. W., 1994, International Amateur-Professional Photoelectric Photometry Communications, 55, 51

Hambálek L., Vaňko M., Paunzen E., Smalley B., 2019, MNRAS, 483, 1642
Hara N. C., Boué G., Laskar J., Correia A. C. M., 2017, MNRAS, 464, 1220
Hara N. C., et al., 2020, A&A, 636, L6
Hardy A., et al., 2015, ApJ, 800, L24
Hartmann L., Herczeg G., Calvet N., 2016, ARA&A, 54, 135
Hastings W. K., 1970, Biometrika, 57, 97
Hatzes A. P., 1995, ApJ, 451, 784
Hawker G. A., Parry I. R., 2019, MNRAS, 484, 4855
Hawker G. A., Madhusudhan N., Cabot S. H. C., Gandhi S., 2018, ApJ, 863, L11
Hayashi C., 1961, PASJ, 13, 450
Hayek W., Sing D., Pont F., Asplund M., 2012, A&A, 539, A102
Haywood R. D., et al., 2014, MNRAS, 443, 2517
Haywood R. D., et al., 2016, MNRAS, 457, 3637
Haywood R. D., et al., 2020, arXiv e-prints, p. arXiv:2005.13386
Hébrard É. M., Donati J. F., Delfosse X., Morin J., Boisse I., Moutou C., Hébrard G., 2014, MNRAS, 443, 2599
Hébrard É. M., Donati J. F., Delfosse X., Morin J., Moutou C., Boisse I., 2016, MNRAS, 461, 1465
Helling C., et al., 2016, MNRAS, 460, 855
Heng K., Marley M. S., 2018, Radiative Transfer for Exoplanet Atmospheres. p. 102, doi:10.1007/978-3-319-55333-7_102
Henry G. W., Winn J. N., 2008, AJ, 135, 68
Henry T. J., Kirkpatrick J. D., Simons D. A., 1994, AJ, 108, 1437
Henry T. J., Jao W.-C., Subasavage J. P., Beaulieu T. D., Ianna P. A., Costa E., Méndez R. A., 2006, AJ, 132, 2360
Henyey L. G., Lelevier R., Levée R. D., 1955, PASP, 67, 154
Herbig G. H., 1978, Can Post-T Tauri Stars Be Found?. p. 171
Hill C. A., Carmona A., Donati J. F., Hussain G. A. J., Gregory S. G., Alencar S. H. P., Bouvier J., Matysse Collaboration 2017, MNRAS, 472, 1716
Hill C. A., Folsom C. P., Donati J. F., Herczeg G. J., Hussain G. A. J., Alencar S. H. P., Gregory S. G., Matysse Collaboration 2019, MNRAS, 484, 5810
Hirano T., et al., 2020, arXiv e-prints, p. arXiv:2006.13243
Holman M. J., Murray N. W., 2005, Science, 307, 1288
Hood C. E., et al., 2020, arXiv e-prints, p. arXiv:2008.11299
Howard R. F., 1992, Sol. Phys., 137, 51
Howard A. W., et al., 2012, ApJS, 201, 15
Howell S. B., et al., 2014, PASP, 126, 398
Huber D., et al., 2016, ApJS, 224, 2
Hughes A. M., Duchêne G., Matthews B. C., 2018, ARA&A, 56, 541
Hussain G. A. J., Jardine M., Collier Cameron A., 2001, MNRAS, 322, 681
Hussain G. A. J., Allende Prieto C., Saar S. H., Still M., 2006, MNRAS, 367, 1699
Husser T. O., Wende-von Berg S., Dreizler S., Homeier D., Reiners A., Barman T., Hauschildt P. H., 2013, A&A, 553, A6
Ibañez Bustos R. V., Buccino A. P., Flores M., Martinez C. I., Maizel D., Messina S., Mauas P. J. D., 2019, MNRAS, 483, 1159
Ida S., Lin D. N. C., 2008, ApJ, 673, 487
Ivanova N., et al., 2013, A&ARv, 21, 59
Jardine M., Barnes J. R., Donati J.-F., Collier Cameron A., 1999, MNRAS, 305, L35
Jeffers S. V., Donati J. F., Collier Cameron A., 2007, MNRAS, 375, 567
Jeffreys H., 1961, Theory of Probability, third edn. Oxford, Oxford, England

Jenkins J. M., et al., 2015, AJ, 150, 56
Jensen E. L. N., 2001, in Jayawardhana R., Greene T., eds, Astronomical Society of the Pacific Conference Series Vol. 244, Young Stars Near Earth: Progress and Prospects. p. 3 (arXiv:astro-ph/0105031)
Jin S., Mordasini C., 2018, ApJ, 853, 163
Johansen A., Lacerda P., 2010, MNRAS, 404, 475
Johansen A., Blum J., Tanaka H., Ormel C., Bizzarro M., Rickman H., 2014, in Beuther H., Klessen R. S., Dullemond C. P., Henning T., eds, Protostars and Planets VI. p. 547 (arXiv:1402.1344), doi:10.2458/azu_uapress_9780816531240-ch024
Johns-Krull C. M., 1996, A&A, 306, 803
Johns-Krull C. M., 2007, ApJ, 664, 975
Johns-Krull C. M., Valenti J. A., 1996, ApJ, 459, L95
Johns-Krull C. M., Valenti J. A., Hatzes A. P., Kanaan A., 1999a, ApJ, 510, L41
Johns-Krull C. M., Valenti J. A., Koresko C., 1999b, ApJ, 516, 900
Johns-Krull C. M., et al., 2016, ApJ, 826, 206
Jones D. E., Stenning D. C., Ford E. B., Wolpert R. L., Loredo T. J., Dumusque X., 2017, arXiv e-prints, p. arXiv:1711.01318
Jurgenson C., Fischer D., McCracken T., Sawyer D., Szymkowiak A., Davis A., Muller G., Santoro F., 2016, in Proc. SPIE. p. 99086T (arXiv:1606.04413), doi:10.1117/12.2233002
Jurić M., Tremaine S., 2008, ApJ, 686, 603
Kaeufl H.-U., et al., 2004, in Moorwood A. F. M., Iye M., eds, Society of Photo-Optical Instrumentation Engineers (SPIE) Conference Series Vol. 5492, Ground-based Instrumentation for Astronomy. pp 1218–1227, doi:10.1117/12.551480
Kalas P., Liu M. C., Matthews B. C., 2004, Science, 303, 1990
Kalas P., et al., 2008, Science, 322, 1345
Kass R. E., Raftery A. E., 1995, Journal of the American Statistical Association, 90, 773
Kasting J. F., Whitmire D. P., Reynolds R. T., 1993, Icarus, 101, 108
Kawaler S. D., 1988, ApJ, 333, 236
Keenan P. C., McNeil R. C., 1989, ApJS, 71, 245
Kenyon S. J., Hartmann L., 1987, ApJ, 323, 714
Keppler M., et al., 2018, A&A, 617, A44
Khodachenko M. L., et al., 2007, Astrobiology, 7, 167
Kiraga M., Stepien K., 2007, Acta Astron., 57, 149
Kirk J., Alam M. K., López-Morales M., Zeng L., 2020, AJ, 159, 115
Kitchatinov L. L., Moss D., Sokoloff D., 2014, MNRAS, 442, L1
Kjeldsen H., Bedding T. R., 1995, A&A, 293, 87
Klein B., Donati J. F., 2019, MNRAS, 488, 5114
Klein B., Donati J. F., 2020, MNRAS, 493, L92
Klein B., et al., 2020, MNRAS,
Klein B., Donati J.-F., Hébrard É. M., Zaire B., Folsom C. P., Morin J., Delfosse X., Bonfils X., 2021, MNRAS, 500, 1844
Knutson H. A., et al., 2007, Nature, 447, 183
Knutson H. A., Charbonneau D., Cowan N. B., Fortney J. J., Showman A. P., Agol E., Henry G. W., 2009, ApJ, 703, 769
Kochukhov O., Lavail A., 2017, ApJ, 835, L4
Kochukhov O., Reiners A., 2020, arXiv e-prints, p. arXiv:2008.10668
Kochukhov O., Makaganiuk V., Piskunov N., 2010, A&A, 524, A5
Koll D. D. B., Komacek T. D., 2018, ApJ, 853, 133
Kopparapu R. K., et al., 2013, ApJ, 765, 131

Kostogryz N. M., Yakobchuk T. M., Berdyugina S. V., 2015, ApJ, 806, 97
Kotani T., et al., 2014, in Ground-based and Airborne Instrumentation for Astronomy V. p. 914714, doi:10.1117/12.2055075
Kreidberg L., 2015, PASP, 127, 1161
Kreidberg L., et al., 2014, ApJ, 793, L27
Kreidberg L., et al., 2020, arXiv e-prints, p. arXiv:2006.07444
Kuhn M. A., Hillenbrand L. A., Sills A., Feigelson E. D., Getman K. V., 2019, ApJ, 870, 32
Kuker M., Rudiger G., 1997, A&A, 328, 253
Küker M., Rüdiger G., 1999, A&A, 346, 922
Küker M., Rüdiger G., 2005, Astronomische Nachrichten, 326, 265
Kurucz R. L., 1993, SYNTHE spectrum synthesis programs and line data
Lafrenière D., Jayawardhana R., van Kerkwijk M. H., 2008, ApJ, 689, L153
Lagrange A. M., et al., 2010, Science, 329, 57
Lambrechts M., Johansen A., 2012, A&A, 544, A32
Lammer H., Selsis F., Ribas I., Guinan E. F., Bauer S. J., Weiss W. W., 2003, ApJ, 598, L121
Lammer H., et al., 2007, Astrobiology, 7, 185
Lammer H., et al., 2009, A&A, 506, 399
Landi Degl'Innocenti E., Landolfi M., 2004, Polarization in Spectral Lines. Vol. 307, doi:10.1007/978-1-4020-2415-3,
Landstreet J. D., Bagnulo S., Andretta V., Fossati L., Mason E., Silaj J., Wade G. A., 2007, A&A, 470, 685
Langer W. D., van Dishoeck E. F., Bergin E. A., Blake G. A., Tielens A. G. G. M., Velusamy T., Whittet D. C. B., 2000, in Mannings V., Boss A. P., Russell S. S., eds, Protostars and Planets IV. p. 29
Lanza A. F., 2020, MNRAS, 491, 1820
Lanza A. F., Molaro P., Monaco L., Haywood R. D., 2016, A&A, 587, A103
Larson R. B., 1969, MNRAS, 145, 271
Larson R. B., 2003, Reports on Progress in Physics, 66, 1651
Lavail A., Kochukhov O., Wade G. A., 2018, MNRAS, 479, 4836
Lecar M., Podolak M., Sasselov D., Chiang E., 2006, ApJ, 640, 1115
Lecavelier Des Etangs A., Pont F., Vidal-Madjar A., Sing D., 2008, A&A, 481, L83
Lecavelier Des Etangs A., et al., 2010, A&A, 514, A72
Lecavelier des Etangs A., et al., 2012, A&A, 543, L4
Leconte J., Forget F., Charnay B., Wordsworth R., Selsis F., Millour E., Spiga A., 2013, A&A, 554, A69
Leger A., Pirre M., Marceau F. J., 1993, A&A, 277, 309
Lehmann L. T., Hussain G. A. J., Vidotto A. A., Jardine M. M., Mackay D. H., 2021, MNRAS, 500, 1243
Leighton R. B., 1969, ApJ, 156, 1
Leighton R. B., Noyes R. W., Simon G. W., 1962, ApJ, 135, 474
Levenberg K., 1944, Quaterly Journal on Applied Mathematics, pp 164–168
Liebert J., Gizis J. E., 2006, PASP, 118, 659
Lin D. N. C., Bodenheimer P., Richardson D. C., 1996, Nature, 380, 606
Lingam M., Loeb A., 2017, ApJ, 848, 41
Lockwood G. W., Skiff B. A., Henry G. W., Henry S., Radick R. R., Baliunas S. L., Donahue R. A., Soon W., 2007, ApJS, 171, 260
Lockwood A. C., Johnson J. A., Bender C. F., Carr J. S., Barman T., Richert A. J. W., Blake G. A., 2014, ApJ, 783, L29
Lomb N. R., 1976, Ap&SS, 39, 447

Lopez E. D., Fortney J. J., 2013, ApJ, 776, 2
Lopez E. D., Fortney J. J., 2014, ApJ, 792, 1
Lopez T. A., et al., 2019, A&A, 631, A90
Louden T., Wheatley P. J., 2015, ApJ, 814, L24
Lovis C., Fischer D., 2010, Radial Velocity Techniques for Exoplanets. pp 27–53
Lovis C., et al., 2006, Nature, 441, 305
Lovis C., et al., 2017, A&A, 599, A16
Luger R., Agol E., Kruse E., Barnes R., Becker A., Foreman-Mackey D., Deming D., 2016, AJ, 152, 100
Luger R., et al., 2017, Nature Astronomy, 1, 0129
Luger R., Kruse E., Foreman-Mackey D., Agol E., Saunders N., 2018, AJ, 156, 99
Lustig-Yaeger J., Meadows V. S., Lincowski A. P., 2019, AJ, 158, 27
Mac Low M.-M., Klessen R. S., 2004, Reviews of Modern Physics, 76, 125
MacDonald R. J., Madhusudhan N., 2019, MNRAS, 486, 1292
MacGregor M. A., et al., 2013, ApJ, 762, L21
MacGregor A. M., Osten R. A., Hughes A. M., 2020, ApJ, 891, 80
Machida M. N., Basu S., 2019, ApJ, 876, 149
Machida M. N., Matsumoto T., 2011, MNRAS, 413, 2767
Macintosh B., et al., 2014, Proceedings of the National Academy of Science, 111, 12661
Madhusudhan N., 2018, Atmospheric Retrieval of Exoplanets. p. 104, doi:10.1007/978-3-319-55333-7_104
Madhusudhan N., 2019, ARA&A, 57, 617
Madhusudhan N., Seager S., 2009, ApJ, 707, 24
Madhusudhan N., Seager S., 2011, ApJ, 729, 41
Madhusudhan N., Knutson H., Fortney J. J., Barman T., 2014a, in Beuther H., Klessen R. S., Dullemond C. P., Henning T., eds, Protostars and Planets VI. p. 739 (arXiv:1402.1169), doi:10.2458/azu_uapress_9780816531240-ch032
Madhusudhan N., Amin M. A., Kennedy G. M., 2014b, ApJ, 794, L12
Madhusudhan N., Bitsch B., Johansen A., Eriksson L., 2017, MNRAS, 469, 4102
Maeder A., 2009, Physics, Formation and Evolution of Rotating Stars, doi:10.1007/978-3-540-76949-1.
Mahadevan S., Ge J., 2009, ApJ, 692, 1590
Mahadevan S., et al., 2014, in Ground-based and Airborne Instrumentation for Astronomy V. p. 91471G, doi:10.1117/12.2056417
Mahmud N. I., Crockett C. J., Johns-Krull C. M., Prato L., Hartigan P. M., Jaffe D. T., Beichman C. A., 2011, ApJ, 736, 123
Malik M., et al., 2017, AJ, 153, 56
Malo L., Doyon R., Feiden G. A., Albert L., Lafrenière D., Artigau É., Gagné J., Riedel A., 2014, ApJ, 792, 37
Mamajek E. E., Bell C. P. M., 2014, MNRAS, 445, 2169
Mamajek E. E., Meyer M. R., Liebert J., 2002, AJ, 124, 1670
Mancini L., et al., 2013, MNRAS, 436, 2
Mann A. W., et al., 2016, ApJ, 818, 46
Manset N., Donati J.-F., 2003, in Fineschi S., ed., Society of Photo-Optical Instrumentation Engineers (SPIE) Conference Series Vol. 4843, Polarimetry in Astronomy. pp 425–436, doi:10.1117/12.458230
Mansfield M., et al., 2018, ApJ, 868, L34
Marcy G. W., Butler R. P., Vogt S. S., Fischer D. A., Henry G. W., Laughlin G., Wright J. T., Johnson J. A., 2005, ApJ, 619, 570

Marois C., Zuckerman B., Konopacky Q. M., Macintosh B., Barman T., 2010, Nature, 468, 1080
Marquardt D. W., 1963, SIAM Journal on Applied Mathematics, 11, 431
Martin E. L., 1997, A&A, 321, 492
Martioli E., et al., 2020a, arXiv e-prints, p. arXiv:2006.13269
Martioli E., Hébrard G., Correia A. C. M., Laskar J., Lecavelier des Etangs A., 2020b, arXiv e-prints, p. arXiv:2012.13238
Masunaga H., Inutsuka S.-i., 2000, ApJ, 531, 350
Masunaga H., Miyama S. M., Inutsuka S.-i., 1998, ApJ, 495, 346
Mayor M., Queloz D., 1995, Nature, 378, 355
Mayor M., et al., 2003, The Messenger, 114, 20
Mayor M., et al., 2011, arXiv e-prints, p. arXiv:1109.2497
Mazeh T., Holczer T., Faigler S., 2016, A&A, 589, A75
McCullough P. R., Crouzet N., Deming D., Madhusudhan N., 2014, ApJ, 791, 55
McLaughlin D. B., 1924, ApJ, 60, 22
Meadows V. S., et al., 2018, Astrobiology, 18, 133
Mennesson B., et al., 2016, in Space Telescopes and Instrumentation 2016: Optical, Infrared, and Millimeter Wave. p. 99040L, doi:10.1117/12.2240457
Mesquita A. L., Vidotto A. A., 2020, MNRAS, 494, 1297
Messina S., et al., 2016, A&A, 596, A29
Metropolis N., Rosenbluth A. W., Rosenbluth M. N., Teller A. H., Teller E., 1953, The Journal of Chemical Physics, 21, 1087
Meunier N., Lagrange A. M., 2013, A&A, 551, A101
Meunier N., Desort M., Lagrange A. M., 2010, A&A, 512, A39
Meunier N., Lagrange A. M., Borgniet S., Rieutord M., 2015, A&A, 583, A118
Meunier N., Mignon L., Lagrange A. M., 2017, A&A, 607, A124
Meyer F., Schmidt H. U., Weiss N. O., Wilson P. R., 1974, MNRAS, 169, 35
Micheau Y., et al., 2018, in Ground-based and Airborne Instrumentation for Astronomy VII. p. 107025R, doi:10.1117/12.2305937
Mihalas D., 1970, Stellar atmospheres
Mihalas D., 1978, Stellar atmospheres
Mills S. M., Mazeh T., 2017, ApJ, 839, L8
Mocák M., Campbell S. W., Müller E., Kifonidis K., 2010, A&A, 520, A114
Mollière P., Wardenier J. P., van Boekel R., Henning T., Molaverdikhani K., Snellen I. A. G., 2019, A&A, 627, A67
Mondrik N., Newton E., Charbonneau D., Irwin J., 2019, ApJ, 870, 10
Mordasini C., 2018, Planetary Population Synthesis. p. 143, doi:10.1007/978-3-319-55333-7_143
Mordasini C., 2020, A&A, 638, A52
Mordasini C., Alibert Y., Benz W., Klahr H., Henning T., 2012a, A&A, 541, A97
Mordasini C., Alibert Y., Klahr H., Henning T., 2012b, A&A, 547, A111
Mordasini C., Alibert Y., Georgy C., Dittkrist K. M., Klahr H., Henning T., 2012c, A&A, 547, A112
Mordasini C., Mollière P., Dittkrist K. M., Jin S., Alibert Y., 2015, International Journal of Astrobiology, 14, 201
Morin J., et al., 2008a, MNRAS, 384, 77
Morin J., et al., 2008b, MNRAS, 390, 567
Morin J., Donati J. F., Petit P., Delfosse X., Forveille T., Jardine M. M., 2010, MNRAS, 407, 2269
Morin J., et al., 2011, in Prasad Choudhary D., Strassmeier K. G., eds, IAU Symposium Vol. 273, Physics of Sun and Star Spots. pp 181–187 (arXiv:1009.2589), doi:10.1017/S1743921311015213
Morley C. V., Kreidberg L., Rustamkulov Z., Robinson T., Fortney J. J., 2017, ApJ, 850, 121

Morris B. M., Agol E., Davenport J. R. A., Hawley S. L., 2018a, ApJ, 857, 39
Morris B. M., et al., 2018b, ApJ, 863, L32
Mortier A., Faria J. P., Correia C. M., Santerne A., Santos N. C., 2015, A&A, 573, A101
Moses J. I., et al., 2011, ApJ, 737, 15
Moses J. I., et al., 2013, ApJ, 777, 34
Moutou C., et al., 2007, A&A, 473, 651
Moutou C., et al., 2017, MNRAS, 472, 4563
Moutou C., et al., 2020, arXiv e-prints, p. arXiv:2008.05411
Nakamura F., Li Z.-Y., 2005, ApJ, 631, 411
Narain U., Ulmschneider P., 1996, Space Sci. Rev., 75, 453
Nelson B. E., et al., 2020, AJ, 159, 73
Nettelmann N., Helled R., Fortney J. J., Redmer R., 2013, Planet. Space Sci., 77, 143
Nortmann L., et al., 2018, Science, 362, 1388
Noyes R. W., Weiss N. O., Vaughan A. H., 1984, ApJ, 287, 769
Nutzman P., Charbonneau D., 2008, PASP, 120, 317
O'Brien M. S., Bond H. E., Sion E. M., 2001, ApJ, 563, 971
O'Dell C. R., Wong K., 1996, AJ, 111, 846
Öberg K. I., Murray-Clay R., Bergin E. A., 2011, ApJ, 743, L16
Offner S. S. R., Clark P. C., Hennebelle P., Bastian N., Bate M. R., Hopkins P. F., Moraux E., Whitworth A. P., 2014, in Beuther H., Klessen R. S., Dullemond C. P., Henning T., eds, Protostars and Planets VI. p. 53 (arXiv:1312.5326), doi:10.2458/azu_uapress_9780816531240-ch003
Oklopčić A., Hirata C. M., 2018, ApJ, 855, L11
Ormel C. W., Liu B., Schoonenberg D., 2017, A&A, 604, A1
Owen J. E., 2019, Annual Review of Earth and Planetary Sciences, 47, 67
Owen J. E., Wu Y., 2013, ApJ, 775, 105
Palle E., et al., 2020, arXiv e-prints, p. arXiv:2006.13609
Panja M., Cameron R., Solanki S. K., 2020, ApJ, 893, 113
Papaloizou J. C. B., Szuszkiewicz E., Terquem C., 2018, MNRAS, 476, 5032
Parker E. N., 1955, ApJ, 122, 293
Pasquini L., et al., 2008, in Ground-based and Airborne Instrumentation for Astronomy II. p. 70141I, doi:10.1117/12.787936
Passegger V. M., Wende-von Berg S., Reiners A., 2016, A&A, 587, A19
Pavlenko Y., Suárez Mascareño A., Rebolo R., Lodieu N., Béjar V. J. S., González Hernández J. I., 2017, A&A, 606, A49
Pepe F. A., Lovis C., 2008, Physica Scripta Volume T, 130, 014007
Pepe F. A., et al., 2010, in Proc. SPIE. p. 77350F, doi:10.1117/12.857122
Pepe F., et al., 2013, Nature, 503, 377
Pepe F., et al., 2020, arXiv e-prints, p. arXiv:2010.00316
Pepper J., et al., 2007, PASP, 119, 923
Perruchot S., et al., 2008, in Proc. SPIE. p. 70140J, doi:10.1117/12.787379
Perryman M., 2011, The Exoplanet Handbook. Cambridge University Press, doi:10.1017/CBO9780511994852
Perryman M., 2018, The Exoplanet Handbook
Perryman M. A. C., et al., 1998, A&A, 331, 81
Pesnell W. D., Thompson B. J., Chamberlin P. C., 2012, Sol. Phys., 275, 3
Petigura E. A., et al., 2017, AJ, 154, 107
Petit P., Donati J. F., Collier Cameron A., 2002, MNRAS, 334, 374
Petit P., et al., 2015, A&A, 584, A84

Phan-Bao N., Lim J., Donati J.-F., Johns-Krull C. M., Martín E. L., 2009, ApJ, 704, 1721
Phillips D. F., et al., 2012, in Proc. SPIE. p. 84468O, doi:10.1117/12.926465
Pierrehumbert R. T., 2010, Principles of Planetary Climate
Pizzolato N., Maggio A., Micela G., Sciortino S., Ventura P., 2003, A&A, 397, 147
Plavchan P., Werner M. W., Chen C. H., Stapelfeldt K. R., Su K. Y. L., Stauffer J. R., Song I., 2009, ApJ, 698, 1068
Plavchan P., et al., 2020a, arXiv e-prints, p. arXiv:2006.13428
Plavchan P., et al., 2020b, Nature, 582, 497
Pluriel W., Zingales T., Leconte J., Parmentier V., 2020, A&A, 636, A66
Pollacco D. L., et al., 2006, PASP, 118, 1407
Pollack J. B., Hubickyj O., Bodenheimer P., Lissauer J. J., Podolak M., Greenzweig Y., 1996, Icarus, 124, 62
Pont F., Knutson H., Gilliland R. L., Moutou C., Charbonneau D., 2008, MNRAS, 385, 109
Preibisch T., Brown A. G. A., Bridges T., Guenther E., Zinnecker H., 2002, AJ, 124, 404
Press W. H., Teukolsky S. A., Vetterling W. T., Flannery B. P., 1992, Numerical recipes in FORTRAN. The art of scientific computing
Probst R. A., et al., 2020, Nature Astronomy, 4, 603
Queloz D., et al., 2001, A&A, 379, 279
Queloz D., et al., 2009, A&A, 506, 303
Queloz D., et al., 2010, A&A, 517, L1
Quirrenbach A., et al., 2012, in Ground-based and Airborne Instrumentation for Astronomy IV. p. 84460R, doi:10.1117/12.925164
Quirrenbach A., et al., 2014, in Ground-based and Airborne Instrumentation for Astronomy V. p. 91471F, doi:10.1117/12.2056453
Rackham B. V., Apai D., Giampapa M. S., 2018, ApJ, 853, 122
Rajpaul V., Aigrain S., Osborne M. A., Reece S., Roberts S., 2015, MNRAS, 452, 2269
Rajpaul V., Aigrain S., Roberts S., 2016, MNRAS, 456, L6
Rajpaul V. M., Aigrain S., Buchhave L. A., 2020, MNRAS, 492, 3960
Ramseyer T. F., Hatzes A. P., Jablonski F., 1995, AJ, 110, 1364
Rasio F. A., Ford E. B., 1996, Science, 274, 954
Rasmussen C. E., Williams C. K. I., 2006, Gaussian Processes for Machine Learning. MIT Press
Rauer H., et al., 2014, Experimental Astronomy, 38, 249
Raymond S. N., Kokubo E., Morbidelli A., Morishima R., Walsh K. J., 2014, in Beuther H., Klessen R. S., Dullemond C. P., Henning T., eds, Protostars and Planets VI. p. 595 (arXiv:1312.1689), doi:10.2458/azu_uapress_9780816531240-ch026
Rayner J., Bond T., Bonnet M., Jaffe D., Muller G., Tokunaga A., 2012, in Ground-based and Airborne Instrumentation for Astronomy IV. p. 84462C, doi:10.1117/12.925511
Rayner J., et al., 2016, in Ground-based and Airborne Instrumentation for Astronomy VI. p. 990884, doi:10.1117/12.2232064
Rebull L. M., Wolff S. C., Strom S. E., 2004, AJ, 127, 1029
Redfield S., Endl M., Cochran W. D., Koesterke L., 2008, ApJ, 673, L87
Reiners A., Basri G., 2006, ApJ, 644, 497
Reiners A., Basri G., 2007, ApJ, 656, 1121
Reiners A., Basri G., 2008, A&A, 489, L45
Reiners A., Basri G., 2009, A&A, 496, 787
Reiners A., Basri G., Browning M., 2009, ApJ, 692, 538
Reiners A., Joshi N., Goldman B., 2012, AJ, 143, 93
Reiners A., Shulyak D., Anglada-Escudé G., Jeffers S. V., Morin J., Zechmeister M., Kochukhov O., Piskunov N., 2013, A&A, 552, A103

Reshetov V., Herriot G., Thibault S., Désaulniers P., Saddlemyer L., Loop D., 2012, in Ground-based and Airborne Instrumentation for Astronomy IV. p. 84464E, doi:10.1117/12.927442
Réville V., Brun A. S., Strugarek A., Matt S. P., Bouvier J., Folsom C. P., Petit P., 2015, ApJ, 814, 99
Rhee J. H., Song I., Zuckerman B., McElwain M., 2007, ApJ, 660, 1556
Ribas I., et al., 2016, A&A, 596, A111
Ribas I., Gregg M. D., Boyajian T. S., Bolmont E., 2017, A&A, 603, A58
Richert A. J. W., Getman K. V., Feigelson E. D., Kuhn M. A., Broos P. S., Povich M. S., Bate M. R., Garmire G. P., 2018, MNRAS, 477, 5191
Ricker G. R., et al., 2015, Journal of Astronomical Telescopes, Instruments, and Systems, 1, 014003
Rincon F., 2019, Journal of Plasma Physics, 85, 205850401
Robinson R. D. J., 1980, ApJ, 239, 961
Robinson R. D., Linsky J. L., Woodgate B. E., Timothy J. G., 2001, ApJ, 554, 368
Rodono M., et al., 1986, A&A, 165, 135
Rodríguez-López C., Gizis J. E., MacDonald J., Amado P. J., Carosso A., 2015, MNRAS, 446, 2613
Ros K., Johansen A., 2013, A&A, 552, A137
Rossiter R. A., 1924, ApJ, 60, 15
Rothman L. S., et al., 1992, J. Quant. Spectrosc. Radiative Transfer, 48, 469
Rothman L., et al., 2010, Journal of Quantitative Spectroscopy and Radiative Transfer, 111, 2139
Route M., 2016, ApJ, 830, L27
Rowe J. F., et al., 2014, ApJ, 784, 45
Rubenstein E. P., Schaefer B. E., 2000, ApJ, 529, 1031
Saar S. H., 1988, ApJ, 324, 441
Saar S. H., 1994, in Rabin D. M., Jefferies J. T., Lindsey C., eds, IAU Symposium Vol. 154, Infrared Solar Physics. p. 493
Saar S. H., Donahue R. A., 1997, ApJ, 485, 319
Saar S. H., Linsky J. L., 1985, ApJ, 299, L47
Salz M., Schneider P. C., Czesla S., Schmitt J. H. M. M., 2015, A&A, 576, A42
Salz M., et al., 2018, A&A, 620, A97
Santerne A., et al., 2016, A&A, 587, A64
Santerne A., et al., 2018, Nature Astronomy, 2, 393
Santos N. C., et al., 2004, A&A, 426, L19
Sanz-Forcada J., Dupree A. K., 2008, A&A, 488, 715
Scargle J. D., 1982, ApJ, 263, 835
Schadee A., 1978, J. Quant. Spectrosc. Radiative Transfer, 19, 517
Scharlemann E. T., 1981, ApJ, 246, 292
Scharlemann E. T., 1982, ApJ, 253, 298
Scherrer P. H., et al., 1995, Sol. Phys., 162, 129
Schmidt S. J., Kowalski A. F., Hawley S. L., Hilton E. J., Wisniewski J. P., Tofflemire B. M., 2012, ApJ, 745, 14
Schöfer P., et al., 2019, A&A, 623, A44
Schoonenberg D., Liu B., Ormel C. W., Dorn C., 2019, A&A, 627, A149
Schreiber M. R., Gänsicke B. T., 2003, A&A, 406, 305
Schwab C., Stürmer J., Gurevich Y. V., Führer T., Lamoreaux S. K., Walther T., Quirrenbach A., 2015, PASP, 127, 880
Schwieterman E. W., et al., 2018, Astrobiology, 18, 663
Seager S., Sasselov D. D., 2000, ApJ, 537, 916
See V., et al., 2019, ApJ, 876, 118

Seidel J. V., Ehrenreich D., Pino L., Bourrier V., Lavie B., Allart R., Wyttenbach A., Lovis C., 2020, A&A, 633, A86
Selsis F., Kasting J. F., Levrard B., Paillet J., Ribas I., Delfosse X., 2007, A&A, 476, 1373
Semel M., 1989, A&A, 225, 456
Semel M., Donati J. F., Rees D. E., 1993, A&A, 278, 231
Sergeev D. E., Lambert F. H., Mayne N. J., Boutle I. A., Manners J., Kohary K., 2020, ApJ, 894, 84
Sezestre É., Augereau J. C., Boccaletti A., Thébault P., 2017, A&A, 607, A65
Sharma S., 2017, ARA&A, 55, 213
Shkolnik E., Walker G. A. H., Bohlender D. A., Gu P. G., Kürster M., 2005, ApJ, 622, 1075
Short C. I., Doyle J. G., 1998, A&A, 331, L5
Showman A. P., Guillot T., 2002, A&A, 385, 166
Showman A. P., Lewis N. K., Fortney J. J., 2015, ApJ, 801, 95
Shulyak D., Reiners A., Engeln A., Malo L., Yadav R., Morin J., Kochukhov O., 2017, Nature Astronomy, 1, 0184
Siess L., Dufour E., Forestini M., 2000, A&A, 358, 593
Sing D. K., López-Morales M., 2009, A&A, 493, L31
Sing D. K., et al., 2011, A&A, 527, A73
Skelly M. B., Unruh Y. C., Collier Cameron A., Barnes J. R., Donati J. F., Lawson W. A., Carter B. D., 2008, MNRAS, 385, 708
Skelly M. B., Donati J. F., Bouvier J., Grankin K. N., Unruh Y. C., Artemenko S. A., Petrov P., 2010, MNRAS, 403, 159
Skilling J., 2006, Bayesian Anal., 1, 833
Skilling J., Bryan R. K., 1984, MNRAS, 211, 111
Snellen I. A. G., de Kok R. J., de Mooij E. J. W., Albrecht S., 2010, Nature, 465, 1049
Snellen I. A. G., de Kok R. J., le Poole R., Brogi M., Birkby J., 2013, ApJ, 764, 182
Snellen I., et al., 2015, A&A, 576, A59
Snellen I., et al., 2019, arXiv e-prints, p. arXiv:1908.01803
Snik F., et al., 2011, The HARPS Polarimeter. p. 237
Sokoloff D. D., Nefedov S. N., Ermash A. A., Lamzin S. A., 2008, Astronomy Letters, 34, 761
Sousa S. G., et al., 2018, A&A, 620, A58
Southworth J., Wheatley P. J., Sams G., 2007, MNRAS, 379, L11
Spake J. J., et al., 2018, Nature, 557, 68
Spiegel E. A., Zahn J. P., 1992, A&A, 265, 106
Spiegel D. S., Silverio K., Burrows A., 2009, ApJ, 699, 1487
Stahler S. W., Palla F., 2005, The Formation of Stars
Stelzer B., Flaccomio E., Briggs K., Micela G., Scelsi L., Audard M., Pillitteri I., Güdel M., 2007, A&A, 468, 463
Stevenson K. B., et al., 2010, Nature, 464, 1161
Stevenson K. B., et al., 2014, Science, 346, 838
Strassmeier K. G., 2009, A&ARv, 17, 251
Strom K. M., Strom S. E., Edwards S., Cabrit S., Skrutskie M. F., 1989, AJ, 97, 1451
Strugarek A., Brun A. S., Matt S. P., Réville V., 2014, ApJ, 795, 86
Strugarek A., Brun A. S., Matt S. P., Réville V., 2015, ApJ, 815, 111
Strugarek A., Brun A. S., Donati J. F., Moutou C., Réville V., 2019, ApJ, 881, 136
Suárez Mascareño A., Rebolo R., González Hernández J. I., 2016, A&A, 595, A12
Suárez Mascareño A., et al., 2020, A&A, 639, A77
Takahashi S. Z., Inutsuka S.-i., 2016, AJ, 152, 184

Tamura M., et al., 2012, in Ground-based and Airborne Instrumentation for Astronomy IV. p. 84461T, doi:10.1117/12.925885
Tennyson J., et al., 2016, Journal of Molecular Spectroscopy, 327, 73
Thibault S., et al., 2012, in Ground-based and Airborne Instrumentation for Astronomy IV. p. 844630, doi:10.1117/12.926697
Thompson S. J., et al., 2016, in Proc. SPIE. p. 99086F (arXiv:1608.04611), doi:10.1117/12.2232111
Tilley M. A., Segura A., Meadows V. S., Hawley S., Davenport J., 2017, arXiv e-prints, p. arXiv:1711.08484
Tinetti G., et al., 2007, Nature, 448, 169
Tokovinin A., Fischer D. A., Bonati M., Giguere M. J., Moore P., Schwab C., Spronck J. F. P., Szymkowiak A., 2013, PASP, 125, 1336
Tomida K., Tomisaka K., Matsumoto T., Hori Y., Okuzumi S., Machida M. N., Saigo K., 2013, ApJ, 763, 6
Torres C. A. O., Ferraz Mello S., 1973, A&A, 27, 231
Torres G., Winn J. N., Holman M. J., 2008, ApJ, 677, 1324
Torres R. M., Loinard L., Mioduszewski A. J., Rodríguez L. F., 2009, ApJ, 698, 242
Tremblin P., Chiang E., 2013, MNRAS, 428, 2565
Triaud A. H. M. J., et al., 2009, A&A, 506, 377
Triaud A. H. M. J., et al., 2010, A&A, 524, A25
Tsapras Y., 2018, Geosciences, 8, 365
Tuomi M., et al., 2013, A&A, 551, A79
Turbet M., Leconte J., Selsis F., Bolmont E., Forget F., Ribas I., Raymond S. N., Anglada-Escudé G., 2016, A&A, 596, A112
Turbet M., et al., 2018, A&A, 612, A86
Turbet M., Bolmont E., Bourrier V., Demory B.-O., Leconte J., Owen J., Wolf E. T., 2020, arXiv e-prints, p. arXiv:2007.03334
Unno W., 1956, PASJ, 8, 108
Vaccaro T. R., Wilson R. E., Van Hamme W., Terrell D., 2015, ApJ, 810, 157
Valenti J. A., Johns-Krull C. M., 2004, Ap&SS, 292, 619
Valenti J. A., Marcy G. W., Basri G., 1995, ApJ, 439, 939
Valenti J. A., Johns-Krull C. M., Piskunov N. E., 2001, in Garcia Lopez R. J., Rebolo R., Zapaterio Osorio M. R., eds, Astronomical Society of the Pacific Conference Series Vol. 223, 11th Cambridge Workshop on Cool Stars, Stellar Systems and the Sun. p. 1579
Vanderbosch Z. P., Clemens J. C., Dunlap B. H., Winget D. E., 2017, in Tremblay P. E., Gaensicke B., Marsh T., eds, Astronomical Society of the Pacific Conference Series Vol. 509, 20th European White Dwarf Workshop. pp 571–574
Vida K., Kővári Z., Pál A., Oláh K., Kriskovics L., 2017, ApJ, 841, 124
Vida K., Oláh K., Kővári Z., van Driel-Gesztelyi L., Moór A., Pál A., 2019, ApJ, 884, 160
Vidal-Madjar A., Lecavelier des Etangs A., Désert J. M., Ballester G. E., Ferlet R., Hébrard G., Mayor M., 2003, Nature, 422, 143
Vidotto A. A., Donati J. F., 2017, A&A, 602, A39
Vidotto A. A., Opher M., Jatenco-Pereira V., Gombosi T. I., 2009, ApJ, 699, 441
Vidotto A. A., Jardine M., Opher M., Donati J. F., Gombosi T. I., 2011, MNRAS, 412, 351
Vidotto A. A., Fares R., Jardine M., Donati J. F., Opher M., Moutou C., Catala C., Gombosi T. I., 2012, MNRAS, 423, 3285
Vidotto A. A., Jardine M., Morin J., Donati J. F., Opher M., Gombosi T. I., 2014a, MNRAS, 438, 1162
Vidotto A. A., et al., 2014b, MNRAS, 441, 2361

Vidotto A. A., Feeney N., Groh J. H., 2019, MNRAS, 488, 633
Virgo W. L., Steimle T. C., Brown J. M., 2005, ApJ, 628, 567
Vogt S. S., Penrod G. D., 1983, Doppler imaging of starspots. pp 379–385, doi:10.1007/978-94-009-7157-8_44
Vogt S. S., Penrod G. D., Hatzes A. P., 1987, ApJ, 321, 496
Vogt S. S., et al., 1994, in Crawford D. L., Craine E. R., eds, Society of Photo-Optical Instrumentation Engineers (SPIE) Conference Series Vol. 2198, Proc. SPIE. p. 362, doi:10.1117/12.176725
Völschow M., Schleicher D. R. G., Banerjee R., Schmitt J. H. M. M., 2018, A&A, 620, A42
Wafflard-Fernandez G., Baruteau C., 2020, MNRAS, 493, 5892
Wakeford H. R., Sing D. K., 2015, A&A, 573, A122
Wakeford H. R., et al., 2017a, Science, 356, 628
Wakeford H. R., Visscher C., Lewis N. K., Kataria T., Marley M. S., Fortney J. J., Mand ell A. M., 2017b, MNRAS, 464, 4247
Waldmann I. P., Tinetti G., Rocchetto M., Barton E. J., Yurchenko S. N., Tennyson J., 2015a, ApJ, 802, 107
Waldmann I. P., Rocchetto M., Tinetti G., Barton E. J., Yurchenko S. N., Tennyson J., 2015b, ApJ, 813, 13
Wang J., Mawet D., Ruane G., Hu R., Benneke B., 2017, AJ, 153, 183
Wargelin B. J., Saar S. H., Pojmański G., Drake J. J., Kashyap V. L., 2017, MNRAS, 464, 3281
Warner B., 1995, Cambridge Astrophysics Series, 28
Watson C. A., de Mooij E. J. W., Steeghs D., Marsh T. R., Brogi M., Gibson N. P., Matthews S., 2019, MNRAS, 490, 1991
Webb R. K., Brogi M., Gandhi S., Line M. R., Birkby J. L., Chubb K. L., Snellen I. A. G., Yurchenko S. N., 2020, MNRAS, 494, 108
Weber E. J., Davis Leverett J., 1967, ApJ, 148, 217
Weidling R., Güttler C., Blum J., 2012, Icarus, 218, 688
Weiss L. M., Marcy G. W., 2014, The Astrophysical Journal, 783, L6
West A. A., et al., 2011, AJ, 141, 97
Wheatley P. J., Louden T., Bourrier V., Ehrenreich D., Gillon M., 2017, MNRAS, 465, L74
Wheatley P. J., et al., 2018, MNRAS, 475, 4476
Wildi F., et al., 2017, in Society of Photo-Optical Instrumentation Engineers (SPIE) Conference Series. p. 1040018, doi:10.1117/12.2275660
Wilking B. A., Gagné M., Allen L. E., 2008, Star Formation in the ρ Ophiuchi Molecular Cloud. p. 351
Williams J. P., Best W. M. J., 2014, ApJ, 788, 59
Williams J. P., Cieza L. A., 2011, ARA&A, 49, 67
Wilner D. J., Andrews S. M., MacGregor M. A., Hughes A. M., 2012, ApJ, 749, L27
Winn J. N., 2009, in Pont F., Sasselov D., Holman M. J., eds, Vol. 253, Transiting Planets. pp 99–109 (arXiv:0807.4929), doi:10.1017/S174392130802629X
Winn J. N., Fabrycky D. C., 2015, ARA&A, 53, 409
Winters J. G., et al., 2015, AJ, 149, 5
Winters J. G., et al., 2019, AJ, 157, 216
Wisniewski J. P., et al., 2019, ApJ, 883, L8
Wittenmyer R. A., et al., 2016, ApJ, 819, 28
Wolf E. T., 2017, ApJ, 839, L1
Wolszczan A., Frail D. A., 1992, Nature, 355, 145
Wood B. E., Linsky J. L., Müller H.-R., Zank G. P., 2001, ApJ, 547, L49
Wright N. J., Drake J. J., 2016, Nature, 535, 526
Wright N. J., Drake J. J., Mamajek E. E., Henry G. W., 2011, ApJ, 743, 48

Wright N. J., Newton E. R., Williams P. K. G., Drake J. J., Yadav R. K., 2018, MNRAS, 479, 2351
Wu Y., Murray N., 2003, ApJ, 589, 605
Wyttenbach A., Ehrenreich D., Lovis C., Udry S., Pepe F., 2015, A&A, 577, A62
Yadav R. K., Christensen U. R., Wolk S. J., Poppenhaeger K., 2016, ApJ, 833, L28
Yelle R. V., 2004, Icarus, 170, 167
Youdin A. N., Goodman J., 2005, ApJ, 620, 459
Yu L., et al., 2017, MNRAS, 467, 1342
Yu L., et al., 2019, MNRAS, 489, 5556
Zarka P., 2007, Planet. Space Sci., 55, 598
Zechmeister M., Kürster M., 2009, A&A, 496, 577
Zechmeister M., et al., 2019, A&A, 627, A49
Zeeman P., 1897, ApJ, 5, 332
Zellem R. T., et al., 2014, ApJ, 790, 53
Zeng L., et al., 2019, Proceedings of the National Academy of Science, 116, 9723
Zhang R., Steimle T. C., 2014, ApJ, 781, 51
Zhang M., Chachan Y., Kempton E. M. R., Knutson H. A., 2019, PASP, 131, 034501
Zirin H., 1982, ApJ, 260, 655
de Kok R. J., Brogi M., Snellen I. A. G., Birkby J., Albrecht S., de Mooij E. J. W., 2013, A&A, 554, A82
ud-Doula A., Owocki S. P., 2002, ApJ, 576, 413
van Dishoeck E. F., Blake G. A., Draine B. T., Lunine J. I., 1993, in Levy E. H., Lunine J. I., eds, Protostars and Planets III. p. 163

List of Figures

List of Tables

A | Complements

A.1 Zeeman-Doppler imaging

Zeeman Doppler Imaging (ZDI, Semel, 1989; Donati et al., 1989; Semel et al., 1993; Brown et al., 1991; Donati & Brown, 1997; Donati, 2001; Donati et al., 2006c) is a technique that inverts a time series of LSD profiles of Stokes parameters into a distribution of brightness and large-scale magnetic field (or of any quantity affecting spectral lines) at the surface of a star. Let us consider a time series of $N_{\rm obs}$ observed LSD profiles $\boldsymbol{Y} = (\boldsymbol{I}, \boldsymbol{Q}, \boldsymbol{U}, \boldsymbol{V})$. $\boldsymbol{Y}$ is a 3D matrix of dimensions $(N_{\rm obs}, 4, N_{\rm pt})$, where $N_{\rm pt}$ is the number of points in each LSD profile. In ZDI, $\boldsymbol{Y}$ is simultaneously modeled by 3D brightness and magnetic maps called $\mathscr{M}$ such that

$$\boldsymbol{Y} = \mathscr{R}(\mathscr{M}) + \boldsymbol{\epsilon} \tag{A.1}$$

where $\mathscr{R}$ is the so-called response function of ZDI (associated to the direct process) that converts $\mathscr{M}$ into a time series of synthetic profiles comparable to the observed ones, and $\boldsymbol{\epsilon}$ is the white noise. In Section A.1.1, we describe how ZDI generates synthetic polarized line profiles from given brightness and magnetic maps, while the inversion process is detailed in Section A.1.2.

A.1.1 Modeling of the stellar surface

General principle

The direct approach consists in computing a set of synthetic unsigned and polarized line profiles from a given model of the stellar surface (i.e., magnetic and brightness distributions). The stellar surface is sampled into a dense grid of typically $N = 10\,000$ cells of identical projected area when crossing the meridian. Each cell of colatitude θ_i and azimuth ϕ_j features a brightness factor $b_{i,j}$ relative to the quiet photosphere (b larger/smaller than 1 for a brighter/darker region) and a vector of magnetic field $\boldsymbol{B}_{i,j} = [B_{\rm r}(\theta_i, \phi_j), B_\theta(\theta_i, \phi_j), B_\phi(\theta_i, \phi_j)]$ (where the components of $\boldsymbol{B}_{i,j}$ are respectively the radial, meridional and azimuthal magnetic field of the cell). In ZDI, the global magnetic field vector $\boldsymbol{B}$ is decomposed into its poloidal and toroidal components, both expressed as weighted sums of spherical harmonics (up to a given order $l_{\rm max}$; see Donati et al., 2006c, for the explicit equations). For each cell, ZDI computes the local line profile $\boldsymbol{F}_{i,j} = (\boldsymbol{I}_{i,j}, \boldsymbol{Q}_{i,j}, \boldsymbol{U}_{i,j}, \boldsymbol{V}_{i,j})$, using the Unno-Rachkovsky's analytical solution of the radiative transfer equations in a plane-parallel Milne-Eddington atmosphere (see Unno, 1956; Landi Degl'Innocenti & Landolfi, 2004, but also the Ph.D. thesis[1] of L. Yu, for a more synthetic description of the equations). The local profile is then Doppler-shifted by $\Delta v_{i,j} = v \sin i_{\rm rot} \sin \phi_j \cos \theta_i$ and weighted according to a linear law in $\cos \theta_i$ to account for stellar limb darkening. The local line profiles are finally combined into a global polarized line profile $\boldsymbol{F}$ such that

[1] https://hal.archives-ouvertes.fr/tel-02799114

$$\boldsymbol{F} = \sum_i \sum_j b_{i,j} \boldsymbol{F}_{i,j}(\Delta v_{i,j}, \boldsymbol{B}_{i,j}) \left[1 - \eta(1 - \cos\theta_i)\right] \tag{A.2}$$

where ϵ is the limb-darkening coefficient generally computed using (Claret et al., 2012) or Claret (2018) (or from the analysis of transit light curves, when available). As the studies presented in this manuscript are based on Stokes I and Stokes V spectra, we limit the further description to these two components.

Filling factors for magnetic field and brightness reconstructions

In the case of slowly-rotating stars, we introduce filling factors f_I and f_V, constant over the stellar surface, defined as the fraction of each cell containing small- and large-scale magnetic field, respectively (Morin et al., 2008b). The local Stokes I and V profiles associated to cell (i, j) are thus given by

$$\left\{ \begin{array}{rcl} \boldsymbol{I}_{i,j} & = & f_I \boldsymbol{I}_{i,j}(\boldsymbol{B}_{i,j}) + (1 - f_I)\boldsymbol{I}_{i,j}(\boldsymbol{B}_{i,j} = \boldsymbol{0}), \\ \boldsymbol{V}_{i,j} & = & f_V \boldsymbol{V}_{i,j}(\boldsymbol{B}_{i,j}), \\ \Delta\lambda_B & = & 4.67 \times 10^{-12} g_{\rm eff} \lambda_0^2 \, \|\boldsymbol{B}_{i,j}\| / f_V, \end{array} \right. \tag{A.3}$$

where $\Delta\lambda_B$ is the Zeeman splitting associated with the intensity of the local magnetic field, $\|\boldsymbol{B}_{i,j}\|$, at the wavelength λ_0 (see Eq. 3.2). Note that we assume that the intensity of the magnetic field is given by $\|\boldsymbol{B}_{i,j}\|/f_V$, i.e., that the small-scale field is distributed as the large-scale field. In practice, ZDI is only sensitive to the large-scale magnetic field (due to flux cancellation effect between closely magnetic regions of opposite polarity) whereas Zeeman broadening is sensitive to all scales of the magnetic field. We thus expect larger values for f_I than for f_V.

In the case of the brightness reconstruction of slowly-rotating stars ($v \sin i_{\rm rot}$ typically lower than $10\,{\rm km\,s^{-1}}$), one can also introduce a filling $C_{i,j}$ associated to each cell (i, j) and such that (Hébrard et al., 2016)

$$\boldsymbol{I}_{i,j} = C_{i,j} \boldsymbol{I}^{(p)}_{i,j} + b(1 - C_{i,j}) \boldsymbol{I}^{(s)}_{i,j} \tag{A.4}$$

where $\boldsymbol{I}^{(p)}_{i,j}$ and $\boldsymbol{I}^{(s)}_{i,j}$ are the local profiles respectively associated with quiet and spotted regions of the photosphere. $1 - C_{i,j}$ is the proportion of the cell (i, j) that is covered by dark spot of given relative brightness b, constant over the stellar surface. In this reconstruction process, the relative brightness b is assumed constant for all spots and the spot occupancy $C_{i,j}$ is reconstructed instead of the brightness.

Generating a time series of polarized line profiles

Using Eq. A.2, ZDI compute the global line profile at the rotational cycle associated to each observation. ZDI also includes differential rotation (DR) in its modeling process (Donati et al., 2000; Petit et al., 2002). Assuming solar-like DR (i.e., the equator rotates faster than the pole), the distribution of the rotation rate $\Omega(\theta)$ at the surface of the star is given by

$$\Omega(\theta) = \Omega_{\rm eq} - (\cos\theta)^2 {\rm d}\Omega, \tag{A.5}$$

where θ is the colatitude, $\Omega_{\rm eq}$, the equatorial rotation rate and, ${\rm d}\Omega$, the difference in rotation rate between the equator and the pole.

A.1.2 Maximum entropy inversion process

We now want to invert Eq. A.1, i.e., to recover brightness and large-scale magnetic topologies from the observed time series of polarized line profiles. The model $\mathscr{R}(\mathscr{M})$ relies on a significantly larger number N_f of free parameters (N and 3 $l_\mathrm{max}(l_\mathrm{max}+2$ free parameters for brightness and magnetic reconstructions, respectively) than the observational constraints and is thus highly-degenerated (the problem is said to be ill-posed). Hence the need to use a maximum-entropy reconstruction algorithm (see the detailed algorithm in Skilling & Bryan, 1984). The goal of the inversion process is to recover the N_f parameters that minimize the chi-square of the model

$$\chi^2 = (\boldsymbol{Y} - \mathscr{R}(\mathscr{M}))^\mathrm{T} \boldsymbol{\Sigma}^{-1} (\boldsymbol{Y} - \mathscr{R}(\mathscr{M})) \tag{A.6}$$

where $\boldsymbol{\Sigma}_{i,j} = \boldsymbol{\sigma}_i \, \delta_{i,j}$, is the diagonal covariance matrix associated to the noise, $\boldsymbol{\sigma}_i$ being the 1σ uncertainties on $\boldsymbol{Y}_i$. To break the degeneracy induced by the large number of free parameters of the model, an additional constraint called entropy, S, is added to the estimator. The problem to solve is then expressed in the Lagrangian multiplier formalism as

$$\max_{\mathscr{M}} \; S(\mathscr{M}) - \lambda \chi^2(\mathscr{M}) \tag{A.7}$$

where λ is the Lagrange multiplier which governs the relative weights between S and χ^2 in the reconstruction process. S quantifies the amount of information in the reconstructed map $\mathscr{M}$. The entropy S_q associated to relative brightness maps is defined by the Shannon entropy of the relative brightness of the cells:

$$S_\mathrm{q}(\mathscr{M}) = -\sum_{i=1}^{N_\mathrm{c}} \omega_i b_i \left[\log\left(\frac{b_i}{A}\right) - 1 \right] \tag{A.8}$$

where ω_i is the projected area of the cell (which acts as a weight, see Brown et al., 1991), and A the relative brightness on unspotted cells (generally assumed to be 1). If we want to reconstruct the photosphere occupancy rather than brightness (like in method 1 described in Section 3.2.2 and used in Hébrard et al., 2016), the entropy S_q is defined from the spot occupancy filling factor C_i of each cell i as (Hussain et al., 2001)

$$S_q(\mathscr{M}) = -\sum_{i=1}^{N_\mathrm{c}} \omega_i \left[C_i \log\left(\frac{C_i}{b}\right) + (1 - C_i) \log\left(\frac{1 - C_i}{1 - b}\right) \right] \tag{A.9}$$

where b is the relative brightness of the features, constant over the stellar surface. Let us call α_i any of the three magnetic field coefficients associated to cell i. The entropy $S_\mathrm{B}^{(i)}$ is given by

$$S_B^{(i)}(\mathscr{M}) = \left[\sqrt{\alpha_i^2 + B^2} - B - \alpha_i \log\left(\frac{\sqrt{\alpha_i^2 + B^2} + \alpha_i}{B} \right) \right] \tag{A.10}$$

where B is the typical value of the magnetic field of the star. The global entropy S_B of the magnetic reconstructions is simply given by

$$S_\mathrm{B}(\mathscr{M}) = \sum_{i=1}^{3l_\mathrm{max}(l_\mathrm{max}+2)} \zeta_i \, S_B^{(i)}(\mathscr{M}) \tag{A.11}$$

where the weights ζ_i are respectively equal to 3 ℓ and ℓ for poloidal and toroidal coefficients (see Hussain et al., 2001). For simultaneous brightness and magnetic reconstructions, the global entropy S of the model is simply given by $S = S_{\rm B} + S_{\rm q}$.

Starting from an initially empty map $\mathscr{M}_{\mathbf{0}}$, ZDI solves Eq. A.7, by iteratively drawing new maps using the conjugate gradient algorithm (e.g., Press et al., 1992). For a given user-provided level of chi-square $\chi^2_{\rm a}$, the estimation process stops when the gradients of S and χ^2 are anti-parallel and $\chi^2 = \chi^2_{\rm a}$. At $\chi^2_{\rm a} = 1$, the data are fitted to the level of the noise. However, as unaccounted systematics might plagued the observed spectra (e.g., due to stellar variability or uncorrected instrumental or telluric pollution), $\chi_{\rm a}$ must generally be empirically scaled so that the algorithm converges.

A ZDI reconstruction depends on a certain number of input stellar parameters (e.g., stellar rotation period, inclination, projected rotational velocity, DR parameters). Modifying one of these parameters will affect the synthetic line profiles generated in ZDI and, thus, our ability to match the observed line profiles to a given $\chi_{\rm a}$. To estimate the parameters that match best the observations, we build a grid of parameters and, for each value of the parameters in this grid, carry out a ZDI reconstruction of the observed profiles for a given amount of information at the surface of the star (i.e., a given amount of spot coverage and/or magnetic field). This process yields a multi-dimensional map of χ^2 from which we estimate the best parameters and their error bars using the method detailed in Appendix A.2.4. Note that a ZDI reconstruction is a rather slow process, which takes more or less time to converge depending on the number of parameters to recover and the number of observations. As a consequence, we recommend either to avoid high-dimensional parameter space exploration or to parallelize it and run it on a computer cluster (as it is the case for a lately implemented version). For the time being ZDI is also too time-consuming to implement a MCMC exploration of the parameter space (see Section A.2.5, even though the estimation of the parameter will highly benefit from such upgrade.

A.2 Maximum a posteriori estimator

A.2.1 Notation: multivariate Gaussian distribution

Let us consider a vector $\boldsymbol{x} = (x_1, ..., x_n)$ of n random variables x_i. If $\boldsymbol{x}$ is drawn from a Gaussian distribution of mean $\boldsymbol{\mu}$ and covariance matrix $\boldsymbol{\Sigma}$, then we note $\boldsymbol{x} \sim \mathscr{N}(\boldsymbol{x}; \boldsymbol{\mu}, \boldsymbol{\Sigma})$ where

$$\mathscr{N}(\boldsymbol{x}; \boldsymbol{\mu}, \boldsymbol{\Sigma}) = \frac{1}{(2\pi)^{n/2}} \frac{1}{\sqrt{|\boldsymbol{\Sigma}|}} \exp -\frac{1}{2}\Big[(\boldsymbol{x} - \boldsymbol{\mu})^{\rm T} \boldsymbol{\Sigma}^{-1} (\boldsymbol{x} - \boldsymbol{\mu})\Big]. \tag{A.12}$$

A.2.2 Posterior density law

Let us consider a set of $N_{\rm d}$ data points (x_i, y_i, σ_i), σ_i being the measurement error on y_i, assumed independent and normally-distributed here, and x_i being the input (e.g., observation times). We model $\boldsymbol{y} = (y_i)_{i=1,...,N_{\rm d}}$ by a function y_p depending on $N_{\rm p}$ parameters $\boldsymbol{\omega} = (\omega^{(1)}, ..., \omega^{(N_{\rm p})})$ and we want to find the parameters for which y_p matches best the observed data set. Let us regard $\boldsymbol{\omega}$ as a random variable of prior density π (i.e., the probability distribution of $\boldsymbol{\omega}$ prior to the observations). The goal is to determine the value of $\boldsymbol{\omega}$ that maximises the probability distribution p of the parameters given the observations and the model, called M in the following. $p(\boldsymbol{\omega}|\boldsymbol{y}, M)$, referred to as the *posterior density* of the parameters, quantifies the amount of information available on the model parameters after the observations have been made. In the Bayesian framework, p can be expressed as a function of π, such that

$$p(\boldsymbol{\omega}|\boldsymbol{y}, M) = \frac{\mathscr{L}(\boldsymbol{y}|\boldsymbol{\omega}, M)\pi(\boldsymbol{\omega})}{f(\boldsymbol{y}|M)}, \tag{A.13}$$

where $f(\boldsymbol{y}|M)$ is the normalizing constant and $\mathscr{L}(\boldsymbol{y}|\boldsymbol{\omega}, M)$ is the so-called likelihood of the data. Since the probability of the data is the same as the probability of the noise, $\mathscr{L}$ is simply Gaussian-distributed such that

$$\mathscr{L}(\boldsymbol{y}|\boldsymbol{\omega}, M) = \mathscr{N}(\boldsymbol{y}; \boldsymbol{y_p}, \boldsymbol{\Sigma}), \tag{A.14}$$

where $\boldsymbol{y_p} = (y_p(x_i))_{i=1,\dots,N_\mathrm{d}}$, and $\boldsymbol{\Sigma}$ is the covariance matrix of the noise in the data, $\boldsymbol{\Sigma}_{i,j} = \sigma_i \delta_{i,j}$, δ being the Kronecker delta. The method consisting in maximising the posterior density to estimate the parameters of the model given from the observations is standardly refereed to as a maximum a posteriori estimator (MAP). To simplify the markings, M is no longer written as an argument of the probability distributions in the following.

A.2.3 Linear model

We consider a simple case where y_p linearly depends on the model parameters. The model is thus written $\boldsymbol{y_p} = \boldsymbol{X}\boldsymbol{\omega}$, where $\boldsymbol{X}$ is a matrix of size $(N_\mathrm{d}, N_\mathrm{p})$, independent of $\boldsymbol{\omega}$. By combining Eq. A.13 and Eq. A.14, the posterior density of the model is given by

$$p(\boldsymbol{\omega}|\boldsymbol{y}) \propto \pi(\boldsymbol{\omega}) \mathscr{N}(\boldsymbol{y}; \boldsymbol{X}\boldsymbol{\omega}, \boldsymbol{\Sigma}). \tag{A.15}$$

By developing Eq. A.15, one can show that

$$p(\boldsymbol{\omega}|\boldsymbol{y}) \propto \pi(\boldsymbol{\omega}) \mathscr{N}\left(\boldsymbol{\omega}; \boldsymbol{A}^{-1}\boldsymbol{b}, \boldsymbol{A}^{-1}\right), \tag{A.16}$$

where

$$\begin{cases} \boldsymbol{A} &= \boldsymbol{X}^\mathrm{T}\boldsymbol{\Sigma}^{-1}\boldsymbol{X} \\ \boldsymbol{b} &= \boldsymbol{X}^\mathrm{T}\boldsymbol{\Sigma}^{-1}\boldsymbol{y}. \end{cases} \tag{A.17}$$

In practice, we generally assume an arbitrarily large (i.e., uninformative) prior density on $\boldsymbol{\omega}$, such as $\pi(\boldsymbol{\omega})$ is constant to the first order. Using a MAP, we find that the best (i.e., most likely) parameters of the model are given by $\boldsymbol{A}^{-1}\boldsymbol{b}$, while their covariance is given by the matrix $\boldsymbol{A}^{-1}$ from which we estimate the dispersion on each parameter.

A.2.4 Chi-square fitting

General principle

We now consider the case of non-linear dependency of the model on the parameters. In this case, the posterior density of the parameters is given by

$$p(\boldsymbol{\omega}|\boldsymbol{y}) \propto \pi(\boldsymbol{\omega}) \mathscr{N}(\boldsymbol{y}; \boldsymbol{y_p(\omega)}, \boldsymbol{\Sigma}). \tag{A.18}$$

In the general case, no analytical development of Eq. A.18 is possible and we need to sample the posterior density of the model to determine its shape. In the case of an arbitrarily large prior density on the parameters, the MAP estimator is similar the Least-Squares estimator, whose principle is to minimize the Chi-Square χ^2 of the residuals of the fit, given by

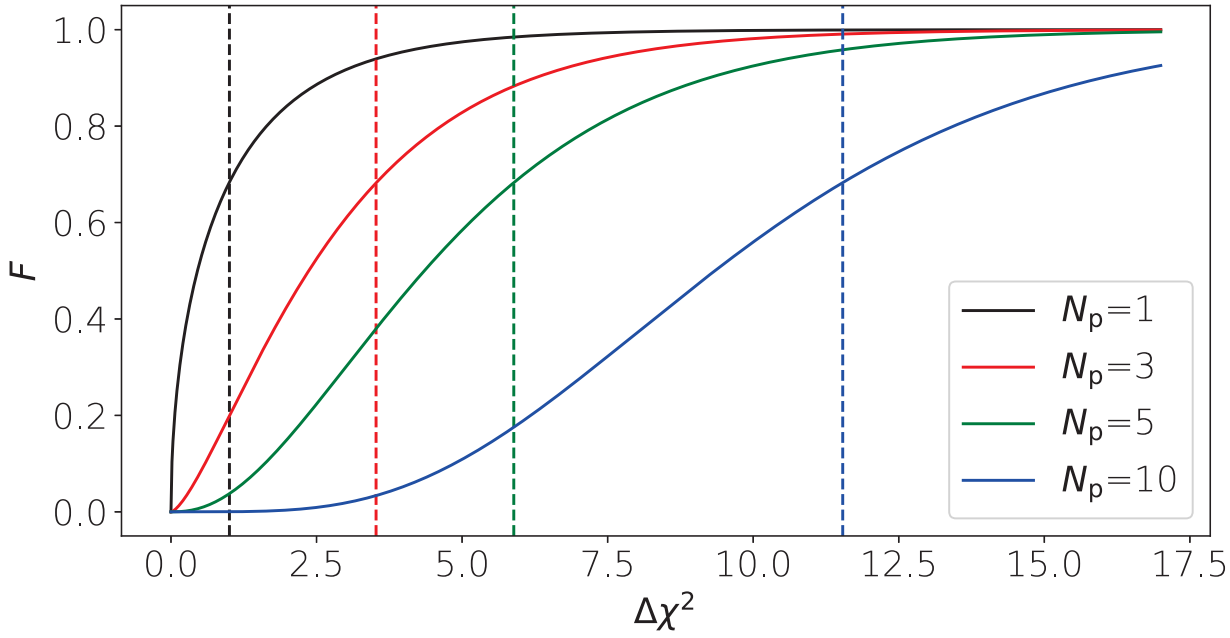

Figure A.1 – Cumulative distribution function of the chi-square probability law for N_p of 1, 3, 5 and 10 parameters. The vertical dashed lines indicate the value of $\Delta\chi^2$ for which $F = 68.27\%$ (corresponding to the 1σ-confidence interval of a normal distribution.

$$\chi^2(\boldsymbol{\omega}) = \sum_{i=1}^{N_\mathrm{d}} \left(\frac{y_i - y_p(x_i;\boldsymbol{\omega})}{\sigma_i} \right)^2 = (\boldsymbol{y} - \boldsymbol{y_p}(\boldsymbol{\omega}))^\mathrm{T} \boldsymbol{\Sigma}^{-1} (\boldsymbol{y} - \boldsymbol{y_p}(\boldsymbol{\omega})) \tag{A.19}$$

For wide parameter spaces, the χ^2 sampling procedure can be time-consuming. Hence the interest to use efficient algorithms like that proposed by Levenberg (1944) and Marquardt (1963) (called LM algorithm in the following), to locate the region of the parameter space where χ^2 is minimum. To determine the best parameters and their uncertainties, we compute χ^2 on a fine grid of parameters around the minimum value identified by the LM algorithm, resulting in a N_p dimension map of χ^2. The best set of parameters $\boldsymbol{\omega_\mathbf{b}}$ is the one that minimises the χ^2 (χ^2 is ideally equal to 1 when the data are fitted to the level of the noise).

Confidence intervals

In this paragraph, we describe how we estimate the 1σ uncertainties on each parameter using χ^2 statistics. Let us call χ^2_min the minimum of χ^2 of the grid. As a sum of independent normally-distributed variables, $\Delta\chi^2(\boldsymbol{\omega}) = \chi^2(\boldsymbol{\omega}) - \chi^2_\mathrm{min}$ follows a *chi-square* probability law whose cumulative distribution function F is given by

$$F(\Delta\chi^2, N_\mathrm{p}) = \gamma(N_\mathrm{p}/2, \Delta\chi^2/2), \tag{A.20}$$

where γ is the incomplete gamma function. Figure A.1 shows how F varies as a function of $\Delta\chi^2$ for different number of parameters.

Let us consider a given parameter $\omega^{(i)}$ of the model. At $\omega^{(i)} = \omega_\mathrm{b}^{(i)} \in \boldsymbol{\omega_\mathbf{b}}$, $\Delta\chi^2 = 0$. The 1σ uncertainty $\delta\omega^{(i)}$ on $\omega^{(i)}$ is the quantity that we need to add (or subtract) to $\omega_\mathrm{b}^{(i)}$, so that

$$\Delta\chi^2(\omega_{\rm b}^{(1)},...,\omega_{\rm b}^{(i-1)},\omega_{\rm b}^{(i)}+\delta\omega^{(i)},\omega_{\rm b}^{(i+1)},...,\omega_{\rm b}^{(N_{\rm p})})=1. \tag{A.21}$$

In other words, $\delta\omega^{(i)}$ is the distance to cover from $\boldsymbol{\omega_{\rm b}}$ along the $\omega^{(i)}$ axis so that 68.27% are included within the contour $\Delta\chi^2=\delta\omega^{(i)}$.

In practice, $\delta\omega^{(i)}$ can be empirically determined from the χ^2map, provided that the sampling is fine-enough. Another option that we use in this manuscript is to fit a $N_{\rm p}$-dimension paraboiloid $\mathscr{P}_{N_{\rm p}}$ to the χ^2 map around $\chi_{\rm min}$ (where $\Delta\chi^2$ depends quadratically on small variations of each parameter to the first order). The coefficients of $\mathscr{P}_{N_{\rm p}}$ are linearly estimated with a linear least-squares estimator (see Section A.2.3). The number of points included in the fit is chosen so that the dispersion of the residuals χ^2 map is of the order of 1. The error bars on each parameter scale with the curvature of the fitted paraboloid (large curvatures are associated with small errors and inversely), that can be analytically determined from the coefficients of the paraboloid. In this manuscript, we encounter cases where $N_{\rm p}$ is equal to 1, 2 and 3. We detail below the relationship between the uncertainties on each parameter, $\Delta\chi^2$, and the coefficients of the paraboloid linearly fitted to the χ^2 map. In the following, we assume that the paraboloid parameters are such that all subsequent relations are well defined mathematically.

- **One parameter:** At $N_{\rm p}=1$, we linearly model the χ^2 distribution using a simple parabola $\mathscr{P}_1$ depending on three real inputs (a,b,c) such that

$$\left\{\begin{array}{lcl}\mathscr{P}_1:\mathbb{R} & \rightarrow & \mathbb{R}\\ x & \rightarrow & ax^2+bx+c\end{array}\right. \tag{A.22}$$

  where $a>0$. The parameter $\omega_{\rm b}^{(1)}$ that minimises $\mathscr{P}$ is simply given by $\omega_{\rm b}^{(1)}=-b/(2a)$ and the uncertainties on $\omega^{(1)}$ are given by $\delta\omega^{(1)}(\Delta\chi^2)=\sqrt{\Delta\chi^2/a}$.
- **Two parameters:** At $N_{\rm p}=2$, we fit the χ^2 distribution using a bivariate paraboloid $\mathscr{P}_2$ given by

$$\left\{\begin{array}{lcl}\mathscr{P}_2:\mathbb{R}^2 & \rightarrow & \mathbb{R}\\ (x,y) & \rightarrow & ax^2+bxy+cy^2+dx+ey+f\end{array}\right. \tag{A.23}$$

  where (a,b,c,d,e,f) are the coefficients of $\mathscr{P}_2$. The parameters $\omega_{\rm b}^{(1)}$ and $\omega_{\rm b}^{(2)}$ that minimize the distribution of χ^2 are given by

$$\left\{\begin{array}{lcl}\omega_{\rm b}^{(1)} & = & (be-2cd)/(4ac-b^2)\\ \omega_{\rm b}^{(2)} & = & (bd-2ae)/(4ac-b^2)\end{array}\right. \tag{A.24}$$

  with the corresponding uncertainties

$$\left\{\begin{array}{lcl}\delta\omega^{(1)}(\Delta\chi^2) & = & \sqrt{\frac{\Delta\chi^2}{a-\frac{b^2}{4c}}}\\ \delta\omega^{(2)}(\Delta\chi^2) & = & \sqrt{\frac{\Delta\chi^2}{c-\frac{b^2}{4a}}}\end{array}\right. \tag{A.25}$$

◦ **Three parameters:** At $N_\mathrm{p}=3$, we fit the χ^2 distribution using a 3D paraboloid $\mathscr{P}_3$ given by

$$\left\{\begin{array}{lcl} \mathscr{P}_3 : \mathbb{R}^2 & \to & \mathbb{R} \\ (x,y,z) & \to & ax^2+by^2+cz^2+dxy+exz+fyz+gx+hy+iz+j \end{array}\right. \tag{A.26}$$

The parameters $\omega_\mathrm{b}^{(1)}$, $\omega_\mathrm{b}^{(2)}$ and $\omega_\mathrm{b}^{(3)}$ that minimize the distribution of χ^2 are given by

$$\left\{\begin{array}{lcl} \omega_\mathrm{b}^{(1)} & = & (ED-FB)/(AB-DC) \\ \omega_\mathrm{b}^{(2)} & = & (IA-BH)/(AD-BG) \\ \omega_\mathrm{b}^{(3)} & = & (LD-KA)/(DB-AJ) \end{array}\right. \tag{A.27}$$

where

$$\left\{\begin{array}{lcl} A & = & 2af-de \\ B & = & 2cd-ef \\ C & = & 4ac-e^2 \\ D & = & df-2be \\ E & = & 2cg-ei \\ F & = & fg-eh \\ G & = & d^2-4ab \\ H & = & dg-2ah \\ I & = & eh-di \\ J & = & f^2-4bc \\ K & = & fh-2bi \\ L & = & fg-di \end{array}\right. \tag{A.28}$$

The corresponding uncertainties on each parameter are then given by

$$\left\{\begin{array}{lcl} \delta\omega^{(1)}(\Delta\chi^2) & = & \sqrt{\frac{\Delta\chi^2}{a-\frac{be^2+cd^2-def}{4bc-f^2}}} \\ \delta\omega^{(2)}(\Delta\chi^2) & = & \sqrt{\frac{\Delta\chi^2}{b-\frac{af^2+cd^2-def}{4ac-e^2}}} \\ \delta\omega^{(3)}(\Delta\chi^2) & = & \sqrt{\frac{\Delta\chi^2}{c-\frac{af^2+be^2-def}{4ab-d^2}}} \end{array}\right. \tag{A.29}$$

A.2.5 MCMC processes

Principle

A Markov Chain Monte Carlo (MCMC) process samples the posterior distribution p of the parameters of the model by building a randomly-driven Markov chain whose equilibrium distribution is p.

Let us call $\boldsymbol{\omega}_n$ the set of parameters generated at iteration n. The principle of a MCMC process is that $\boldsymbol{\omega}_{n+1}$ is generated from a probability distribution P_r which only depends on the present value of the parameters $\boldsymbol{\omega}_n$, and on the probability law p to sample, such that

$$P_\mathrm{r}(\boldsymbol{\omega}_{n+1}|\boldsymbol{\omega}_n, \boldsymbol{\omega}_{n-1}, ..., \boldsymbol{\omega}_0, \boldsymbol{y}) = P_\mathrm{r}(\boldsymbol{\omega}_{n+1}|\boldsymbol{\omega}_n, \boldsymbol{y}). \tag{A.30}$$

MCMC processes allow to sample the whole posterior distribution without being trapped in local minimums, which is a major advantage over sampling methods based on predefined grids of parameters. Moreover, since the samples of the chain are independent from their previous counterparts, the resulting posterior distribution does in principle not depend on the initial set of the parameters, contrary to standard minimization algorithms (e.g., LM algorithm). However, the aforementioned properties require the convergence of the MCMC (i.e., the state where the drawn sets of parameters systematically belong to the posterior distribution) to be verified. In principle, MCMC processes always converge, but reaching the convergence state will take more or less iterations depending on the choice of P_r and $\boldsymbol{\omega_0}$. There is no easy rule to determine whether a given MCMC process has converged. One possibility is to compute the so-called *autocorrelation time* τ of the chain, which measures the number of iterations needed to produce independent samples of p (e.g., Foreman-Mackey et al., 2013), and to take a significantly larger number of iterations for the MCMC process[2]. In all cases, many iterations are needed to ensure a dense coverage of p, which generally makes MCMC processes time-consuming. Many different types of MCMC samplers exist in the literature. We give below a short description of the two MCMC algorithms that are used in this manuscript and redirect the reader to the review of Sharma (2017) and the tutorials therein.

Metropolis-Hastings algorithm

The standard MCMC algorithm is the so-called Metropolis-Hastings (MH) algorithm (Metropolis et al., 1953; Hastings, 1970). At each iteration n of the MH process, a new set of parameters is drawn from a proposal density $q(\boldsymbol{\omega}_{n+1}|\boldsymbol{\omega}_n)$ (typically Gaussian). The proposed set of parameters is then accepted with a probability $\alpha(\boldsymbol{\omega}_{n+1}|\boldsymbol{\omega}_n)$ given by

$$\alpha(\boldsymbol{\omega}_{n+1}|\boldsymbol{\omega}_n) = \min\left[1, \frac{\mathrm{p}(\boldsymbol{\omega}_{\mathrm{n}+1}|\boldsymbol{y})\mathrm{q}(\boldsymbol{\omega}_{\mathrm{n}}|\boldsymbol{\omega}_{\mathrm{n}+1})}{\mathrm{p}(\boldsymbol{\omega}_{\mathrm{n}}|\boldsymbol{y})\mathrm{q}(\boldsymbol{\omega}_{\mathrm{n}+1}|\boldsymbol{\omega}_{\mathrm{n}})}\right]. \tag{A.31}$$

If the proposed set of parameter is not accepted, then $\boldsymbol{\omega}_{n+1} = \boldsymbol{\omega}_n$ and a new set of parameter is proposed. Note that choosing a symmetric density law for q (e.g., Gaussian distribution) reduces the acceptance probability to the ratio of the posterior densities. The proposal density of the MH controls its convergence (by controlling the size of the jump from one set of parameters to the next) and must be wisely tune to optimally sample the posterior density. The mean acceptance rate over the chain is a good proxy to tune q. To illustrate this point, let us consider a case where $N_\mathrm{p} = 1$ (i.e., one parameter to recover) and where q is a Normal distribution of standard deviation $\sigma\mathrm{j}$. If $\sigma\mathrm{j}$ is too large compared to the typical standard deviation of its posterior distribution, then the proposed samples will be quasi-systematically rejected and α will be arbitrarily low. In contrast, if $\sigma\mathrm{j}$ is too small compared to the typical standard deviation of p, then α will be close to 1 and the MCMC process will take an arbitrarily long time to sample the posterior density. In practice, we empirically tune q by running a few MCMC processes of typically 10 000 iterations each and iteratively rescaling the jumps (e.g., the covariance matrix of the proposal density) until the mean acceptance rate lies close to the values recommended in Gelman et al. (1996) (typically 0.25-0.3).

[2] See also the following tutorial of the convergence of MCMC processes: https://emcee.readthedocs.io/en/stable/tutorials/autocorr/

Adaptive MCMC samplers

In practice, more efficient MCMC samplers able to adapt their proposal density according to the previous samples in the chain are generally preferred to MH algorithms (Haario et al., 2001). In particular, the affine-invariant sampler EMCEE described in Goodman & Weare (2010) and implemented as a python package in Foreman-Mackey et al. (2013)[3] is one of the most widely used MCMC sampler in the community. This sampler allows for an efficient exploration of the parameter space based on the fact that the proposal density is randomly modified (using affine laws) at each iteration which allows to rapidly decrease the correlation between the samples of the chain and thus converge more efficiently. In practice, EMCEE runs simultaneously evolving chains (called walkers) sampling the same posterior density. At each iteration, the proposal density of a given walker is randomly modified depending on the current value of the other walkers.

Other stochastic samplers are particularly efficient to avoid being trapped in local minimums. For example, parallel Tempering (e.g., Gregory, 2005a,b) consists in sampling the posterior density using several chains in parallel. Each chain features a so-called *temperature* that controls the proposal density: the larger the temperature, the higher the acceptance rate of the samples. Another promising method is the so-called *diffusive nested sampling* (DNS), introduced by Skilling (2006) and Brewer et al. (2009) and recently applied to exoplanetology in Brewer (2014) and Faria et al. (2016), whose formalism allows to change the dimension of the parameter space. This method is thus well suited to compare models searching for different numbers of planet signatures in RV data.

A.2.6 Marginalization of the likelihood over linear parameters

Reminder: the matrix inversion lemma

Let us consider four matrices $\boldsymbol{A}$, $\boldsymbol{B}$, $\boldsymbol{C}$, $\boldsymbol{D}$ of respective dimensions (M, M), (M, N), (N, N) and (N, M), where M and N are two arbitrary strictly positive integers.

If $\boldsymbol{A}$ and $\boldsymbol{C}$ are invertible, then

1. $\left(\boldsymbol{A} - \boldsymbol{B}\boldsymbol{C}^{-1}\boldsymbol{D}\right)$ invertible $\Leftrightarrow$ $\left(\boldsymbol{C} - \boldsymbol{D}\boldsymbol{A}^{-1}\boldsymbol{B}\right)$ invertible
2. $\left(\boldsymbol{A} - \boldsymbol{B}\boldsymbol{C}^{-1}\boldsymbol{D}\right) = \boldsymbol{A}^{-1} + \boldsymbol{A}^{-1}\boldsymbol{B}\left(\boldsymbol{C} - \boldsymbol{D}\boldsymbol{A}^{-1}\boldsymbol{B}\right)^{-1}\boldsymbol{D}\boldsymbol{A}^{-1}$

This lemma can be extended to the calculation of the determinant of a sum of matrix, such that, under the same assumptions

$$|\boldsymbol{A} + \boldsymbol{B}\boldsymbol{D}| = |\boldsymbol{A}|\left|\boldsymbol{I} + \boldsymbol{D}\boldsymbol{A}^{-1}\boldsymbol{B}\right| \tag{A.32}$$

where $\boldsymbol{I}$ is the identity matrix.

Deriving the marginal density law

Let us consider a data set $\boldsymbol{V}_\mathbf{r}$ containing N_d data points. We model $\boldsymbol{V}_\mathbf{r}$ as a linear combination of N_l parameters $\boldsymbol{\omega}$ embedded in Gaussian correlated noise, such that

$$\boldsymbol{V}_\mathbf{r} = \boldsymbol{X}\boldsymbol{\omega} + \boldsymbol{V}_\mathbf{j}(\boldsymbol{\theta}) + \boldsymbol{\epsilon}, \tag{A.33}$$

where $\boldsymbol{V}_\mathbf{j}(\boldsymbol{\theta})$ and $\boldsymbol{\epsilon}$ are drawn from centered Gaussian density laws of respective covariance matrices $\boldsymbol{K}(\boldsymbol{\theta})$, modeled by a set of N_nl non-linear free parameters $\boldsymbol{\theta}$, and $\boldsymbol{\Sigma}$, a diagonal matrix of known terms (i.e., uncorrelated uncertainties of each data point). $\boldsymbol{X}$ is a known matrix of dimensions

[3] https://emcee.readthedocs.io/en/stable/user/sampler/

(N_d,N_l). In what follows, we define $\boldsymbol{\Lambda} = \boldsymbol{K}(\boldsymbol{\theta}) + \boldsymbol{\Sigma}$ as the covariance matrix of the correlated noise in the data set.

The posterior density of the parameters of the model is given by

$$p(\boldsymbol{\omega}, \boldsymbol{\theta}|\boldsymbol{V_\mathrm{r}}) = \pi(\boldsymbol{\theta})\pi(\boldsymbol{\omega})\mathscr{L}(\boldsymbol{V_\mathrm{r}}|\boldsymbol{\omega}, \boldsymbol{\theta}), \tag{A.34}$$

where $\pi(\boldsymbol{\theta})$ and $\pi(\boldsymbol{\omega})$ are the prior densities on the non-linear and linear parameters of the model. In particular, we assume that $\pi(\boldsymbol{\omega})$ is drawn from a Gaussian density law of mean $\boldsymbol{m}$ and standard deviation $\boldsymbol{S}$, $\pi(\boldsymbol{\omega}) \sim \mathscr{N}(\boldsymbol{m}, \boldsymbol{S})$. As the correlated noise is assumed Gaussian, the likelihood of the data is thus given by

$$\mathscr{L}(\boldsymbol{V_\mathrm{r}}|\boldsymbol{\theta}, \boldsymbol{\omega}) = \frac{1}{(2\pi)^{N_\mathrm{d}/2}} \frac{1}{|\boldsymbol{\Lambda}|} \exp\left(-\frac{1}{2}(V_\mathrm{r} - \boldsymbol{X\omega})^\mathrm{T} \boldsymbol{\Lambda}^{-1} (V_\mathrm{r} - \boldsymbol{X\omega})\right), \tag{A.35}$$

where we assumed that $\boldsymbol{\omega}$ and $\boldsymbol{\theta}$ are independent. We integrate Eq. A.34 on $\boldsymbol{\omega}$, which gives

$$p(\boldsymbol{\theta}|\boldsymbol{V_\mathrm{r}}) = \pi(\boldsymbol{\theta}) \int_\omega \mathscr{L}(\boldsymbol{V_\mathrm{r}}|\boldsymbol{\omega}, \boldsymbol{\theta})\pi(\boldsymbol{\omega})\mathrm{d}\boldsymbol{\omega}. \tag{A.36}$$

The only way that the integrand in Eq. A.36 depends on $\boldsymbol{\omega}$ is through an exponential of a quadratic form of $\boldsymbol{\omega}$, such that

$$\int_\omega \mathscr{L}(\boldsymbol{V_\mathrm{r}}|\boldsymbol{\omega}, \boldsymbol{\theta})\pi(\boldsymbol{\omega})\mathrm{d}\boldsymbol{\omega} \propto \int_\omega \exp -\frac{1}{2}\left(\boldsymbol{\omega}^\mathrm{T}\boldsymbol{\Gamma\omega} - 2\boldsymbol{\beta}^\mathrm{T}\boldsymbol{\omega}\right) \propto \sqrt{\frac{(2\pi)^{N_\mathrm{l}}}{|\boldsymbol{\Gamma}|}} \exp\left(\frac{1}{2}\boldsymbol{\beta}^\mathrm{T}\boldsymbol{\Gamma}^{-1}\boldsymbol{\beta}\right), \tag{A.37}$$

where

$$\begin{cases} \boldsymbol{\Gamma} &= \boldsymbol{X}^\mathrm{T}\boldsymbol{\Lambda}^{-1}\boldsymbol{X} + \boldsymbol{S} \\ \boldsymbol{\beta} &= \boldsymbol{X}^\mathrm{T}\boldsymbol{\Lambda}^{-1}\boldsymbol{V_\mathrm{r}} + \boldsymbol{S^{-1}m}. \end{cases} \tag{A.38}$$

By expressing Eq. A.36 using Eq. A.37, we find

$$p(\boldsymbol{\theta}|\boldsymbol{V_\mathrm{r}}) = \pi(\boldsymbol{\theta}) \sqrt{\frac{2\pi^{N_\mathrm{l}-N_\mathrm{d}}}{|\boldsymbol{S}||\boldsymbol{\Gamma}||\boldsymbol{\Lambda}|}} \exp -\frac{1}{2}\left(\boldsymbol{V_\mathrm{r}}^\mathrm{T}\boldsymbol{\Lambda}^{-1}\boldsymbol{V_\mathrm{r}} + \boldsymbol{m}^\mathrm{T}\boldsymbol{S}^{-1}\boldsymbol{m} - \boldsymbol{\beta}^\mathrm{T}\boldsymbol{\Gamma}^{-1}\boldsymbol{\beta}\right). \tag{A.39}$$

By developing the exponential term of equation A.39 using the matrix inversion lemma, we find that

$$p(\boldsymbol{\theta}|\boldsymbol{V_\mathrm{r}}) \propto \pi(\boldsymbol{\theta})\, \mathscr{N}\left(\boldsymbol{V_\mathrm{r}}; \boldsymbol{Xm}, \boldsymbol{\Lambda} + \boldsymbol{XSX}^\mathrm{T}\right), \tag{A.40}$$

which is unsurprisingly a Gaussian distribution. In practice, we use an arbitrarily large prior distribution on $\boldsymbol{\omega}$ which is similar as assuming an improper uniform prior distribution on $\mathbb{R}$ for $\boldsymbol{\omega}$. The posterior density of Eq. A.40 is sampled using z MCMC process. After removing a sufficiently long burn-in period from the chain (of a few autocorrelation times), we compute the best estimates of $\boldsymbol{\theta}$, $\boldsymbol{\theta_{\mathrm{best}}}$ (with a maximum a posteriori estimator) and the error bars (by taking the 16^{th} and 84^{th} percentiles of each individual distribution) from the posterior distribution on $\boldsymbol{\theta}$.

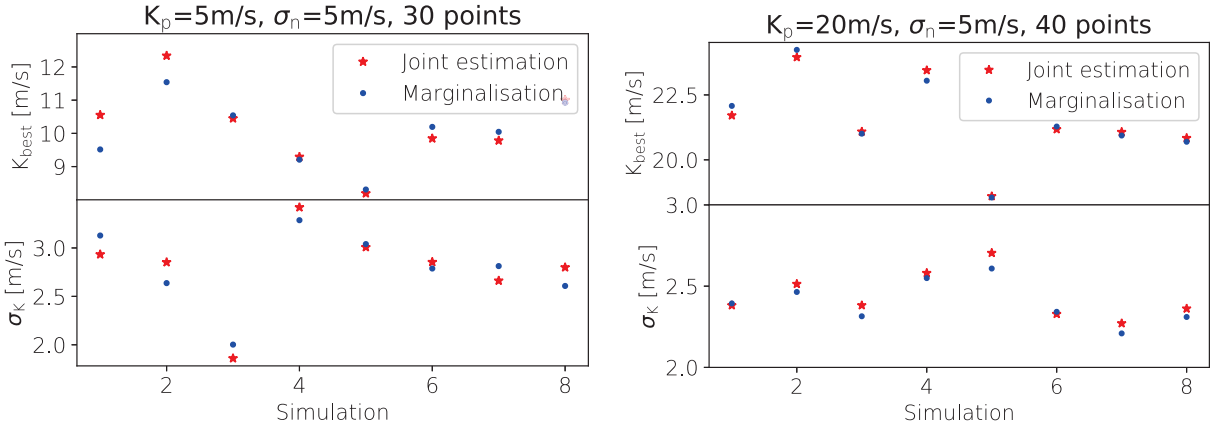

Figure A.2 – Comparison of the best estimates of the semi-amplitude of K2-33 b (top panels) and its 1σ-uncertainties (bottom panels) recovered in case D_1 (left panel) and D_2 (right panel). In each panel, the blue dots are the values obtained by sampling the posterior distribution of the model marginalized over the planet parameter, while the red stars are obtained by jointly sampling the planet and stellar activity parameters with a MCMC process.

Recovering the linear parameters

For a given set of non-linear parameters $\boldsymbol{\theta}$, the linear parameters of the model are simply recovered from a Least-Squares estimator (see Appendix A.2.3), and their posterior densities are drawn from a multivariate Gaussian distribution:

$$p(\boldsymbol{\omega}|\boldsymbol{V_r}, \boldsymbol{\theta}) \sim \mathcal{N}\left(\boldsymbol{A}^{-1}(\boldsymbol{\theta})\boldsymbol{b}(\boldsymbol{\theta}), \boldsymbol{A}^{-1}(\boldsymbol{\theta})\right) \tag{A.41}$$

where

$$\begin{cases} \boldsymbol{A}(\boldsymbol{\theta}) &= \boldsymbol{X}^{\mathrm{T}}[\boldsymbol{K}(\boldsymbol{\theta}) + \boldsymbol{\Sigma}]^{-1}\boldsymbol{X} \\ \boldsymbol{b}(\boldsymbol{\theta}) &= \boldsymbol{X}^{\mathrm{T}}[\boldsymbol{K}(\boldsymbol{\theta}) + \boldsymbol{\Sigma}]^{-1}\boldsymbol{V_r}, \end{cases} \tag{A.42}$$

assuming an arbitrarily large prior density on $\boldsymbol{\omega}$. To ensure a robust estimation of $\boldsymbol{\omega}$ and its error bars, we compute the posterior distribution of $\boldsymbol{\omega}$ using Eq. A.41 for all the samples $\boldsymbol{\theta}$ obtained from the MCMC process, and convolve the resulting distribution with $p(\boldsymbol{\omega}|\boldsymbol{V_r}, \boldsymbol{\theta_{best}})$.

Validation of the method

To ensure that the process described above yields estimates of $\boldsymbol{\omega}$ consistent with those that would have been obtained by sampling $p(\boldsymbol{\omega}, \boldsymbol{\theta}|\boldsymbol{V_r})$ (i.e., joint posterior density), we carried out specific tests on synthetic RV time-series generated in Chapter 2 to simulate RV observations of K2-33. We created two sets of 8 RV time-series, called D_1 and D_2, with different realizations of a $5\,\mathrm{m\,s^{-1}}$ Gaussian white noise. D_1 and D_2 contain respectively 30 and 40 data points and a single planet RV signature of 5 and $20\,\mathrm{m\,s^{-1}}$. Here, $\boldsymbol{V_r}$ refers to a given RV data set, while $\boldsymbol{\omega}$ and $\boldsymbol{\theta}$ are respectively the planet and stellar activity parameters. We assume that the orbital phase of the planet is known, leaving the semi-amplitude of the planet RV signal, K_p as the only parameter to recover. Each data set is independently modeled by (i) jointly sampling the planet and stellar activity parameter using a MCMC process, and (ii) marginalizing over the planet parameters using the method described

above (i.e., sampling of the posterior density on $\boldsymbol{\theta}$ using Eq. A.40 and estimation of the planet parameters using Eq. A.41. The estimates of K_p are shown in Figure A.2. We first note that the two estimators yield consistent estimates of K_p and its error bars. In particular, no systematic trend is noted between the two estimations. This validation procedure was also applied to synthetic RV time-series of TRAPPIST-1, leading to the same conclusion.

A.3 Gaussian Processes

Definition and general principle

By definition, a Gaussian Process (GP) is a *collection of random variables, any finite number of which have a joint Gaussian distribution* (Rasmussen & Williams, 2006). A GP is characterized by its mean function $t \to m(t)$, and its covariance kernel $(t,t') \to k(t,t')$, where t is the input (assumed to be the time here, but can represent any kind of input, even in higher dimensional spaces), and generally noted $\mathscr{GP}(m,k)$. Let us consider of scalar function $f(t)$. If f is modeled by a GP, then, for any discrete time vector $\boldsymbol{t} = \{t_i\}_{i=1..N}$, the corresponding values of f, $\boldsymbol{F} = \{f(t_i)\}_{i=1..N}$ are assumed to be drawn from a joint Gaussian distribution of mean $\boldsymbol{m} = \{m(t_i)\}_{i=1..N}$ and covariance matrix $\boldsymbol{K} = \{k(t_i,t_j)\}_{i,j=1..N}$, such that

$$\boldsymbol{F} \sim \mathscr{N}(\boldsymbol{F}; \boldsymbol{m}, \boldsymbol{K}). \tag{A.43}$$

Gaussian process regression

Gaussian Process Regression (GPR) consists in modeling a given quantity y by a GP of mean m and covariance kernel k. Let us consider that N measurements of y were collected at times $\boldsymbol{t} = \{t_i\}_{i=1..N}$ with a Gaussian uncorrelated error bar σ_i on each measurement y_i. In GPR, we want to determine m and k so that our model for y matches best our data set $\boldsymbol{y} = \{f(t_i)\}_{i=1..N}$. In parametric approaches, both m and k are respectively described by parameters $\boldsymbol{\eta}$ and $\boldsymbol{\theta}$ whose posterior density $p(\boldsymbol{\eta}; \boldsymbol{\theta} | \boldsymbol{y})$ is sampled using a MCMC process (see Rasmussen & Williams, 2006, and the references therein for a introduction to non-parametric GP modeling). In the Bayesian framework, p is expressed as

$$p(\boldsymbol{\eta}; \boldsymbol{\theta} | \boldsymbol{y}) \propto \pi(\boldsymbol{\eta}, \boldsymbol{\theta})\, \mathscr{N}(\boldsymbol{y}; \boldsymbol{m}(\boldsymbol{\eta}), \boldsymbol{K}(\boldsymbol{\theta} + \boldsymbol{\Sigma})), \tag{A.44}$$

where π is the joint prior density on $\boldsymbol{\eta}$ and $\boldsymbol{\theta}$, and where $\boldsymbol{\Sigma}_{i,i} = \sigma_i \delta_{i,j}$, where δ is the Kronecker delta. The best parameters of the model, $\boldsymbol{\eta}_\mathbf{b}$ and $\boldsymbol{\theta}_\mathbf{b}$, are estimated by maximizing the sampled posterior distribution obtained after removing a burn-in period. In case of large data set, inverting the GP covariance matrix at each iteration of the MCMC process is time-consuming. We thus decompose $\boldsymbol{K}(\boldsymbol{\theta} + \boldsymbol{\Sigma})$ into a triangular matrix using Cholesky decomposition, which in practice allows to gain a precious time in the optimization process.

One of the strengths of the GP framework is that, once we have modeled the data set $\boldsymbol{y}$, it is possible to predict their value of the quantity y at any time with the associated uncertainty. In our example, we know the mean $\boldsymbol{m}_\mathbf{b} = \boldsymbol{m}(\boldsymbol{\eta}_\mathbf{b})$ and covariance matrix $\boldsymbol{K}_\mathbf{b} = \boldsymbol{K}(\boldsymbol{\theta}_\mathbf{b})$ of the GP that maximises the posterior density of the model given our observations. Let us assume that we want to predict the value of y at times $\boldsymbol{t}^* = \{t_j^*\}_{j=1..M} \neq \boldsymbol{t}$. Since y is modeled by a GP, we know from Eq. A.43 that $\boldsymbol{y}^* = \{y(t_j^*)\}_{j=1..N}$ is drawn from a Gaussian distribution of mean $\boldsymbol{m}^*$ and covariance matrix $\boldsymbol{K}^*$. By using the properties of Gaussian vectors on $[\boldsymbol{y}, \boldsymbol{y}^*]$, we find

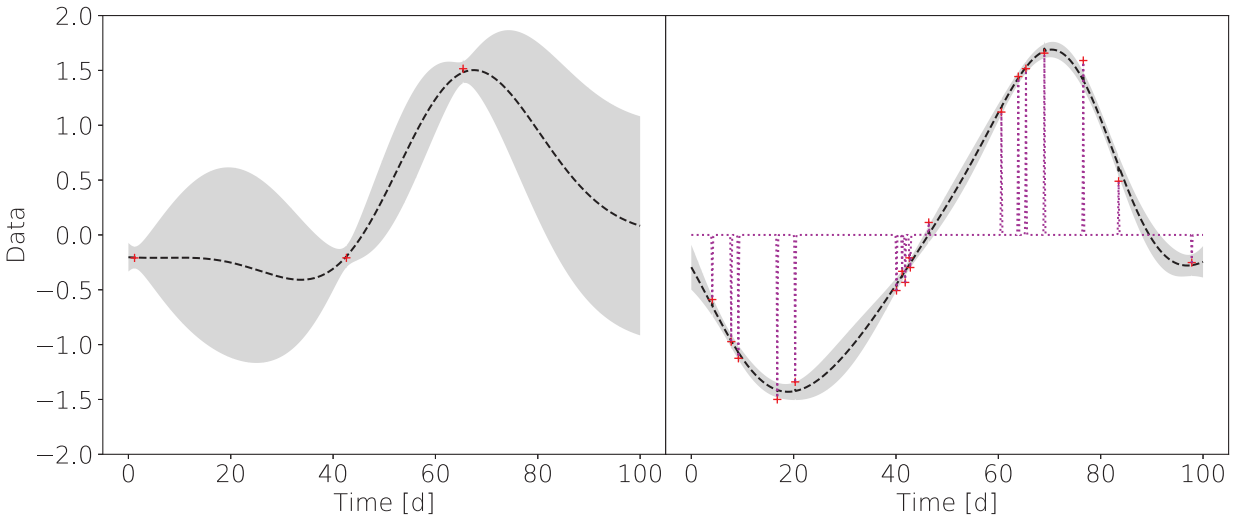

Figure A.3 – Example of GPR of data sets containing 3 points (left panel) and 20 points (right panel), generated using a square-exponential covariance kernel (amplitude: 1.0, decay time: 20 d). In each panel, the data points are indicated by red crosses and GP prediction assuming a square-exponential covariance kernel (amplitude: 1.0, decay time: 20 d) is shown as a black dashed line. The gray error bands are the $\pm 1\,\sigma$ predictions of the GP. In the right panel, the magenta dotted line is the GP prediction assuming a quasi-periodic GP kernel with an arbitrarily low smoothing parameter (i.e., the correlation between pair of data points is quasi-null).

$$\begin{cases} \boldsymbol{y}^* &= \boldsymbol{m}^* + \boldsymbol{K}(\boldsymbol{t}^*, \boldsymbol{t})[\boldsymbol{K}_\mathbf{b} + \Sigma]^{-1}(\boldsymbol{y} - \boldsymbol{m}) \\ \boldsymbol{\sigma}^* &= \boldsymbol{K}^* - \boldsymbol{K}(\boldsymbol{t}^*, \boldsymbol{t})[\boldsymbol{K}_\mathbf{b} + \Sigma]^{-1}\boldsymbol{K}(\boldsymbol{t}, \boldsymbol{t}^*), \end{cases} \tag{A.45}$$

where $\boldsymbol{\sigma}^* = \{\sigma_j^*\}_{j=1..M}$ are the 1σ uncertainties on $\boldsymbol{y}^*$, and where $\boldsymbol{K}(\boldsymbol{t}^*, \boldsymbol{t}) = (k(t_i, t_j^*)_{i<N, j<M})$.

Choosing the covariance kernel

GPR allows to jointly model deterministic and stochastic processes in a given data set. The components a known functional form (e.g., planetary RV signatures) are directly modeled by the mean function of the GP. In contrast, signals which are only known from their statistical properties (e.g., through their autocorrelation function like stellar activity RV signals) are modeled by parametrizing the covariance function of each pair of observations. The covariance kernel contains all the physical information that we have about the statistical properties of the stochastic signal to model and must be chosen wisely in order for the GP prediction to physically realistic. Several covariance kernels are commonly found in the literature. The so-called *square exponential* kernel is defined by

$$k(t_i, t_j) = \theta_1^2 \exp\left(-\frac{(t_i - t_j)^2}{\theta_2}\right), \tag{A.46}$$

where t_i and t_j are the time associated with observations i and j. The square exponential kernel depends on two hyperparameters: its maximum amplitude θ_1 and the time scale θ_2 on which the correlation decreases. Examples of GPR of data sets respectively containing 3 and 20 points are shown in the left- and right-hand panels of Figure A.3. To describe the quasi-periodic fluctuations induced by stellar activity on photometric and RV curve, a so-called *quasi-periodic kernel* is generally used in the literature:

$$\mathrm{k}(t_i, t_j; \boldsymbol{\theta}) = \theta_1^2 \exp\left[-\frac{(t_i - t_j)^2}{\theta_2^2} - \frac{\sin^2 \frac{\pi(t_i - t_j)}{\theta_3}}{\theta_4^2} \right]. \tag{A.47}$$

In this case, k is the combination of period and square exponential kernels. This kernel, fully described in Section 2.2.1.3, relies on four hyperparameters: the GP amplitude θ_1, the correlation decay time θ_2, the reccurrence time scale (or period) θ_3 and the smoothing parameters θ_4. As illustrated on the right-hand panel of Figure A.3 (magenta dotted line), arbitrarily low values of θ_4 in k imply that the correlation between each pair of data points is $\sim$0 and the data set is completely overfitted. Hence the need to wisely choose the prior density adopted for each parameter to ensure that the GP parameters remain physically realistic. Other GP kernels (e.g., Matèrn class kernels) are sometimes used to model stellar activity signals and the reader is invited to see Chapter 4 of Rasmussen & Williams (2006) for a detailed list of the different GP covariance functions and when they can be used.

A.4 Statistical evidence of planets in RV time-series

How many planetary signatures are present in a given RV time-series? What is the significance that a planet signature modulated at a given period is indeed present in the data? These fundamental questions remain challenging to answer and there is no consensus on a robust method to estimate the statistical significance of planets from RV time-series. In this section, we briefly introduce the most commonly used techniques to quantify the evidence for a planet in a given RV data set in Section **??**, before detailing the method of Chib & Jeliazkov (2001) that we preferentially use in this manuscript. For more information, the interested reader is invited to read the extensive comparison of the methods of Nelson et al. (2020).

A.4.0.1 Lomb-Scargle periodograms and derivatives

The search for planet signatures in RV time-series was historically carried out using the so-called Lomb-Scargle (LS) periodograms (Lomb, 1976; Scargle, 1982). In its basic version, a LS periodogram consists in fitting (e.g., using a linear least-squares estimator, see Section A.2.3) a simple sine-wave function (i.e., a circular planet signature) to a given RV time-series for a dense grid of periods. From the distribution of the goodness of the fit (e.g., χ^2 or likelihood) as a function of the period, one estimates the period at which the signal is most likely modulated. The LS-periodogram has undergone several improvements over the past few years, such as the inclusion in the model of an offset component (Ferraz-Mello, 1981) as well as independent uncertainties on the RV measurements (in the so-called generalized LS periodogram introduced in Zechmeister & Kürster, 2009, which is widely used by the community), and the transposition of the method in the Bayesian framework (Bayesian generalized LS periodogram; Mortier et al., 2015). Periodograms aimed at searching for Keplerian planet signatures have also been introduced by Cumming (2004) and Zechmeister & Kürster (2009). The process is however much more time-consuming than standard LS-periodograms as keplerian planet RV signatures depend on 3 non-linear parameters (orbital period, phase and eccentricity) and need optimized algorithms to efficiently sample the parameter space and get rid of local minima (Baluev, 2015).

The so-called *false alarm probability* (FAP) is computed to assess the significance of the most prominent peak of a given periodogram. It corresponds to the probability that the peak is due to a white noise realization. Each type of periodogram features a different FAP computation method (e.g., Baluev, 2008, 2015, for circular and elliptical planet orbits, respectively). For multiplanet systems, iterative algorithms like the *Matching Pursuit* (or pre-whitening; Gray & Desikachary,

1973) were widely used in early exoplanetology to estimate the number of planets in a given RV time-series. The goal is to identify the period P_0 of the prominent peak of the periodogram, to fit a planet signature assuming an orbital period of P_0 to the data set, and repeat the process with the residuals of the fit until no more peak lies above a given FAP level (typically 0.1 or 0.01%). These methods are however particularly affected by spurious signals (e.g., due to aliases in the sampling strategy or stellar activity signals) that could result in false positives if not identified (e.g., Rajpaul et al., 2016).

A.4.0.2 Marginal likelihood

Let us consider a model $\mathscr{M}_n$ relying on a set of parameters $\boldsymbol{\theta}$ searching for n planets in a RV time-series $\boldsymbol{V_r}$. In order to estimate the model parameters and their uncertainties, one samples the posterior density $p(\boldsymbol{\theta}|\boldsymbol{V_r}, \mathscr{M}_n)$ of the model parameters (e.g., using a MCMC process). To quantify the significance of the RV signature of planet n in the data, we compute the so-called *posterior odds ratio* $p(M_n|\boldsymbol{V_r})/p(M_{n-1}|\boldsymbol{V_r})$. In the Bayesian framework, the posterior odds ratio is expressed as

$$\frac{p(M_n|\boldsymbol{V_r})}{p(M_{n-1}|\boldsymbol{V_r})} = \frac{p(M_n)}{p(M_{n-1})} \frac{p(\boldsymbol{V_r}|M_n)}{p(\boldsymbol{V_r}|M_{n-1})}, \tag{A.48}$$

where the first term of the right-handed side of Eq. A.48 is known as the prior odds ratio (set to 1 in our case) and the second term, known as the Bayes factor BF_n, is the ratio of the so-called marginal likelihoods (MLs) of models containing n and $n-1$ planets, defined by:

$$p(\boldsymbol{V_r}|M_n) = \int_{\boldsymbol{\theta}} \pi(\boldsymbol{\theta}|\mathrm{M_n})\, \mathrm{p}(\boldsymbol{V_r}|\boldsymbol{\theta}, \mathrm{M_n})\, \mathrm{d}\boldsymbol{\theta}. \tag{A.49}$$

According to Jeffreys (1961) and Kass & Raftery (1995), $\ln \mathrm{BF}$s larger than 5 will be interpreted as a definite planet detection. Estimating the ML is however a tricky process as analytically integrating Eq. A.49 over the whole parameter space is often mathematically intractable. Several methods are used by the community to overcome this difficulty and estimate BF (e.g., importance and Nested-samplings, diffusive Nested-sampling; see Nelson et al., 2020, for an overview). The so-called *one-block MH* method, used in this manuscript, is described in following section.

A.4.1 Practical implementation of the one-block MH sampling of the marginal likelihood

Description of the method

Let us consider a RV time-series $\boldsymbol{V_r}$ and a model M_d relying on a set of non-linear parameters $\boldsymbol{\theta}$ whose posterior distribution is sampled with a MCMC process. The marginal likelihood (ML) of the model is given by

$$p(\boldsymbol{V_r}|M_\mathrm{d}) = \int_{\boldsymbol{\theta}} \pi(\boldsymbol{\theta}|\mathrm{M_d})\, \mathrm{p}(\boldsymbol{V_r}|\boldsymbol{\theta}, \mathrm{M_d})\, \mathrm{d}\boldsymbol{\theta}. \tag{A.50}$$

Chib & Jeliazkov (2001)'s method consists in expressing the ML as a function of quantities related to the MCMC process of the model parameters. In the Bayesian framework, the ML is simply given by

$$p(\boldsymbol{V_r}|M_\mathrm{d}) = \frac{\mathscr{L}(\boldsymbol{V_r}|\boldsymbol{\theta}, M_\mathrm{d})\,\pi(\boldsymbol{\theta}|\mathrm{M_d})}{\pi(\boldsymbol{\theta}|\boldsymbol{V_r}, \mathrm{M_d})}. \tag{A.51}$$

The denominator of Eq. A.50, called the posterior ordinate, is computed using the posterior distributions of the parameters sampled with the MCMC process. In standard Metropolis-Hastings moves, a candidate set of parameters $\boldsymbol{\theta'}$ is drawn from an initial set of parameter $\boldsymbol{\theta}$ through a proposal density $q(\boldsymbol{\theta}, \boldsymbol{\theta'}|V_\mathrm{r})$. The proposed value is then accepted with a probability $\alpha(\boldsymbol{\theta}, \boldsymbol{\theta'}|V_\mathrm{r})$. Using the Bayes theorem, we can show that the posterior ordinate can be expressed at any point $\boldsymbol{\theta^*}$ of the chain with (see the demonstration of Chib & Jeliazkov, 2001):

$$p(\boldsymbol{\theta^*}|\boldsymbol{V_r}) = \frac{\frac{1}{M}\sum_{m=1}^{M}\alpha(\boldsymbol{\theta_m}, \boldsymbol{\theta^*}|V_\mathrm{r})q(\boldsymbol{\theta_m}, \boldsymbol{\theta^*}|V_\mathrm{r})}{\frac{1}{J}\sum_{j=1}^{j=J}\alpha(\boldsymbol{\theta^*}, \boldsymbol{\theta_j}|V_\mathrm{r})}, \tag{A.52}$$

where we removed the model M_d from the notations for clarity purposes, and where M and J are arbitrary integers, generally taken as large as possible. Eq. A.52 is valid for all $\boldsymbol{\theta^*}$ of the chain, and in particular at $\boldsymbol{\theta^*} = \boldsymbol{\theta_b}$, where $\boldsymbol{\theta_b}$ is the set of parameters that maximises the posterior density of the model. In this case, $\alpha(\boldsymbol{\theta_m}, \boldsymbol{\theta^*}|V_\mathrm{r}) = 1$, as a $\boldsymbol{\theta_b}$ will be accepted from any given other set of parameters. Once the posterior ordinate is computed, the natural logarithm of the marginal likelihood of the model is simply given by

$$\ln p(\boldsymbol{V_r}|M_\mathrm{d}) = \ln \mathscr{L}(\boldsymbol{V_r}|\boldsymbol{\theta_b}, M_\mathrm{d}) + \ln \pi(\boldsymbol{\theta_b}|\mathrm{M_d}) - \ln \pi(\boldsymbol{\theta_b}|\boldsymbol{V_r}, \mathrm{M_d}) \tag{A.53}$$

Practical implementation

The posterior distribution of the model parameters is sampled using EMCEE whose proposal density is not trivial to compute. To compute the marginal likelihood of the model, we run another MCMC process, this time using Metropolis-Hastings steps with a Gaussian proposal density

$$q(\boldsymbol{\theta_m}, \boldsymbol{\theta_b}|V_\mathrm{r}) = \exp\left[-\frac{1}{2}(\boldsymbol{\theta_m} - \boldsymbol{\theta_b})^\mathrm{T}\boldsymbol{\Sigma_j}\boldsymbol{\theta_m} - \boldsymbol{\theta_b})\right], \tag{A.54}$$

where $\boldsymbol{\Sigma_j} = \mathrm{diag}(\sigma_1, ..., \sigma_{n_\mathrm{p}})$ is the covariance matrix of the MCMC jumps, n_p being the number of parameters of the model. The values of σ_i are initially set to the 1σ error bars determine from the posterior distribution of the parameter $\theta^{(i)}$ obtained with EMCEE. We then empirically tune $\boldsymbol{\Sigma_j}$, by typically running MH processes of 10 000 iterations each and rescaling the jumps until the acceptance rate of the MCMC process lies around the values recommended in Gelman et al. (1996) (typically $\sim$0.28 when n_p=4). We then run the MH process on typically $M = 300\,000$ iterations. Using the distribution of samples in the chain, we compute the numerator of the posterior ordinate using Eq. A.54. The denominator is empirically computed by running typically $J = 300\,000$ MH starting from $\boldsymbol{\theta_b}$, each of a single iteration and using the same proposal density as for the main MH, and take the average acceptance rate over the J iterations. The marginal likelihood is finally computed using Eq. A.53, assuming that $\pi(\boldsymbol{\theta_b}|\mathrm{M_d}) = 0$.

B | Publications

B.1 List of publications

- **Klein** et al., *Investigating the young AU Mic system with SPIRou: large-scale stellar magnetic field and close-in planet mass*, submitted to MNRAS
- **Klein** et al., *The large-scale magnetic field of Proxima Centauri near activity maximum*, accepted in MNRAS
- Martioli et al., 2020, *Spin-orbit alignment and magnetic activity in the young planetary system AU Mic*, A&A, 641, L1 (I am author 18). https://ui.adsabs.harvard.edu/abs/2020A%26A...641L...1M/abstract
- Moutou et al., 2020, *Early science with SPIRou: near-infrared radial velocity and spectropolarimetry of the planet-hosting star HD 189733*, accepted to A&A (I am author 17) https://ui.adsabs.harvard.edu/abs/2020arXiv200805411M/abstract
- Jauzac, **Klein** et al., 2020, *Galaxy cluster cores as seen with VLT/MUSE: new strong-lensing analyses of RX J2129.4+0009, MS 0451.6-0305 & MACSJ2129.4-0741*, submitted to MNRAS https://ui.adsabs.harvard.edu/abs/2020arXiv200610700J/abstract
- Tam et al., 2020, *The distribution of dark matter and gas spanning 6 Mpc around the post-merger galaxy cluster MS 0451−03*, MNRAS, 496, 4032 https://ui.adsabs.harvard.edu/abs/2020MNRAS.496.4032T/abstract
- **Klein** & Donati, 2020, *Simulated mass measurements of the young planet K2-33b*, MNRAS, 493, L92 https://ui.adsabs.harvard.edu/abs/2020MNRAS.493L..92K/abstract
- **Klein** & Donati, 2019, *Simulating radial velocity observations of trappist-1 with SPIRou*, MNRAS, 488, 5114 https://ui.adsabs.harvard.edu/abs/2019MNRAS.488.5114K/abstract

B.2 Publications as a first author

In this Section, I provide the first page of my publications (arXiv version) as a first author. The full versions of the articles are available online using the links provided in each subsection.

B.2.1 Investigating the young AU Mic system with SPIRou: large-scale stellar magnetic field and close-in planet mass

Full version of the article: https://arxiv.org/abs/2011.13357.

MNRAS **000**, 1–16 (2020) Preprint 13 October 2020 Compiled using MNRAS LATEX style file v3.0

Investigating the young AU Mic system with SPIRou: large-scale stellar magnetic field and close-in planet mass

Baptiste Klein[1]★, Jean-François Donati[1], Claire Moutou[1], Xavier Delfosse[2], Xavier Bonfils[2], Eder Martioli[3,4], Pascal Fouqué[1,5], Ryan Cloutier[6], Étienne Artigau[7], René Doyon[7], Guillaume Hébrard[3], Julien Morin[8], Julien Rameau[2], Peter Plavchan[9], Eric Gaidos[10]

[1]*Université de Toulouse, CNRS, IRAP, 14 av. Belin, 31400 Toulouse, France*
[2]*CNRS, IPAG, Université Grenoble Alpes, 38000 Grenoble, France*
[3]*Institut dAstrophysique de Paris, UMR7095 CNRS, Université Pierre & Marie Curie, 98bis boulevard Arago, 75014 Paris, France*
[4]*Laboratorio Nacional de Astrofisica (LNA/MCTI), Rua Estados Unidos, 154, Itajuba, MG, Brazil*
[5]*CFHT Corporation; 65-1238 Mamalahoa Hwy; Kamuela, Hawaii 96743; USA*
[6]*Center for Astrophysics | Harvard & Smithsonian, 60 Garden Street, Cambridge, MA, 02138, USA*
[7]*Institut de Recherche sur les Exoplanètes (IREx), Département de Physique, Université de Montréal, C.P. 6128, Succ. Centre-Ville, Montréal, QC, H3C 3J7,Canada*
[8]*LUPM, Université de Montpellier, CNRS, Place Eugène Bataillon, F-34095 Montpellier, France*
[9]*Department of Physics and Astronomy, George Mason University, Fairfax, VA, 22030, USA*
[10]*Department of Earth Sciences, University of Hawai'i at Manoa, Honoluu, HI 96822 USA*

Accepted XXX. Received YYY; in original form ZZZ

ABSTRACT

We present a velocimetric and spectropolarimetric analysis of 27 observations of the 22-Myr M1 star AU Microscopii (AU Mic) collected with the high-resolution *YJHK* (0.98-2.35 μm) spectropolarimeter SPIRou from 2019 September 18 to November 14. Our radial velocity (RV) time-series exhibits activity-induced fluctuations of 45 m s^{-1} RMS, ∼3× smaller than those measured in the optical domain, that we filter using Gaussian Process Regression. We report a 3.9σ-detection of the recently-discovered 8.46 d-transiting planet AU Mic b, with an estimated mass of $17.1^{+4.7}_{-4.5}$ $M_\oplus$ and a bulk density of 1.3 ± 0.4 g cm^{-3}, inducing a RV signature of semi-amplitude K=$8.5^{+2.3}_{-2.2}$ m s^{-1} in the spectrum of its host star. A consistent detection is independently obtained when we simultaneously image stellar surface inhomogeneities and estimate the planet parameters with Zeeman-Doppler Imaging (ZDI). Using ZDI, we invert the time series of unpolarized and circularly-polarized spectra into surface brightness and large-scale magnetic maps. We find a mainly poloidal and axisymmetric field of 475 G, featuring, in particular, a dipole of 450 G tilted at 19° to the rotation axis. Moreover, we detect a strong differential rotation of $d\Omega = 0.167 \pm 0.009$ rad/d shearing the large-scale field, about twice stronger than that shearing the brightness distribution, suggesting that both observables probe different layers of the convective zone. Even though we caution that more RV measurements are needed to accurately pin down the planet mass, AU Mic b already appears as a prime target for constraining planet formation models, studying the interactions with the surrounding debris disk, and characterizing its atmosphere with upcoming space- and ground-based missions.

Key words: planets and satellites: formation – stars: magnetic fields – stars: imaging – stars: individual: AU Microscopii – techniques: radial velocities – techniques: polarimetry

1 INTRODUCTION

Close-in planetary systems orbiting and transiting pre-main-sequence (PMS) stars are key targets to improve our understanding of how planets form and evolve. Their orbital parameters (e.g., orbit ellipticity and spin-orbit obliquity) and the composition of their atmosphere can yield essential information about their formation history (Baruteau et al. 2016; Madhusudhan 2019). Moreover, the evolution of their bulk density during the early stages of their lives is critically needed to constrain planet formation and evolution models (e.g. Alibert et al. 2005; Mordasini et al. 2012a,b). This requires to precisely measure both planet masses, by monitoring the radial velocity (RV) of their host star, and radii, through the relative depth of their photometric transit curve.

★ E-mail: baptiste.klein@irap.omp.eu

B.2.2 The large-scale magnetic field of Proxima Centauri near activity maximum

Full version of the article: https://arxiv.org/abs/2010.14311.

MNRAS **000**, 1–7 (2020) Preprint 14 October 2020 Compiled using MNRAS LATEX style file v3.0

The large-scale magnetic field of Proxima Centauri near activity maximum

Baptiste Klein[1],★ Jean-François Donati[1], Élodie M. Hébrard[1], Bonnie Zaire[1], Colin P. Folsom[1], Julien Morin[2], Xavier Delfosse[3], Xavier Bonfils[3]

[1]*Université de Toulouse, CNRS, IRAP, 14 av. Belin, 31400 Toulouse, France*
[2]*LUPM, Université de Montpellier, CNRS, Place Eugène Bataillon, F-34095 Montpellier, France*
[3]*CNRS, IPAG, Université Grenoble Alpes, 38000 Grenoble, France*

Accepted XXX. Received YYY; in original form ZZZ

ABSTRACT

We report the detection of a large-scale magnetic field at the surface of the slowly-rotating fully-convective M dwarf Proxima Centauri. Ten circular polarization spectra, collected from April to July 2017 with the HARPS-Pol spectropolarimeter, exhibit rotationally-modulated Zeeman signatures suggesting a stellar rotation period of 89.8 ± 4.0 d. Using Zeeman-Doppler Imaging, we invert the circular polarization spectra into a surface distribution of the large-scale magnetic field. We find that Proxima Cen hosts a large-scale magnetic field of typical strength 200 G, whose topology is mainly poloidal, and moderately axisymmetric, featuring, in particular, a dipole component of 135 G tilted at 51° to the rotation axis. The large-scale magnetic flux is roughly 3× smaller than the flux measured from the Zeeman broadening of unpolarized lines, which suggests that the underlying dynamo is efficient at generating a magnetic field at the largest spatial scales. Our observations occur ∼1 yr after the maximum of the reported 7 yr-activity cycle of Proxima Cen, which opens the door for the first long-term study of how the large-scale field evolves with the magnetic cycle in a fully-convective very-low-mass star. Finally, we find that Proxima Cen's habitable zone planet, Proxima-b, is likely orbiting outside the Alfvèn surface, where no direct magnetic star-planet interactions occur.

Key words: techniques: polarimetric – stars: low-mass – stars: magnetic field – stars: rotation – stars: individual: Proxima Centauri

1 INTRODUCTION

Late M dwarfs are primary targets in the quest for Earth twins (Kasting et al. 1993). Their small masses and radii, as well as close-in habitable zones (HZ), make the detection of temperate Earth-like planets around them easier than around solar-like stars. As a result, the most favorable planets to further investigate habitability with forthcoming telescopes like the JWST and ELTs orbit stars with spectral type later than M4 (e.g., Berta-Thompson et al. 2015; Anglada-Escudé et al. 2016; Gillon et al. 2017; Dittmann et al. 2017; Astudillo-Defru et al. 2017b). However, these stars exhibit strong magnetic activity (e.g., West et al. 2011), whose manifestations, such as high-energy winds or frequent flaring events, are likely to affect the properties of the planets in their HZ. Therefore, understanding the processes underlying activity phenomena is a major prerequisite to study the conditions of habitability around low-mass stars (Lammer et al. 2007; France et al. 2016).

Late M dwarfs are fully-convective (FC; Baraffe et al. 1998). Their underlying dynamo processes remain mysterious, despite recent advances in the explanation of observations by numerical models (Yadav et al. 2015, 2016). Spectropolarimetric observations of FC stars have revealed a bimodal distribution of their magnetic properties with either strong axisymmetric dipoles, or weaker non-axisymmetric complex fields (Donati et al. 2006a; Morin et al. 2008, 2010; Kochukhov & Lavail 2017). The origin of this bimodality, tentatively explained by bistability in the dynamo process (Morin et al. 2011; Gastine et al. 2012, 2013), or a single oscillatory dynamo process (Kitchatinov et al. 2014), is still debated in the literature. However, most of the observational results currently available involve very active stars whose dynamo lies in the so-called saturated regime, i.e., on the plateau of the activity-Rossby number[1] relationship (typically, Rossby number $Ro \lesssim 0.1$ which corresponds to a rotation period of roughly 10 d for a mid-M dwarf; Pizzolato et al. 2003; Kiraga & Stepien 2007; Shulyak et al. 2017; Astudillo-Defru

★ E-mail: baptiste.klein@irap.omp.eu

[1] The Rossby number is defined as the stellar rotation period normalized to the convective turnover time, set to $\sim 143^{+31}_{-22}$ d for Proxima Cen using Wright et al. (2018) empirical relationship.

B.2.3 Simulated mass measurements of the young planet K2-33b

Full version of the article: https://arxiv.org/abs/2001.04304.

Monthly Notices
of the
ROYAL ASTRONOMICAL SOCIETY

MNRAS **493,** L92–L97 (2020)
Advance Access publication 2020 January 16

doi:10.1093/mnrasl/slaa009

Simulated mass measurements of the young planet K2-33b

Baptiste Klein[1,2]★ and J.-F. Donati[1,2]

[1]*Universite de Toulouse, UPS-OMP, IRAP, 14 Avenue E. Belin, Toulouse F-31400, France*
[2]*CNRS, IRAP/UMR 5277, Toulouse, 14 Avenue E. Belin, Toulouse F-31400, France*

Accepted 2020 January 12. Received 2020 January 10; in original form 2019 October 15

ABSTRACT

In this paper, we carry out simulations of radial velocity (RV) measurements of the mass of the 8–11 Myr Neptune-sized planet K2-33b using high-precision near-infrared velocimeters like SPIRou at the Canada–France–Hawaii Telescope. We generate an RV curve containing a planet signature and a realistic stellar activity signal, computed for a central wavelength of 1.8 μm and statistically compatible with the light curve obtained with K2. The modelled activity signal includes the effect of time-evolving dark and bright surface features hosting a 2 kG radial magnetic field, resulting in an RV signal of semi-amplitude $\sim$30 m s^{-1}. Assuming a 3-month visibility window, we build RV time series including Gaussian white noise from which we retrieve the planet mass while filtering the stellar activity signal using Gaussian process regression. We find that 35/50 visits spread over three consecutive bright-time runs on K2-33 allow one to reliably detect planet RV signatures of, respectively, 10 and 5 m s^{-1} at precisions $>3\sigma$. We also show that 30 visits may end up being insufficient in some cases to provide a good coverage of the stellar rotation cycle, with the result that the planet signature can go undetected or the mass estimation be plagued by large errors.

Key words: methods: statistical – techniques: radial velocities – stars: activity – stars: individual: K2-33 – planetary systems.

1 INTRODUCTION

Planet formation and evolution models critically need observational constraints on how planet bulk densities vary with time in the early stages of their lives (e.g. Mordasini et al. 2012; Alibert et al. 2013). This requires to measure radii of transiting planets through the relative depths of their photometric transits on the one hand, and masses through the semi-amplitudes of their radial velocity (RV) curves, on the other hand. Both measurements are challenging for pre-main-sequence (PMS) stars known to exhibit intense magnetic activity (e.g. Bouvier & Bertout 1989) inducing photometric and RV fluctuations that largely overshadow the planet signatures (e.g. Crockett et al. 2012). As a result, only a handful of candidate close-in giant planets younger than 20 Myr have been unveiled so far, either using RV observations (Donati et al. 2016; Johns-Krull et al. 2016; Yu et al. 2017) or transit photometry (David et al. 2016; Mann et al. 2016; David et al. 2019a,b). None of them have a well-measured bulk density.

Observing PMS stars in the near-infrared (nIR) rather than in the *V* band should make it easier to separate the planet signature from the stellar activity signal as the latter is expected to be weaker in this domain (Mahmud et al. 2011) and the stars are significantly reddened. High-precision nIR velocimeters like SPIRou (Donati et al. 2018), CARMENES (Quirrenbach et al. 2014), GIARPS (Claudi et al. 2017), or NIRPS (Wildi et al. 2017) are thus the most promising instruments worldwide to carry out mass measurements of close-in transiting planets orbiting PMS stars. Magnetic fields are however expected to affect stellar RV activity signals (Reiners et al. 2013; Hébrard et al. 2014), making the problem non-trivial and worth a detailed simulation study. This is especially relevant given that 300 nights of Canada-France-Hawaii Telescope (CFHT) time are already allocated to the SPIRou Legacy Survey (SLS), some of them being dedicated to the RV follow-up of stars hosting transiting planets, with the goal of measuring the planet masses.

K2-33 is an 8–11 Myr M3 PMS star located in Upper Scorpius that was shown to host a 5-$R_\oplus$ close-in transiting planet (David et al. 2016; Mann et al. 2016, hereafter D16 and M16, respectively) from the 80-d continuous light curve obtained during campaign 2 of the K2 mission (Howell et al. 2014). K2-33 will be observed with SPIRou as part of the SLS in an attempt to measure the mass of its close-in planet through RV observations. In this study, we propose to use K2-33 as a representative of the PMS stars to be observed within the SLS. We simulate SPIRou RV observations of this star and attempt retrieving the RV signature of the Neptune-sized planet assuming various planet masses, sampling schemes and levels of white noise. In Section 2, we outline how we generate the realistic synthetic time series for K2-33 and, in Section 3, their modelling in order to filter the stellar activity signal while estimating the

★ E-mail: baptiste.klein@irap.omp.eu

B.2.4 Simulating radial velocity observations of trappist-1 with SPIRou

Full version of the article: https://arxiv.org/abs/1907.05710.

Monthly Notices of the ROYAL ASTRONOMICAL SOCIETY

MNRAS **488,** 5114–5126 (2019) doi:10.1093/mnras/stz1953
Advance Access publication 2019 July 15

Simulating radial velocity observations of trappist-1 with SPIRou

Baptiste Klein[1,2]★ and J.-F. Donati[1,2]

[1]*Universite de Toulouse, UPS-OMP, IRAP, 14 Avenue E. Belin, Toulouse F-31400, France*
[2]*CNRS, IRAP/UMR 5277, Toulouse, 14 Avenue E. Belin, Toulouse F-31400, France*

Accepted 2019 July 11. Received 2019 July 8; in original form 2019 January 29

ABSTRACT

We simulate a radial velocity (RV) follow-up of the TRAPPIST-1 system, a faithful representative of M dwarfs hosting transiting Earth-sized exoplanets to be observed with SPIRou in the months to come. We generate an RV curve containing the signature of the seven transiting TRAPPIST-1 planets and a realistic stellar activity curve statistically compatible with the light curve obtained with the *K2* mission. We find a ± 5 m s^{-1} stellar activity signal comparable in amplitude with the planet signal. Using various sampling schemes and white noise levels, we create time-series from which we estimate the masses of the seven planets. We find that the precision on the mass estimates is dominated by (i) the white noise level for planets c, f, and e and (ii) the stellar activity signal for planets b, d, and h. In particular, the activity signal completely outshines the RV signatures of planets d and h that remain undetected regardless of the RV curve sampling and level of white noise in the data set. We find that an RV follow-up of TRAPPIST-1 using SPIRou alone would likely result in an insufficient coverage of the rapidly evolving activity signal of the star, especially with bright-time observations only, making statistical methods such as Gaussian Process Regression hardly capable of firmly detecting planet f and accurately recovering the mass of planet g. In contrast, we show that using bi-site observations with good longitudinal complementary would allow for a more accurate filtering of the stellar activity RV signal.

Key words: techniques: radial velocities – stars: individual: TRAPPIST-1 – stars: activity – methods: statistical.

1 INTRODUCTION

Transiting Earth-sized exoplanets are prime targets to better understand planet formation and evolution. In addition to estimating planet radii from transit depths, one can also measure planet masses through ground-based follow-ups of the host star radial velocity (RV) using high-precision velocimeters. The resulting mass-radius relations are used to constrain the planet interior structures and, beyond that, the whole paradigm of planet formation (e.g. Weiss & Marcy 2014; Zeng, Sasselov & Jacobsen 2016; Alibert & Benz 2017; Dorn et al. 2018). However, most of Earth-sized planets unveiled with the *Kepler* space telescope through transit photometry lack mass measurement, as they produce low-amplitude RV signatures ($\lesssim$1 m s^{-1}) on stars that are too faint for RV surveys in the *V* band. As a result, the mass–radius diagram of Earth-sized planets is populated by only a handful of planets with well-constrained bulk density (Santerne et al. 2018).

M dwarfs are the most promising targets to unveil Earth-like exoplanets with precise masses and radii. Beyond the fact that they largely outnumber stars with earlier spectral type in the solar neighbourhood (Henry et al. 2006), they feature smaller sizes and masses, and more compact habitable zones (HZ), making HZ terrestrial planets easier to detect as well as rosy candidates for further atmosphere characterization with the *James Webb Space Telescope* (Morley et al. 2017). Over the past few years, a growing number of attractive Earth-sized exoplanets have been discovered around M dwarfs from photometric surveys (Berta-Thompson et al. 2015; Dittmann et al. 2017; Gillon et al. 2017). This trend is expected to step up with the ongoing TESS mission (Ricker et al. 2015) as M dwarfs are known to frequently host multiple terrestrial planetary systems (e.g. Bonfils et al. 2013; Dressing & Charbonneau 2015; Gaidos et al. 2016).

The Spectro-Polarimetre Infra-Rouge (SPIRou; see Donati et al. 2018 for a complete review of the instrument and related science) is a near infrared (nIR) échelle spectropolarimeter at the Canada–France–Hawaii Telescope (CFHT) whose science observations have recently started. The combination of a resolving power of $\sim$70 000 over the *YJHK* bands and a goal RV precision of $\sim$1 m s^{-1} makes SPIRou ideally suited for detecting Earth-twins around M dwarfs, not least in the HZ where they typically produce an RV stellar reflex motion of $\sim$1 m s^{-1} (Artigau et al. 2018).

★ E-mail: baptiste.klein@irap.omp.eu

B.3 Press release

The work published in Klein et al. (2020) was accompanied by a national Press Release, aimed at presenting SPIRou capabilities (Donati et al., 2020a) and first results on the benchmark star HD 189733 (Moutou et al., 2020) and on the science target AU Mic (Martioli et al., 2020a; Klein et al., 2020), to which I contributed. The official version of the CNRS Press Release is included below (in French), whereas English versions can be found on the IRAP website[1], CFHT website[2] and SPIRou website[3].

[1] https://www.irap.omp.eu/en/2021/02/spirou-stares-at-a-young-rebel-the-au-mic-planetary-system/
[2] https://www.cfht.hawaii.edu/en/news/AUMicb/
[3] http://spirou.irap.omp.eu/News-Discoveries/News/2021-February-SPIRou-stares-at-a-young-rebel-the-AU-Mic-pla

COMMUNIQUE DE PRESSE NATIONAL – PARIS – 2 FEVRIER 2021

Exoplanète : première mesure de la densité d'une très jeune planète avec SPIRou

Menée par des scientifiques de l'Irap (CNRS/CNES/UT3-Paul Sabatier) et de l'Ipag (CNRS/UGA)[1], une équipe de recherche vient de mesurer pour la première fois la densité interne d'une très jeune exoplanète en orbite autour d'une étoile nouvellement formée et extrêmement active. Une performance obtenue grâce au « chasseur de planètes » SPIRou du télescope Canada-France-Hawaï (TCFH) et malgré le « vacarme » généré par l'activité de l'étoile. Ces résultats sont publiés dans *MNRAS* le 2 février 2021.

Elle n'a pas plus de 22 millions d'années, soit à peine quelques mois si l'on ramène la durée de vie d'une étoile à celle d'un être humain. L'étoile AU Microscopii (AU Mic) est donc très jeune, tout comme le système planétaire qui l'entoure, où réside la planète géante gazeuse nommée AU Mic b.

Cette exoplanète avait d'abord été détectée par la sonde TESS de la Nasa, et le spectropolarimètre SPIRou vient de révéler sa masse et sa densité. Elles sont très proches de celles de Neptune qui est son ainée de plus de 4 milliards d'années. Mais AU Mic b orbite 450 fois plus près de son étoile que Neptune ne le fait autour du Soleil. Son atmosphère atteint 300°C et on la classe donc dans la famille des « Neptune chauds ».

Son étoile, très active en raison de son jeune âge, génère d'intenses champs magnétiques qui rendent l'analyse du signal d'AU Mic b très complexe. Ce sont les capacités de SPIRou associées aux travaux pilotés par les scientifiques de l'Irap et de l'Ipag qui ont finalement permis de déterminer sa masse, et donc sa densité, malgré le « vacarme » engendré par l'activité d'AU Mic.

C'est la première fois que les astronomes ont accès à la fois la masse, grâce à SPIRou, et au rayon, grâce à TESS, d'une exoplanète de moins de 200 millions années. C'est également la première exoplanète dont la masse est mesurée par SPIRou, instrument de nouvelle génération conçu et construit sous la direction des équipes françaises et récemment installé au Télescope Canada-France-Hawaii (TCFH).

Dans trois autres articles[2] publiés récemment, les équipes de recherche associées à SPIRou ont également confirmé les performances inégalées dont ce nouvel instrument est capable, et étudié une autre caractéristique d'AU Mic b : l'inclinaison de son orbite. Celle-ci s'est révélée être bien alignée sur le plan équatorial de son étoile hôte, ce qui laisse penser que sa formation n'a pas été perturbée par d'autres objets massifs, comme l'a mis en évidence l'étude menée par l'Institut d'astrophysique de Paris (CNRS/Sorbonne Université).

Tous ces résultats apportent de nouvelles informations qui aideront à préciser les modèles de formation et de migration des planètes.

Notes

1- L'Institut de recherche en astrophysique et planétologie (CNRS/CNES/Université Toulouse III - Paul Sabatier) et l'Institut de planétologie et d'astrophysique de Grenoble (CNRS/UGA). Ont également participé à ces recherches des scientifiques du Laboratoire univers et particules de Montpellier (CNRS/Université Montpellier) et de l'Institut d'astrophysique de Paris (CNRS/Sorbonne Université). Ces études ont bénéficié d'un financement de l'ERC (NewWorlds #740651) et de l'ANR (SPlaSH ANR-18-CE31-0019)

2- https://doi.org/10.1051/0004-6361/202038695 ; https://doi.org/10.1051/0004-6361/202038108 ; https://doi.org/10.1093/mnras/staa2569

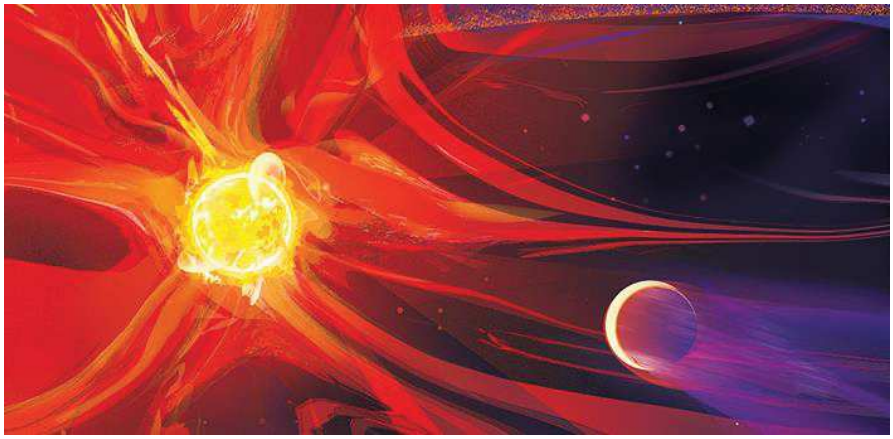

Vue d'artiste de la très jeune naine rouge éruptive AU Mic et de sa planète nouvellement découverte AU Mic b, avec au loin le disque de débris qui a donné naissance à la planète.
© NASA-JPL/Caltech

Bibliographie

Investigating the young AU Mic system with SPIRou: large-scale stellar magnetic field and close-in planet mass. Klein Baptiste, Donati Jean-François, Moutou Claire, Delfosse Xavier, Bonfils Xavier, Martioli Eder, Fouqué Pascal, Cloutier Ryan, Artigau Étienne, Doyon René, Hébrard Guillaume, Morin Julien, Rameau Julien, Plavchan Peter et Gaidos Eric. *MNRAS*, le 2 février 2021. https://doi.org/10.1093/mnras/staa3702

Contacts

Chercheur CNRS | Jean-Francois Donati | jean-francois.donati@irap.omp.eu

Chercheuse CNRS | Claire Moutou | claire.moutou@irap.omp.eu

Ex-doctorant CNRS (en post-doctorat à l'Université d'Oxford) | Baptiste Klein | baptiste.klein@physics.ox.ac.uk

Presse CNRS | François Maginiot | **T +33 1 44 96 43 09** | francois.maginiot@cnrs.fr